UCONN LIBRARY

University of Connecticut
OpenCommons@UConn

Doctoral Dissertations | University of Connecticut Graduate School

9-11-2017

Electrosprayed Polymerization: A Green, Additive Approach for Making Highly Tunable Polyamide Films for Desalination

Md Maqsudur Rahman Chowdhury
University of Connecticut, USA, mdmaqsudur.chowdhury@uconn.edu

Follow this and additional works at: https://opencommons.uconn.edu/dissertations

Recommended Citation
Chowdhury, Md Maqsudur Rahman, "Electrosprayed Polymerization: A Green, Additive Approach for Making Highly Tunable Polyamide Films for Desalination" (2017). *Doctoral Dissertations*. 1567.
https://opencommons.uconn.edu/dissertations/1567

Electrosprayed Polymerization: A Green, Additive Approach for Making Highly Tunable Polyamide Films for Desalination

Md Maqsudur Rahman Chowdhury, PhD

University of Connecticut, 2017

In membrane based desalination processes, the thin film composite (TFC) membrane is an industry standard which uses *interfacial polymerization* technique to form an ultra-thin polyamide layer on the surface of polymeric substrates. Remarkably, in 30 years of using this approach, the RO industry has yet to create a polyamide film onto a supporting membrane with controllable thickness, roughness and properties that are independent from the substrate properties. While the film formation essentially is "self-controlled", the reaction itself is simply allowed to proceed uncontrolled. Thickness and roughness impact membrane permeance and fouling propensity, respectively, and controlling these parameters could greatly benefit any process that uses a TFC membrane.

We developed a highly scalable, and green method for making tunable polyamide films for desalination. The method uses electrospraying technique to spray-deposit monomer solutions directly on to substrate which react to form the polyamide film. This is achieved through the use of lypophilic ionic liquid in the organic phase that contains one of the monomers. Comparable desalination performance to that of commercial membranes with sub-2 nm smoothness and a sub-4 nm resolution in film growth was achieved regardless of substrate properties. We also demonstrated the formation of a bulky 1 μm thick polyamide film of similar chemical structure for the first time. We further verified a two orders of magnitude lower chemical footprint using electrosprayed polymerization than the conventional method.

Electrosprayed Polymerization: A Green, Additive Approach for Making Highly Tunable Polyamide Films for Desalination

Md Maqsudur Rahman Chowdhury

B.S., Bangladesh University of Engineering and Technology, 2011
M.S., University of Connecticut, 2015

A Dissertation

Submitted in Partial Fulfillment of the

Requirements for the Degree of

Doctor of Philosophy

at the

University of Connecticut

2017

Copyright by

Md Maqsudur Rahman Chowdhury

2017

APPROVAL PAGE

Doctor of Philosophy Dissertation

Electrosprayed Polymerization: A Green, Additive Approach for Making Highly Tunable Polyamide Films for Desalination

Presented by

Md Maqsudur Rahman Chowdhury, B.S., M.S.

Major Advisor: _____

Jeffrey McCutcheon

Associate Advisor: _____

Ranjan Srivastava

Associate Advisor: _____

Leslie Shor

Associate Advisor: _____

Richard Parnas

Associate Advisor: _____

Rob McGinnis

University of Connecticut

2017

Acknowledgments

My greatest gratitude is toward my father Md Abdur Rahim Chowdhury and my mother Ms. Nargis Akhter. Their unselfish dedication and sacrifice toward the betterment of my education, wellbeing, and happiness is the driving force that pushed me forward (like forward osmosis) to achieve and do great things. My wife Fatema Parvez has always been there during the difficult times and throughout the ups and downs of graduate school. Her relentless support helped me focus on my research greatly. My brother Md Mahbubur Rahman Chowdhury and my sister Ms. Rahima Akhter consoled me in difficult times and took care of our parents. They made way for me so that I can pursue this dream of getting a PhD.

When I started out in 2012, I could not probably have asked for a better thesis advisor, mentor, and guide than Dr. Jeffrey McCutcheon. Dr. McCutcheon has always been there when I needed him. I truly appreciate that he understood my situation with my family and always gave me good advice and helped me to get what I needed and when I needed it. His critical but constructive comments have always made me a better researcher, planner, writer, and speaker. I appreciate his effort on making me a better presenter. I am sure this will be helpful throughout my whole career and I cannot thank him enough.

I would like to thank Dr. Brian Willis, and Dr. Brian Huey for allowing me to use their equipment which helped immensely in the thesis. I would like to acknowledge Dr. Ranjan Srivastava, Dr. Leslie Shor, Dr. Richard Parnas, and Dr. Rob McGinnis for agreeing to be on my thesis committee. The feedback I got from them during my proposal defense, made a grand contribution toward tuning and finalizing my thesis work.

I want to thank and acknowledge my lab mates whom I met at the McCutcheon lab. Dr. Ngoc Bui, Dr. Seetha Manickam, Dr. Dan Anastasio, Dr. Liwei Huang, Dr. Jason Arena, Dr. Jian Ren, Mr. Kevin Reimund, Ms. Lingling Xia, Ms. Nicole Beauregard, Ms. Yichen Wang, Mr. Mustafa Al-furaizi, Ms. Basma Waisi, Mr. Alan Ambrosi, Mr. Cong Ma, and Mr. Wenming Hao thank you all for making this a pleasant journey. I want to thank my undergraduate student mentee Brielle Cash, Caylin Cyr, and Steven Olenski with whom I really enjoyed working.

I would like to acknowledge Ms. Leah Winterberger, Ms. Susan Soucy, and Ms. Marita Decozio-Wiley for their administrative help throughout these years. The help and suggestion I got from Mr. Joe Csiki, Mr. John Pudelkiewicz, and Mr. Mark Drobney were very helpful. I would finally like to thank Dr. Lichun Zhang, Dr. Roger Ristau, Ms. Laura Pinatti, Dr. Maritza Abril, and Dr. Xuanhao Sun for their help in using characterization tools.

Table of contents

Chapter 1

State of desalination: Focusing on reverse osmosis (RO) and forward osmosis (FO)

1.1. Introduction

Access to fresh water has become a global concern in recent years for many countries. According to World Economic Forum, in the near future, the probability of occurrence of a major water crisis is inevitable and the impact it will have on human lives across the globe will be immense [1]. Countries like Bangladesh will be effected the most. Although there is an economic benefit for investment on sanitation and water, access to freshwater is limited [2]. Only 0.75 % of the earth's fresh water is available for withdrawal and human use globally while 97.5% of earth's water is saline [3]. As a result, a lot of focus have been given to desalination to produce fresh water. Multi stage flash distillation (MSF) and reverse osmosis (RO) are the most widely used technologies for desalination [4–6]. But newer technologies such as electro dialysis (ED), multi-effect distillation (MED), membrane distillation (MD) and forward osmosis (FO) have been in spot light to look for a less energy intensive process than MSF or RO [7–11].

In forward osmosis, a high osmotic pressure solution called the draw solution draws water from contaminated feed with a lower osmotic pressure across a semi-permeable membrane. Reverse osmosis, on the other hand, applies hydraulic pressure to reverse the natural osmosis process across a membrane to generate fresh water. FO has demonstrated a greater potential to desalinate seawater or purify waste water using the natural process of osmosis [11] but due to the thermodynamic irreversibility of FO process, recent studies have shown that FO requires more energy than today's RO plant which tend to shift FO focus on separating something more challenging like oil and gas produced water, municipal waste water, pre-treatment to RO etc. [12,13]. While this is true, focus areas such as membrane design to meet particular separation characteristics, system optimization, draw solution recovery and scale up of the FO process have been studied extensively [10], [14–26].

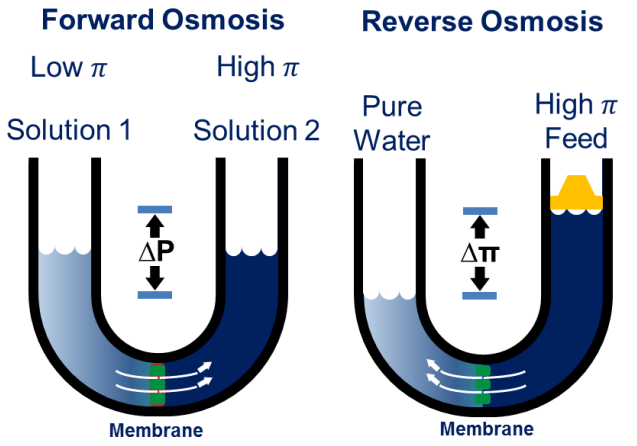

For RO, due to the simplicity of the process and development of high performance membranes (greater than 99.5% salt rejection) has led RO to be commercially successful [6], [27–30]. In terms of membrane development, initially, the focus for RO was asymmetric membrane which was first developed by Loeb and Sourirajan back in 1960 (Fig. 1.1a) [6]. They used a cellulose tri-acetate base polymer and made a cast membrane which had a dense thin layer and a porous support layer. Although, the membrane performed poorly, it was a breakthrough in desalination which led to further development of RO asymmetric membrane. The invention of thin film composite membrane (TFC) in 1980 by Cadotte, was a leap forward in making RO desalination technology commercially feasible (Fig. 1.1b) [28]. This led to subsequent innovation

and production of a variety of RO membrane to address issues like fouling, pH sensitivity, chlorine resistivity, module design, spacer design and system design [32–40]. Later, introduction of nanomaterial to make novel RO mixed matrix membrane got attention as the RO membrane fabrication using conventional technique was saturating [40–42].

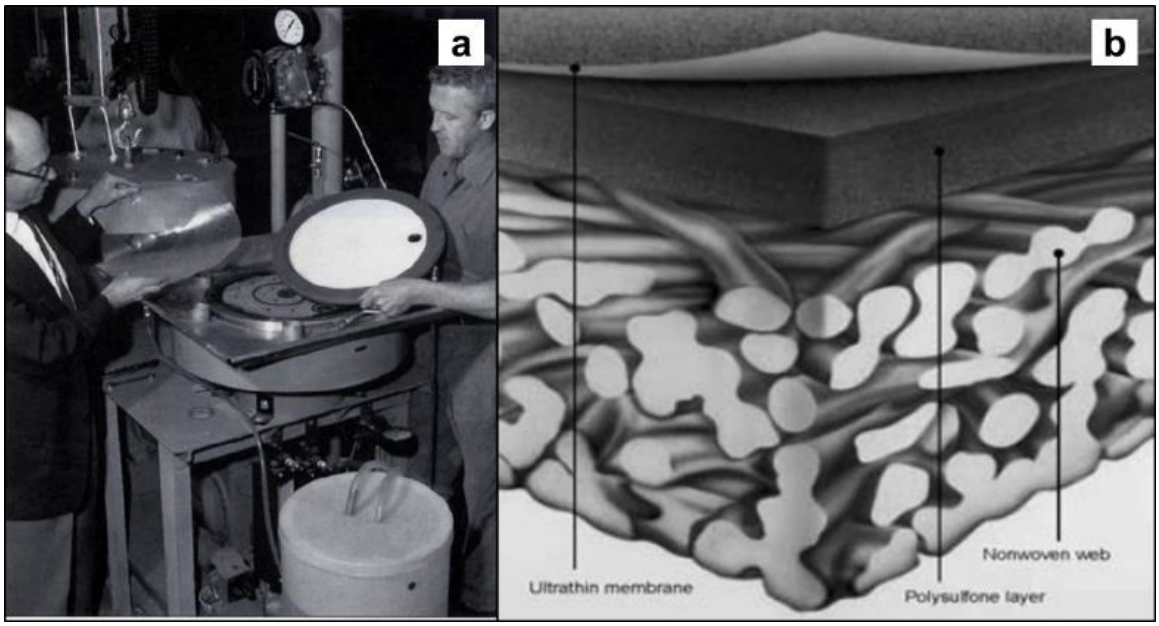

Figure 1.1: The first RO asymmetric membrane by Loeb-Sourirajan (a) and RO thin film composite membrane Cadotte (b)

This situation is also reflected in the research on FO where, at first, the focus was how to make RO membrane work for FO using different surface modification techniques (Fig. 1.2, a and b) [44]. Later, researchers started investigating more into the fundamentals of forward osmosis and found out the support structure needs to be redesigned to tailor it for FO application. This led to a series of papers looking at FO osmotic performance using different support materials. Inspired by the Loeb-Sourirajan cellulose based membrane, Hydration Technology Innovations (HTI) developed the first commercial FO asymmetric membrane using cellulose tri-acetate (CTA) [27]. Later HTI also developed a TFC version of FO membranes which demonstrated average osmotic performance as compared to other lab based TFC membrane (Fig. 1.2c) [45]. Yip et al produced a

lab scale TFC membrane using polysulfone as the support material which was casted over a PET fabric layer with subsequent IP [46]. The membrane demonstrated a finger like pore structure with a spongy thin layer on top. This created better mass transport due to a lower tortuosity in the support structure. The spongy thin layer supported the thin selective polyamide layer made through conventional IP (Fig. 1.2e). Bui et al used a lab scale electrospun nanofiber as the support material to create TFC membrane for FO (Fig. 1.2d) [47]. The membrane used polyacrylonitrile (PAN) as the polymer. The membrane was able to produce better osmotic performance with enhanced membrane intrinsic characteristics due to a highly porous hydrophilic support. Wang et al studied TFC membranes in a hollow fiber configuration (Fig. 1.2f) [48]. The idea for this membrane was to have a large packing density inside modules to have a higher throughput. The membrane had similar finger like pore structure as the membrane made by Yip et al with a polyamide on top the hollow fiber support. The membrane also demonstrated high osmotic flux than commercial flat sheet FO membrane.

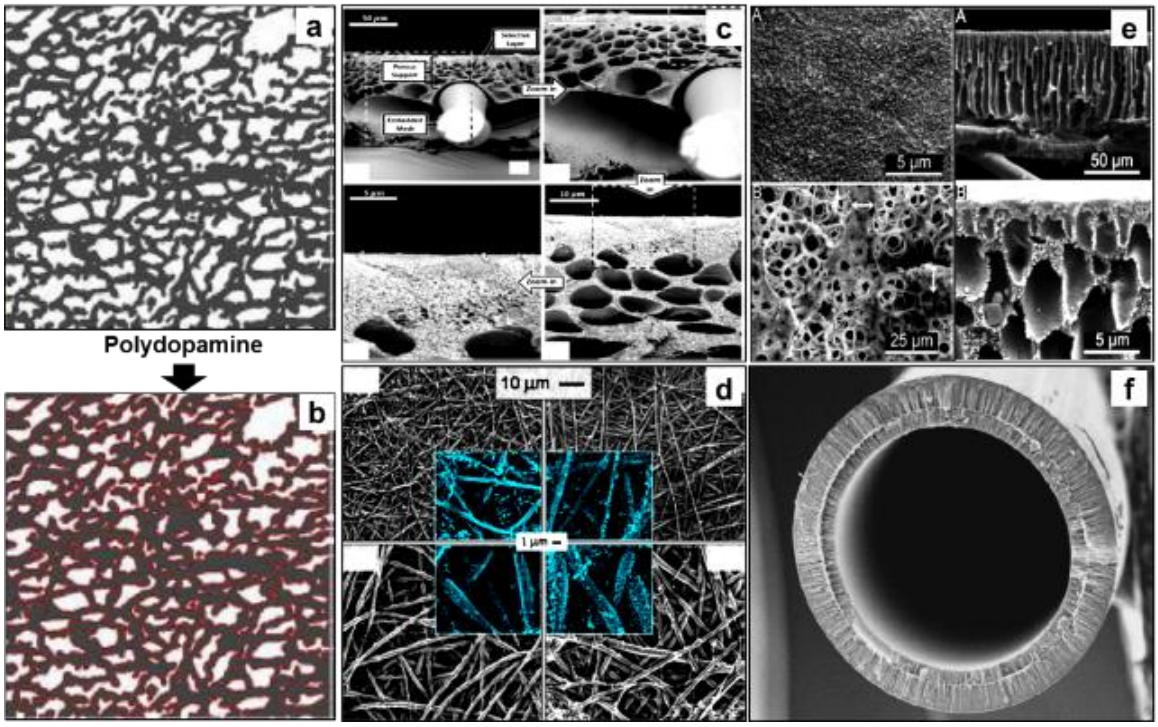

Figure 1.2: A review of FO membrane reflecting how the membrane focus has shifted from modification of RO membrane support to making novel support material specifically for FO.

Apart from membrane design, system design for large scale operation is also becoming more and more important for FO as it continues to mature as a desalination technology. Studies on utilizing FO to treat oil and gas produced water has been studied extensively [25,49–63]. Models for FO were also developed to understand the transport of mass across the membrane [21,64–66]. Some models also tried to incorporate the effect of changes in operating condition on the FO performance [63,64,67–70]. At a pilot scale, these operating condition can have a difference in FO performance compared to the bench-scale studies. Pilot scale studies of FO and FO hybrid system using element-size FO membrane is relatively new. Depending on what the end application is, FO can be utilized in a lot of different way. It can act as a dewatering technology such as in produced water, dilution technology such as fertigation, or even desalination such as using RO as a recovery step. These are new territories which are being explored now and it is still difficult to say whether FO can truly be used in one of these areas and be sustainable while doing it.

1.2. Objective and scope of dissertation

The objective of this dissertation work include:

1. Development of a bench-scale system and a mathematical model that can study and predict high recovery of industrial waste water using forward osmosis.
2. Develop a comprehensive mass and heat transfer model for forward osmosis targeting real operating scenarios.
3. Fabrication, installation, and commissioning of a pilot scale hybrid forward osmosis and reverse osmosis system to study recovery and to understand system behavior rising from process variables.
4. Characterize commercial membranes for a side by side comparison between coupon-scale and element-scale.
5. Exploration of commercial nanofiber based platform to make a high performance thin film composite membrane for forward osmosis.
6. Development of a method for making thin film composite membranes to address challenges associated with conventional interfacial polymerization.

1.3. Thesis organization

This thesis comprises of 7 chapters discussing different aspect of polymeric membrane based desalination. A cartoon figure of the layout of the thesis is presented in Fig. 1.3. The thesis focuses both aspect of membrane based desalination. From design of systems and modelling perspective, **Chapter 2, 3,** and **4** are presented. **Chapter 5** acts as a bridge between **Chapter 2-4** and **5-6**. **Chapter 6** introduces the concept of conventional IP while **Chapter 7** focuses on development of a new method for making TFC membranes. As each chapters addresses different issue associated

with desalination, an introduction is presented at the beginning of each chapter followed by methods, results, and conclusions. **Chapter 4** is still *in progress*, therefore a generic report is presented for this chapter. Appendixes are included at the end of the concluding remarks. The references are listed at the end of the thesis.

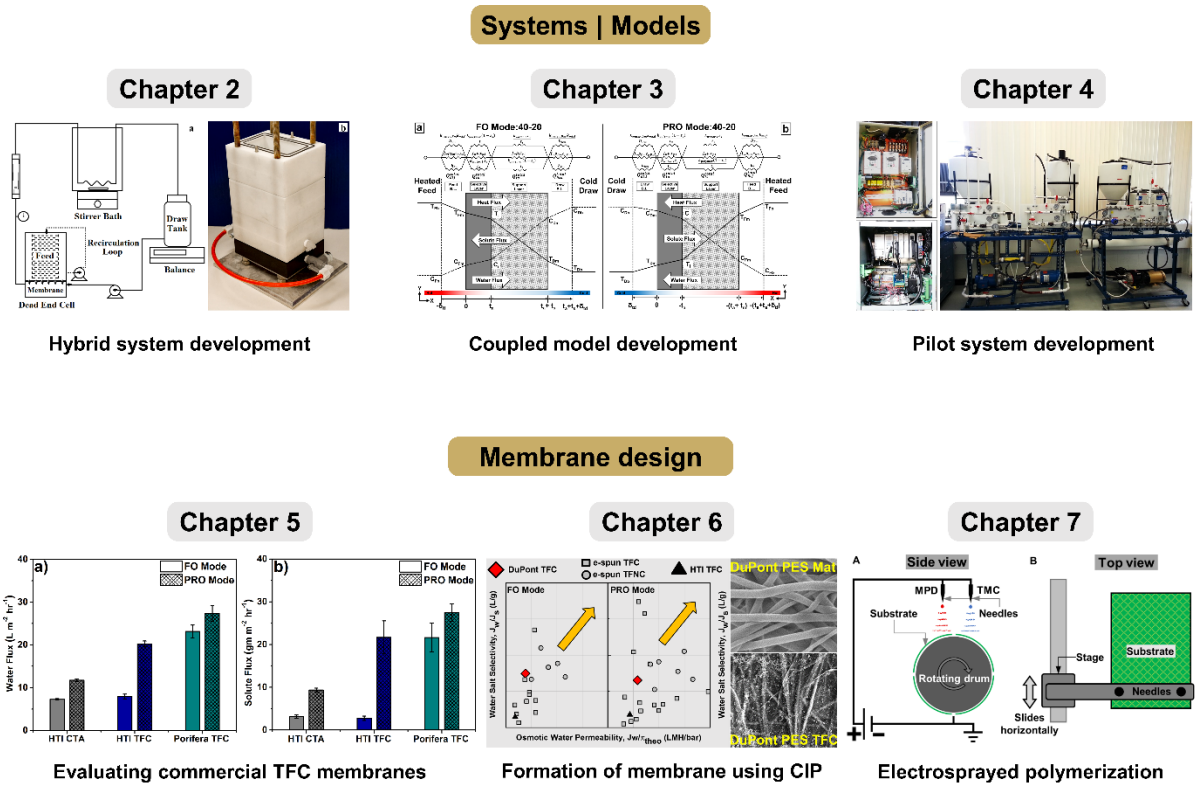

Figure 1.3: A diagram of the layout of the thesis.

In **Chapter 2**, a hybrid dead-end cross-flow bench-scale system and a mathematical mass transfer model was developed to study high recovery of difficult to treat waste water such as an oil and gas produced water. This was done using forward osmosis. Generally, cross-flow bench-scale setups are used for this but they have issues with regard to high hold-up volume resulting in limited recovery that can be achieved with these systems. They also require longer operation time and damage system parts. The system developed here addresses these issues.

This work was published in *Desalination*, 2016 (doi.org/10.1016/j.desal.2016.08.021)

In **Chapter 3,** a coupled heat and mass transfer model is being developed that tries to address the limitation of current generation of mass transfer models. Specfically, the current models ignore variability of solution properites through a membrane and effect of different temperature acrhoss the membrane, and uses an outdated method for osmotic pressure calculation. The developed model is built in such a way that it can accurately predict water and solute flux in forward osmosis for varying operating conditions that are typically seen in real application environment.

This work is currently under review in *Journal of membrane science*, 2017.

In **Chapter 4**, a brief discussion on the development of a pilot scale hybrid forward osmosis (FO) and reverse osmosis (RO) is presented. The pilot system comprises of element scale membrane modules for both FO and RO. The idea is to evaluate FORO performance under a variety of operating conditions and with real wastewater streams to understand the process, develop design of experiment, and evaluate key performance metric and compare it to a coupon-scale system developed in **Chapter 2** and verify model prediction developed in **Chapter 3**.

This work is still under progress and is being handed over to a new student to finish the project goals.

In **Chapter 5**, a new thin film composite membrane from Porifera was evaluated with regard to its osmotic performance. Other characterizations were also performed to compare to studies which

used the same membrane for different application. Focus was given on membrane performance between coupon-scale and element-scale (**Chapter 4**) and overall membrane design.

This work is directly connected to **Chapter 4** and still under progress.

In **Chapter 6**, the evaluation of a commercial nanofiber platform was explored based on previous knowledge of how a membrane's intrinsic separation characteristics influences performance at a bench-scale (**Chapter 2 and 3**) and at a pilot scale (**Chapter 4 and 5**) level for FO. A high performance thin film composite membrane was developed using commercial nanofiber platform for the first time for FO application by performing conventional interfacial polymerization (CIP). Limitations of CIP identified which led to the development of a new method for polyamide formation as discussed in **Chapter 7**.

This work is published in *Industrial & Engineering Chemistry Research*, 56, 2017, 1057-1063.

In **Chapter 7**, a method for forming tunable polyamide films for making thin film composite membrane is being developed. CIP (as discussed in **Chapter 6**) is unable to control polyamide thickness and roughness, and is a highly substrate dependent process. CIP has issues with regard to using large chemical baths and generating large chemical waste as well. A highly scalable and green method called electrosprayed polymerization (ESP) enabled us to address these key issues with the CIP method while being able to make sub-2 nm scale smooth and sub-4 nm thickness controlled polyamide films for desalination. We also demonstrate substrate independent formation of polyamide and made bulky polyamide film over 1 μm thick using the chemistry used in CIP to perform fundamental characterization.

This work is currently in manuscript preparation stage and will be submitted very soon.

Some concluding remarks been made at the end of **Chapter 7** with discussion on the future prospect of the ESP method.

1.4. Key contributions

In this thesis, a broader framework has been presented to address one of the key issue faced in membrane manufacturing. The bench-scale systems, coupled model, and pilot-scale systems helped understand the importance of membrane design and how system performance is greatly affected by membrane intrinsic properties. This led to the development of a high performance TFC membrane for FO using conventional IP method. Finally, a closer look at the CIP method reveals the challenges associated with it and why industry have been reluctant to change the process in the last 37 years since its inception. The ESP method provides a ground-breaking solution to these challenges.

The major contributions are summarized below:

A. Developed a simple methodology for dewatering produced water by a factor of 20. Mimicked performance of an element-scale membrane using a coupon-scale membrane.
B. More accurate prediction was achieved by coupling heat and mass transfer model. Identified feed temperature having a more pronounced impact on osmotic performance. Developed method to find overall heat transfer coefficient with validation using a model.
C. Fabricated an element-scale hybrid pilot systems coupling forward and reverse osmosis. Identified impact of different testing conditions such as flowrate, recovery rate, and pressure at element-scale. Flowrate has a more profound impact on osmotic performance for FO pilot system at element-scale.
D. The commercial nanofiber supported TFC membranes demonstrated very good osmotic performance compared to other lab-scale nanofiber based TFC membranes. The membranes

exhibited the best in-class mechanical properties.

E. Developed a novel method to make TFC membrane with modest desalination performance. The method has a very small chemical footprint and is highly scalable. The ESP method showed capability in controlling polyamide thickness at sub-4 nm resolution with controlling roughness at sub-2 nm scale. The method demonstrated substrate independence with regard to thickness, roughness, film formation, and NaCl salt rejection.

CHAPTER 2

Hybrid system development: Enabling high recovery study using FO

Originally published as:
A hybrid dead-end/cross-flow forward osmosis system for evaluating osmotic flux performance at high recovery of produced water
Maqsud R. Chowdhury, Jian Ren, Kevin Reimund, and Jeffrey R. McCutcheon in *Desalination, In Press*, 2016, doi.org/10.1016/j.desal.2016.08.021

2.1. Introduction

With the increased demand of petroleum based products there has been a substantial investment in expanding the hydrocarbon production infrastructure. In the past decade, unconventional production techniques such as fracking and horizontal drilling, have become commonplace as we extract oil and gas from shale formations around the United States [71]. These techniques require the use of large quantities of water along with chemical additives [72]. In fracking, about 50-70% of the injected water comes back up as flow-back water. In general, these, and other type of water recovered during the production of oil and gas, are known as produced water [73]. Different approaches have been considered for managing produced water. Large evaporation ponds [74], direct well injection, media filtration, adsorption, oxidation, chemical treatment [75], reverse osmosis [51,76], forward osmosis [50,53–56], membrane distillation [77] etc. are a few examples. Among these, forward osmosis is a relative newcomer. It has been advertised as being a technology with a low fouling propensity [78,79] and the capability of handling high TDS water sources in comparison to other technologies [77,80,81].

The academic community has long been challenged to demonstrate the efficacy of forward osmosis, especially in its ability to recover large percentages of water from feed solutions. Demonstrating high recovery requires substantial membrane area with membranes that exhibit high flux. Only recently have membranes been available to academics that exhibit high flux, either through making such membranes or by purchasing them from a company that manufactures them. The difficulty in making membranes or obtaining enough membrane has long necessitated the conservation of membrane material and has resulted in the preferred use of small membrane coupons in benchtop test rigs. These membrane areas (sometimes reported as being below 20 cm^2) are not large enough to generate high recoveries in short amount of time with conventional crossflow systems [82]. Recovery is also limited by the amount of the feed solution required to run the system. The pumps must be primed, the heat exchangers must be filled, and the tubes must all contain water free of air, meaning that hold up volumes may approach 30-50% of the total volume of feed solution. Holdup volumes could be reduced by reducing tubing size or heat exchanger area but these changes will increase pressure drop in the system and may limit temperature control capability, respectively.

Many of these problems could be solved by simply testing with full-scale modules. A number of them are now out on the market and have been tested and described in the literature in rare instances [53,83,84] . However, the standard operating procedures for these modules has not yet been established across the spectrum of possible feed and draw solutions. Furthermore, modules are expensive to purchase and therefore researchers are hesitant to use them with high fouling feeds, such as produced waters. If the module fouls, they may be cleaned, but they will likely never work as they did when they were first installed. Coupon testing allows for membranes to simply

be disposed of after use, which is especially valuable when conducting tests with high fouling solutions.

However, without the capability of testing FO performance of coupons at high recovery for these fouling solutions, we are forced to *simulate* high recovery by starting with a higher TDS feed solution. This is possible if these solutions can be synthesized. For example FO performance for a seawater feed at 50% recovery can be simulated by using a feed solution containing ~74,000 ppm TDS. However, if a non-synthetic feed that is difficult to replicate is provided, the only way to concentrate it for testing is to evaporate the water to the desired "recovery" level (i.e. evaporating half of the water to simulate 50% recovery). Heating a solution, especially if it contains volatiles or salts with retrograde solubility, can change the chemistry substantially during this "pre-concentration" process. Furthermore, if one wishes to study fouling phenomenon as a function of recovery, this approach effectively bypasses the early part of the process. Some have attempted to get around this with coupon test systems by simply running experiments for extended periods of time [53]. However, this can occupy conventional benchtop crossflow systems for days and make tubing and instrumentation on the feed side of the system susceptible to damage from long term exposure to high salinity or solutions that cause fouling. While mathematical modeling of FO could be used to calculate recovery, most of the modeling efforts in the literature have been focused on finding membrane properties and osmotic performance [18-23]. While these models on membrane performance may be used to predict recovery, many of them are prone to inaccuracy [86].

Dead-end cell based laboratory testing is commonly used in ultrafiltration and microfiltration applications and sometimes to characterize nanofiltration and reverse osmosis membranes [87]. To the best of our knowledge, dead-end cells have never been used in FO, except for u-tube

osmometers, which could be construed as being a dead-end FO system [88]. Here, we propose a new hybrid dead-end cross-flow cell bench top FO system to study flux performance of any solution at high recovery. A hybrid dead-end cross-flow FO system is unique as it provides relatively consistent driving force from the draw solution which flows through the cell in a crossflow nature and can be made in relatively large volumes (liters). The feed is kept in a stirred chamber on the opposite side of the membrane, allowing small volumes (half a liter or less) to be rapidly concentrated. Such a method has value in measuring possible recovery levels for various water sources using FO in a reasonable amount of time with coupon based membranes. Such a system also reduces risks to component damage due to scaling and fouling by limiting the feed solution to a dead-end chamber with few additional components. We demonstrate the value of this system using oil field produced water provided by Chevron Corporation. We used our data to develop a mathematical model to understand and predict water flux, feed, and draw concentration changes over a range of recoveries for the hybrid system.

2.2. Materials and methods

2.2.1. Materials

Commercial asymmetric cellulose triacetate (CTA) and thin film composite (TFC) forward osmosis (FO) membrane coupons were used for this study. Forward osmosis membranes were provided by HTI (Hydration Technology Innovations, Albany, OR). The membranes were stored in DI water at 5°C. An 8 cm x 3 cm size membrane coupon was used for each experiment. Sodium chloride was purchased from Fisher Scientific (Pittsburgh, PA). Deionized water (DI) was obtained from a Milli-Q ultrapure water purification system (Millipore, Billerica, MA) which was used for solution preparation. Produced Water (PW) was provided by Chevron Corporation. Produced water samples were sent out to commercial testing facilities (Geo-Chemical Water

Analysis, Midway Laboratory Inc.) to find different chemical constituents and properties of produced water. A number of standard methods were used to find the concentration of cations and anions. These includes SM2320 B (HCO_3^{-1}, CO_3^{-2}, OH^{-1}), SM4500-Cl^{-1} (Cl^{-1}), SM4500-SO_4^{-2} (SO_4^{-2}), SM4500-S^{-2} (S^{-2}), SM4500-SO_3^{-2} (SO_3^{-2}), ASTM D 6919 (NH_4^{-1}), EPA 200.7 (Ba^{2+}, B^{3+}, Ca^{2+}, Fe^{3+}, Mg^{2+}, K^{1+}, Na^{1+}, Sr^{2+}, As^{3+}, SiO_2), API RP 45 (Na^{1+}, Cl^{1-}) according to the report [89–92]. The chemical properties of the produced water are shown in Table 2.1. The total hardness of the water was 178.8 mg/L with a Langelier Stability Index (LSI) [93] of 0.67 and a Stiff & Davis Stability Index (S&DSI) [94] of 0.59. LSI and S&DSI are used to express the scaling potential of $CaCO_3$. For waters which have a TDS less than 10000 mg/L (brackish water), LSI is more appropriate to use. For TDS levels higher than that (seawater), S&DSI is used [95].

Table 2.1

Chemical properties of produced water

Cations	Conc. mg/L	Anions	Conc. mg/L	Other	Conc. mg/L
Na^+	2710	HCO_3^{-1}	677.6	SiO_2	159
Ca^{2+}	57.8	Cl^{-1}	4010	TOC*	67
Mg^{2+}	8.34	SO_4^{-2}	67.7	TRPH†	1.7
K^+	54.7			pH	7.87
B^{3+}	34.5			TSS‡	9.33
Fe^{3+}	0.54				

* TOC: Total organic carbon
† TRPH: Total recoverable petroleum hydrocarbon
‡ TSS: Total suspended solids

2.2.2.Methods

2.2.2.1. Control solutions

Produced water contains a number of species which have a high fouling propensity. These include organics, oils, and scalants. Because of the myriad of foulants, we used a control solution containing just salts as a baseline for performance comparison at various water recovery levels. The control solutions were prepared using sodium chloride and had the same total dissolve solids (TDS) level as the produced water at various projected recoveries.

2.2.2.2. Pre-concentration of produced water

To evaluate the performance of conventional crossflow FO systems and how it compares to a hybrid dead-end cross-flow setup, we pre-concentrated the produced water to simulate high recovery. Pre-concentrated produced water was prepared by evaporation at 60˚C. Concentration factors of 1.33, 2 (equivalent to 0.26 M NaCl control solution), 3.33, and 10 (equivalent to 1.28 M NaCl control solution) were achieved through evaporation to simulate recoveries of 25%, 50%, 70% and 90%, respectively (assuming complete inorganic and non-volatile organic retention). According to Table 2.1, TOC for the produced water was 67 mg/L while the TRPH (total recoverable petroleum hydrocarbon) was 1.7 mg/L. This means that there is only a very small quantity of organics present which are extractable from the unprocessed produced water. For this reason, we assumed that the loss of volatiles from the solution had a negligible impact on the solution properties. The pre-concentrated solutions were cooled down to room temperature and were not filtered before testing in the conventional FO systems.

2.2.2.3. Conventional cross-flow system

Conventional FO tests were conducted using a system described by our previous studies [67,82]. The FO mode orientation (support layer facing the draw solution) was applied in all experiments. The temperature of the feed and draw solution was maintained at 20˚C. Experiments using only NaCl were used as control tests. These synthetic controls allowed for easy simulation

of TDS levels at various recoveries. For example, 1.28 M NaCl solution has the same TDS as the produced water sample after 90% recovery. The feed concentration was varied from DI water to 1.28 M NaCl solution for different draw solution concentrations ranging from 2 M to 5 M NaCl solution. A volume of 2 liters of feed solution and 2 liters of draw solution was used in all experiments. Similar pressures (~3 psi) were maintained on both feed side and draw side to prevent membrane damage and the flow velocities were kept at 0.24 ms^{-1}. The Reynolds number was 1130 for both channels. These controls were compared to tests using pre-concentrated (by evaporation) produced water against a 3M NaCl draw solution.

2.2.2.4. Hybrid dead-end cross-flow system

A novel dead-end filtration cell was designed to be mounted onto one-half of a crossflow FO cell (See Fig. 2.1a). The cells were made using Delrin® (McMaster-Carr # 8739K81) with a chemical resistant O-ring (McMaster-Carr # 8333T284). The draw solution circulates as it would have for a conventional cross flow system (with temperature control) through the cross-flow cell. The feed solution remains in the dead-end cell and is either recirculated using a small external gear pump (1 LPM) (Model: 75211-22, Cole Parmer, IL, USA) or an overhead mixer (500 RPM) (Model: S-50006-01, Cole Parmer, IL, USA) to promote mixing in the dead-end cell. The impeller is a straight two blade impeller having a diameter of 1.2 inch. The dead-end cell consists of four parts with each part having an inside dimension of 12 cm x 6 cm x 6 cm with a volume of ≈ 550 cm^3 (Fig. 2.1b). The water column pressure inside the dead-end chamber can be as high as 0.5 psi, hence some back pressure in the draw channel may be necessary depending on the pressure drop in the system. A cross-flow flow velocity of 0.24 ms^{-1} was used on the draw side and the draw side pressure was kept at 3 psi. A solution of 0.13 M NaCl was used as a baseline feed (same TDS as the unprocessed produced water). Typical duration of each experiments were 10 hrs for a 500 ml

feed solution. During this time, there was no addition of stock NaCl solution to the draw side of the FO system to account for the dilution of the draw solution since the dilution was limited by the small overall flux volume.

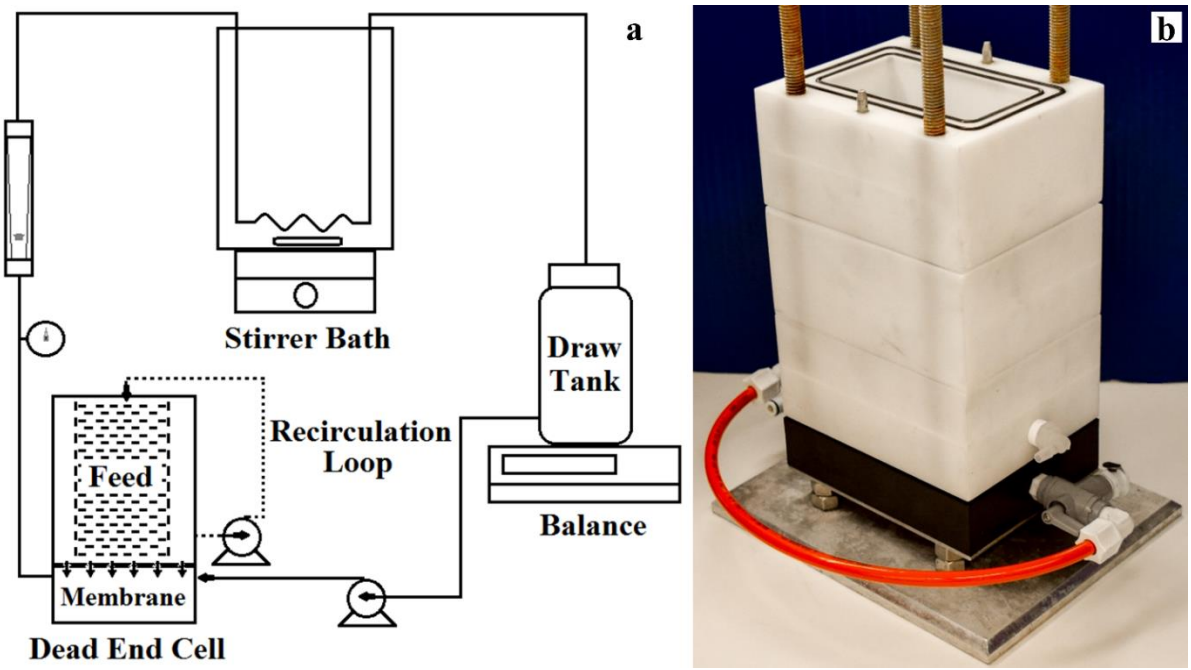

Figure 2.1: Schematic diagram of a hybrid dead-end cross-flow cell forward osmosis system (a) and a picture of the dead-end cell (b). The dashed line in Fig. 2.1a indicates the dead-end recirculation pump feed stream and solid line indicates crossflow draw stream. When an overhead stirrer is used, the recirculation loop is sealed off.

2.2.2.5. Reverse osmosis characterization

A conventional bench-top RO system was used to find the pure water permeance A and solute permeability B for the HTI TFC and HTI CTA membrane [67]. Here, the system was kept at 20˚C ± 1˚C and the flow velocity was maintained at 0.24 ms^{-1}. Pure water permeance was calculated at 75, 125, 175 and 225 psi with DI water as feed. Solute permeability was calculated at 225 psi using a 2000 ppm NaCl solution.

2.2.2.6. Microscopy characterization

A cold cathode field emission scanning electron microscope (FESEM) (JEOL 6335F) was used to examine the surface of the membrane after a test. The membrane sample was vacuum dried and sputter coated with a thin layer of gold (Au) and platinum (Pt) for 30 sec using a Polaron E5100 SEM coating unit. An accelerating voltage of 15kV was used for imaging. A Thermo Noran System Six EDS was also used to analyze the surface composition of the membrane. It should be mentioned here that the depth resolution of energy dispersive spectroscopy (EDS) is in the range of 20-2000 nm [96].

2.2.3.Mass transfer Model

2.2.3.1. Model development

The development of the model is restricted for the FO mode where the membrane selective layer is placed against the feed solution (Fig. 2.2). Here, water flows from the feed side towards the draw side and solutes also flow from the draw solution to the feed side. We assume that the system is at steady state, flow is fully developed across the membrane, and a no-slip condition exist at the membrane surface. Based on how we calculate Reynolds number in the dead-end chamber, two different models were proposed. In the crossflow model (used for the recirculating pump approach), the velocity and the hydraulic diameter of the crossflow side of the cell are used. For the mixer model, the diameter and speed of the impeller are used to calculate the Reynolds number based on established models described in literature [97]. Spreadsheets that were used to calculate the Reynolds number for both systems are provided as supplementary materials. We start the mass transfer analysis by using a 1-D mass balance across the selective layer for the solutes. The solute flux is related to the membrane solute permeability and the interface concentrations by the following equation [21,98]:

$$-J_s = -D_s \frac{dC}{dy} + J_w C = -B(C_i - C_{Fm}) \qquad (2.1)$$

Additionally, mass balances were performed on the feed and draw side boundary layer

$$-J_s = -D_{Fb}\frac{dC}{dy} + J_w C = -B(C_i - C_{Fm}) \tag{2.2}$$

$$-J_s = -D_{Db}\frac{dC}{dy} + J_w C = -B(C_i - C_{Fm}) \tag{2.3}$$

Using boundary conditions from Fig. 2.2 and Table H1, (2.1)-(2.3) are solved for C_i, C_{Fm} and C_{Dm} which is shown in the following steps for C_{Fm} (The remaining derivations are presented in the supplementary material).

$$\int_{-\delta_{tf}}^{0} dy = \frac{1}{D_{Fb}}\int_{C_{Fb}}^{C_{Fm}} \frac{dC}{J_w C + B(C_i - C_{Fm})}$$

$$\Rightarrow \frac{C_{Fm}\frac{J_w}{D_{Fb}} + \frac{B}{D_{Fb}}(C_i - C_{Fm})}{C_{Fb}\frac{J_w}{D_{Fb}} + \frac{B}{D_{Fb}}(C_i - C_{Fm})} = exp^{\frac{J_w \delta_{tf}}{D_{Fb}}}$$

$$\Rightarrow \quad C_{Fm} = C_{Fb} exp\left(\frac{J_w}{k_{mtf}}\right) + \frac{B}{J_w}(C_i - C_{Fm})\left\{exp\left(\frac{J_w}{k_{mtf}}\right) - 1\right\} \tag{2.4}$$

$$C_i = C_{Dm} exp\left(-\frac{J_w S}{D_{Db}}\right) + \frac{B}{J_w}(C_i - C_{Fm})\left\{exp\left(-\frac{J_w S}{D_{Db}}\right) - 1\right\} \tag{2.5}$$

$$C_{Dm} = \frac{C_{Db} exp\left(-\frac{J_w}{k_{mtd}}\right)\left[1 + \frac{B}{J_w}\left\{exp\left(\frac{J_w}{k_{mtf}}\right) - exp\left(-\frac{J_w S}{D_{Db}}\right)\right\}\right] - \frac{B}{J_w} C_{Fb} exp\left(\frac{J_w}{k_{mtf}}\right)\left\{exp\left(-\frac{J_w}{k_{mtd}}\right) - 1\right\}}{1 + \frac{B}{J_w}\left[exp\left(\frac{J_w}{k_{mtf}}\right) - exp\left\{\left(-\frac{J_w S}{D_{Db}}\right) + \left(-\frac{J_w}{k_{mtd}}\right)\right\}\right]} \tag{2.6}$$

Osmotic pressure was calculated using Pitzer correlations instead of Van't Hoff equation for finding osmotic coefficients for NaCl solutions at different concentrations and temperatures [99,100]. The equations for osmotic coefficient and osmotic pressure can be written as (details are presented in supplementary material):

$$\varphi_m - 1 = |z_+ z_-| f^{\varphi} + m\left(\frac{2\vartheta_+\vartheta_-}{\vartheta}\right) B_{MX}^{\varphi} + m^2\left(\frac{2(\vartheta_+\vartheta_-)^{3/2}}{\vartheta}\right) C_{MX}^{\varphi} \tag{2.7}$$

$$\pi = \vartheta R T \varphi^m \frac{M_w m}{v_{water}} \tag{2.8}$$

Finally, water flux and reverse salt flux can be calculated using the following two equations and the concentration values from (2.4)-(2.6) [19,29,98].

$$J_w = A(\pi_i - \pi_{Fm}) \quad (2.9)$$

$$J_s = B(C_i - C_{Fm}) \quad (2.10)$$

Previously, most of the models that were developed for forward osmosis used bulk solution concentration and properties in predicting water flux and reverse solute flux. In reality, the solutions that are near the selective layer and support layer interface can have substantially different properties (density, viscosity, diffusivity) than the bulk. We addressed this issue by developing fitted equations to experimental datasets for solution properties (Eqs. H10-H14) and incorporated the equations in the calculation of the solution properties across the selective layer [101,102]. We further extended the analysis to account for changes in volume of the feed and draw solutions which allow for proper accounting of changes in osmotic driving force as a function of time (Table H2). We coupled this analysis with equations (2.4)-(2.10) to predict water and solute flux.

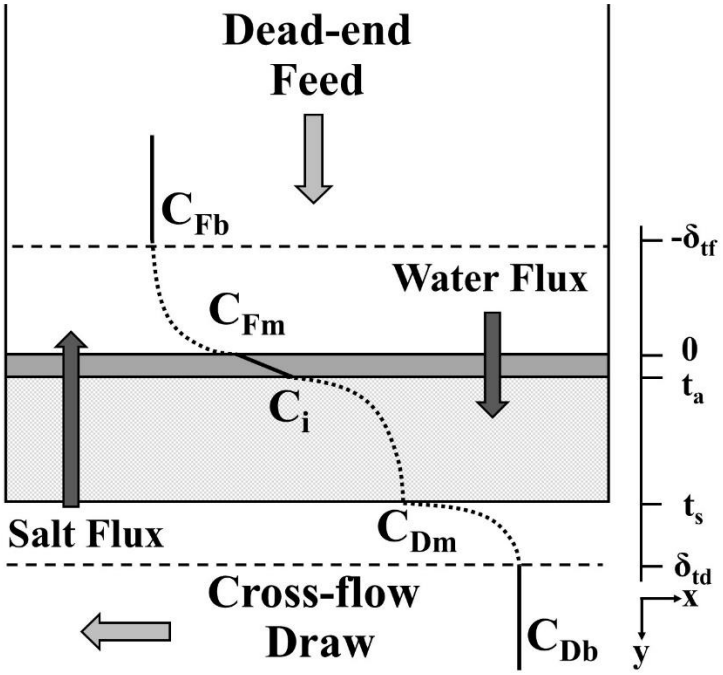

Figure 2.2: Concentration profile in a hybrid dead-end cross-flow system

2.2.3.2. Model Calculation

The models use Microsoft Excel spreadsheet solver to solve equations (2.4)-(2.10) (Appendix H). The macro incorporates these equations to calculate water and solute flux over a function of time. Volume and solute concentration are calculated, and used to define a new osmotic driving force using a 6-minute time step. A flow chart and solution property relationships are presented in the supplementary material.

2.3. Results & discussion

2.3.1. Membrane characterization

The two membranes were characterized based on their pure water permeance (A), salt permeability (B) and observed rejection (% R). The pure water permeance (A) for HTI CTA and HTI TFC membrane were 0.66 $Lm^{-2}hr^{-1}bar^{-1}$ and 1.503 $Lm^{-2}hr^{-1}bar^{-1}$ respectively. The NaCl salt permeability (B) for HTI CTA and HTI TFC were 0.61 $Lm^{-2}hr^{-1}$ and 1.79 $Lm^{-2}hr^{-1}$ respectively. The observed salt rejections of the HTI CTA and HTI TFC were 93% and 84%. The HTI TFC demonstrated less selectivity than its CTA counterpart while its water permeance was more than two times greater than the CTA membrane. This is in accordance with the recent study done by Ren [27].

2.3.2. Simulated recoveries of produced water

Using sodium chloride as a control, we simulated various levels of recovery for the produced water (minus fouling and scaling effects). Fig. 2.3 shows the result of these simulated recoveries. All the experiments were done on the conventional cross-flow forward osmosis setup. As expected, water flux increases with increasing draw solution concentration and it decreases with increasing simulated feed recovery. The HTI TFC membrane performs better than the HTI CTA membrane at low recoveries. This is due to the higher pure water permeance of HTI TFC membrane than its CTA counterpart. However, at the highest simulated recovery (1.28M NaCl feed), water fluxes for

both membranes were found to be equal to each other. This is attributed to mass transfer resistances in the support layer (known as internal concentration polarization (ICP)) [67,85,103] and on the feed side at the selective layer (external concentration polarization (ECP)) [64]. As mass transfer resistance become severe at high draw and feed concentrations, membrane permselectivity becomes less important.

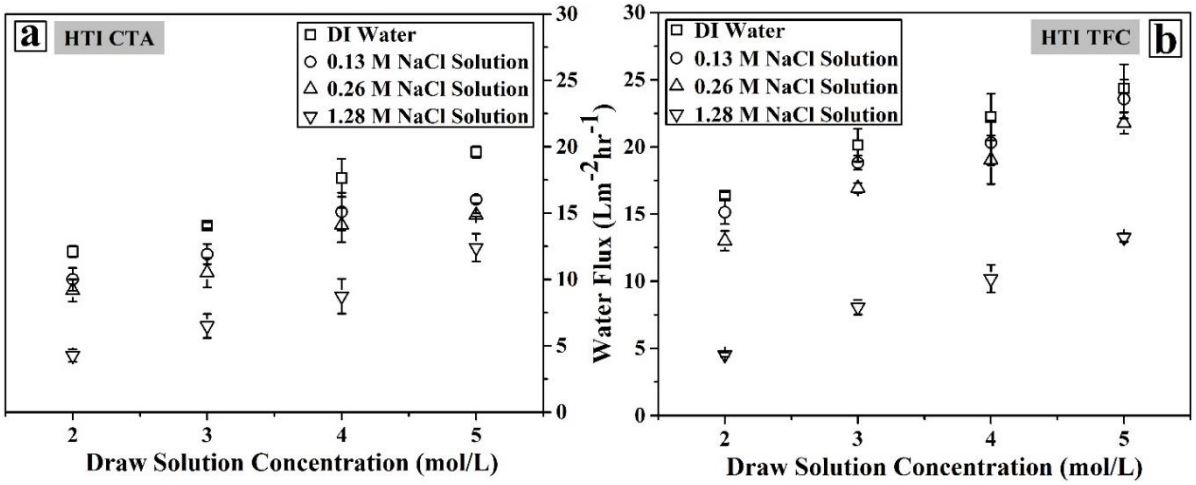

Figure 2.3: Effect of high feed recovery on water flux for different draw solution concentration in FO mode for HTI CTA (a) and HTI TFC (b) membrane. Experimental Conditions: Feed- DI water, 0.13 M (0% recovery), 0.26 M (50% recovery), 1.28 M (90% recovery) NaCl Solution; Draw- 2 M, 3 M, 4 M, 5 M NaCl Solution; Membrane- HTI CTA (a), HTI TFC (b); Cross-flow velocity: 0.24 m/sec; 20˚C; 3 psi pressure on feed and draw side. The error bar represents standard deviation for 3 tests at each condition.

2.3.3. Performance of the cross-flow system

Water flux performance using pre-concentrated produced water is shown in Fig. 2.4. Interestingly, the pre-concentrated produced water performs similarly to the control solutions. With the presence of scalable salts, however, we were expecting lower flux performance. We analyzed the pre-concentrated water (Table 2.2) and noted reductions in Ca^{2+}, HCO_3^{-1}, Fe^{3+} ions. Heating the solution likely caused HCO_3^{-1} to be removed as CO_2 and possible scaling of salts occurred in small quantities on the kettle. This dataset exemplifies why a conventional cross-flow

system is not ideal for high recovery tests and why pre-concentration of non-synthetic feed through evaporation is prone to error.

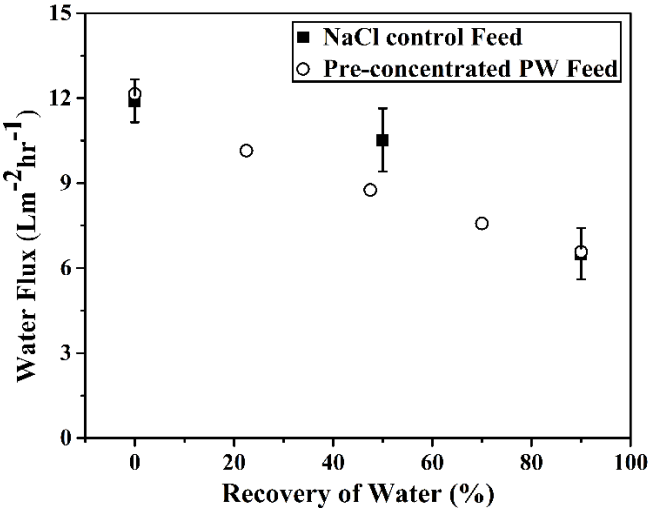

Figure 2.4: Comparison between pre-concentrated produced water to the NaCl control feed at simulated recoveries. Experimental Condition: Feed: Pre-concentrated produced water and NaCl control solutions varying from 0% to 90% recovery; Draw: 3 M NaCl solution; other conditions are similar to Fig. 2.3.

Table 2.2: Chemical properties at different recoveries for pre-concentrated produced water

Species	Recovery level			Species	Recovery level		
	0%	50%	75%		0%	50%	75%
	Concentration (mg/L)				Concentration (mg/L)		
Cations				**Anions**			
Na^{+}	2710	5660	11400	HCO_3^{-1}	678	442	139
Ca^{2+}	58	19	22	Cl^{-1}	4010	8550	16500
Mg^{2+}	8.3	14.5	15.4	SO_4^{-2}	68	297	506
K^{+}	55	115	250	CO_3^{-2}	0	98	373
B^{3+}	35	58	114	**Other**			
Fe^{3+}	0.54	0.027	0.002	SiO_2	159	325	143
				LSI	0.67	1.07	1.74

2.3.4. Performance of the hybrid dead-end cross-flow system

In Fig. 2.5, the experimental and model water flux performances of the dead-end cross-flow system are shown. Critical to the performance of dead-end system is the ability to adequately mix the system. The flux and recovery data from the two mixing approaches are presented in Fig. 2.5

using both the unprocessed produced water and a control test with NaCl at equal TDS. The recirculating pump approach is shown in Fig. 2.5a and the overhead motor-driven turbine mixer is shown in Fig. 2.5b.

The experimental data show that both mixing schemes allow for high recovery of the produced water and the control and show decline of water flux to zero as recovery approaches its maximum. The final recovery was lower with the recirculating pump (89 %) than it was with the overhead mixer (94 %). This corresponds to an 88,000 ppm solution for the recirculating pump and 143,000 ppm for the overhead mixer. This result shows just how critical mixing is for maximizing recovery for the hybrid system

To better quantify the differences between these mixing approaches, the model discussed above was applied and plotted in both Fig. 2.5a and 2.5b for both systems. The model for the mixer (denoted as mixer model) is relatively accurate in predicting water flux and ultimate recovery in the system. However, the model for the recirculating pump (denoted as crossflow model) deviates from the experimental data for both flux and recovery. We believe that the source of this deviation in the crossflow model is the calculation of the Reynolds number using an incorrect hydraulic diameter. Since the chamber is open and flow is being taken from both sides of the chamber, an accurate calculation of hydraulic diameter is difficult. Furthermore, this model fails to take into consideration the unrecoverable feed solution that remains in the recirculation tubes when a pump was used (about 40 mL). While this is a small volume, it becomes substantial at high recovery. This issue is likely the cause of the discrepancy between the predicted recovery of 94% and the actual recovery of 89%. On the other hand, modeling the overhead mixer Reynolds numbers is easier using established model [104]. This approach also keeps all of the liquid in the chamber

itself. As such, the models more closely predicted water flux and, more importantly, ultimate recovery.

Based on these results, it is clear that the greater agitation caused by the impeller mixer as well as the lack of holdup volume in a recirculating pump results in higher recoveries and more predictable results. Caution using an overhead stirrer is warranted, however, especially when working with slurries or suspended solids. A mixer may agitate these solids and cause abrade delicate and thin selective layers.

Based on the accurate prediction of recovery using the mixer model, we moved forward by extending this model to predicting concentrations of the feed and draw solution as a function of time during the NaCl control test. Fig. 2.6 shows the experimental concentrations of the feed and draw solution during the test. The draw solution shows modest decreases in concentration while the feed solution rapidly concentrates. This is due to the difference in volumes between the two solutions and, depending on the volume of draw solution being used, the dilution rate could be adjusted. A large volume of draw solution, for instance, would take longer to dilute and would create a flatter profile.

We applied the mixer model to Fig. 2.6 as well and saw some deviation with the experimental data. This matches the control data from Fig. 2.5b which shows differences in flux as water is recovered, but ultimately the final concentration is predicted. The higher predicted water fluxes from the model in Fig. 2.5b cause the earlier concentration of the feed in Fig. 2.6. We then varied the Re value in the model until it overlaid the data more accurately and found that a Re of 30 generated good agreement. While the calculated Re was 6500, our system is likely causing dead zones near the corners of the chamber due to non-optimum mixing, which can dramatically lower Re in these regions of the membrane [105]. Agreement between the model and the data improves

as recovery increases and flux declines because mass transfer resistances, like concentration polarization, become less important. Interestingly, in spite of this apparent limitation in the model to accurately predict mass transfer coefficient, the final prediction of recovery is quite accurate. If new dead-end cells are made with baffles or use a cylindrical geometry to produce more predictable mixing patterns, predicting concentration of the solutions at any time during the test would be possible. This is not necessary, however, to predict final recovery at osmotic equilibrium.

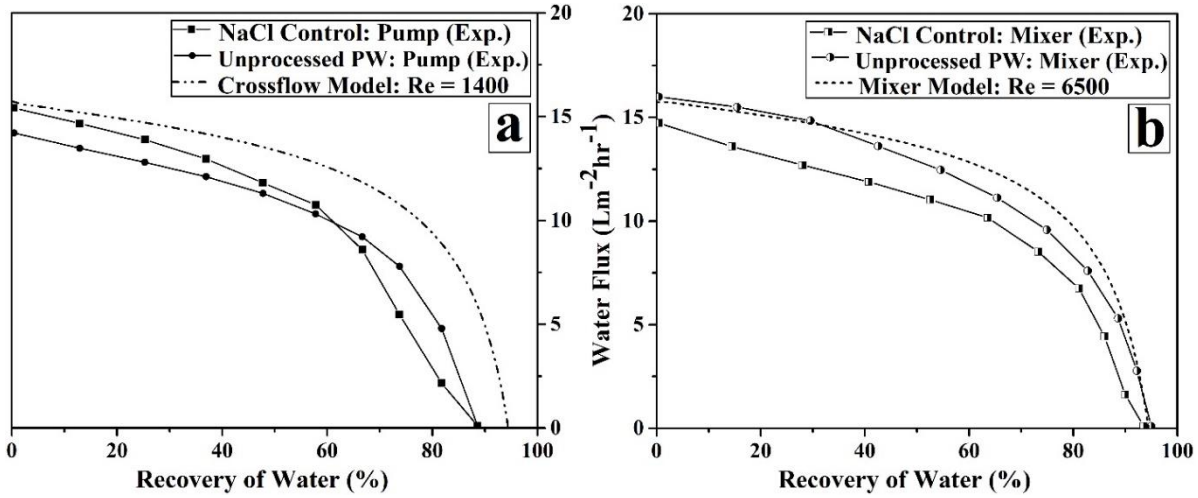

Figure 2.5: Comparison of water flux data between unprocessed produced water (PW), 0.13M NaCl control solution as feed with regard to experimental and modelled water flux for two different mixing systems. In (a), experimental and crossflow model predicted water flux for the recirculation pump, and in (b), experimental and mixer model predicted water flux for the mixer are presented. Experimental Conditions- Draw side: 3 M NaCl solution, 0.24ms^{-1}, 3 psi; Feed side: 0.13 M NaCl control and unprocessed produced water, 500 rpm (mixer)/ 1 LPM (pump), 0 psi; Membrane-HTI CTA.

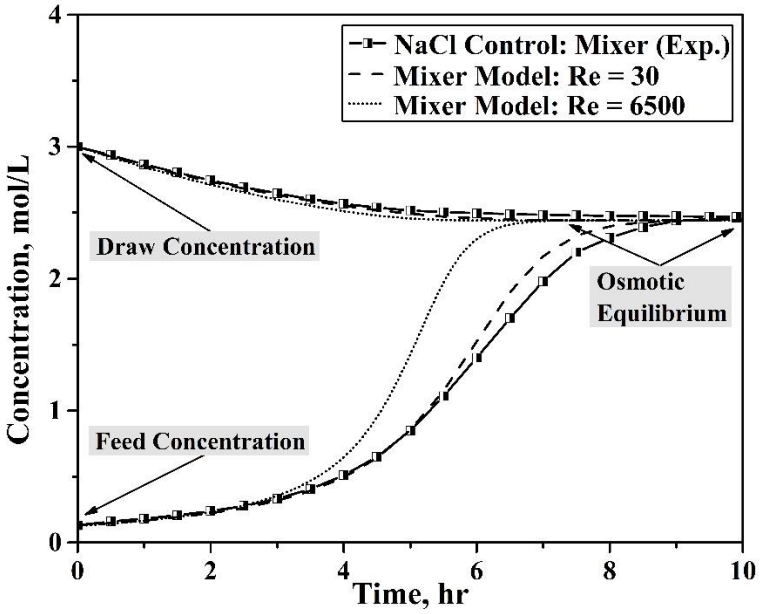

Figure 2.6: Comparison of concentration profile during recovery for the mixer models and the NaCl control experiment with the mixer. Experimental conditions are presented in Fig. 2.5.

2.3.5. Scaling behavior

An added benefit of the dead-end approach is that fouling and scaling can be rapidly studied using small amounts of membrane and without risk to salt and organic deposition throughout a crossflow system. Fig. 2.7a and 2.7b shows the image of the membrane after a 90 % recovery test of the control and unprocessed produced water, respectively. As expected, the NaCl control resulted in no noticeable scaling while the produced water produced significant scaling. The overhead mixer was used to agitate the feed. Your attention is drawn to the pattern on the scaled membrane, which is circular and roughly the same size of the impeller blades. The arrows indicate regions of dead-zone on the membrane surface (as suggested by the mixer model) where the deposition of salts is substantial. A closer look at these deposits (Fig. 2.7c) reveals the fouling on the surface of the membrane. The patterning on the membrane is consistent with the embedded mesh that HTI uses as a supporting material in its membrane. Scale formation is noted to form primarily between these mesh fibers since that is where the membrane is the thinnest and the flux

is the highest. Fig. 2.7d shows the EDS analysis of the deposits on the membrane that consists substantial quantities of Na, Cl, and Fe with lesser amounts of Ca, Si (as SiO_2), K, and Mg. Carbon and oxygen signals are likely from the membrane itself, though it is likely that carbonate and bicarbonate are also deposited on the surface. This demonstrates that fouling and scaling phenomenon can be studied with this this type of hybrid system.

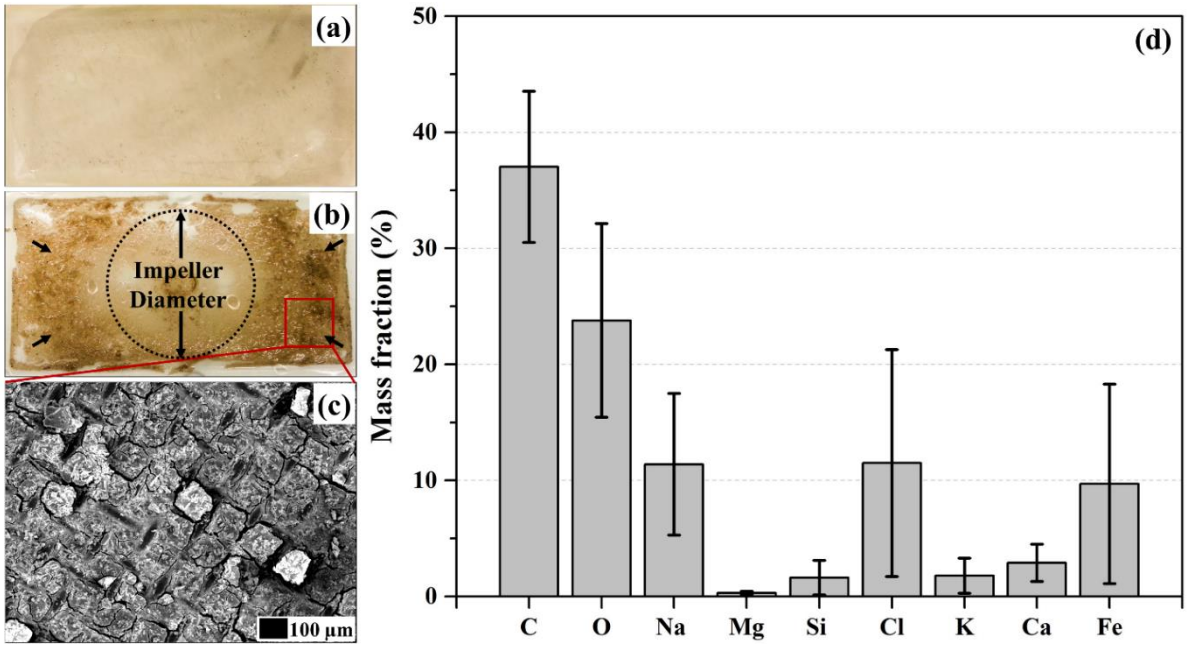

Figure 2.7: Membrane condition after a FO mode hybrid dead-end cross-flow test using a NaCl control (a) and unprocessed produced water as feed (b). The arrows in (b) indicate dead-zones on the membrane. The system operating conditions are similar to that mentioned in Fig. 2.5. Scanning electron micrographs of membrane (b) is shown in (c) at 95x magnification. Energy-dispersive X-ray spectroscopy (EDS) analysis of the selective layer surface is shown in (d).

2.3.6. Conclusion

The method presented demonstrates that testing of FO performance at high recovery is possible using coupon-scale membranes using the hybrid dead-end/cross-flow system. High recovery testing of raw waters with high fouling propensity is now possibly without the need to use large membrane areas or costly elements. In addition to saving membrane, this approach saves time and

feed solution. Faster testing enables higher throughput evaluations of membranes, feed solutions, and draw solution options. Saving feed solution can dramatically lower the cost of testing, especially when considering expensive feed solutions. While these benefits were shown to be effective when evaluating FO performance with produced water, these benefits easily translate to other feed solutions as well, including foods (juices, dairy) and pharmaceuticals (proteins, drugs).

Nomenclature

J_w	Water flux (L m^{-2} hr^{-1})
J_s	Salt Flux (gm m^{-2} hr^{-1})
ρ	Density of solution (Kg m^{-3})
C_{Fb}	Bulk feed concentration (mol L^{-1})
C_{Fm}	Feed side near membrane concentration (mol L^{-1})
C_i	Interfacial concentration between the active and support layer (mol L^{-1})
C_{Dm}	Draw side near membrane concentration (mol L^{-1})
C_{Db}	Bulk draw concentration (mol L^{-1})
A_m	Membrane area (m^2)
D_{Fb}	Feed side diffusivity of salt (m^2 s^{-1})
D_{Db}	Draw side diffusivity of salt (m^2 s^{-1})
Ds	Solute diffusion coefficient inside the support layer (m^2s^{-1})
k_{mtf}	Feed side mass transfer coefficient (m s^{-1})
k_{mtd}	Draw side mass transfer coefficient (m s^{-1})
t_s	thickness of support layer of the membrane (m)
B	Salt permeability (L m^{-2} hr^{-1})
S	Structural parameter (m)
τ	Membrane support layer tortuosity (dimensionless)
A	Pure water permeance (L m^{-2} hr^{-1} bar^{-1})
R	Ideal gas constant (L atm $mol^{-1}K^{-1}$)
δ_{tf}	Feed side mass transfer boundary layer thickness (m)
δ_{td}	Draw side mass transfer boundary layer thickness (m)
φ_m	Pitzer osmotic coefficient (dimensionless)
z_+	Charge on cation (dimensionless)
z_-	Charge on anion (dimensionless)
f^{φ}	Function of ionic strength (also temperature and solvent properties) expressing the effect of the long-range electrostatic forces (dimensionless)
m	Molality (mol/Kg)
υ_+	Number of cations (dimensionless)
υ_-	Number of anions (dimensionless)
B_{MX}^{φ}	Pairwise ion-interaction parameter of Pitzer's equation for the Gibbs energy (Kg/mol)
C_{MX}^{φ}	Triplet ion-interaction parameter of Pitzer's equation for the Gibbs energy (Kg/mol)
π	Osmotic pressure (atm)
T	Temperature (°C)
M_w	Molecular weight of water (Kg/mol)
υ_{water}	Molar volume of pure water (m^3/mol)
π_i	Osmotic pressure at the selective and support layer interface (atm)
π_{Fm}	Osmotic pressure at the feed side B.L. and selective layer interface (atm)

Chapter 3

Coupled model development: Accounting for simultaneous heat and mass transfer in FO

Originally submitted as:
Elucidating the impact of temperature gradients across membranes during forward osmosis: coupling heat and mass transfer models for better prediction of real osmotic systems
Maqsud R. Chowdhury and Jeffrey R. McCutcheon, under review, Journal of Membrane Science (2017)

3.1. Introduction

Forward osmosis is a process that has shown great promise as a technology for desalination and dewatering using the natural process of osmosis [11]. Although FO is thought of being an energy efficient process, the choice of draw solute and its recovery process largely governs the economics [12,50]. To this effect, several draw solutes have been considered [10,11,15–18]. Reverse osmosis [6,39], nano filtration [106], absorption/stripping [11,25] and membrane distillation [107–110] are some of the more often discussed processes which can be used to recover most of the types of draw solutes cited above. Reverse osmosis based draw solute recovery processes, while relying on a well-established technology, are not economically feasible for recovering high concentration of draw solutions due to the thermodynamic restrictions of osmotic pressure [111]. As a result, thermolytic recovery processes such as absorption/stripping and evaporative processes like membrane distillation have gained interest as they are not as thermodynamically restricted and only require low grade heat to operate [11,19,110]. However, this recovery process may leave the regenerated draw solution at an elevated temperature. If a heated draw solution is returned to the FO element, mass transfer will be impacted by different

solution properties such as density, viscosity, diffusivity, heat capacity and thermal conductivity. The same is true for feed solutions which, depending on their source, may be hot or cold. The situation is even more complicated if the feed and draw solution vary in temperature and if temperature gradients exist within the membrane element or train. This will result in the solution properties of both the feed and draw to vary with position.

Previous studies on FO have shown higher water and solute flux at elevated system temperature when both feed and draw temperatures are elevated [24,67,112,113]. Others have shown similar trends in changes in water flux performance when an temperature gradient was applied between the feed and the draw solution [70,114]. However, no studies have modeled the coupled heat and mass transfer effects on osmosis. Those that have included a modeling component [70] use assumptions with limited accuracy such as using average temperature rather than interface temperature to determine membrane intrinsic properties, using the Van't Hoff equation to determine osmotic pressure [64,70], and ignoring changes in solution properties as a function of position. Models which fail to account for these features are prone to error as FO finds new opportunities in hypersaline waters since solution property changes are substantial across the thermal and mass transfer boundary layers and along the module. Better predictive models are also becoming increasingly important as FO moves toward larger scale elements [25,115] and commercial systems [116].

We demonstrate here the hybridizing of well-established mass transfer models [63,64,67–69] with heat transfer models [70] to develop a more powerful predictive tool for FO water and solute transport. This comprehensive model allows for accurate prediction of osmotic performance under temperature gradients. The model incorporates the variability of solution properties (diffusivity, viscosity, density, thermal conductivity, and heat capacity) with well-established dependencies on

temperature and concentration to better predict these properties at different locations in the membrane. A detailed mass and heat transfer model is formulated in each region within the membrane and boundary layer outside the membrane. Osmotic pressures are calculated using Pitzer correlations [117] for osmotic coefficients to cover solution concentration ranging from very dilute to very high. We use experiments to verify model validity with a well characterized forward osmosis membrane and perform sensitivity analysis on key parameters to further optimize the model.

3.2. Materials and methods

3.2.1. Materials

Cellulose triacetate (CTA) membrane from HTI (Hydration Technology Innovations, Albany, OR) having an overall thickness of 85 μm is used for this study. The support layer porosity of the membrane was measured to be 0.57 using a gravimetric method described in [118] while the dense selective layer porosity was approximated as 0.0001. The membranes are stored in DI water at 4 ˚C. Sodium Chloride (Fisher Scientific, Pittsburgh, PA) is used to prepare the draw solution using deionized water (DI) which is collected from a Milli-Q ultrapure water purification system (Millipore, Billerica, MA).

3.2.2. Methods

3.2.2.1. Membrane intrinsic properties

Pure water permeance, and solute permeability coefficient of the membrane were characterized using a reverse osmosis bench-scale test setup [25, 26]. The test setup includes three cross-flow membrane cells where the membrane coupons were placed. Using DI water as feed, the pressure was varied from 75 psi to 225 psi with a constant flow velocity of 0.23 ms^{-1}. The calculated Reynolds number for the flow channel was found to be 1150. Three different temperatures were

studied where it was varied between 20, 30, and 40 ˚C. For each pressure, permeate was collected and weighted to get the water flux. A linear graph of water flux against feed pressure was generated the slope of which was noted as the pure water permeance (A). To measure solute rejection and permeability coefficient, a 2000 ppm feed solution was used as the feed without replacing the membranes in the cross-flow cell. Permeates were collected for 175 and 225 psi which were weighted and the conductivity of permeate was measured using conductivity probe. The solute permeability coefficient (B) was then calculated according to [27–29].

3.2.2.2. Osmotic test

Forward osmosis tests were carried out using a bench top FO system which is described in our previous work [19,44]. To control the temperature of each solution independently, two separate heat exchangers and baths were used (see Fig. 3.1). Four different temperature pairings were considered. Initially, both the feed and draw solution temperature were kept at 20 °C (designated as 20-20). Later, the feed solution temperature was raised from 20 °C to 40 °C while keeping the draw solution at 20 °C (designated as 40-20 or heated feed). The feed solution was then cooled to 20 °C and the draw solution was heated to 40 °C (designated as 20-40 or heated draw). The feed solution was then heated to 40 °C while the draw was retained at 40 °C (designated as 40-40). For each case, the solutions were circulated to heat and cool to their desired temperature prior to exposing them to the membrane using a bypass. Tests were conducted in both the FO and PRO orientations [67]. The transmembrane pressure was kept at zero and both sides were operated at 3 psi with a flow velocity of 0.24 m s^{-1}. Tests were conducted without any channel spacers for all conditions.

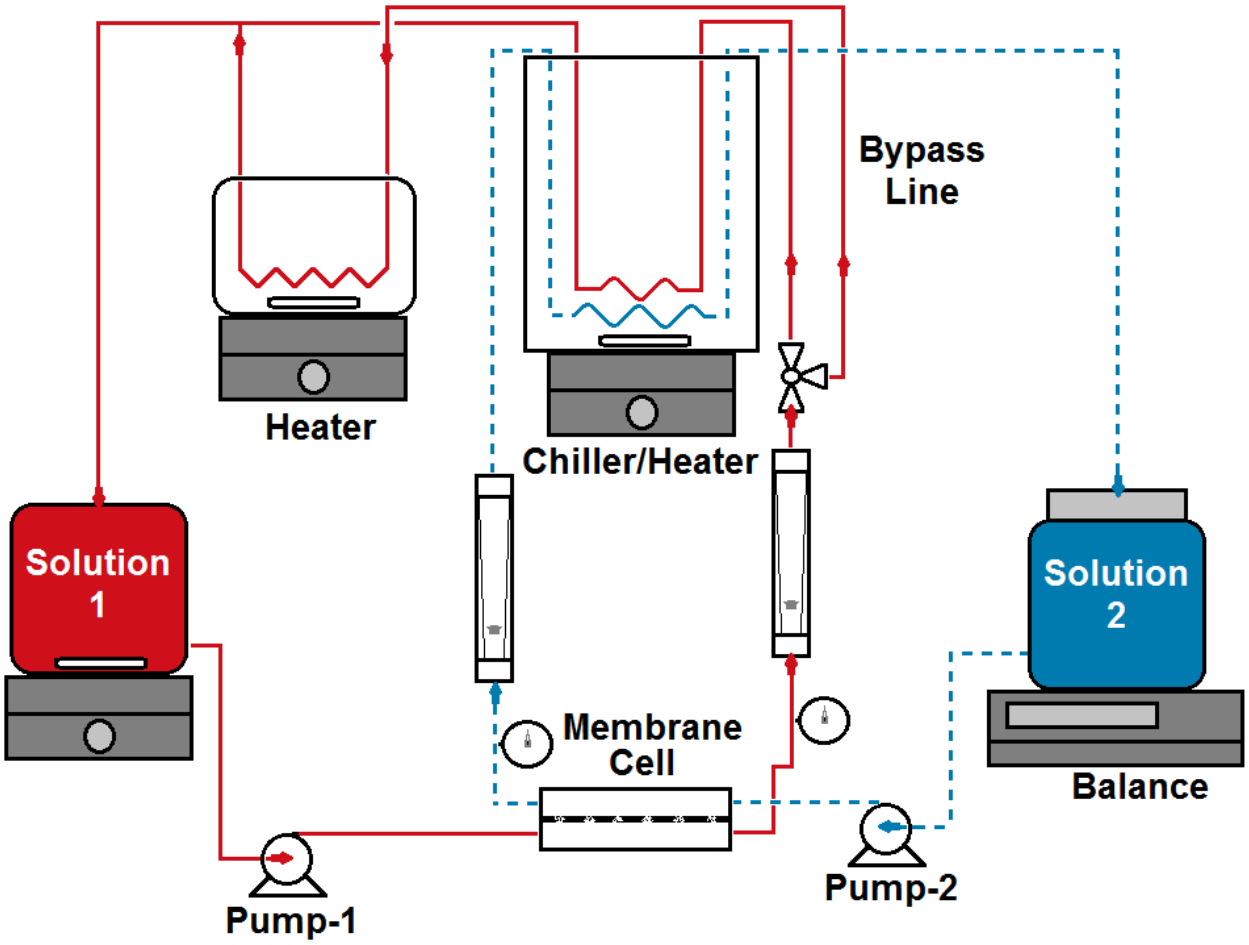

Figure 3.1. Schematic diagram of a cross flow forward osmosis system. The solid line indicates the stream for solution 1 and dashed line indicates stream for solution 2. The bypass line can be used to run the entire system at a single temperature or at two different temperatures.

3.2.2.3. Heat flux measurement

We applied a new method to measure heat flux in FO using a hybrid dead-end/cross-flow system which was introduced in our recent work [63]. This system consists of a cross-flow half-cell which is married to a dead-end cell block. Fig. 3.2 presents a schematic of the hybrid system where solution 1 (1 Liter) remains in the dead-end cell while solution 2 (2 Liters) recirculates through the cross-flow half-cell at a velocity of 0.24 m s^{-1} and 3 psi pressure. Depending on the operating mode (FO or PRO) and temperature conditions, the solutions in the two tanks and the membrane orientation were swapped. For example, in FO mode (membrane selective layer facing

the feed solution), the draw solution was kept in the cross-flow side for heated draw case while it was swapped to the dead-end side for the heated feed case. For PRO mode, this process was reversed with the membrane support layer facing the feed solution side. The temperature of the solution in the dead-end cell was always kept at 20 ˚C in the beginning of the experiment and was monitored using three different thermometers placed at different positions and depths to ensure accurate measurement of the temperature and to note, if any, temperature variability in the dead-end cell. An overhead mixer operating at 1000 rpm was used to distribute the heat uniformly and to reduce both temperature and concentration polarization. The temperature of the cross-flow side was kept at 40 °C throughout the experiment with a temperature difference between the inlet and outlet of the cross-flow side being less than 0.5 °C. The flowlines were also insulated to reduce heat loss and a thermometer was used to monitor the temperature of solution 2. A stop watch was used to monitor the time while changes in temperature in the dead-end cell was noted from the three thermometers. Simultaneously, water flux and reverse solute flux were measured using a weight balance and a conductivity probe respectively. Tests were run in triplicate. Additionally, two tests were run where both sides only contained DI water to measure heat transfer in the absence of mass transfer.

At first, the temperatures from the three thermometers at the beginning (denoted as $T_{DE,\ Initial}$ in Eq. 3.1) and end (denoted as $T_{DE,\ Final}$ in Eq. 3.1) of the experiment were averaged (the difference between them was less than 0.5 °C) and were used in Eq. 3.1 to calculate the sensible heat gain by solution 1 in the dead-end cell (started at 20 °C) from the heat transferred by solution 2 in the cross-flow side (kept at 40 °C) through the membrane. As heat was transferred by the hot solution 2 through the membrane, an overall heat transfer coefficient U_{OHT} was used to represent the heat transfer resistance. The changes in temperature across the membrane was then calculated.

This was done by taking an average of the temperature of solution 1 in the dead-end chamber from the initial to the final time period of experiment (denoted as $T_{DE,\,Avg}$ in Eq. 3.1) and then subtracted from the temperature of solution 2 in the cross-flow side for the same time period (denoted as $T_{CF,\,Avg}$ in Eq. 3.1). Due to the short operation time (less than 10 minutes), the temperature rise in the dead-end chamber was approximately 2-4 °C. For this calculation, it was assumed that the heat flow is one directional (perpendicular to the membrane) with negligible heat loss to the surrounding because of short test period and relatively thick wall of the dead-end cell (3.5 cm).

The calculated heat flux was used to find out the overall heat transfer coefficient across the membrane for different operating conditions [119].

$$Q_{DE} = \frac{mass\, c_{p.\ DE}\,(T_{DE.\ \ Final} - T_{DE.\ Initial})}{time} = U_{OHT} A (T_{CF.\ Avg} - T_{DE.\ Avg}) \qquad (3.1)$$

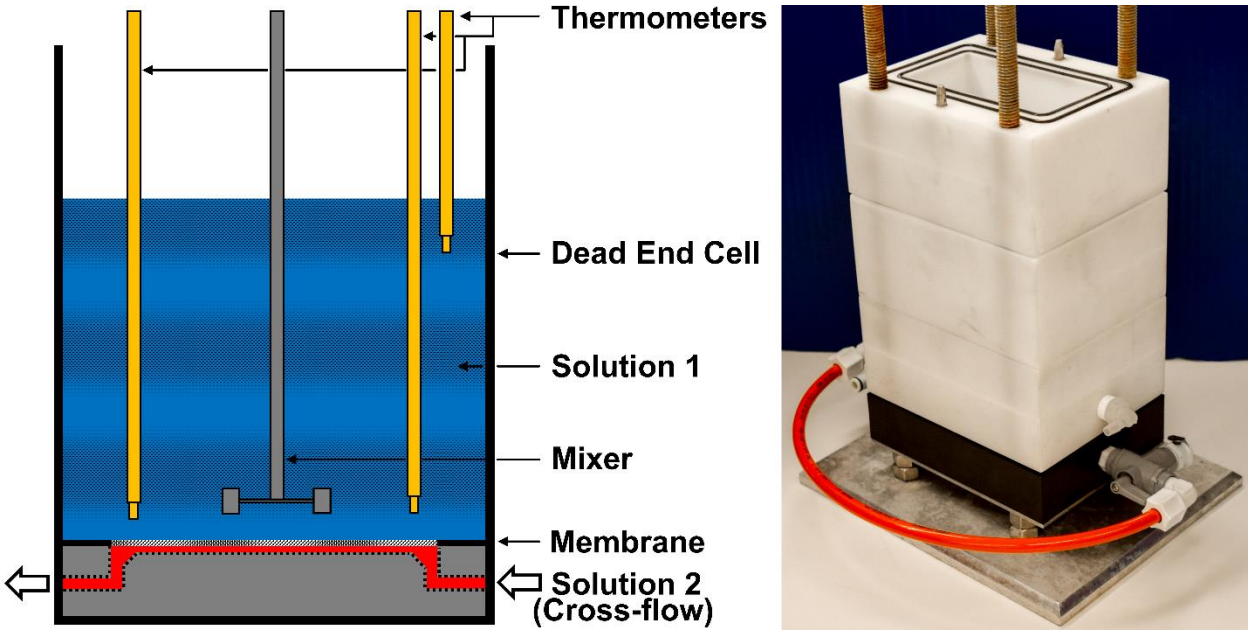

Figure 3.2. A dead-end/cross-flow system for heat flux measurement. The left image is a schematic of the setup and the right figure shows the actual dead-end/cross-flow cell [63] (reprinted by permission of Elsevier). Experimental Conditions: Feed- DI water, Draw- 3 M NaCl solution, 3 psi on cross-flow side, 0.24 m s^{-1}, mixer speed: 1000 RPM, temperature : 20 ˚C/40 ˚C. For 20-40 case: solution 1- feed/ solution 2- draw; for 40-20 case: solution 1- draw/ solution 2- feed.

3.3. Model development

3.3.1. Heat transfer model

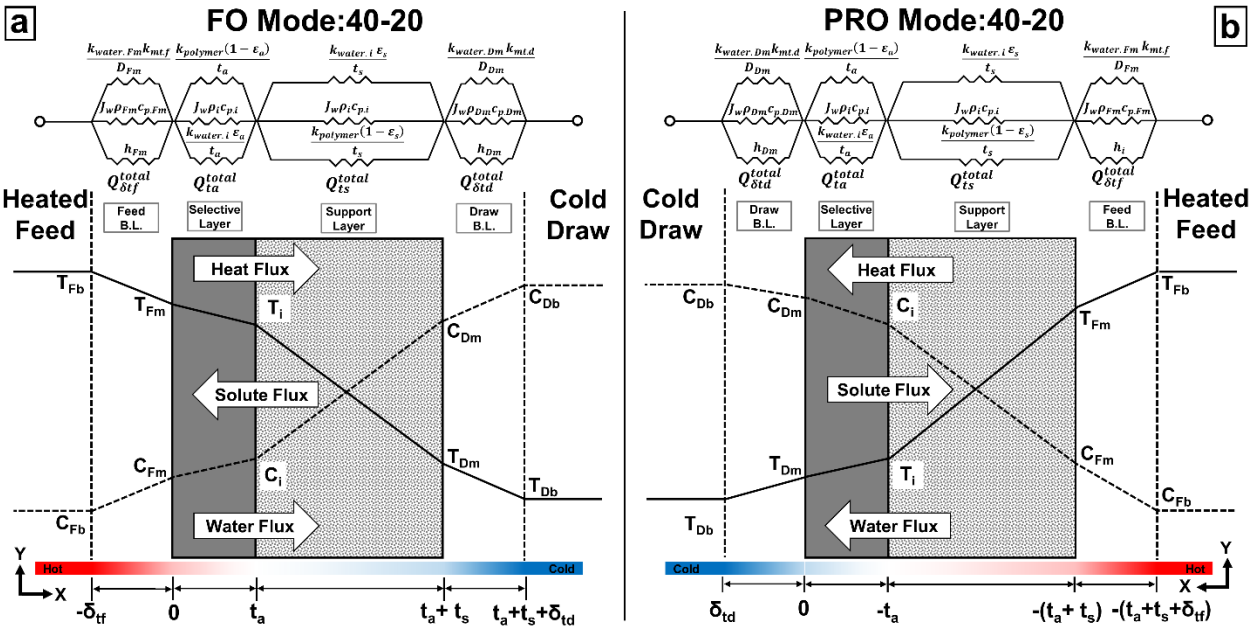

Figure 3.3. Schematics of heat and mass transfer profiles in (a) FO mode and (b) PRO mode processes for case where the feed is warmer than the draw solution (40-20 case). The heat and mass transfer profiles are abstract in nature. Please note that this figure is best viewed in color.

Fig. 3.3 shows the heat and mass transfer profiles for two different operation modes. The circuit diagram above the profiles illustrates the number of parallel processes that contribute to net heat transfer in each region. These profiles are divided into four different regions as follows: feed side boundary layer ($\delta_{t.f}$), membrane selective layer (t_a), membrane support layer (t_s) and draw side boundary layer ($\delta_{t.d}$). The model is developed based on the following assumptions:

1. Flow of heat is unidirectional i.e. X-direction and there is no concentration gradient in Y-direction

2. The system is at steady state. The temperature between the solid phase and liquid phase is same inside the membrane matrix. Additionally, heat transfer is parallel between the solid and liquid phase meaning that heat is flowing in X direction in both the solid and liquid phase and they do not exchange heat with each other while flowing in X direction.

3. It is assumed that the support layer is isotropic and we ignore the asymmetry in the porous structure. It also assumed that the heat is being transferred by convection due to the water flux through the support and conduction through the porous polymeric material and the water filled pores. The overall thermal conductivity of the membrane support layer averages the thermal conductivity of the polymer phase and liquid phase inside the membrane based on volume fraction. The volume fraction of solid and liquid phase in the support is calculated from support layer porosity (ε_s). We incorporate these conductive contributions into an average thermal conductivity of the support layer:

$$\lambda_{membrane} = \lambda_{water}\varepsilon_s + \lambda_{polymer}(1 - \varepsilon_s) \quad (3.2)$$

4. For the selective layer, conductive heat transport through the polymer and liquid phase both are considered. Similar to the support, there is convective heat transport as well through the selective layer. We also assume that the selective layer intrinsic separation properties (permeance, permeability coefficient) changes with temperature.

5. Radiative heat transfer, thermal dispersion, and work done by pressure changes are negligible in the liquid phase. Heat transfer induced mass transfer has also been ignored as the osmotic driving force is much greater than thermal driving force for mass transfer. The system is continuous and the flow conditions are fully developed with a no slip condition near the boundary layer.

6. In the feed and draw side boundary layer, heat is being transferred by conduction through the liquid film in X-direction (according to Fig. 3.3) and by convection due to the motion of the liquid that is flowing above the membrane. Conductive and convective heat transports occur in parallel to each other which are shown in terms of heat transfer resistances on Fig. 3.3.

To calculate conductive heat transfer, the general one dimensional heat flux equation is used [119] as follows:

$$Q = -\lambda A_m \int \frac{dT}{dx} \quad (3.3)$$

To show how we developed the heat transfer model, an example is provided here for the selective layer region. Integrating equation 3.3 using appropriate boundary conditions from Table 3.1 yields:

$$Q_{ta}^{cond} = \frac{\lambda_{polymer}}{t_a}(1-\varepsilon_a)A_m(T_{Fm} - T_i) \quad (3.4)$$

There is also convective heat flux due to mass transport occurring through the selective layer. This convective heat is the product of amount of water being transported, membrane area, heat capacity and temperature difference across the selective layer and can be written as:

$$Q_{ta}^{conv} = J_{w.FO}\ \rho_i\ c_{p.i}\ A_m(T_{Fm} - T_i) \quad (3.5)$$

Combining Eqs. 3.4 and 3.5 provides the total heat that is being transferred through the selective layer of the membrane which is given by Eq. 3.6 as follows:

$$Q_{ta}^{total} = Q_{ta}^{cond} + Q_{ta}^{conv} = (J_{w.FO}\ \rho_i\ c_{p.i} + \frac{\lambda_{polymer}}{t_a}(1-\varepsilon_a))(T_{Fm} - T_i)A_m = B_{ta}(T_{Fm} - T_i)A_m \text{ (Selective layer)} \quad (3.6)$$

In a similar fashion, total heat transferred for the other three regions can be found and are presented below (see supplementary documents for details):

$$Q_{\delta t.f}^{total} = (h_{Fb} + J_{w.FO}\ \rho_{Fm}\ c_{p.Fm} + \frac{\lambda_{water} k_{mt.f}}{D_{Fb}})(T_{Fb} - T_{Fm})A_m = B_{\delta t.f}(T_{Fb} - T_{Fm})A_m \quad \text{(Feed side B.L.)} \quad (3.7)$$

$$Q_{ts}^{total} = (J_{w.FO}\ \rho_i\ c_{p.i} + \frac{\lambda_{membrane}}{t_s})(T_i - T_{Dm})A_m = B_{ts}(T_i - T_{Dm})A_m \quad \text{(Support layer)} \quad (3.8)$$

$Q_{\delta t.d}^{total} = (h_{Db} + J_{w.FO}\,\rho_{Db}\,c_{p.Db} + \frac{\lambda_{water}\,k_{mt.d}}{D_{Db}})(T_{Dm} - T_{Db})A_m = B_{\delta t.d}(T_{Dm} - T_{Db})A_m$ (Draw side B.L.) (3.9)

Eqs. 3.6-3.9 represents the heat fluxes which can be used to give different heat transfer resistances in the different regions in the membrane as shown graphically on Fig. 3.3. At steady state, the rate of heat transfer between each region is equivalent to each other. Equating Eqs. 3.6-3.9 using this argument, the different interfacial temperatures T_{Fm}, T_i and T_{Dm} are found. We show this procedure for T_{Fm} in FO mode as follows:

$$Q_{\delta tf}^{total} = Q_{ta}^{total} = Q_{ts}^{total} = Q_{\delta td}^{total} \quad (3.10)$$

Inserting the short form of Eqs. 3.6-3.9 in Eq. 3.10 we have,

$$B_{\delta t.f}(T_{Fb} - T_{Fm})A_m = B_{ta}(T_{Fm} - T_i)A_m = B_{ts}(T_i - T_{Dm})A_m = B_{\delta t.d}(T_{Dm} - T_{Db})A_m \quad (3.11)$$

By comparing the first two terms in Eq. 3.11 we get

$$T_{Fb} - T_{Fm} = \frac{B_{ta}}{B_{\delta t.f}}T_{Fm} - \frac{B_{ta}}{B_{\delta t.f}}T_i$$

$$\Rightarrow T_{Fm}\left(1 + \frac{B_{ta}}{B_{\delta t.f}}\right) = T_{Fb} + \frac{B_{ta}}{B_{\delta t.f}}T_i$$

$$\Rightarrow T_{Fm} = \frac{B_{\delta t.f}}{(B_{\delta t.f} + B_{ta})}T_{Fb} + \frac{B_{ta}}{(B_{\delta t.f} + B_{ta})}T_i \quad (3.12)$$

In a similar fashion we derived equations for T_i and T_{Dm} as follows (details are in the supplementary document of Appendix A):

$$T_i = \frac{B_{ta}}{B_{ta}+B_{ts}}T_{Fm} + \frac{B_{ts}}{B_{ta}+B_{ts}}T_{Dm} \quad (3.13)$$

$$T_{Dm} = \frac{B_{ts}}{B_{ts}+B_{\delta t.d}}T_i + \frac{B_{\delta td}}{B_{ts}+B_{\delta t.d}}T_{Db} \quad (3.14)$$

Knowing the temperature at different boundaries in the membrane (the four boundaries as shown in Fig. 3.3) is important because these allow us to calculate the solution properties and,

subsequently, the effective osmotic pressures at those boundaries. The properties at the selective layer boundary is most important since it dictates both water and solute flux across the membrane.

We note that Eqs. 3.12-3.14 satisfy the FO mode for equal temperatures (isothermal cases) and elated feed temperature (heated feed case). The equations for the FO mode heated draw case and all the PRO mode cases are provided in the supplementary document of Appendix A.

Table 3.1
Concentration and temperature boundary conditions for the heat and mass transfer model for FO and PRO mode of operation. Positions are marked in Fig. *3.*3 for each mode.

FO Mode			**PRO Mode**		
Position in x-direction	Concentration, C (mol L^{-1})	Temperature, T (°C)	Position in x-direction	Concentration, C (mol L^{-1})	Temperature, T (°C)
$-\delta_{t.f}$	C_{Fb}	T_{Fb}	$\delta_{t.d}$	C_{Db}	T_{Db}
0	C_{Fm}	T_{Fm}	0	C_{Dm}	T_{Dm}
t_a	C_i	T_i	$-t_a$	C_i	T_i
t_a+t_s	C_{Dm}	T_{Dm}	$-(t_a+t_s)$	C_{Fm}	T_{Fm}
$t_a+t_s+\delta_{t.d}$	C_{Db}	T_{Db}	$-(t_a+t_s+\delta_{t.f})$	C_{Fb}	T_{Fb}

3.3.2. Mass transfer

3.3.2.1. Forward osmosis mode

In FO mode operation, the feed solution faces the active layer of the membrane and water is transported from the feed to the draw side (Fig. 3.3a). At the same time, the solute from the draw solution is transported into the feed. The FO mode mass transport model is similar to the one we published recently [63]. In short, to model the mass transfer of solutes, a mass balance which accounts for the diffusive solute flux (due to concentration gradient) and the negative convective solute flux (due to water transport) can be equated to calculate the total change in solute flux J_s.

This solute flux can be related to the solute permeability coefficient (B) of the membrane selective layer and the concentration difference as shown below [120].

$$-J_{s.FO} = -D_s \frac{dC}{dx} + J_{w.FO} C = -B(C_i - C_{Fm}) \quad (3.15)$$

Similarly, two solute mass balances in the feed and draw side boundary layer yields

$$-J_{s.FO} = -D_{Fm} \frac{dC}{dx} + J_{w.FO} C = -B(C_i - C_{Fm}) \quad (3.16)$$

$$-J_{s.FO} = -D_{Dm} \frac{dC}{dx} + J_{w.FO} C = -B(C_i - C_{Fm}) \quad (3.17)$$

Integration of Eqs. 3.15-3.17 using the boundary conditions from Table 3.1 provide the concentrations at the interfaces. These concentrations take into account the different concentration polarization that are known to be present in FO process [64,68,85].

$$C_i = \frac{C_{Fm}(1-P_{ts.FO}) - C_{Dm}\frac{J_{w.FO}}{B}}{1-P_{ts.FO}\left(\frac{J_{w.FO}}{B}+1\right)} \quad (3.18)$$

$$C_{Fm} = C_{Fb} P_{\delta m.f} - \frac{B}{J_{w.FO}} (C_i - C_{Fm})\left(1 - P_{\delta m.f}\right) \quad (3.19)$$

$$C_{Dm} = C_{Db} P_{\delta m.d} + (P_{\delta m.d} - 1) \frac{B}{J_{w.FO}} (C_i - C_{Fm}) \quad (3.20)$$

Where

$$P_{ts.FO} = exp\left(\frac{J_{w.FO} S}{D_i}\right); \mathrm{S} = \frac{t_s \tau}{\varepsilon}; P_{\delta m.f} = exp\left(\frac{J_{w.FO}}{k_{mt.f}}\right); P_{\delta m.d} = exp\left(-\frac{J_{w.FO}}{k_{mt.d}}\right)$$

To calculate osmotic pressure, all of the mass transfer models so far developed, uses the Van't Hoff equation for conversion of concentration to osmotic pressure although it is only applicable for very dilute solutions [99]. To address this issue, we used Pitzer correlations for finding osmotic coefficients for NaCl solutions at different concentrations and temperatures [63,99,100]. The osmotic coefficient equation can be written as (details are provided in the supplementary material of Appendix B):

$$\varphi_m - 1 = |z_+ z_-| f^{\varphi} + m\left(\frac{2\vartheta_+\vartheta_-}{\vartheta}\right) B_{MX}^{\varphi} + m^2 \left(\frac{2(\vartheta_+\vartheta_-)^{3/2}}{\vartheta}\right) C_{MX}^{\varphi} \quad (3.21)$$

$$\pi = \vartheta RT\varphi^m \frac{M_w m}{v_{water}} \quad (3.22)$$

Finally, solute flux and water flux for the different temperatures and concentrations are found [19,29,98] using Eqs. 3.23-3.24.

$$J_{w.FO} = A(\pi_i - \pi_{Fm}) \quad (3.23)$$

$$J_{s.FO} = B(C_i - C_{Fm}) \quad (3.24)$$

3.2.1.1. Pressure retarded osmosis mode

In PRO mode, active layer of the membrane faces the draw solution side (Fig. 3.3b). Mass transfer analysis in PRO mode is similar to FO mode and the following equations are obtained for the different concentrations at the interfaces (details are presented in the supplementary document of Appendix B).

$$C_{Fm} = C_{Fb}P_{\delta m.f} + \frac{B}{J_{w.PRO}}(C_{Dm} - C_i)\{P_{\delta m.f} - 1\} \quad (3.25)$$

$$C_i = \frac{\frac{B}{J_{w.PRO}}C_{Dm}(1-P_{ts.PRO})+C_{Fm}}{\frac{B}{J_{w.PRO}}+P_{ts.PRO}\left(1-\frac{B}{J_{w.PRO}}\right)} \quad (3.26)$$

$$C_{Dm} = C_{Db}P_{\delta m.d} + \frac{B}{J_{w.PRO}}(C_{Dm} - C_i)(P_{\delta m.d} - 1) \quad (3.27)$$

Where $P_{ts.PRO} = exp\left(-\frac{J_{w.PRO}\,S}{D_i}\right)$

3.2.2. Coupling heat and mass transfer models

Fig. 3.4 represents a flowchart for the combined model which employs an optimization approach using Microsoft Excel spreadsheet solver. The solver uses a GRG Nonlinear mode for minimizing one condition using 7 constraints with a tolerance of 1E-06. These constraints use predictions from T_{Fm}, T_i, T_{Dm}, C_{Fm}, C_i, C_{Dm} and J_w to find J_w and J_s at each temperature condition. It is critical for the model to choose the initial guesses wisely. The initial guesses for C_{Fm}, C_i, and C_{Dm} needs to be greater than zero while following the order of the physical gradient i.e. $C_{Fm} < C_i$

$< C_{Dm}$. The initial guesses for T_{Fm}, T_i, and T_{Dm} needs to be greater than 273 K while following the order of the physical gradient i.e. $T_{Fm} > T_i > T_{Dm}$ for heated feed and $T_{Dm} > T_i > T_{Fm}$ for heated draw solution. Based on these restrictions, a unique solution to the system of equations could be achieved. Additionally, Eqs. D1-D5 (see Appendix D) are used in conjunction to find solution properties at the interface across the selective layer [63,101,102,121–124]. The equations for the different solution properties i.e. density, viscosity, diffusivity, heat capacity, thermal conductivity etc. were developed by fitting experimental data from literature to show temperature and concentration dependence [63]. Pitzer correlations to find osmotic coefficient was used to predict osmotic pressure which is also temperature and concentration dependent.

We distinguished mass and heat transfer effects by developing two separate models. In Model MT, only mass transfer effects were considered to calculate effective osmotic pressure driving force. This model is similar to the most recently developed model for FO [63,64] but it includes additional equations to capture variability in solution properties due to changes in concentration as a function of position. Solution and membrane properties that are dependent on temperature were calculated using bulk temperatures while the properties that change with position (X-direction on Fig. 3.3), were evaluated at different boundary concentrations.

In the second model, we incorporated both heat and mass transfer effects (Model HTMT) to calculate the effective osmotic pressure across the selective layer. The effect of heat transfer is evaluated by an integrated system of equations which include all the solution properties (Eqs. D1-D5), membrane intrinsic properties (Eqs. C1-C4 in Appendix C), Model MT (Eqs. 3.18-3.20, 3.25-3.27), Model HTMT (Eqs. 3.12-3.14, 3.18-3.20, 3.25-3.27), and virial coefficients (Eqs. B7-B15 in Appendix B) in Pitzer equation which are dependent on temperature, concentration and change in position. It should be mentioned that the mass transfer models for the FO and PRO modes are

different whereas the heat transfer model is identical for both modes. The concentrations at different interfaces are calculated using Eqs. 3.18-3.20 (for FO) and Eqs. 3.25-3.27 (for PRO). The developed heat transfer model uses Eqs. 3.12-3.14 to calculate heat flux for both FO and PRO modes as it is only dependent on temperature differences and direction of mass flow and is not impacted by the orientation of the membrane. Further details are presented in the supplementary section of Appendix A along with spreadsheets for each model in Appendix F.

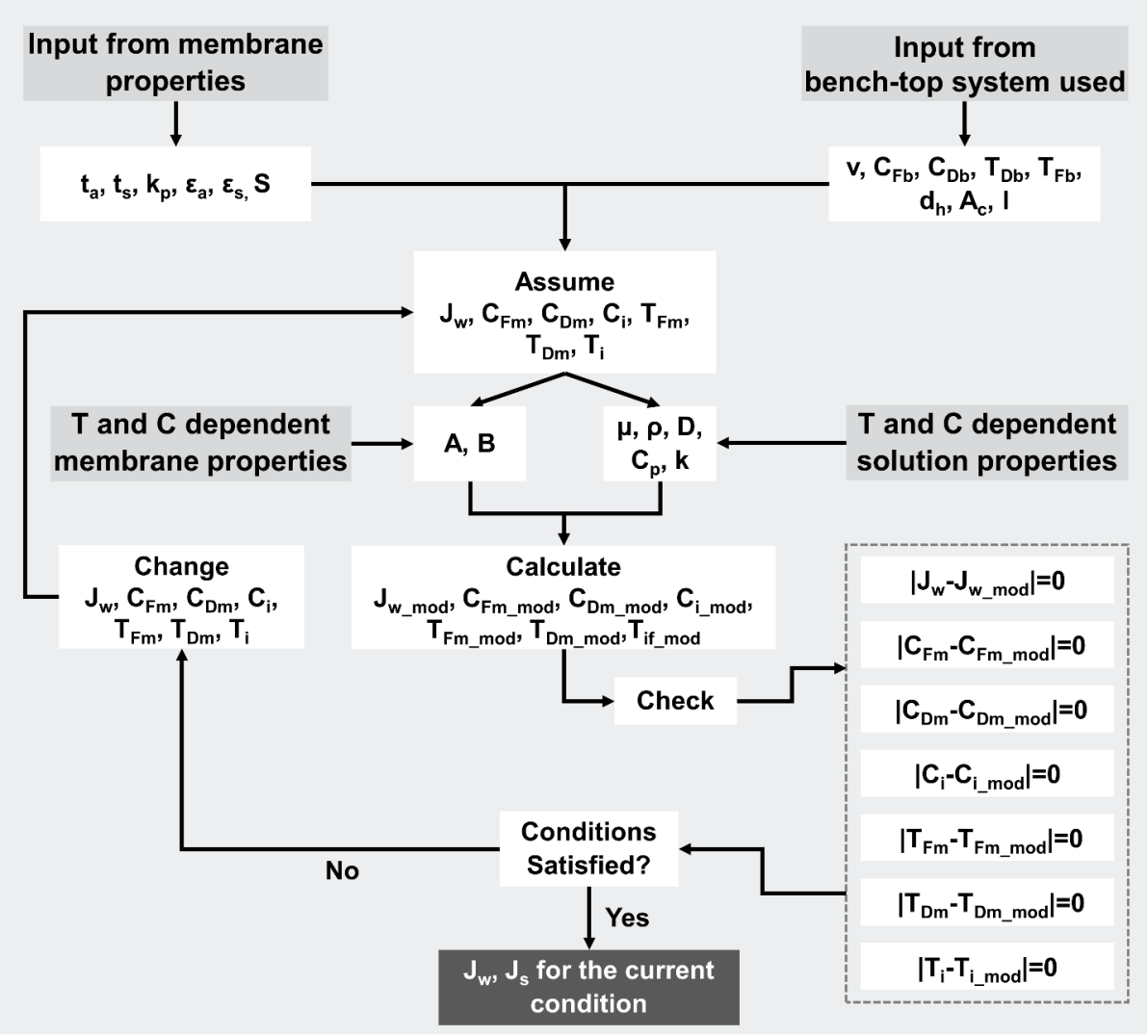

Figure 3.4: Flowchart for the prediction of J_w, J_s, C_{Fm}, C_{Dm}, C_i, T_{Fm}, T_{Dm}, T_i using Model HTMT. Model MT uses a similar flowchart but only uses bulk temperatures instead of boundary temperatures at different interfaces.

3.3. Results and discussion

3.3.1. Effect of temperature on membrane intrinsic properties

Pure water permeance and solute permeability coefficient data are presented for different temperatures on Fig. 3.5 for the HTI CTA membrane. As anticipated, pure water permeance (A) and solute permeability coefficient (B) both increases with temperature since, as the temperature is elevated, the solution properties such as diffusivity increases while viscosity decreases. Thus it allows the solute and the solvent to move at a faster rate through the membrane selective layer resulting in higher A and B values.

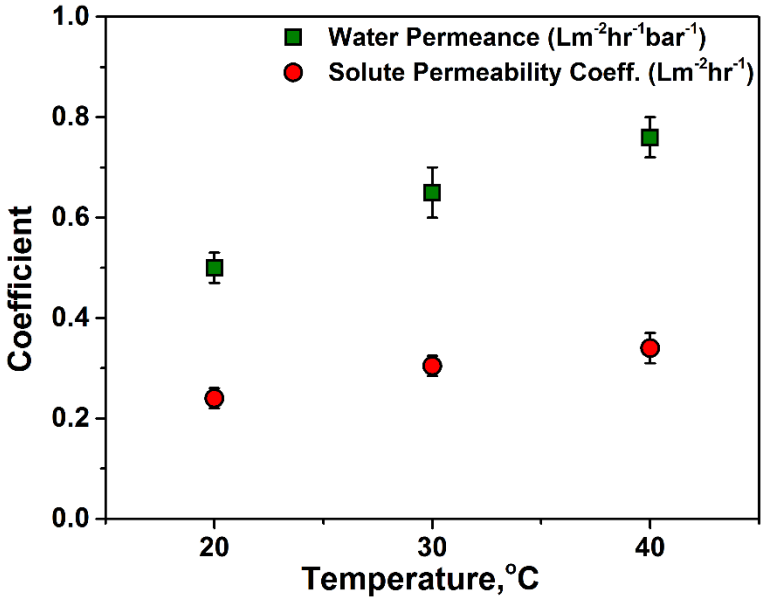

Figure 3.5: Comparison of water permeance and solute permeability coefficient at different temperatures for HTI CTA membrane using a reverse osmosis test setup. Experimental conditions: Feed-DI water/2000 ppm sodium chloride salt solution; Membrane-HTI CTA; Cross-flow velocity of 0.24 m s^{-1}, Pressure was varied from 75 - 225 psi. The error bar represents standard deviation between three experiments for each temperature.

3.3.2. Effect of temperature gradients on water and solute flux

In Fig. 3.6b, the FO mode water fluxes from experiments and model predictions are summarized for the four different cases. Under isothermal conditions across the membrane (designated by 20-20 and 40-40), a 100 % increase in water flux is observed for the 40-40 case as

compared to the 20-20 case. Solution properties such as density, viscosity, diffusivity, heat capacity and thermal conductivity change with temperature and impact mass transfer. Higher temperatures improve mass transfer, lessen the effects of ICP and ECP, and allow for higher water and solute flux in FO [24,67,70,113,114]. Similar results are noted for the PRO mode isothermal cases (Fig. 3.6a), which exhibited a 65 % increase in water flux at elevated temperatures. These results are consistent with previous studies on temperatures impacts on osmotic flow [125].

The gradient tests showed different results. For the FO mode, we observed an approximate 25-50 % increase in water flux when either the feed or draw solution was elevated in temperature. We discuss this in terms of membrane orientation, intrinsic properties, and the direction of mass flux with respect to heat flux. For FO mode, heating the draw solution decreases ICP by increasing diffusivity and reducing viscosity. Increasing the feed temperature results in the warming of the draw solution as convective heat flux increases the temperature of the solution immediately downstream of the selective layer within the support and has a similar effect.

In the PRO mode, an increased water flux was also observed for a warmer feed solution. However, for a heated draw solution with a cooler feed (20-40), a very small, and statistically negligible increase in flux was observed over the 20-20 case. This was surprising since the assumption of a warmer draw solution would have all of the benefits mentioned above. However, Fig. 3.6a shows that the water flux difference in the PRO mode between the gradient cases are noticeably high, meaning that the convective heat transfer from a cold feed into a heated draw solution will have a substantially greater cooling effect than it would be with the FO mode. This cooling due to convective heat transfer nullifies the benefits of heating the draw solution since the draw solution near the selective interface is very nearly the temperature of the feed solution. Similar reasoning could be applied for the heated feed case as well.

Fig. 3.7 summarizes the FO and PRO mode solute fluxes for different cases. For the FO mode, we observe a marginal increase in solute flux when either solution (or both) is raised from 20 ˚C to 40 ˚C (Fig. 3.7b). This is due to the increased solute permeability coefficient at higher temperature across the selective layer. However, the increase is partly subdued by the higher forward water permeation at higher temperature. For the PRO mode (Fig. 3.7a), changes in solute flux are modest. A slight increase in solute flux is noted for the cases of heated feed solutions and when both solutions are heated. There is no increase in solute flux when the feed is kept cool since, as was noted with the water flux data, the temperature across the selective layer is close to the feed temperature because of the convective heat transport from the feed to the draw and very small heat transfer resistance of the selective layer.

Fig. 3.6 and 3.7 also present the model predicted values using Model MT and Model HTMT for FO and PRO modes. Except for the water flux in FO mode 20-40 case, better predictions were achieved with Model HTMT for the different cases over Model MT. From RMSE analysis for the two model (Table 3.2), we confirm the accuracy of the Model HTMT over Model MT as we see worse performance by Model MT in PRO mode. This demonstrates the importance of incorporation of heat transport elements into model calculation.

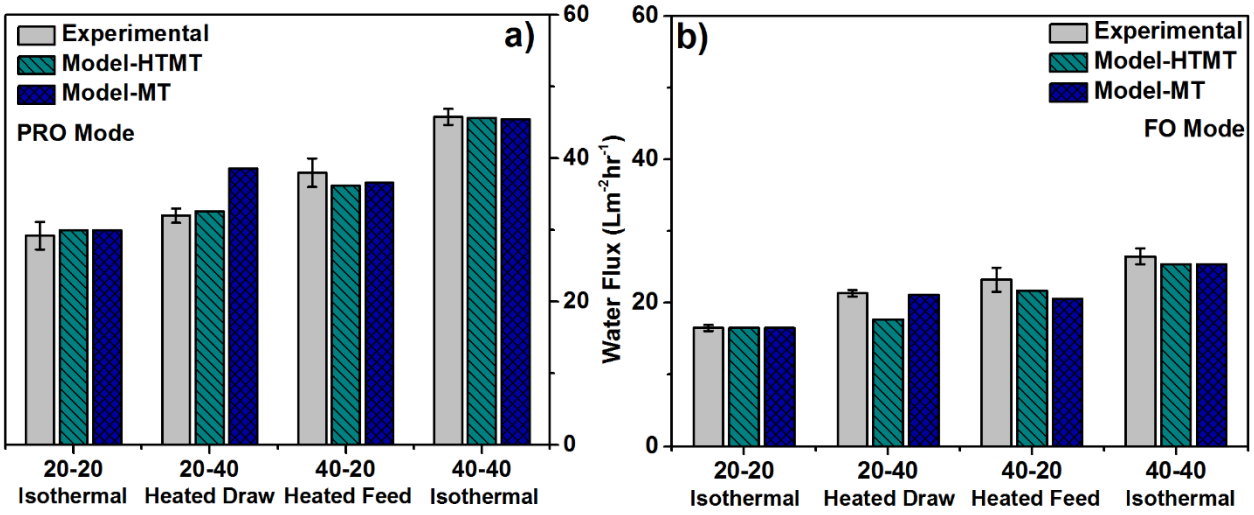

Figure 3.6: Comparison of water flux data for different modes of osmotic operation at different temperatures using the bench-top cross-flow setup shown in Fig. 3.1. Experimental Conditions: Feed-DI water; Draw- 3 M NaCl solution; Membrane-HTI CTA; Cross-flow velocity of 0.24 m s^{-1}; 3 psi pressure on both stream. The error bar represents standard deviation between three experiments for each condition. Model conditions: fluid velocity, v: 0.19 m s^{-1}; selective layer thickness, t_a: 100 nm; support layer thickness, t_s: 85 µm; selective layer porosity, ε_a: 0.0001; support layer porosity, ε_s: 0.57; polymer thermal conductivity, $\lambda_{polymer}$: 0.17 W m^{-1} K^{-1}; structural parameter, S_{FO}: 350 µm & S_{PRO}: 625 µm (see Appendix E for details); hydraulic diameter: 6.3 mm; cross-sectional area: 24 cm^2; feed solute concentration, C_{Fb}: 0 mol L^{-1}; draw solute concentration, C_{Db}: 3 mol L^{-1}; Model-HTMT: includes both heat and mass transfer effects; Model-MT: includes mass transfer effects only.

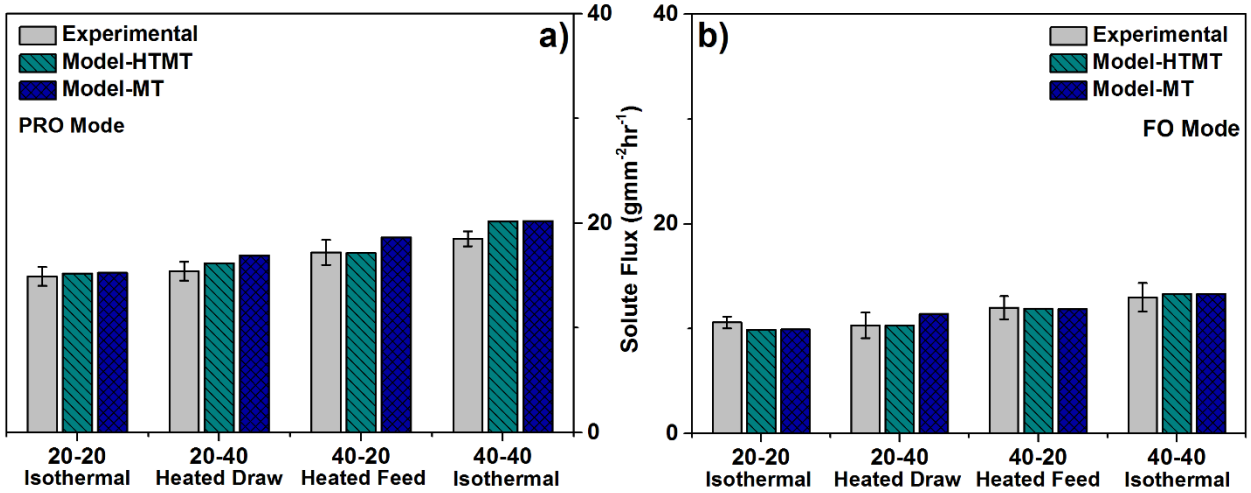

Figure 3.7: Comparison of reverse solute flux data for different modes of osmotic operation at different temperatures. Experimental conditions: same as described under Fig. 3.6.

Table 3.2: Root mean squared error (RMSE) for FO and PRO mode experimental data and the two models.

FO Mode				PRO Mode			
Water Flux (L m^{-2} hr^{-1})		Solute Flux (gm m^{-2} hr^{-1})		Water Flux (L m^{-2} hr^{-1})		Solute Flux (gm m^{-2} hr^{-1})	
Model HTMT	Model MT	Model HTMT	Model MT	Model HTMT	Model MT	Model HTMT	Model MT
2.05	1.44	0.38	0.66	1.59	3.56	0.93	1.35

3.3.4.Effect of convective heat transport

3.3.4.1.Heat Flux and Resistance

Fig. 3.8 and 3.9 can be used to further illustrate the impact of mass transfer on heat transfer.

In Figure 8, the vertical axis represents the positive and negative heat flux and resistance incurred

due to the direction of heat and mass transfer in the different regions shown in the horizontal axis. These same regions are shown in length scale on Fig. 3.9 with the origin being at the selective layer. Looking at the PRO mode only (similar results are noted for the FO mode as the temperatures at different boundaries are similar as shown in Fig. 3.9), Fig. 3.8 delineates the contributions to heat fluxes and heat resistances in each region of the membrane (including the external boundary layers) for both the heated feed and heated draw case. The model prediction did not change between the two operating modes i.e. FO and PRO. Considering first the heat fluxes, Fig. 3.8a and 3.8b show the net heat fluxes through each region as well as the heat fluxes that are induced by the water flux (MT assisted HT) and those heat fluxes that would occur in the absence of water flux (unassisted HT). As is necessary, the net heat flux through each region is equivalent for each of the two conditions in all regions. However, the contributions to these net fluxes is quite different.

For the heated feed case, the MT and HT are occurring in the same direction. In the draw and feed side boundary layers, there are equal contributions from the mass transfer induced HT and the unassisted HT. In the support layer of the membrane, water flux induced HT is more important because of the region is unstirred and conduction is slow (the region is very thick). This results in large temperature polarization in the support as well which can be seen from the differences between T_i and T_{Dm} (FO mode heated feed case on Fig. 3.9), and T_i and T_{Fm} (PRO mode heated feed on Fig. 3.9). In the selective layer, the layer is so thin that conduction dominates and MT induced HT is negligible. The temperature differences across the selective layer are also marginally different as a result.

For the heated draw case, MT and HT are occurring in opposite directions. The cold water flux lessens the net heat flux substantially and results in a lower heat flux when compared to the heated feed case. In all regions of the membrane, the MT induced heat flux is negative but the

quantity is different between the two cases for each region. The higher heat flux due to MT assisted HT in the draw side B.L. of Fig. 3.8b compared to Fig. 3.8a is due to the large temperature difference between T_{Db} and T_{Dm} for heated draw compared to the heated feed (Fig. 3.9). Said simply, based on our model, most of the cooling of the draw solution takes place in the draw side boundary layer.

Heat resistances are quantified in Figs. 3.8c and 3.8d. For the heated feed case, since MT is occurring in the same direction as HT, the MT assisted heat transfer corresponds to a negative heat transfer resistance. The net resistance is evaluated by adding MT assisted HT resistance to Unassisted HT. As an example, for a heated feed in the support layer of the membrane, a resistance of $-0.096\ \mathrm{K\ W^{-1}}$ (for MT assisted HT) is added to a resistance of $0.508\ \mathrm{K\ W^{-1}}$ (for Unassisted HT) to have a net resistance of $0.412\ \mathrm{K\ W^{-1}}$. For the heated draw, a resistance of $0.097\ \mathrm{K\ W^{-1}}$ is being added to a resistance of $0.508\ \mathrm{K\ W^{-1}}$ to have a net resistance of $0.605\ \mathrm{K\ W^{-1}}$. Note that if the resistance from MT assisted HT becomes larger than the Unassisted HT as is the case for the selective layer in the heated feed case, a negative net resistance is being calculated.

As anticipated, we observe very low overall resistance to heat flux for heated feed case compared to heated draw in all regions except for the support and selective layer of the membrane. Breaking down this case into the four heat transfer zones (Fig. 3.8c), we note significant resistance in the support layer of the membrane. This makes sense as the support layer acts as an insulator. The reduction of resistance caused by mass transfer is also less than the other regions because mass transfer is hindered in the support layer. One might refer to it as *internal temperature polarization*. Looking at the other zones, we note that in the external boundary layers, the net heat transfer resistance is nearly zero as reduced heat transfer resistance caused by water flux nearly equals that of the boundary layer resistance in the absence of mass transfer. In the selective layer, the

standalone resistance to heat transfer, in this case by conduction alone, is negligible (a value of 0.0002 K W^{-1}) given the thinness of the selective layer. Therefore, the overall resistance is negative and entirely brought on by the flux of the hot feed.

For the heated draw, the calculated resistance in all regions were found to be nearly equivalent to each other (Fig. 3.8d). The summed resistances in all these regions inhibit heat transfer from the warm draw solution into the cold feed. We note similar contributions in resistances from Unassisted HT and MT Assisted HT in the two boundary layers (Fig. 3.8d), yet the temperature difference across the feed side B. L. (~ 3.4 ˚C in FO mode and ~ 4.3 ˚C in PRO mode as shown in Fig. 3.9) is significantly lower than that of the draw side B. L. (~ 16.6 ˚C in FO mode and ~ 15.6 ˚C in PRO mode). As the direction of the cold feed is against the direction of the heat transfer, it acts toward resisting the heat flow from the draw into the membrane resulting in a lower value for T_{Dm} (Fig. 3.9). Unlike the heated feed, no internal temperature polarization was observed within the membrane support for heated draw as convection from MT was in opposite direction to HT resulting in higher resistance than the heated feed (Fig. 3.8c). In the feed side B.L., MT Assisted HT increases net resistance than the heated feed which results in lower values for T_{Fm} in heated draw case. Also, high resistances in the draw side boundary layer decreases the temperature at the selective layer (T_i = 24.3 °C on Fig. 3.9 for heated draw) than the temperature (T_i = 27.5 °C on Fig. 3.9 for heated feed) obtained for the heated feed. A lower temperature yields lower values for membrane intrinsic parameters (i.e. A and B), diffusivity, and density and a higher value for viscosity. The culmination of these effects largely subdues the benefit of having a warmer draw solution and hence demonstrates inferior osmotic performance than the heated feed case (Fig. 3.6 and 3.7).

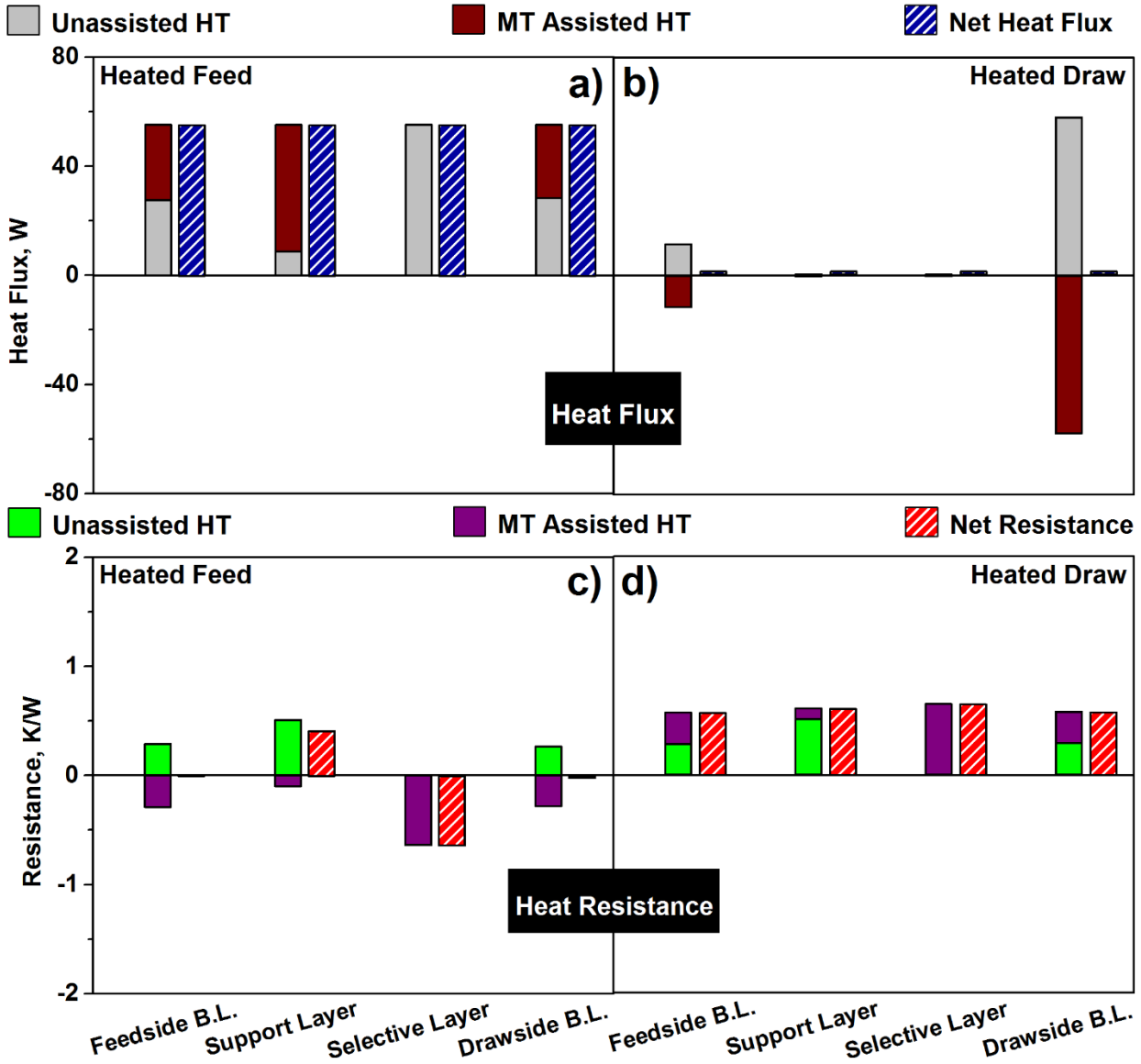

Figure 3.8: Heat flux (a, b) and resistance (c, d) predicted from Model HTMT for heated feed (a, c) and heated draw (b, d) cases. Both FO and PRO mode models have similar predictions. Legend description: Unassisted HT- heat flux associated with conduction through the polymer and convection in the two boundary layers due to fluid flow; MT assisted HT- heat flux associated with conduction through the flowing liquid and convection due to mass transfer; all of the model conditions are specified under Fig. 3.6.

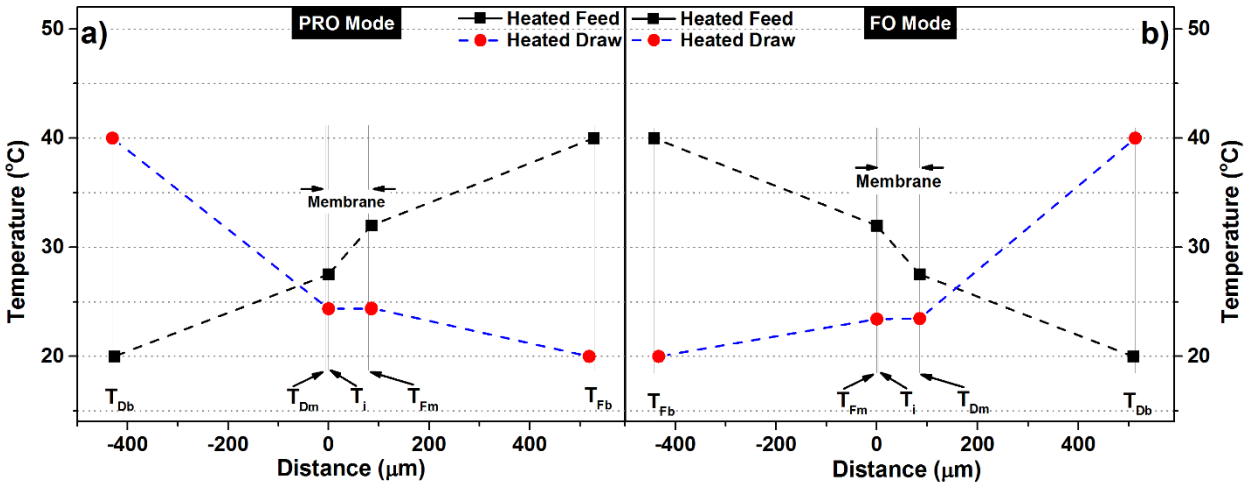

Figure 3.9: Predicted temperature profiles for heated feed and heated draw case in PRO (a) and FO (b) modes of operation using Model HTMT. Only the black and red markers are predicted using the model while dotted lines are presented as a guide. The vertical lines are representative of the membrane interfaces with the external solution. The selective layer data point is not visible since the model predicts that the temperature on the upstream and downstream side of this layer are nearly equivalent. Model conditions are described in Fig. 3.6.

3.3.4.2. Overall heat transfer coefficient

The influence of convective heat transport and feed temperature was further validated by evaluating the overall heat transfer coefficient (U_{OHT} calculated using Eq. 3.1) experimentally and using Model HTMT as seen on Fig. 3.10. For the two different temperature gradients (heated feed and heated draw), three different operating modes were considered: DI water on both sides (i.e. no water flux), FO mode, and PRO mode. In the case of no mass flux (DI water), we note that there was no difference in heat transfer coefficient with regard to membrane orientation. However, when MT assisted HT was present, substantial differences in heat transfer coefficients were found between the two cases. For the heated feed, overall heat transfer coefficient was higher than the heated draw case because mass and heat transfer were in the same direction (lower HT resistance). For the heated draw, mass and heat transfer were in opposite directions, resulting in a lower overall heat transfer coefficient (higher HT resistance). Model prediction also aligned well with the experimentally obtained result for the two gradient conditions further confirming the model's

reliability. What can be concluded from this discussion is that the direction of heat and mass transport has an immediate and profound effect on solution properties near the selective and support layer interface, and as MT always occurs from the feed to the draw solution, feed temperature has more influence in determining membrane osmotic performance than the draw temperature.

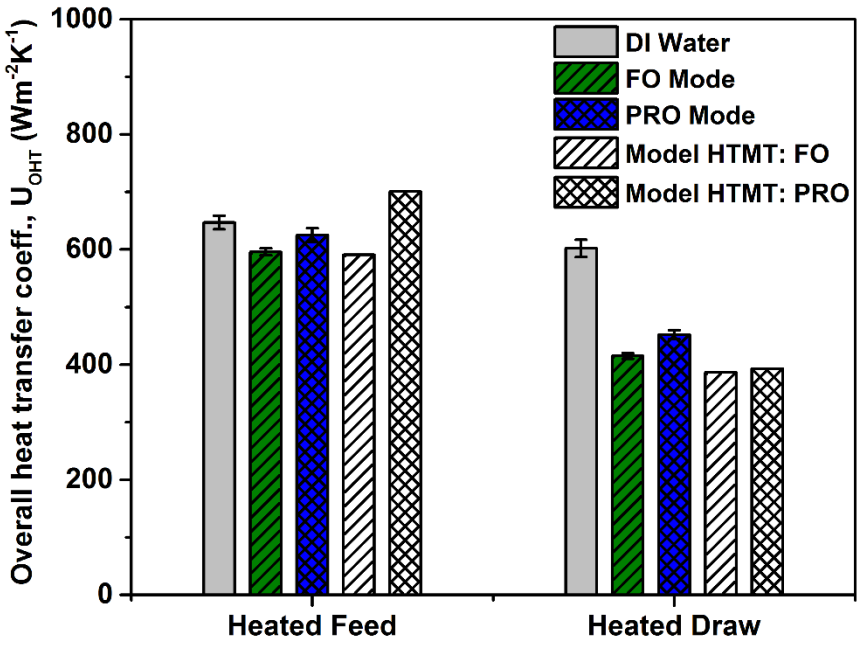

Figure 3.10: Comparison of overall heat transfer coefficient at different temperatures using the hybrid dead-end cross-flow system shown in Fig. 3.2. Experimental conditions: Feed- DI water; Membrane- HTI CTA; Cross-flow velocity of 0.23 m s^{-1}; Pressure- 3 psi; legend description: DI Water Heated Feed - DI water on both side with selective layer facing the hot side; DI Water Heated Draw - DI water on both side with selective layer facing the cold side; Colored bars are experimental results while blank patterned bars represent predicted data using Model HTMT. The error bar represents standard deviation between three experiments for each condition.

3.4. Conclusion

As FO finds more opportunities in different separations processes, there is a strong likelihood that unique feeds and regenerated draw solutions will be of different temperatures. Benchtop FO studies up to now, however, have largely used idealized conditions where both solutions have been kept at the same temperature. The FO community must shift toward exploring less ideal conditions

so that important performance relationships can be established. This work provides insight into how one deviation from this ideality, temperature gradients, can impact key performance metrics like water and solute flux. Identifying that feed temperature plays a more crucial role in overall osmotic performance than draw temperature does, will enable better system design, process integration in terms of heating and cooling, and economics. For large scale optimization, variability in solution properties due to a change in concentration, temperature and flow conditions needs to be accounted for. Failure to include these variations could lead to erroneous process design and poor performance of the system. Additionally, avoiding Van't Hoff equation and using Pitzer correlations to calculate osmotic pressure, makes this model applicable to solution concentrations of all ranges. This fundamental understanding of transport phenomenon will be essential in predicting and optimizing performance at the element and system scale as FO begins its long-awaited emergence from academic research into commercial applications.

Nomenclature

A	pure water permeance (L m^{-2} hr^{-1} bar^{-1})
A_m	membrane area (m^2)
A_φ	Debye-Hückel constant for the osmotic coefficient (Kg $^{1/2}$ $mol^{-1/2}$)
B	solute permeability coefficient (L m^{-2} hr^{-1})
b	"Ion size" parameter in Pitzer's equations, b = 1.2 Kg $^{1/2}$ $mol^{-1/2}$
B_{MX}^{φ}	pairwise ion-interaction parameter of Pitzer's equation (Kg mol^{-1})
C	concentration (mol L^{-1})
C_{MX}^{φ}	triplet ion-interaction parameter of Pitzer's equation (Kg mol^{-1})
c_p	specific heat capacity for water (J Kg^{-1} K^{-1})
D	diffusion coefficient of salt (m^2 s^{-1})
d_h	hydraulic diameter (m)
D_s	support layer effective diffusivity, $D_s = \frac{D\varepsilon_s}{\tau}$ (m^2 s^{-1})
e	electronic charge of an electron (C)
f^{φ}	function of ionic strength (also temperature and solvent properties) expressing the effect of the long-range electrostatic forces (dimensionless)
h	heat transfer coefficient (W m^{-2} K^{-1})
I	ionic strength of the liquid (mol Kg^{-1})
J	flux (L m^{-2} hr^{-1} or gm m^{-2} hr^{-1})
k_{mt}	mass transfer coefficient (m s^{-1})

L	length of the channel (m)
m	molality of solution (mol Kg^{-1})
mass	mass of liquid in the dead-end system (Kg)
M_w	molecular weight of water (Kg mol^{-1})
N_A	Avogadro's number (dimensionless)
P	concentration polarization factor (dimensionless)
Pr	Prandtl number (dimensionless)
Q	heat transfer rate from the hot side to the cold side (W)
R	ideal gas constant (L atm $mol^{-1}K^{-1}$)
Re	Reynolds number (dimensionless)
S	structural parameter (m)
Sc	Schmidt number (dimensionless)
Sh	Sherwood number (dimensionless)
T	temperature (˚C)
$T_{DE, Avg}$	average dead-end system temperature (˚C)
$T_{DE, Final}$	final temperature of the liquid in the dead end system (˚C)
$T_{DE, Initial}$	initial temperature of the liquid in the dead end system (˚C)
$T_{Draw, Avg}$	average draw temperature (˚C)
t_a	thickness of active layer of the membrane (m)
time	time of experiment (sec)
t_s	thickness of support layer of the membrane (m)
U_{OHT}	overall heat transfer coefficient (W m^{-2} K^{-1})
z_-	number of charge on anion (dimensionless)
z_+	number of charge on cation (dimensionless)
Greek symbols	
Δ	difference
α	Ionic strength dependence parameter in Pitzer's eq., $\alpha = 2$ $Kg^{1/2}$ $mol^{-1/2}$
$\beta_{MX}^{(0)}$	1st virial coefficient (Kg mol^{-1})
$\beta_{MX}^{(1)}$	2nd virial coefficient (Kg mol^{-1})
δ	thickness of momentum transfer boundary layer (m)
δ_m	thickness of mass transfer boundary layer (m)
δ_t	thickness of heat transfer boundary layer (m)
ε_a	membrane selective layer porosity (dimensionless)
ε_s	membrane support layer porosity (dimensionless)
ε_0	vacuum permittivity (A^2 sec^4 kg^{-1} m^{-3})
ε_r	relative permittivity (dimensionless)
$\lambda_{membrane}$	thermal conductivity of the membrane (W m^{-1} K^{-1})
$\lambda_{polymer}$	thermal conductivity of the polymer (W m^{-1} K^{-1})
λ_{water}	thermal conductivity of water (W m^{-1} K^{-1})
ρ	density of solution (Kg m^{-3})
τ	membrane support layer tortuosity (dimensionless)
υ_-	stoichiometric coefficient of anions (dimensionless)
υ_+	stoichiometric coefficient of cations (dimensionless)
υ_{water}	molar volume of pure water (m^3 mol^{-1})

φ_m	Pitzer osmotic coefficient (dimensionless)
π	osmotic pressure (bar)
Superscripts	
cond	conductive heat transport
conv	convective heat transport
total	total heat transport across each region
Subscripts	
CF	cross-flow
d	draw side
Db	bulk draw solution
DE	dead end cell
Dm	interface between membrane and draw side boundary layer
f	feed side
Fb	bulk feed solution
Fm	interface between membrane and feed side boundary layer
FO	forward osmosis
i	interface between membrane selective and support layer
mod	model prediction
PRO	pressure retarded osmosis
s	solute species
ta	selective layer region
ts	support layer region
w	water species
δm.d	mass transfer boundary layer region on the draw side
δm.f	mass transfer boundary layer region on the feed side
δt.d	heat transfer boundary layer region on the draw side

CHAPTER 4

Pilot system development: Demonstrating concept of FORO for water treatment

Project in progress:
Elucidating fundamental performance parameters for a hybrid forward osmosis and reverse osmosis system.
Maqsud R. Chowdhury, Caylin Cyr, Brielle Cash, and Jeffrey R. McCutcheon

4.1. Introduction

Forward osmosis is an emergent technology that enables high quality water production from highly impairs waters with high levels of suspended and dissolve solids. It has found excellent niche applications in brine treatment, produced water treatment [50], and dewatering of complex fluids. FO has great opportunity when working with solutions that cannot be treated by RO alone. FO operates by using a concentrated draw solution that has a high osmotic pressure to draw water osmotically across a semi-permeable membrane that has a high degree of salt rejection. The system can be separated into an FO membrane system and a draw solute recovery system. The FO step spontaneous, with water moving by osmosis across the membrane. The draw solute recovery step requires an energy input that enables concentration of the draw solution for reuse while removing clean water from the process. In essence, every FO system with draw solute recovery is a "hybrid" system. It is this recovery system which requires the vast majority of the energy in the overall process. The recovery process is also draw solution specific and therefore can take many forms. The vast majority of draw solute options combined with the multitude of recovery separation processes generates uncertainty in the design process. In the end, some

wonder why FO should be considered since a second process is needed. Can RO not work better on its own as a single step process?

The answer to that question is multi-faceted. RO does work quite well for many processes. It is highly productive, efficient, and selective. It is well designed for inorganic salt removal in waters with low salinity and a low propensity to foul. However, in reuse applications, challenges arise. Both domestic and industrial wastewaters are laden with organic foulants that have long been problematic for RO membranes. This has led to substantial research efforts to modify RO membranes to prevent fouling. Designers of small and large RO plants require extensive pretreatment schemes which are designed to remove foulants before they ever reach the RO membrane [126]. These efforts, while showing some success, have added to the cost of RO and taken away some of its perceived simplicity.

Furthermore, RO is incapable of handling solutions of high salinity. Osmotic pressure will ultimately limit recovery in RO, meaning that wastewaters with high salinity will be untreatable with RO, or wastewaters of low salinity will be limited in recovery by osmotic pressure. FO has been demonstrated as an effective process to treating and concentrating brines [80] because the limitation of recovery is determined by the osmotic pressure of the draw solution. It is far easier to dissolve more solute in the draw solution than it is to operate your RO membrane at every increasing pressure. Lastly, RO has had difficulty at removing some contaminants in water. Boron from seawater and small organic molecules have been found to pass through RO membranes [127]. These low rejections may necessitate the use of double-pass RO systems to increase overall system rejection. This adds to both capital cost and energy costs for treating the water and doesn't alleviate the other challenges mentioned above. FO hybrid systems address each of these challenges. FO has been demonstrated to have fouling resistance and cleanability far in excess to that of reverse

osmosis alone. This makes FO a candidate for RO pretreatment. As the draw solution pulls water out of the dirty feed water, the RO can concentrate the pristine draw solution and send it back to the system. This inherently creates a "double barrier" separation system, where all contaminants that end up in the product water must pass through both the FO and RO process. Since FO membranes are designed with similar chemistry to RO membranes, their selectivity is similar. This suggests that FO-RO systems can have the same selectivity as double-pass RO systems. FO is also uniquely suited to handle solutions of high osmotic pressure. To remove water from high TDS solutions, FO operators can simply use a higher concentration draw solution. However, care must be taken when considering the appropriate recycling process of the concentrated draw. If RO is used to recycle the draw solution, it is subject to the same limitations as a single pass RO system as described above. RO cannot re-concentrate high salinity brines.

Because the draw solution can be made from literally anything that dissolves in water, the user has the ability to select, or even design, the draw solution with that can be recovered easily, completely, and cheaply. Herein lies the elegance of the FO hybrid process. A system designer can select a draw solution that is easily regenerated based on local energy sources. Such flexibility offers a degree of freedom in system design that RO lacks on its own. A number of solutes have been discussed in the literature [10,11,15–18]. Among the most popular solutes can be recovered with low grade waste heat. Overall, a draw solute can be chosen with an appropriate recovery step that is designed to work with a specific feed water. A draw solution that is designed for high salinity may not necessarily work for a low salinity feed. Some of the more complicated draw solutes require even more complicated recovery systems. Thermolytic salts require stripping and absorption columns. Macromolecular solutes require ultrafiltration recovery and handling of more viscous fluids. Other emergent draw solutions, such as switchable polarity solvents [18], low

critical solution temperature polymers, and hydrogels are all unique draw solutions based on exciting science, but lack a degree of simplicity that is required when demonstrating system level performance. Using simple, safe, and inexpensive draw solutes with well-proven membrane processes that are commercially available are more effective at providing a clear platform for demonstrating technology.

It is important to mention two important caveats of forward osmosis that sometimes gets lost in its description in the literature. First, *FO is not intended to replace RO.* RO is a high performance technology that works well with low salinity waters with low fouling propensity. FO can handle higher salinity feeds and can be hybridized with RO to act as a pretreatment when high fouling solutions are involved. Second, FO *will not use less energy than reverse osmosis*. This is an important fact to keep in mind to those who have heard or read the opposite. The fact that FO can take what used to be a single step and make it into two would suggest the opposite, actually. In fact, FO will generally use more energy than RO alone [12]. The advantages to FO are not connected with energy use. They are limited to managing high fouling and high salinity fluids which may contain contaminants that require two-barrier protection. This makes the process valuable to reuse applications. Almost all of the early work on forward osmosis membrane testing has involved testing at the benchtop scale. These small systems will typically use small volumes of liquid and small membrane coupons with surface areas ranging from 4-20 cm^2. However, many in the industrial community have mentioned that, even though the science is good, the data from these systems is not representative of real systems. In coupon testing, the single pass recovery is very low because of low residence time in the cell. In a module, the residence time is much larger, meaning that the draw solution will dilute and the feed solution will concentrate to a much greater extent before exiting the module. We must be able to account for this very important difference

when considering how a system will behave at scale, so developing correlative relationships between coupon testing and module testing is needed. The literature has many studies that claim to evaluate hybrid FO systems [126,128–138], though a vast majority of them in fact either only evaluate systems theoretically or with benchtop testing equipment with coupon-type membrane cells. The only way to evaluate how a real system will perform is to build a real system with commercial scale elements and modules.

The objective of this work is to evaluate a FORO system with regard to recovery, energy use, contaminant removal, and operating condition:

1. **Compare coupon and module performance to understand fundamental differences and similarities between the two.** *Hypothesis: Modules will have much lower flux per unit area of membrane. This will happen because the concentrations, and hence osmotic pressures, are changing throughout the membrane. These effects will be more severe in the spiral wound element than they are in the plate and frame element because inherent inefficiencies cause by dead zones within the spiral architecture of the module.*
2. **Evaluate electrical energy use and contaminant removal capabilities of a FO-RO system.** *Hypothesis: The FO-RO system will use more energy than RO alone, though the contaminant removal be higher than a single pass RO unit alone because of the dual-barrier protection.*
3. **Quantify the losses of draw solute through the FO membrane and the recovery step and estimate the draw solute makeup cost.** *Hypothesis: Draw solute losses will be substantially higher with smaller molecular weight salts (NaCl). FO-RO will also lose draw solute through the RO process.*

4. **Based on evaluation of FO-RO, quantify energy use and contaminant removal capabilities in a real reuse scenario with actual secondary effluent and reclaimed water.** *Hypothesis: FORO will have superb TOC and large molecule removal. Salt removal will be excellent with dual barrier protection. Contaminants will build up in the draw solution loop over time, but those concentrations will be at equilibrium with the feed concentration.*
5. **Quantify the benefit or drawbacks of using either the FO-RO system over existing system for producing water.** *Hypothesis: The FO-RO system will make more sense for lower salinity feeds, such as a reclaimed wastewater*

4.2. Fabrication, installation, and commissioning of FORO

A process flow diagram of the FORO hybrid system was conceptualized (Fig. 4.1). In this system, the feed in the FO side goes through the FO membrane and concentrates and the draw solution dilutes down as a result. This diluted draw outlet becomes the feed for the RO system and feeds into a RO feed buffer tank before going through the high pressure RO pump. Under an applied pressure, a permeate water is generated while the RO concentrate/retentate is sent back to the draw tank on the FO side. The permeate water is collected as the final product water. To monitor flux, pH, conductivity, and electricity use, multiple flow sensors, pH and conductivity probes, and current sensors are located across the system. The sensor output are recorded via a programmable logic controller unit which is connected to a laptop computer for data acquisition.

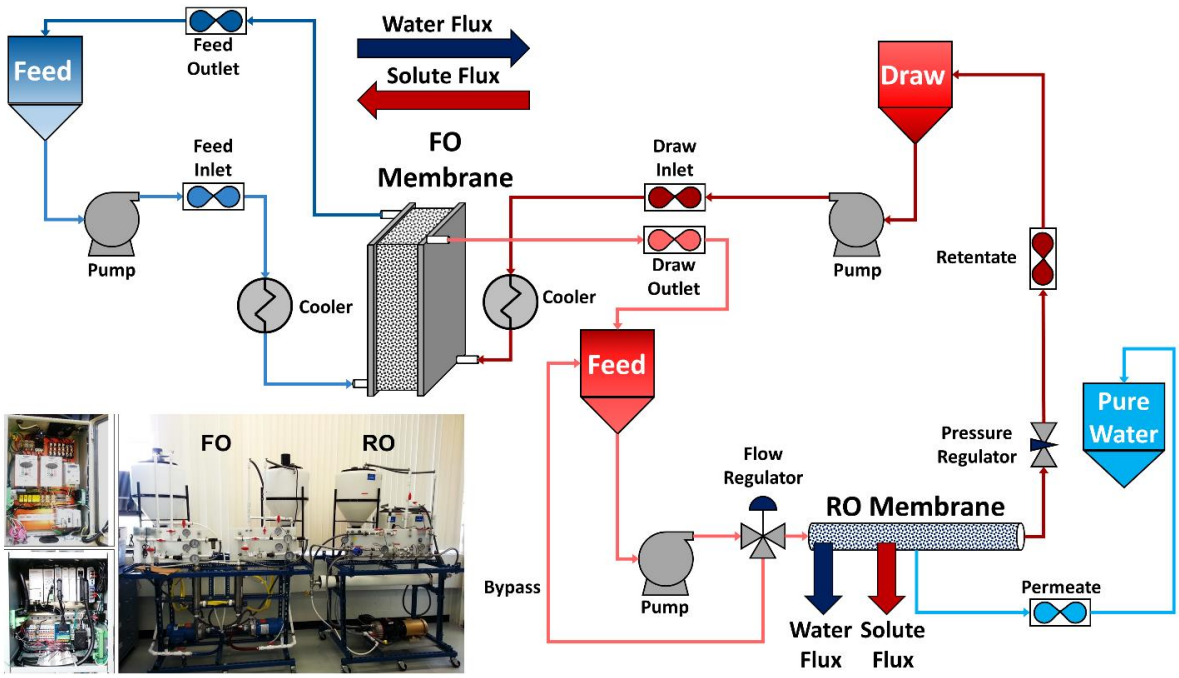

Figure 4.1: A process flow diagram of the FORO hybrid system with the actual system shown at the bottom left corner.

4.3. Experimental plan

Fig. 4.2 presents the experimental plan that is currently being used to evaluate the performance of the FORO hybrid system. Initially, a benchmark is performed using DI water as the feed in the FO side. For the draw solution, NaCl salt solution of concentration varying from 0.25 to 1 M is selected. Using this, three different module type are being studied. A plate and frame module from Porifera, a spiral wound module from FTSH$_2$O, and a hollow fiber module from Aquaporin. It should be noted here that the module not only differ in configuration and module design but in the type of membrane being used as well. Porifera uses a TFC membrane in the plate and frame module, FTSH$_2$O uses a cellulose tri-acetate (CTA) based asymmetric membrane in the spiral wound module, and Aquaporin uses aquaporin as fillers in a polymer matrix in the hollow fiber module. Although, it would have been a proper comparison if all the modules had similar membranes with similar intrinsic properties. However, it is not possible to have that as different

manufacturers make membranes in different configuration and with different material. Next, several operating conditions are being tested. This include: changes in flowrates ranging from 0.75 GPM to upto 2 GPM, changes in applied pressure in RO ranging from 200 psi to 700 psi, changes in temperature ranging from 20°C to 40°C, and draw concentration ranging from 0.25 M to 1 M NaCl salt solution. Plans for alternative draw solution such as KCl, and $MgCl_2$ are also present and will follow a similar evaluation path. After initial benchmarking is performed, focus will be given on self-regulation concept using just the RO pressure, double barrier concept for contaminant removal, energy usage, recovery, and fouling behavior. Finally, all these will be repeated for a variety of feed sources such as industrial waste water, municipal waste water, and oil and gas produced water.

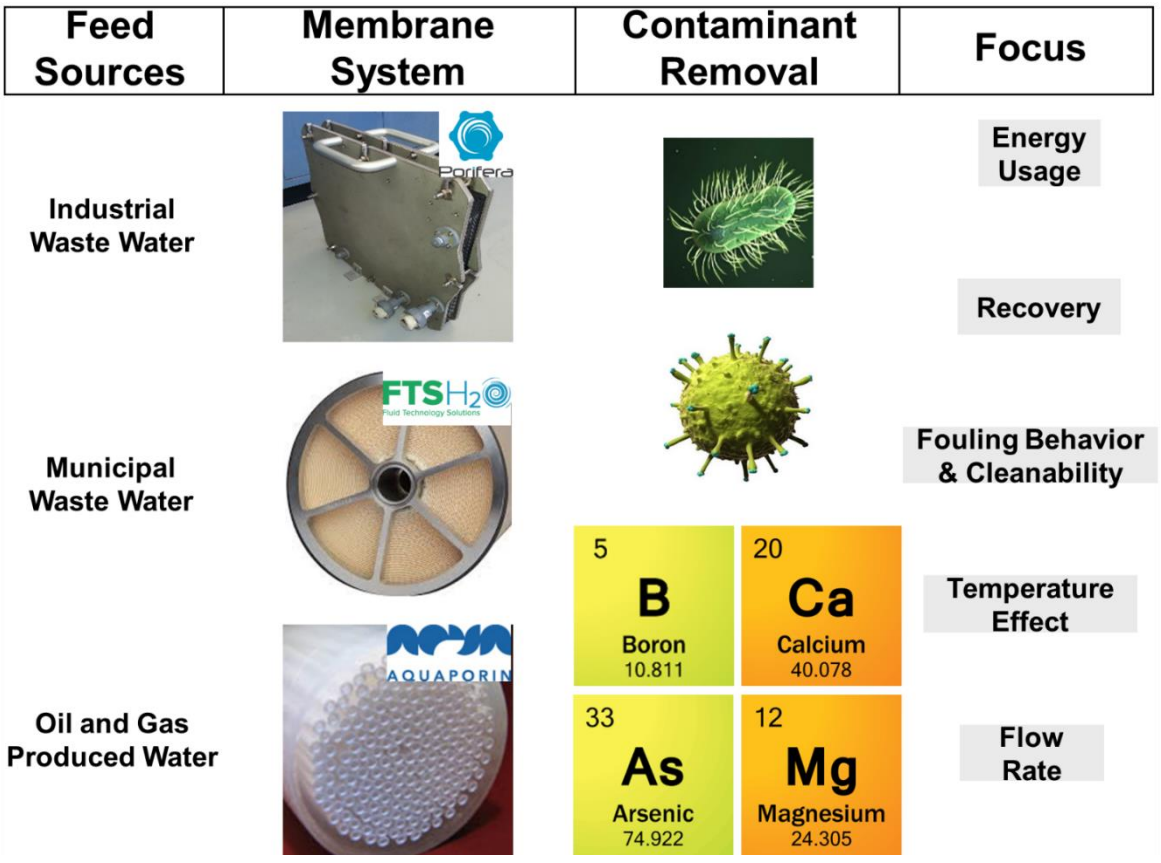

Figure 4.2: Design of experiments to be used in the FORO pilot.

4.4. Preliminary results

Initial evaluation of the FORO hybrid system was performed in two separate ways. At first, individual systems were evaluated. This means when RO pilot was operated, FO pilot was switched off and vice versa. Some of these results are presented on Fig. 4.3. Starting with RO, two different situations were studied. In the first instance, RO was operated at a constant recovery mode where a certain percentage of the feed was recovered. For 10 % recovery, five different feed flowrates were evaluated. During tests these flowrates were kept constant while the applied pressure was adjusted to maintain the recovery of feed at 10 %. For 50 % recovery, only two flowrates were used as the feed tank volume could not hold more liquid to study high flow recovery. From the recovery tests, we see that the time it takes to recover the feed, becomes shorter at higher feed flowrate. In the second instance, the applied pressure was kept constant at 100 psi and 400 psi while the recovery was left to vary and the same flow rates were studied. In the constant pressure mode, it can be seen that the recovery starts off high but eventually goes to zero as the osmotic pressure and hydraulic pressure difference becomes zero.

For the FO benchmarking, the effect of flow rate on osmotic performance was evaluated. We see a clear trend of how changing the flowrate of the FO feed and draw, dramatically improves water flux of the membrane while the salt flux remains somewhat similar. This is due to the residence time inside the module being shorter for the draw solution which reduces dilution through the length of the module and reducing the driving force for water transport.

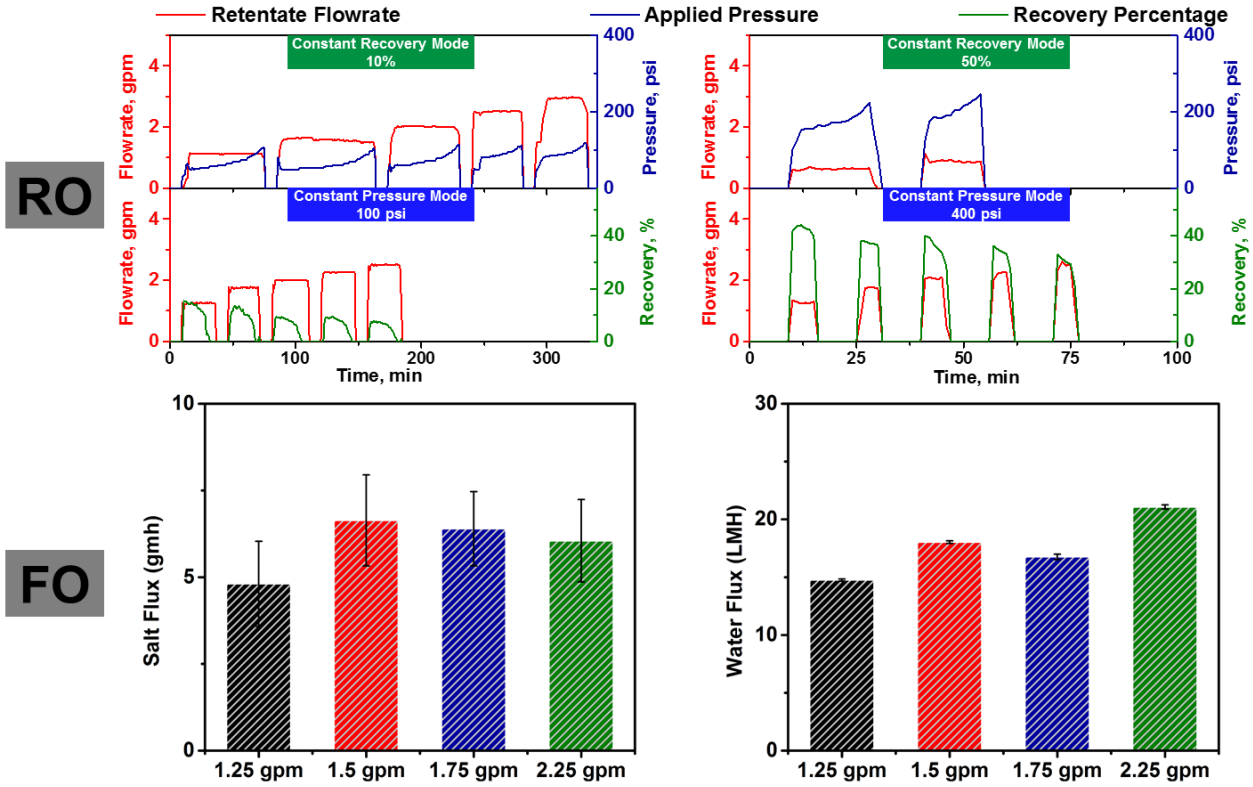

Figure 4.3: Initial bench-mark results with the FO and RO system operating in a stand-alone mode. Operating condition, RO: 2000 ppm NaCl salt solution, pressure- 100 to 400 psi, temperature- 25 °C, flowrate- 1.25 to 2.75 GPM, membrane- Dow SW30XLE. Operating condition, FO: feed-DI water, draw- 1 M NaCl solution, temperature- 25°C, flowrate, 1.25 to 2.25 GPM, membrane- Porifera 1m^2 plate and frame module.

In the second phase of evaluation of the FORO hybrid, both systems were operated together. We studied three different draw solution concentration as shown in Fig. 4.4. Starting with 0.25 M NaCl as draw solution, the FO system was operated until the FO water flux was stabilized. During this time, the RO pressure was kept at 200 psi and draw solution was circulating through the two system. From Fig. 4.4B, the draw solution kept diluting at these condition and as the difference between the osmotic pressure and the applied pressure was negligible resulting zero permeate flow in the RO as can be seen in Fig. 4.4A. Then, the RO pressure was increased from 200 psi to 500 psi abruptly to induce a sudden disturbance in the system and to see how the system dynamic changes due to this. The pressure was kept at 500 psi until the RO tank ran out of since

water was being recovered at a fast rate as can be seen by the high permeate flux (Fig. 4.4A). The permeate flux starts off high and gradually decreases as the draw (RO feed) concentration increases significantly (Fig. 4.4B). We also see the FO water flux increasing dramatically during this time due to the increased available osmotic pressure difference across the FO membrane. The RO rejection also starts off high and then starts to decrease as more of the RO feed/ FO draw gets concentrated. This behavior is seen across the three different draw concentration studied. At the highest concentration studied here, we see the RO rejection dropping significantly due to a significant amount of solutes in RO feed/FO draw solution. This also demonstrates the operating regime for RO in terms feed salinity. Interestingly, in any of the cases, the response to the sudden change in RO pressure was instantaneous. Although, we believe depending on how large the feed and draw tanks are, this time can vary a lot. Eventually, we want to observe the self-regulating nature of this FORO system but we were unable to observe that due to tank size limitation.

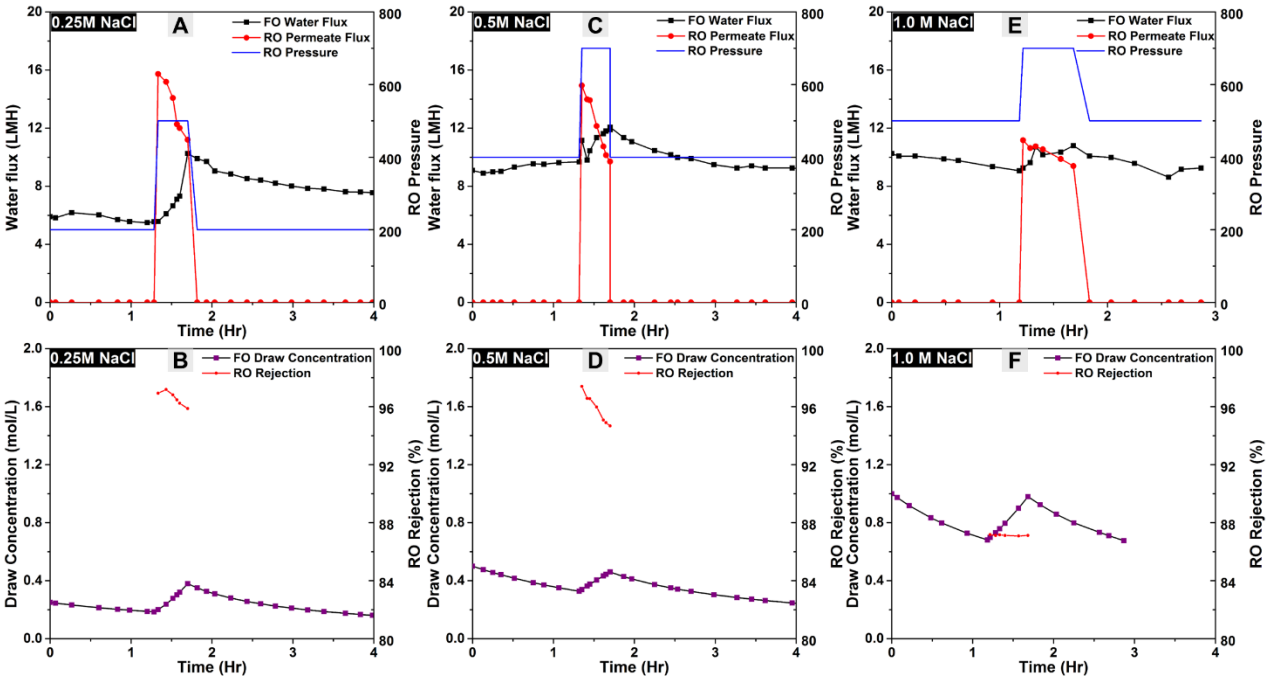

Figure 4.4: Hybrid FORO demonstration where response to a step change in pressure in the RO system is evaluated on the overall process dynamics. Operating condition, RO: Pressure- 200 to 700 psi, temperature- 25 °C, flowrate- 1.25 GPM, membrane- Dow SW30XLE. Operating

condition, FO: feed-DI water, draw- 0.25 to 1 M NaCl solution, temperature- 25°C, flowrate, 1.25 GPM, membrane- FTS H2O 3.5 m^2 spiral wound module.

4.5. Conclusion and future work

In this work, an element-scale hybrid pilot systems coupling forward and reverse osmosis was fabricated. Impact of different testing conditions such as flowrate, recovery rate, and pressure was identified at element-scale. We observed that flowrate has a more profound impact on osmotic performance for FO pilot system at element-scale with the Porifera plate and frame module. At constant pressure, recovery rate reduces during the course of RO plant operation which could act as a control mechanism for controlling FO recovery rate as well. Future work will include developing a robust methodology to study the performance of FORO with regard to Fig. 4.2 as this project continues on.

CHAPTER 5

Evaluating commercial TFC membranes: A side-by-side comparison

A detailed evaluation of a new commercial thin film composite membrane from Porifera for forward osmosis
Maqsud R. Chowdhury, Jeffrey R. McCutcheon

5.1. Introduction

Forward osmosis (FO) technology have revived tremendously over the last decade as a mean to treat wastewater or desalinate seawater to address the global water crisis [1]. System design and integration, draw solute, and membrane design have been the key areas where a significant amount of research is going on [10,12,13,62,135,139–142]. As FO utilizes the natural osmotic pressure gradient of two solutions separated by a semi-permeable membrane, it can be applied in areas such as potable water production, fertigation, osmotic membrane bioreactor, food processing etc. The growing demand of FO have put forth the commercialization of a number of FO membrane manufacturing companies include companies like Porifera [143], Aquaporin [144], and FTSH_2O (former HTI) [145] primarily. These companies manufacture FO membranes as modules for large scale industrial systems or as loose flat sheets for distribution and sales among academic groups and researchers. Among these, only Porifera manufactures thin film composite (TFC) based FO membrane [146] which has demonstrated good osmotic performance. Being the only provider of TFC FO membrane, the Porifera TFC membrane is being used widely for bench-scale testing such as waste water treatment [59], fouling and scaling study [60,147,148], draw solution design [149],

TrOCs rejection [150], and fertigation [151]. However, a comprehensive characterization similar to [27] which was done for the HTI TFC membrane have not been performed yet using the standard methodology proposed by [113].

Here, we present a detailed characterization of Porifera TFC FO membrane in terms of membrane osmotic performance, intrinsic properties, surface roughness, hydrophilicity, and morphology. We compare this membrane with other commercially available membrane such as HTI CTA, and HTI TFC in terms of their osmotic performance and find that Porifera TFC FO membrane surpasses either of the two HTI membranes in performance.

5.2. Experimental

5.2.1. Materials

The commercial membrane used in this study was provided by Porifera, Inc. (Hayward, CA, USA). According to company's website, these membranes have proprietary composition and structure which creates a thin, open-pore structure. These membranes are manufactured on commercial 40-inch roll-to-roll lines [143]. Membranes were stored dry away from sunlight. When used, the membranes were submerged in deionized (DI) water for 24 hours at 4 ˚C. TFC and CTA membrane were also provided by HTI (Albany, OR). The membrane were stored in 5 ˚C after received. A 8 cm × 3 cm membrane coupon was used for each experiment. For draw solutions, NaCl (sodium chloride, USP/FCC/EP/BP, colorless to white crystalline granules, Fisher Scientific, IL, USA), $MgCl_2$ (magnesium chloride hexahydrate, $MgCl_2$ / 6 H_2O, 99 % for analysis, MW=203.31 gm, Acros Organics, NJ, USA) and DI water (Millipore Integral 10 water system, Millipore, CA, USA) were used.

5.2.2. Membrane characterization

A sessile drop method was used to find the contact angles of the selective and support layer of the membrane. To do this, a CAM 101 series contact angle goniometer (KSV Company, MD, USA) was used. Following a sessile drop method, a droplet volume of 10 ± 1 μL of DI water was used for each test where six different random locations were chosen for selective and support layer side of the membrane. The contact angle was measured within a second of the droplet being deposited on the surface. The tests were conducted at room temperature with a relative humidity of 60 %. To investigate selective and support layer chemistry, attenuated total reflection Fourier-transform spectroscopy (ATR-FTIR) study was conducted. For this, a FT/IR 670 plus (Jasco, Easton, MD) with a variable angle ATR attachment coupled to a 45˚ germanium crystal in an argon environment was used. Each sample location was scanned for 60 times and repeated on three different location for 3 different sample membranes for each layer. The final result was taken as the average of each dataset. A scanning electron microscopy (SEM) system was used to image the selective layer, support layer and cross-section morphology of the membrane. A FEI TeneoLoVac SEM (Hillsboro, OR) was used. For imaging surface morphology, membrane samples were dried, attached to the SEM stub, and sputter coated with a thin layer of gold (Au) and platinum (Pt) under vacuum (0.6 torr). A coating time of 30 seconds with 20 mA current was selected. After coating, membranes were imaged in the SEM using a 15 kV accelerating voltage, a working distance of 10.5 mm, and the ETD detector using SE mode. Surface roughness of the selective layer of the HTI TFC and Porifera TFC was measured using an atomic force microscopy (AFM) instrument (Asylum Research MFP-3D, Santa Barbara, CA) with a silicon AFM tip (Pointprobe, Nanoworld Innovative Technologies Switzerland). The samples were first dried, attached to glass slides using double sided tape. The measurement was taken at 1 Hz for a sample area of $3 \times 3\ \mu m^2$ using non-contact mode (AC mode). Three samples were selected for each membrane and 3 scans were

performed for each sample. The result is presented as root mean square roughness (Rq), average roughness (Ra), and surface area difference (SAD) [152].

5.2.3. Water permeance and solute permeability

Pure water permeance, solute permeability and solute rejection of the membrane were characterized using a reverse osmosis bench-scale test setup [44,47]. The test setup includes three cross-flow membrane cells where the membrane coupons were placed. Using DI water as feed, the pressure was varied from 75 psi to 225 psi with a constant flow velocity of 0.23 ms^{-1}. The calculated Reynolds number for the flow condition was found to be 1150. The temperature of the system was maintained at 20 ˚C. For each pressure, permeate was collected and weighted to get the water flux. A linear graph of water flux against feed pressure was generated the slope of which was noted as the pure water permeance. To measure solute rejection and permeability, a 2000 ppm feed solution was used as the feed without replacing the membranes in the cross-flow cell. Permeates were collected for 175 and 225 psi which were weighted and the conductivity of permeate was measured using conductivity probe. The solute observed rejection (% R) was calculated using the following equation:

$$\%R = \left(1 - \frac{C_{permeate}}{C_{Feed}}\right) \times 100\% \quad (5.1)$$

Here, $C_{permeate}$ is the concentration of solute in permeate and C_{Feed} is the concentration of solute in the feed solution. Solute permeability (B) was then calculated using the following equation:

$$B = J_w \left(\frac{1-R}{R}\right) exp\left(-\frac{J_w}{k_{mt}}\right) \quad (5.2)$$

Here, J_w is water flux, R is the observed rejection from Eq. 5.1 and k_{mt} is the mass transfer coefficients [85,153,154].

5.2.4. Osmotic flux testing

In the osmotic flux tests, water flux and reverse solute flux were measured using a forward osmosis bench scale setup [11,44,85,113,155]. The temperature of the setup was maintained at 20

˚C ± 1 ˚C with both feed and draw side flowing at a velocity of 0.23 ms^{-1} and at 3 psi. The calculated Reynolds number for the cell was found to be 1150. Water flux was measured gravimetrically using a balance (Denver Instruments, NY). Using a conductivity probe, the reverse solute flux was calculated by measuring the change in conductivity of the feed solution from the start and till the end of the experiment. Two different membrane orientation was studied which are known as FO and PRO mode. While the selective layer faces the feed side in FO, in PRO, selective layer faces the draw side. Tests were repeated for each mode to have confirm consistency of the result.

5.2.5. Membrane structural parameter

In FO, the asymmetric nature of the membrane imparts resistance to diffusion of solutes which creates a polarization phenomenon known as internal concentration polarization (ICP) [67,103,120,156]. The severity of ICP in any FO membrane controls the membrane performance. ICP can be related back to the membrane support layer structure by a parameter known as structural parameter, S. This parameter is defined as the product of tortuosity (τ) and thickness (t) of the membrane normalized by support layer porosity (ε) of the membrane. Using an empirical relationship between structural parameter, membrane intrinsic properties and osmotic flux performance, the value of S was calculated [156].

$$S = \left(\frac{D_{Db}}{J_w}\right) ln \frac{B + A\pi_{Db}}{B + J_w + A\pi_{Fm}} \quad 5.3$$

Here, J_w is the experimentally obtained water flux in FO mode, B is the solute permeability, A is the pure water permeance, D_{Db} is the solute diffusivity at bulk concentration, π_{Db} and π_{Fm} are the osmotic pressures at bulk draw solution concentration and feed solution concentration near the feed side membrane boundary layer respectively.

5.3. Results and discussion

5.3.1. Membrane characterization

5.3.1.1. Scanning electron microscopy

SEM images of the Porifera TFC membrane are presented in Fig. 5.1. A defect free and uniform layer of polyamide as the selective layer can be seen in Fig. 5.1a. Magnification of this layer reveals the typical ridge and valley like structure which is coherent with the m-phenylenediamine / tri-mesoylchloride chemistry based polyamides [39,60]. From Fig. 5.1c and 4.1d, a porous surface morphology with homogenously distributed pores in the range of 20 ± 6 nm (using ImageJ) is visible for the support layer which, reportedly, has polysulfone in it [60,148]. Cross-sectional image of the Porifera TFC membrane (Fig. 5.1e, 5.1f) reveal the overall thickness of the membrane to be ~ 48 ± 5 µm with an embedded mesh with fiber diameter of 35 µm for mechanical support. Compared to the HTI TFC membrane, the Porifera TFC is 60 % thinner with much higher surface pore density [27]. It has been discussed widely on the importance of making FO membranes thin, highly porous, and straight to reduce the tortuosity factor in the support layer which reduces overall mass transfer resistance and improves osmotic performance [44,47,157]. Porifera have engineered their TFC membrane to have all these features, and yet made it mechanically strong to create a high performance membrane that can be incorporated into modules which has been a limiting factor for a large number of novel membranes for FO [46,47,158–171].

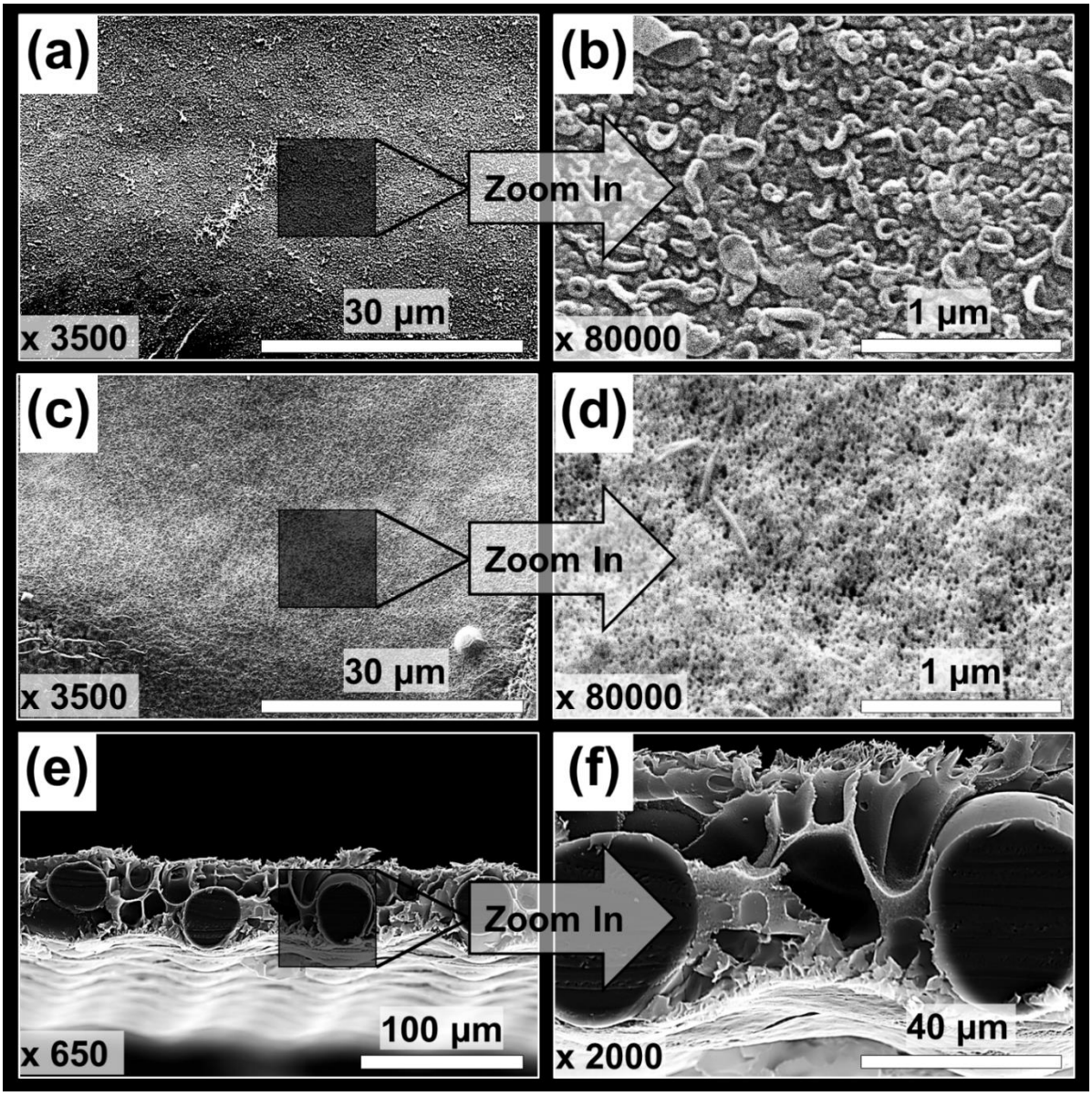

Figure 5.1. Scanning electron micrographs (SEM) of the selective layer (a, b), support layer (c, d), and the cross-section (e, f) are presented. Selective and support layer are imaged at 3500 × (a, c) and at 80000 × (b, d). The cross-section SEM images were taken at 650 × (e) and 2000 × (e) magnification.

5.3.1.2. Surface roughness and hydrophilicity

Surface roughness is an important parameter for any FO membrane as FO have often been considered to treat highly fouling feeds. In Fig. 5.2, the AFM 3-D surface profiles are presented for the HTI TFC and Porifera TFC membrane. Qualitatively, it can be said that the HTI TFC has

a rougher surface than Porifera TFC membrane as was also found from the calculated roughness (R_q, R_a) shown in Table 5.1. While having a rough surface provide higher water permeance due to increased surface area difference (SAD) [172], a smooth surface should provide very good anti-fouling properties [173]. Although Porifera have succeeded in the reduction of roughness compared to the HTI TFC, recent work on fouling and scaling reveals that fouling and scaling remains an issue [60,147,148,174,175].

Table 5.1
Calculated RMS roughness, average roughness, and surface area difference for the HTI TFC and Porifera TFC membrane.

Membrane	RMS roughness Rq	Average roughness Ra	Surface area difference (SAD)
HTI TFC	44 ± 2	44 ± 1	53 ± 5
Porifera TFC	35 ± 4	27 ± 3	14 ± 4

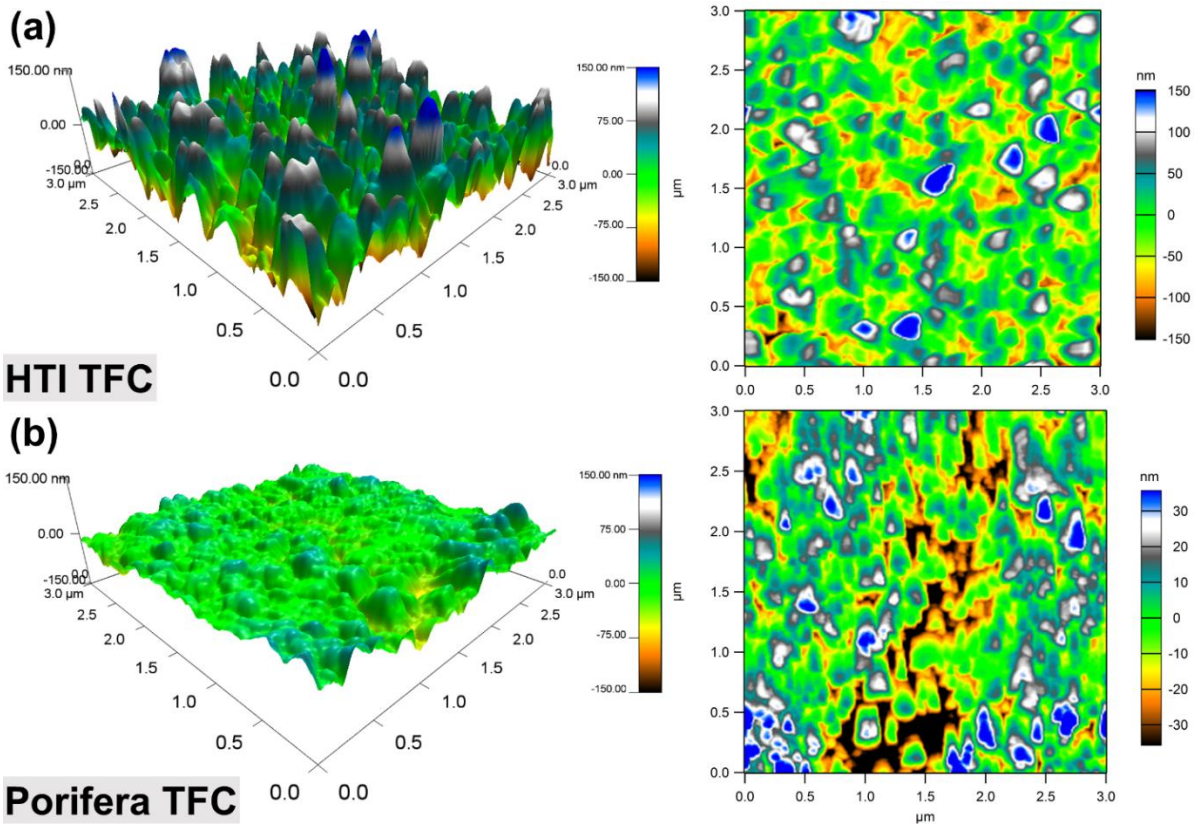

Figure 5.2. Atomic force microscopy (AFM) 3-D surface images of the selective layer for HTI TFC (a) and Porifera TFC (b) membrane are presented.

The Porifera TFC membrane is also hydrophilic in nature for both of its' support and selective layer (Table 5.2). Compared to the HTI TFC membrane, this membrane is less hydrophilic [27] but is similar to other polyamide based high performance TFC FO membranes [46][176]. Generally, a hydrophilic surface with low roughness demonstrated to have high anti-fouling property [173].

Table 5.2: Contact angle of the Porifera TFC membrane

Membrane Orientation		Contact angle
Selective layer	65˚± 5˚	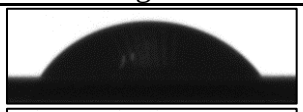
Support layer	70˚± 5˚	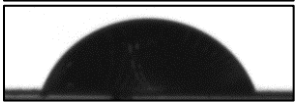

5.3.1.3. Attenuated total reflection Fourier-transform infrared spectroscopy

From the ATR-FTIR analysis (Fig. 5.3) of the selective and support layer, both layer contains characteristic peaks. Due to the large penetration depth of the laser (~ 300 nm), the selective layer spectrum contains all the peaks from the support layer in addition to the peaks specific to the polyamide film. These peaks are found at 1541 cm^{-1} (arrow 1: N-H in plane bending and C-N stretching vibration of a –CO-NH- group of the polyamide film), 1610 cm^{-1} (arrow 2: N-H deformation vibration of the aromatic amide), 1661 cm^{-1} (arrow 3: C=O stretching of the amide linkage), 3000-2900 cm^{-1} (arrow 4, 5: aliphatic C-H stretching), and 3300 cm^{-1} (arrow 6: stretching vibration of N-H and –COOH groups of the polyamide layer) [155,177].

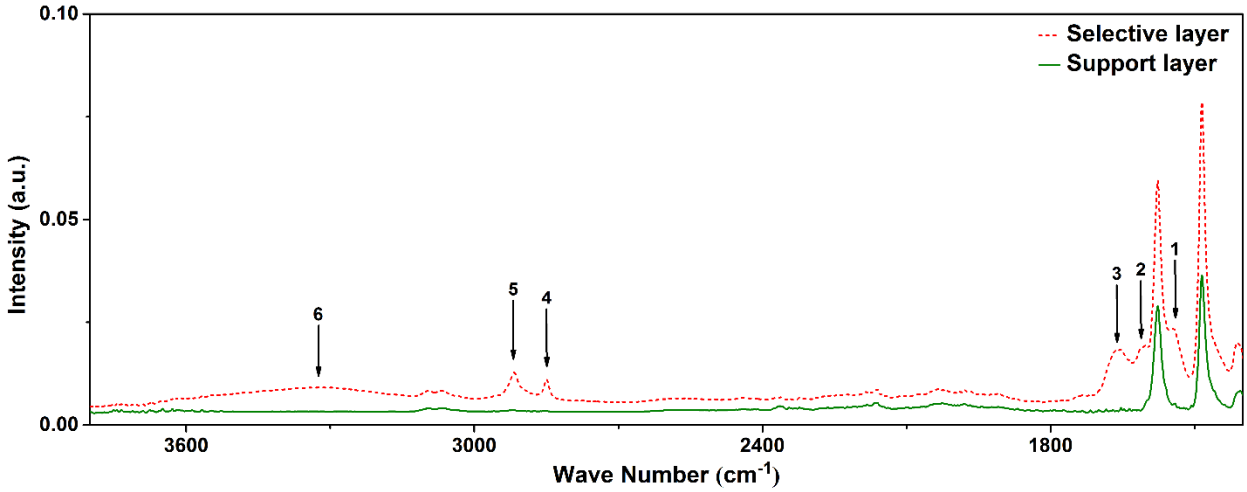

Figure 5.3. ATR-FTIR spectrum of the Porifera TFC membrane support (green solid line) and selective (red dotted line) layer. Arrows in the figure are specific to the selective layer.

5.3.2. Membrane intrinsic properties

Fig. 5.4 represents the membrane intrinsic properties for three different membranes. Porifera TFC membrane shows significantly higher pure water permeance than either of the HTI membrane while having equivalent solute permeability compared to the HTI TFC membrane (Fig. 5.4a). However, the solute rejection of the Porifera TFC membrane exhibits lower value than the HTI CTA and TFC membrane. This is not surprising as all these membranes were not designed to withstand high hydraulic pressure. As a result, Porifera TFC have been used in pressure retarded osmosis (PRO) applications due to its high mechanical integrity. Better permselectivity of the Porifera TFC membrane can be attributed to its thinner membrane structure.

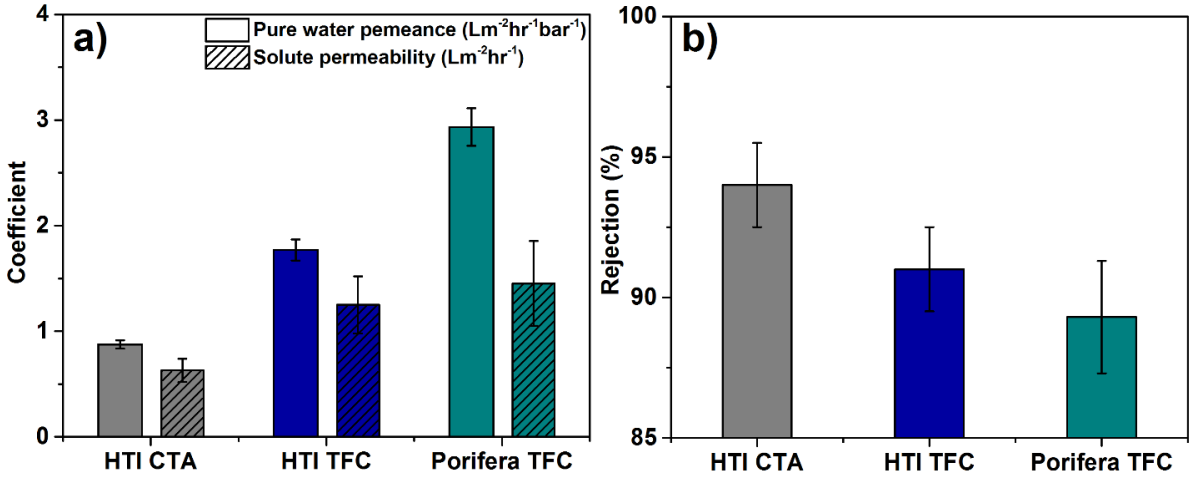

Figure 5.4. Comparison of (a) pure water permeance A, (b) solute permeability B, and solute rejection of HTI CTA, HTI TFC, and Porifera TFC membrane. Experimental condition: Feed- DI water/2000 ppm NaCl solution; Membrane- HTI CTA, HTI TFC, and Porifera TFC; Cross-flow velocity- 0.23 m s^{-1}, Pressure- 75-225 psi. The error bar represents standard deviation between three experiments.

5.3.3. Osmotic performance

In Fig. 5.5, osmotic performance of the Porifera TFC and the HTI CTA, and TFC are presented. In FO mode, Porifera TFC membrane achieved more than two times higher water flux than either of the HTI membranes while PRO mode water flux for the Porifera TFC was found to be 50 % more than that of the HTI TFC (Fig. 5.5a). Typically, TFC membranes demonstrate better permselectivity than asymmetric membranes which is true for both HTI TFC and Porifera TFC membrane [178] as a result of the thin, dense, and highly cross-linked polyamide structure. The solute flux for the Porifera TFC membrane was found to be significantly higher than the HTI CTA, and TFC membranes (Fig. 5.5b). The high water and reverse salt flux of the Porifera TFC membrane can be attributed to its high A and B, and lower rejection found in the RO characterization.

Comparing the FO and PRO mode water and flux for the Porifera TFC, it is also interesting to note that the difference between the two modes is not significant. This implies that the internal concentration polarization (ICP) of the Porifera TFC membrane under FO mode is significantly

reduced which can be related back to the thinner membrane with high surface porosity compared to the HTI TFC. Additionally, the membrane hydrophilicity also imparted its contribution toward this. As a result, in PRO mode we do not see significant improvement over the osmotic performance. In general, ICP remained an issue with previous generation of FO membranes. With this new class of TFC membrane from Porifera, it is now possible to focus on other issues such as fouling, chlorine tolerance etc. The water flux for the porifera membrane matches well to the one presented in chapter 4, Fig. 4.3 using the FORO system. Although, the salt flux is double of what is seen in the pilot scale system. This is probably due to the use of a cross-flow cell and using O-ring to seal the membrane in the bench-scale setup while commercial modules are more robust.

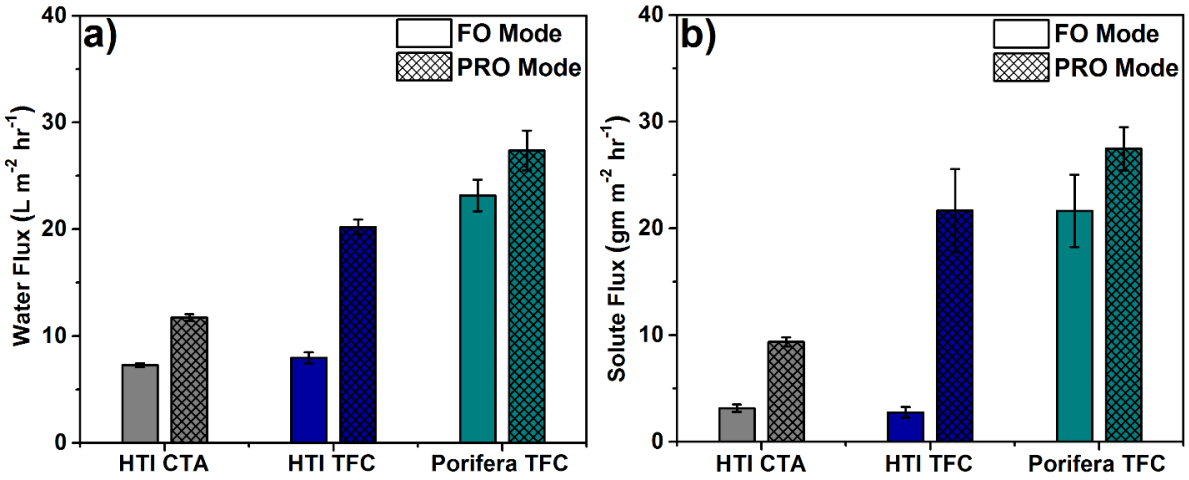

Figure 5.5. Water flux (a) and solute flux (b) performance of HTI CTA, HTI TFC, and Porifera TFC membrane. Experimental condition: Feed- DI water; Draw- 1 M NaCl solution; Membrane- HTI CTA, HTI TFC, and Porifera TFC; Cross-flow velocity- 0.23 m s^{-1}; Pressure- 3 psi on both side.

5.3.4. Structural parameter

Fig. 5.6 presents the structural parameter, S, for the three different membranes. The structural parameter for the HTI CTA, and TFC were found to be similar to [27] and are higher than the Porifera TFC which is expected, given that the Porifera membrane has much better osmotic performance than either of the membrane. A structural parameter of ~330 µm for the Porifera TFC

suggests that the ICP is reduced significantly. This is also in accord with the image and contact angle characterization which highly suggested that the membrane has a highly porous, minimally tortuous, and thinner support structure. Comparable structural parameter to this membrane are reported by several publications where novel material such as nanofibers, nanocomposites, hydrophilic, and highly tuned support etc. are used [47,68,160,164,165,179–184].

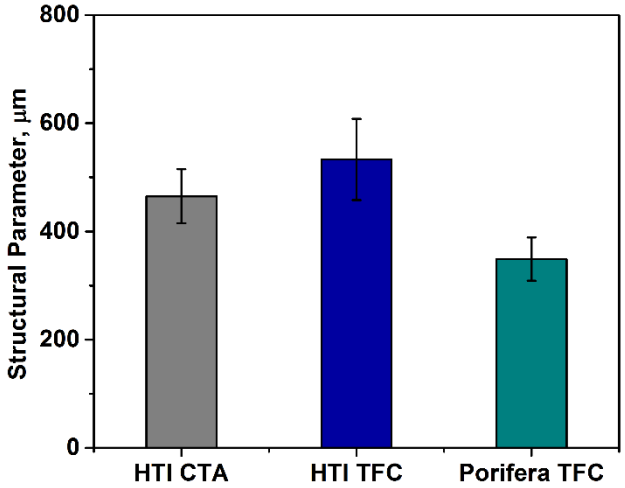

Figure 5.6. Structural parameter, S, of HTI CTA, HTI TFC, and Porifera TFC membrane. The structural parameter model was taken from [156].

5.4. Conclusions

With very limited commercial availability of the TFC FO membrane, the Porifera TFC will certainly become a standard for academics, national laboratories, and new FO startups who are trying to expand and discover newer application of FO. In addition, the benefit of having a high performing membrane such as the Porifera TFC membrane was needed for a long time in FO community and is available commercially as loose flat-sheets and in modules. Nevertheless, novel platforms such as nanofiber and nanocomposites based supports, anti-fouling, chlorine, and pH tolerant membranes are still need to be investigated furthermore as the application of FO is seen more into treating challenging water sources.

CHAPTER 6

Formation of TFC membrane using CIP: Utilizing commercial nanofibers as substrate

Originally published as:
Thin film composite membranes for forward osmosis supported by commercial nanofiber nonwovens
Maqsud R. Chowdhury, Liwei Huang, and Jeffrey R. McCutcheon, Industrial & Engineering Chemistry Research, 56, 1057-1063 (2017)

6.1. Introduction

The thin film composite (TFC) membrane design consists of a porous support structure on which a highly selective thin film is formed by in-situ interfacial polymerization [29,39,154]. This has been a popular platform for making membranes for forward osmosis (FO) because each layer can be tuned independently in order to serve a specific purpose [28,36,185]. A thin selective layer can be made to have high rejection and permeance [157] while a supporting layer (or layers) can be designed with a low structural parameter to minimize internal concentration polarization [46,67,156,158–160,186] yet still retain strength for fabrication and handling. Many different support layer structures and chemistries have been proposed for TFC FO membranes [27,44,46,47,158,161,162,169,171,186–192]. Of these many options, nanofiber nonwovens are considered among the more novel support structures because of their deviation in structure and fabrication method from conventional nonsolvent induced phase inversion casting. A few groups have made these membranes using electrospinning to fabricate the nanofiber nonwoven supports to demonstrate the high performance of these membranes for FO [158,160]. This enhanced

performance was attributed to the highly porous and non-tortuous structure of the nanofiber mat. Since these initial studies, further work has explored nanofiber nonwovens as a support for FO TFC membranes. [47,163–165,167,168,180,181,187], but all were made by electrospinning. Electrospinning is an excellent method that can create nanofiber nonwovens, but has shown some limitations when it comes to manufacturing at scale. While significant strides have been made in making roll-to-roll electrospinning systems in a commercial setup [193–195], the material can be expensive to make at large in a laboratory setup. Furthermore, the standalone strength of nanofiber nonwovens is typically very limited and its thickness is limited due to spinning process constraints [196]. Typical range of tensile strength for electrospun fibers are in the range of 0.05-0.2 GPa [190,197–200] whereas those produced for application using melt-spinning range from 0.1-2 GPa [201,202].

A number of companies offer commercially manufactured nanofiber technology platforms that are used for a variety of applications [193,203–207]. Air filtration, battery separators, apparel industries, medical devices and liquid filtration [206,207] are some examples. Among them, DuPont offers, a nanofiber based nonwoven material produced by a proprietary electroblowing process, which creates a uniform web or randomly deposited fine fibers having some of the same key attributes of electrospun nanofibers (e.g. high porosity, low tortuosity), while exhibiting better mechanical strength.

In this work, we demonstrate that a commercially available unsupported nanofiber nonwoven material can be used as a support for a robust and high performing TFC membrane for forward osmosis. The polyethersulfone (PES) based nanofiber mat from DuPont is used due to its commercial availability and good mechanical properties. Using conventional interfacial polymerization technique, the membranes were fabricated and then tested to measure mechanical

properties, characterize surface chemistry and morphology, and osmotic performance. The inherent properties and commercial availability of the nanofiber based nonwoven suggests that nanofiber supported TFC membranes may be a viable high performance commercial FO membrane.

6.2. Materials and methods

6.2.1. Materials

The DuPont nanofiber based nonwoven used for this study was made from Polyether sulfone (PES) (denoted as DuPont PES). The unsupported nanoweb had been process in a way to improve the mechanical integrity and strength. The resulting structure was less than 50 µm thick, had a total porosity below 50 %, and a mean flow pore size below 1 µm.

A commercial thin film composite forward osmosis membrane was provided by Hydration Technology Innovations (HTI, Albany, OR) which was used as a benchmark. m-phenylenediamine (MPD, > 99 %) and 1,3,5- benzenetricarbonyl trichloride (TMC, 98 %) were purchased from Sigma-Aldrich. Hexane (HPLC grade, > 99 %) and Sodium chloride (NaCl, crystalline, certified ACS) were purchased from Fisher Scientific (Pittsburgh, PA). Deionized water (DI) was collected from Millipore Integral 10 water system (Millipore, Billerica, MA).

6.2.2. Interfacial polymerization to make TFC membrane

The polyamide selective layer was formed on one side of the DuPont PES material using a modified conventional approach [39,178]. For consistency, the side on which the polyamide layer was formed was marked for repeatability. The DuPont PES nanofiber mat was first taped on to a glass plate which was then submerged into a bath of 2 % (wt. /vol. of solvent) MPD in DI water for 2 minutes. After removing it from the bath, a rubber roller was used to remove excess MPD from the surface of the mat. The membrane was dipped into a different bath of 0.15 % (wt./vol. of

solvent) TMC in hexane for 1 minute. Due to the immiscible nature of the two solutions and a high degree of reactivity between the two monomers, a highly cross-linked polyamide film was formed at the interface. The DuPont PES TFC membrane was then oven cured at 75 °C for 5 minutes to remove excess solvents. Subsequently, the TFC membrane was stored in DI water at 4 °C for further analysis [178].

6.2.3. Membrane characterization

The DuPont PES nanofiber mat and the nanofiber supported TFC membrane (DuPont PES TFC) were imaged with a scanning electron microscope (SEM) (JEOL 6335F). The membranes were dried under vacuum (0.6 torr) and sputter coated with gold (Au) and platinum (Pt) using a Polaron E5100 SEM coating unit. A sputtering time of 30 seconds was used with a 20 mA current. After coating, the samples were inserted into the SEM for imaging at an accelerating voltage of 15 kV and a working distance of 13.4 mm. The images were used to determine fiber size distribution using ImageJ image processing software and to qualitatively evaluate the polyamide structure. Attenuated total reflection Fourier-transform infrared (ATR-FTIR) spectroscopy was used to confirm the formation of a polyamide selective layer. The spectra was taken using a FT/IR 670 plus (Jasco, Easton, MD) with a variable angle ATR attachment coupled to a 45 ° germanium crystal in an argon environment. A total of 60 scans were taken for each sample location. This was repeated for three different location on each sample and three different samples were used and all the data were averaged. A CAM 101 series contact angle goniometer was used to measure the contact angle of the DuPont PES mat using deionized water. A sessile drop method was used where the droplet volume was 10 ± 1 μL and 6 different locations were selected for each sample. The contact angle was measured within a second of the droplet being deposited on the sample [47]. The measurement was repeated for both top and bottom part of the marked nanofiber mat.

Mechanical properties of DuPont PES mat and DuPont PES TFC membrane were evaluated using an Instron microforce tester at 25 °C. A dynamic mechanical analysis (DMA) controlled force (type-tension for film) module was selected with a loading rate of 0.5 N/min. Both types of materials were evaluated in their wet and dry conditions. Each material was kept in DI water for 7 days before they were tested. At the time of testing, samples were taken out of DI water bath and immediately attached to the testing device. The test took only 2-4 minutes and the samples remained wet even after it was done. The reported values are an average of 6 different samples.

6.2.4. Membrane osmotic performance tests

A conventional forward osmosis bench scale setup was used for the evaluation of the DuPont PES TFC membrane. The details of the cross-flow system is presented in our previous work [11,82]. A membrane coupon of 8 cm × 3 cm was used for all tests. Both the FO mode (membrane polyamide selective layer facing the feed solution) and PRO mode (the membrane polyamide selective layer facing the draw solution) were tested. The draw solution was slightly pressurized (1psi above the feed), to facilitate the detection of defects during operation. Any defects are easy to detect as the conductivity in the feed solution would rapidly rise. To support the membrane under this slight pressure differential, a support spacer was inserted on the feed side. An open channel crossflow velocity of 0.11 m s^{-1} with a Reynolds number of 1100 (assuming the open channel velocity for both sides) was maintained across the membrane. After equilibration, the system kept running for 1 hour during which water permeated into the draw solution side and solutes from the draw solution diffused into the feed

6.3. Results and discussion

6.3.1. Membrane characteristics

6.3.1.1. Contact angle

Contact angle measurements of the DuPont PES mat indicated mild hydrophobicity. The front of the material (which is in contact with the polyamide) measured 89 ° ± 2 and the contact angle of the back side was found to be 99 ° ± 10 (with a p-value of 0.0175 which is statistically significant). Typical hydrophilic nanofiber materials have contact angles less than 90 ° whereas hydrophobic materials have contact angles greater than 90 ° [208]. Mild hydrophobicity is beneficial for nanofiber based material as supports for TFC membranes as these would not swell and possibly delaminate the polyamide layer [158,209–211] from the support membrane structure. However, if the fibers are too hydrophobic, the material would not wet and solutes and water would be unable to transport across the TFC membrane.

6.3.1.2. Scanning electron microscopy

A series of scanning electron micrographs of DuPont PES nanofiber mat and DuPont PES TFC membrane are shown in Fig. 6.1. The top surface, shown in Fig. 6.1a, differs from the bottom surface, shown in Fig. 6.1b. Fig. 6.1b shows fused fibers that are more densely packed, while the top surface is more loose and open. This asymmetry is likely a result of the proprietary manufacturing process, but this fusion of fibers on the bottom are a source of mechanical strength for the material overall. A flatter surface also reduces roughness and subsequently increases hydrophobicity as was found in the previous section [212,213]. The average fiber diameter based on the histogram in Fig. 6.1c was found to be 450 ± 130 nm (Fig. 6.1c). Imaging of the DuPont PES TFC membrane selective layer (Fig. 6.1d) shows a uniform and defect free polyamide film that was formed on the top side of the DuPont PES mat. A closer look at this layer reveals the typical ridge and valley like structure of conventional polyamide films (Fig. 1e) [178,211]. Zooming in further and focusing on the edge of the sample (Fig. 6.1f), shows the polyamide layer thickness as approximately 150 - 200 nm.

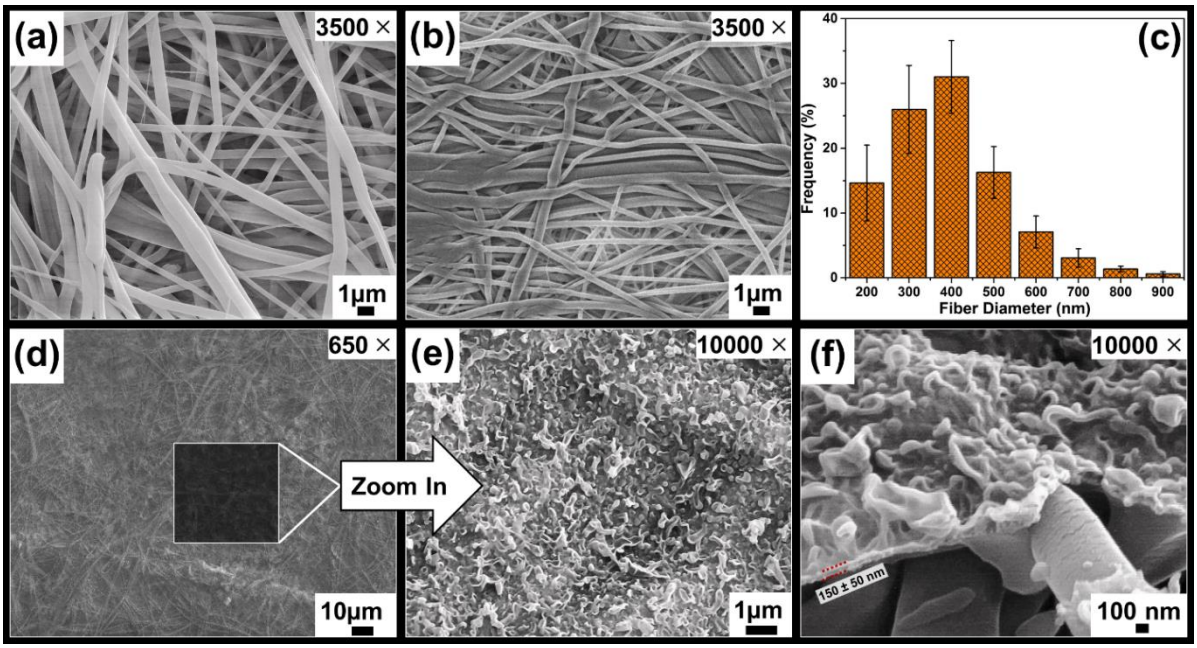

Figure 6.1. Scanning electron micrographs (SEM) of the top (a) and bottom (b) surface of DuPont PES nanofiber mat at 3500 × magnification. Fiber size distribution of the mat is shown in (c). The DuPont PES TFC membrane at magnifications of 650 × (d), 10,000 × (e), and 35,000 × (f) is also presented.

6.3.1.3. ATR-FTIR

The successful formation of polyamide film on the DuPont PES mat was further confirmed using ATR-FTIR analysis (Fig. 6.2). By comparing the DuPont PES mat with the DuPont PES TFC membrane, additional peaks are observed for the DuPont PES TFC membrane. All of these peaks correspond to the different groups in the polyamide structure that have been described in other publications[155,177]. These visible peaks are found at 1541 cm^{-1} (arrow 1 is characteristic of a N-H in plane bending and C-N stretching vibration of a –CO-NH- group), 1610 cm^{-1} (arrow 2 is characteristic of a N-H deformation vibration of the aromatic amide) and 1661 cm^{-1} (arrow 3 is characteristic of a C=O stretching of the amide linkage).

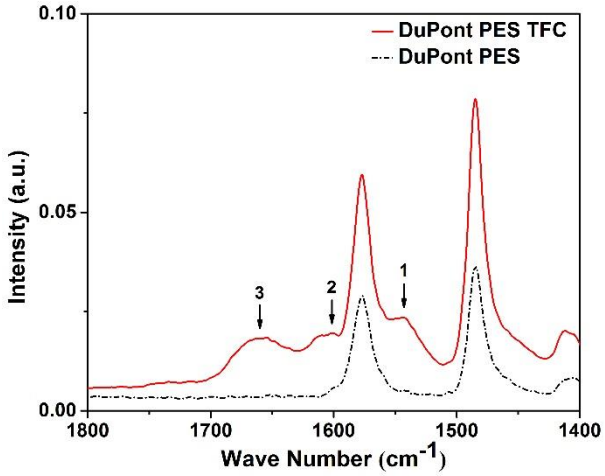

Figure 6.2. ATR-FTIR spectrum of the DuPont PES TFC membrane and the unmodified DuPont PES mat. The arrows indicate peaks associated with the polyamide selective layer.

6.3.1.4. Dynamic Mechanical Analysis

Since the early work on nanofiber supported TFC membranes, it has been challenging to make a membrane with good mechanical properties in wet conditions [178]. In Fig. 6.3, the mechanical properties of the DuPont PES mat and the DuPont PES TFC membrane is compared to laboratory scale nanofiber supported TFC membrane from the literature [209] for both wet and dry conditions. As anticipated, the DuPont PES TFC membrane has an order of magnitude higher Young's modulus than the lab-scale produced membranes (Fig. 6.3a). This may be due to the significant fiber-to-fiber contact in the DuPont PES nanofiber structure. The superior rigidity compared to conventional electrospun mats is preferred, since a stiff support may prevent defect formation or delamination of the selective layer (which itself is quite rigid) over time.

These membranes had modestly higher tensile strength as well. The DuPont PES did show reduced strength when wet, which may suggest that wetting causes fibers to plasticize and/or detach from one another, but the composite DuPont PES TFC demonstrated better strength in both wet and dry conditions. As was found in previous work on nanofiber TFC membranes [47], the formation of the composite of the nanofiber layer and the rigid aromatic polyamide layer [214] is

stronger than either layer alone. The composite also showed resiliency when wet and did not exhibit strength degradation compared to the dry membrane.

A further comparison chart is presented on Fig. 6.4 between different electrospun (e-spun) nanofiber based TFC with the DuPont PES TFC in terms of both tensile strength and modulus. It can be seen that the DuPont PES TFC membrane has superior mechanical properties than most of the nanofiber based TFC membrane for FO to date. Only the e-spun TFNC (thin film nanocomposite) [215] demonstrate equivalent mechanical characteristic to the DuPont PES TFC membrane as they used multi-walled carbon nanotube which are known to improve mechanical properties of materials [216]. Additionally, when the mechanical properties of these e-spun TFC membranes are compared with commercial Kevlar fibers [217], we see several orders of magnitude higher strength and modulus. However, such high degree of strength are irrelevant for low pressure filtration application such as FO and we believe the mechanical properties of commercial nanofibers like the DuPont PES are more than sufficient.

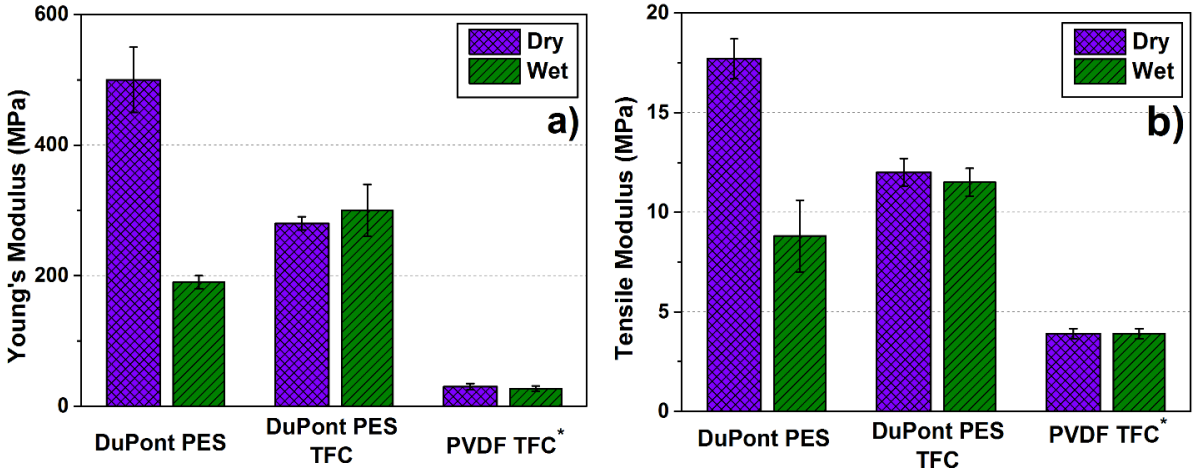

Figure 6.3. Mechanical properties of DuPont PES and nanofiber supported thin film composite (DuPont PES TFC) membrane in both wet and dry conditions: (a) Young's modulus (MPa), (b) Tensile Strength (MPa). The error bar represents standard deviation between six samples.
* The data for PVDF TFC were taken from [209].

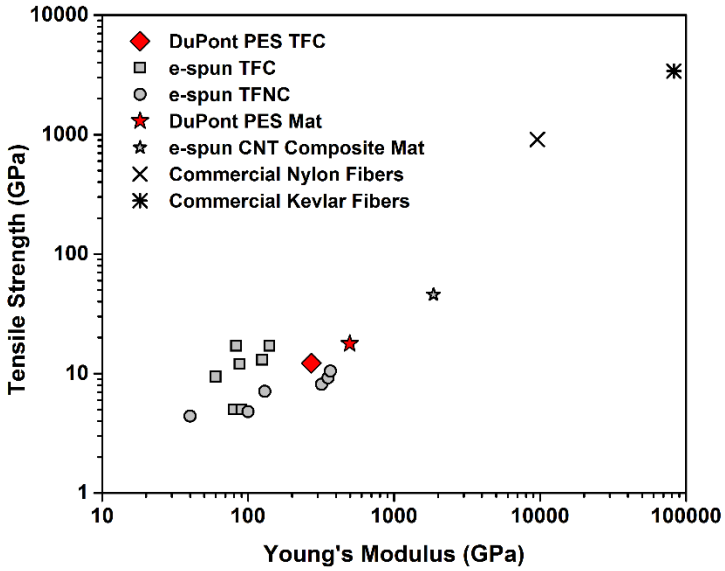

Figure 6.4. Comparison of mechanical properties of DuPont PES mat and TFC membrane with published literature on e-spun mat and TFC and commercial fibers [167,209,215,217–219]. All data represent dry samples only.

6.3.2. Osmotic performance

The osmotic water flux and reverse solute flux of the DuPont PES TFC membrane is presented on Fig. 6.5a and 6.5b, respectively, and is compared to a commercial TFC membrane from Hydration Technology Innovations (HTI TFC) and a lab-scale Nylon coated PVDF nanofiber supported TFC (PVDF TFC) [209]. We chose this PVDF TFC membrane for comparison as the osmotic testing was done using the same FO characterization setup with similar feed and draw solution concentrations. The DuPont PES TFC membrane has similar FO mode and PRO mode water flux in comparison to the PVDF TFC membrane while it has 200 % higher water flux in FO mode and 130 % in PRO mode than the commercial HTI TFC membrane. As has been observed in many earlier studies on FO membranes, water flux in FO mode was lower than PRO mode due to more severe internal concentration polarization (ICP) that occurs in the support of the membrane. Compared to the HTI TFC membrane, the difference between FO and PRO mode water flux is smaller which suggests that both ICP and structural parameter are smaller as well.

From the reverse solute flux data in Fig. 6.5b, we see substantial difference between the DuPont PES TFC and PVDF TFC membranes in PRO mode while both show similar solute flux in FO mode. Generally, an increase in water flux is correlated to an increase in solute flux. This was found to be true for the commercial HTI TFC and lab-scale PVDF TFC. The low reverse solute flux in PRO mode for the DuPont PES TFC membrane can be attributed to its much higher mechanical rigidity and strength compared to the PVDF TFC membrane implying that the polyamide was well-integrated into the support structure of the DuPont PES mat. The outperformance of this membrane relative to commercial TFC membranes is meaningful given that the DuPont PES was not specifically designed for this application nor was modified in any way.

A further comparison between the laboratory scale nanofiber based TFC and the DuPont PES nanofiber TFC are presented on Fig. 6.6 for both FO and PRO mode using a method proposed by Bui et al [167]. Ideally, a FO membrane should be have high water flux relative to low reverse solute with a high osmotic water permeability. From Fig. 6.6a, we see that the DuPont PES TFC membrane compares well with bulk of the e-spun TFC membrane for FO mode operation. Only the e-spun TFNC membranes outperform the DuPont PES TFC membrane due to their superior hydrophilicity and porosity induced by the nanoparticle [167,168]. In PRO mode, a similar performance was also observed compared to e-spun TFC membranes. This is quite impressive as these material were not modified or tailored for FO, yet they produce impressive osmotic performance.

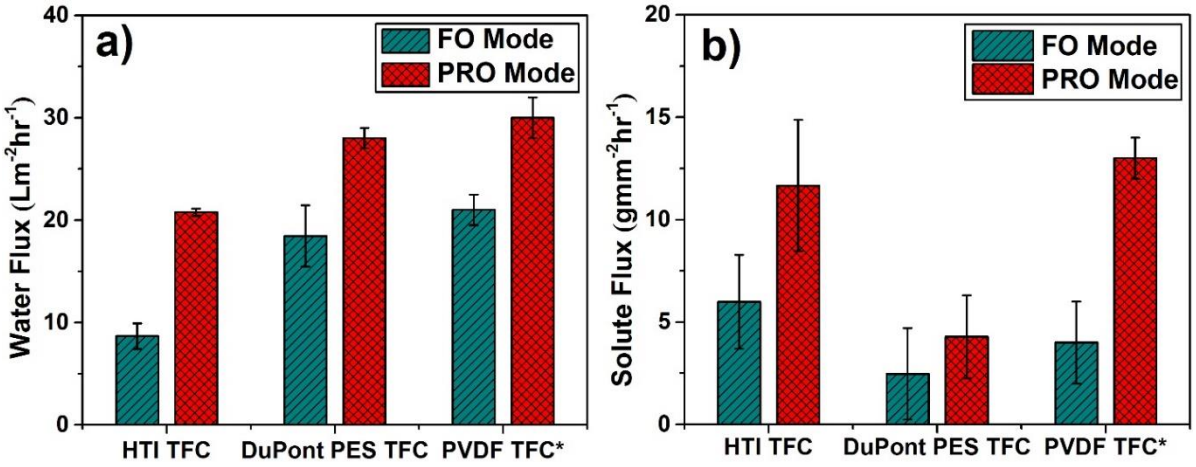

Figure 6.5. Water flux (a) and reverse solute flux (b) for the DuPont PES TFC, HTI TFC and PVDF TFC membranes in FO and PRO mode. Experimental condition: Feed- DI water, 20°C, 2psi, 0.6 LPM, spacer for support; Draw- 1 M NaCl solution, 20°C, 3 psi, 0.6 LPM. The error bar represents standard deviation in water flux obtained from triplicate tests.
* Data for PVDF TFC were taken from [209]. Experimental conditions are similar except the feed and draw side pressure was maintained at 3 psi for the PVDF TFC without any spacer in the feed channel.

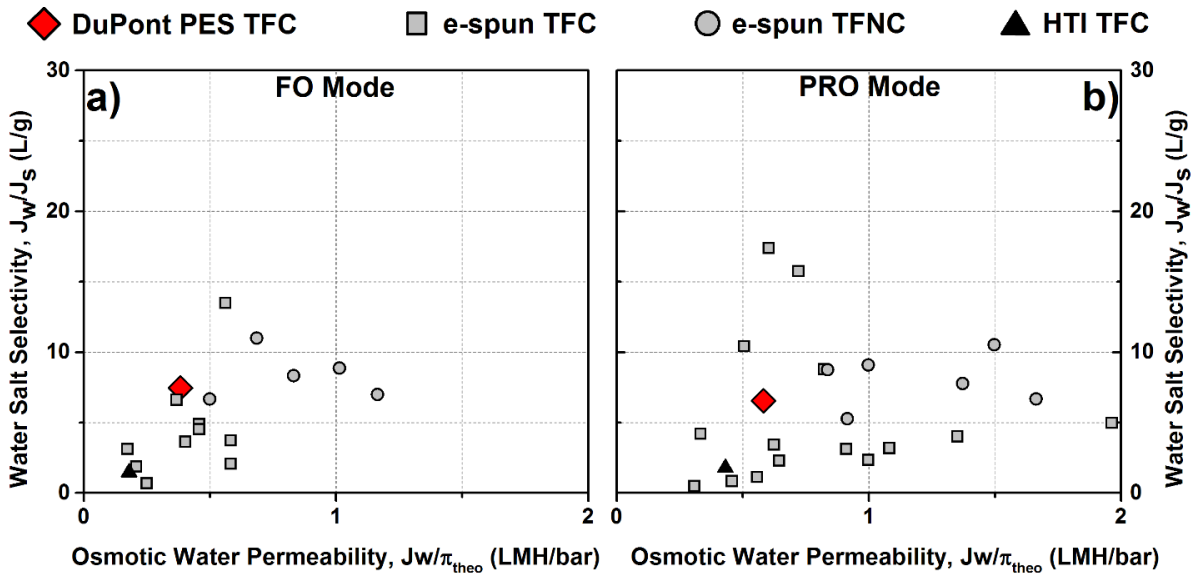

Figure 6.6. Comparison between water salt selectivity (J_w / J_s) to osmotic water permeability ($J_w / \Delta\pi_{Theo}$) for electrospun nanofiber supported thin film composite membrane (e-spun TFC) found in literature to date for FO mode [47,163,166–168,209] and PRO mode [47,163,167,168,209,220,221]. The polymers for nanofiber mat comprises of polyacrylonitrile (PAN), polyvinylidene fluoride (PVDF), nylon 66, polyethersulfone (PES), polysulfone (PSu), cellulose acetate (CA), polyethylene terephthalate (PET), polyvinyl alcohol (PVA), and polyethylenimine (PEI). E-spun TFNC contains silica nanoparticles and multi-walled carbon nanotubes in the nanofiber mat and data for commercial HTI TFC was added as a bench-mark.

6.4. Conclusion

The use of nanofibers as supports for TFC membranes for forward osmosis has so far been limited to lab produced electrospun materials. In this study, we demonstrated that a commercially available, unsupported PES nanofiber based nowoven could be used to prepare a TFC membrane with superior performance. It is stipulated that the inherent properties of the nanofiber mat enabled the creation of high quality, mechanically robust, TFC membrane, having good flux and increased selectivity compared to commercial membrane benchmarks. In addition, optimization of the nanofiber mat structure could potentially enable further performance improvements of these novel nanofiber supported TFC membranes. Furthermore, the availability, the consistency and the uniformity over long lengths (e.g. rolls) of these commercially produced nanofiber products is key to the potential scale up and commercialization of this technology.

Chapter 7

Electrosprayed polymerization: Making highly tunable TFC membranes for desalination

Manuscript in preparation:
Printed polyamide desalination membranes with sub-2 nm roughness and sub-4 nm thickness control
Maqsud R. Chowdhury, and Jeffrey R. McCutcheon

7.1. Introduction

In chapter 1, we discussed membrane design for desalination industry briefly. Here, an in-depth review of asymmetric membranes will be provided. Asymmetric membranes are the industry standard for a number of membrane separation technologies. The development of the first asymmetric membranes by Sidney Loeb and Srinivasa Sourirajan revolutionized the field of membrane science by developing the first asymmetric membrane through the phase inversion method [222–224]. This technique, initially created with cellulose acetate, created the first integrally-skinned membrane. This skin layer moderated the membrane's selectivity and permeance and was so thin that membrane resistance had been remarkably reduced compared to more symmetric membranes. This enabled reverse osmosis to operate at lower, more reasonable pressures and ushered in a new era of membrane separations. For reverse osmosis, however, cellulose acetate, had its drawbacks. Aside from being susceptible to hydrolysis and having limited pH and temperature tolerances, the membrane still required substantial pressures to generate reasonable fluxes. Single pass NaCl rejection also never reached the required 99.4% for seawater, which is the target necessary to ensure total dissolved solids levels low enough for drinking.

The thin film composite (TFC) membrane first developed by Cadotte [39] created a new type of membrane that substituted the integrated structure with one of a layered composite structure. This platform involved the use of a selective barrier film layer that was comprised of a different material than the support. Cadotte screened a number of chemistries, but he, as others have done, focused on the aromatic polyamides with rigid structures and exceptionally high selectivity as a material of choice for the TFC selective layer. An added benefit of this chemistry was that the layer could be formed *in-situ* directly onto a porous supporting material (Fig. 7.1) through a very well understood polycondensation reaction between an amine and an acid chloride [178]. A thin film could be created by placing these monomers in two separate and immiscible phases. The aqueous phase would contain a diamine, such as m-phenylene diamine (MPD), and be soaked into the porous support layer. The acid chloride (trimesoyl chloride or TMC) would be dissolved into an organic phase (such as hexane or Isopar^{TM}) and then poured onto the soaked support. The MPD and TMC would react quickly and easily, but since neither phase was miscible in the other, the reaction would occur only at the interface between the two phases. The reaction rate would decrease as the rapid formation of the dense and crosslinked structure would prevent more monomers from moving to the phase boundary. This self-limiting behavior led to the creation of exceedingly thin films being formed directly on top of the supporting layer. The thin nature of these membranes led to an order of magnitude increase in water permeance compared to cellulose acetate membrane while the extensive crosslinking of the polymer led to an order of magnitude decrease in salt passage. This method and chemistry would remain as the industry standard for the next few decades and remains so today [225].

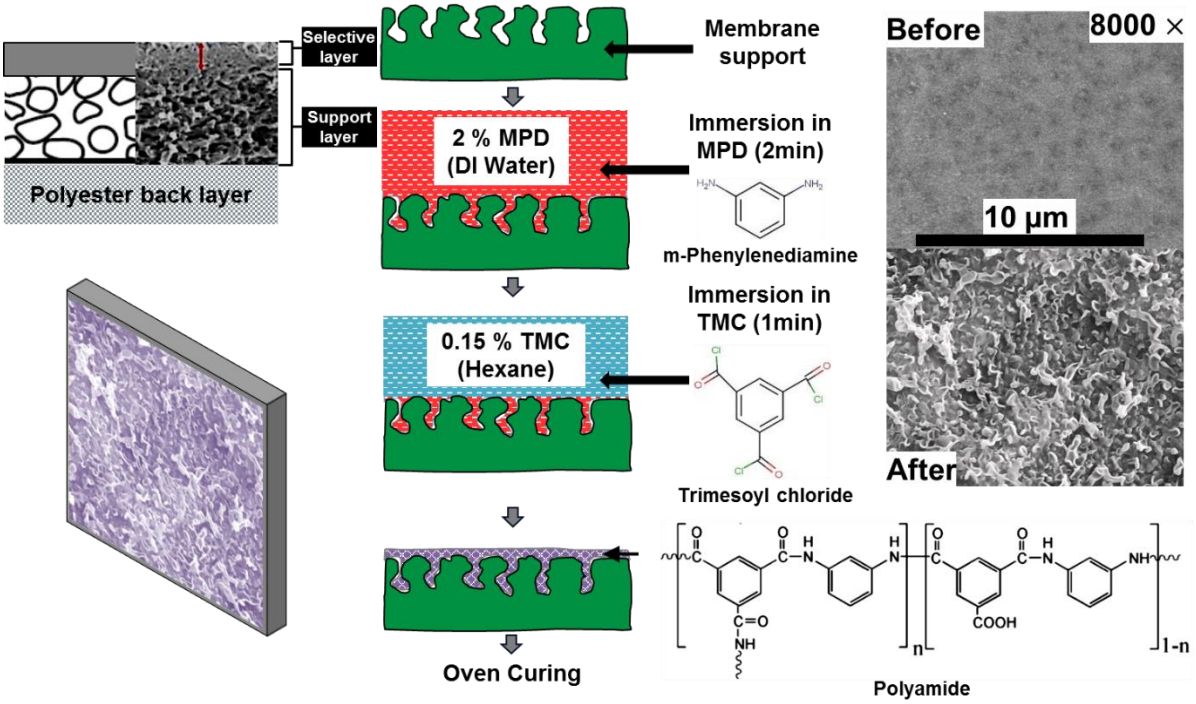

Figure 7.1: Conventional interfacial polymerization technique to produce thin film composite membrane using recipe developed by Cadotte [36,39].

While the interfacial polymerization technique is elegant and creates membranes of high quality for industrial uses, the reaction is relatively uncontrollable and therefore difficult to tailor. Permselectivity can be altered by changing, for instance, amine type or concentration [226], but these approaches have often been used to make membranes of lower selectivity (such as nanofiltration) than those created conventional MPD and TMC monomers. MPD and TMC have long been considered to form the most selective membranes for the most challenging desalination processes, such as seawater desalination [178].

If membrane fabricators are limited to MPD and TMC monomers due to selectivity requirements, other aspects of the membrane, such as thickness and roughness, become very difficult or impossible to control. Thickness is determined largely by the degree to which the reaction self-limits and reduces the diffusion of monomers to the interface. While some papers have suggested that long reaction times will increase film thickness [227], thicker films are

generally not a desired result because of a greater membrane resistance to water transport. Thinner membranes are very hard to make because the reaction is so fast that the film forms to its near complete thickness before the reaction can be quenched. Overall, the result is a selective layer between 100 and 200 nm in thickness and, with two notable exception to be discussed below [214,228], the layer cannot be made thinner with conventional interfacial polymerization.

Furthermore, the characteristic roughness of polyamides formed by conventional interfacial polymerization has long been documented [229]. This roughness has been attributed to substantial fouling propensity in TFC membranes for RO and nanofiltration (NF) processes [214,230]. The cause of the roughness has been credited to a number of factors, including penetration of the amine into the organic phase prior to reaction, as well as heat of reaction which causes wrinkling of the surface [231]. The uncontrolled nature of the reaction prevents much tuning of this roughness. As such, studies have focused on finding ways to modify the surface of RO membranes to lessen fouling [232–234]. Often these approaches reduce permeance by adding resistive layers or they are not resilient under operating conditions or cleaning cycles.

Lastly, the support layer poses challenges for creating consistent films. The support layer has its own structural and chemical features that will impact *in-situ* film formation. Pore size, pore spacing, surface porosity, and surface chemistry will all impact the interface between the two phases and thus impact film properties. The relationships between pore size and chemistry and the film properties have been explored [188,229,235], but definitive approaches to controlling for changes in support features are non-existent.

Unique approaches (Fig. 7.2) to making TFC membranes have been developed in an attempt to control thickness and roughness. One such approach (Fig. 7.2B), recently published in *Science*, describes using a nanostrand supporting layer to form smooth, ultra-thin polyamide films [214].

The nanostrand midlayer allows for the use of low concentrations of monomer because the open structure enables better reaction between the phases. Lowering amine concentration was demonstrated to reduce film roughness by slowing the reactions and generating less heat. The paper conjectured that local heat generation caused by the rapid kinetics is one cause of polyamide roughness and that by reducing the speed of reaction with lower reactant concentrations, a smoother film resulted. The films exhibited a root-mean-squared (RMS) roughness of less than 1 nm, compared to approximately 70 nm for conventional IP. The lower amine concentration also enable a thinner film (as thin as 10 nm) to be formed. The film exhibited exceptional organic solvent transport properties but was never tested under desalination conditions.

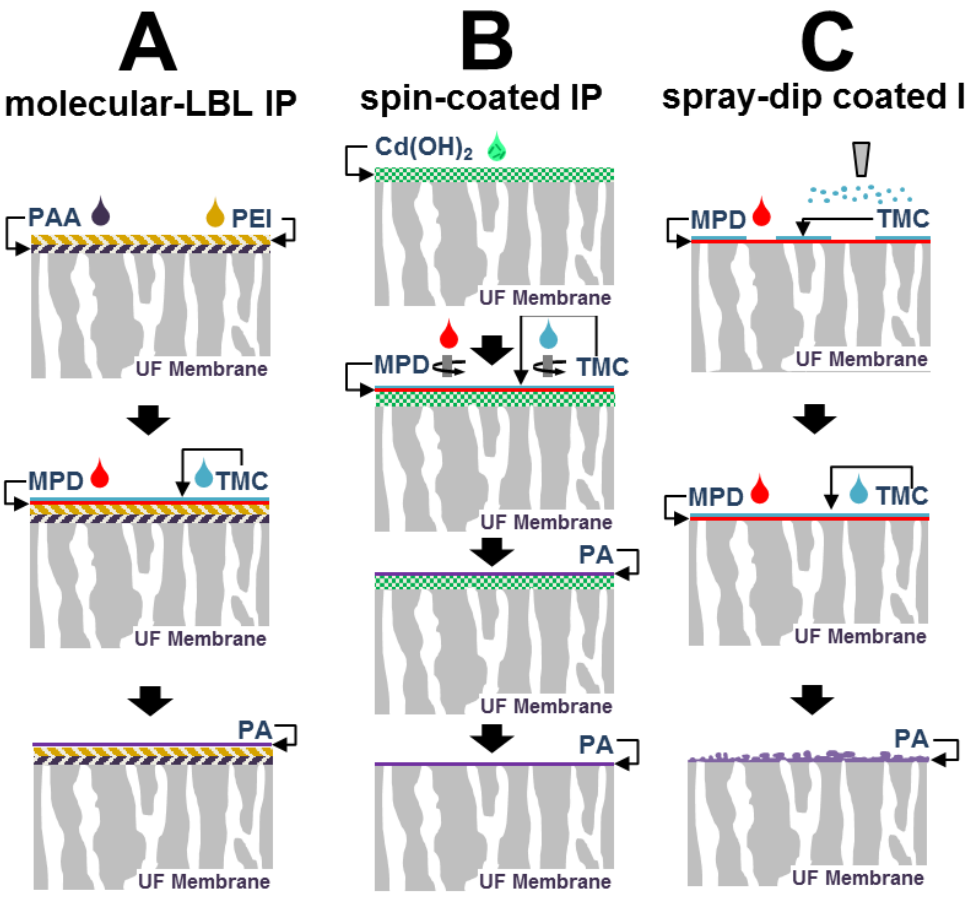

Figure 7.2: Unconventional method for making polyamide films [214,228,236].

While the approach was incredibly innovative, it has some notable drawbacks. First, the nanostrand layer was designed to be sacrificial. After it was used to support the layer formation of the film, it would be dissolved and the polyamide layer would float off and be relaminated onto a support layer. This approach is essentially impossible for larger membrane areas. The largest self-supported membrane area shown in this study was a 1.5 cm disc (which is smaller than most any test cell used today for testing membrane properties in RO conditions).

A layer-by-layer method (Fig. 7.2A) for making polyamides was developed at NIST as a means of enabling control of film thickness and roughness. This particular approach used a technique known as *molecular* layer-by-layer assembly (mLBL). The approach uses sequential exposure of a surface to alternating chemistries (MPD and TMC) and washes after each exposure to ensure that only 1 molecular layer reacted. The result is a dense, smooth polyamide structure with thickness tunability down to about 9 angstroms. The NIST group has built these films on silica wafers for further characterization [237]. They have also constructed TFC membranes with this technique [17]. Because of the molecular thickness of these films, the porous supports had to be primed using polyelectrolytes (what the authors referred to as an interlayer). The team was able to produce membranes with a salt rejection of greater than 95% with a membrane as thin as 30nm.The permeance of these membranes was 80% higher than that of a TFC membrane made from conventional IP using a conventional recipe on the same support. The membrane also exhibited superb smoothness (RMS of 3.4 nm) and as such exhibited fouling resistance to membranes made from conventional IP. This interesting approach resulted in a tunable desalination membrane, but the method likewise has its drawbacks. mLBL requires a thorough washing step after each molecular layering step to remove the excess chemicals. This creates substantial waste and adds time to membrane fabrication.

Another method developed in 2013 uses a twostep process where a combination of the conventional IP and air brush based spraying technique was used to make the polyamide based TFC membrane as shown in Fig. 7.2C [236]. They also tried just using air brush to deposit the organic phase but did not achieve good desalination performance. This shows why such method has not been adopted as a go-to method for forming the TFC membrane. With the spray-dip coated IP, they were able to achieve decent desalination performance from the TFC membrane but the method still suffers from the drawbacks we see in the conventional IP approach. Additional research have been published in recent years who have tried to address these issues with conventional IP [163,238–240] but have issues with regard to scalability, generating large chemical waste, and having support dependency while making TFC membranes.

An ideal method for TFC membrane formation needs to have certain properties to address challenges associated with the TFC membrane platform. This is shown in a cartoon format on Fig. 7.3. An ideal film formation method would need to be substrate independent. What this means is that the method would be able to form the same kind of polyamide film having similar thickness, roughness, and separation performance regardless of substrate hydrophilicity, pore size and density, or even a completely impermeable substrate such as an aluminum foil or silicon wafer. While doing this, the method needs to be able to independently control thickness and surface roughness of the polyamide film. Finally, it also needs to be easy for scale-ups, easy to retrofit, and a green technology. None of these metric can be fulfilled with the methods developed thus far which begs the question of what other methods could be used for making the polyamide films with tunable properties.

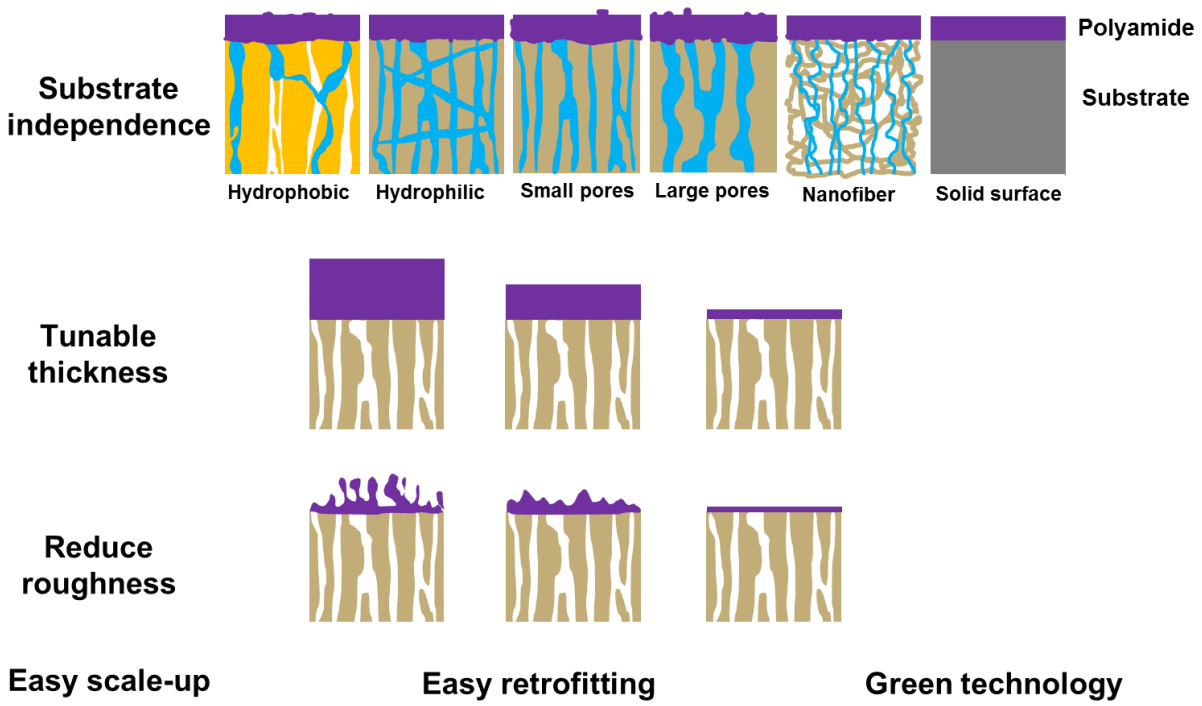

Figure 7.3: A depiction of an ideal method required for TFC membrane formation.

Fig. 7.4 depicts methods to form different kind of films on different substrates. Method such as chemical vapor deposition (CVD), physical vapor deposition (PVD), and electroplating are typically used for metal film formation. There are some reports of using CVD for polymer film deposition [241] but the method itself has issues with scalability and they were not studied for making the aromatic polyamide that is used in making the TFC membranes for desalination. Knife casting, spin coating, and atomization have been seen in application for making polymeric flat sheets in the range of 1 to 1000 μm. While all of these later methods have been used in making polyamide, there are issues related to tenability of polyamide films, scale-ups and desalination performance as discussed earlier.

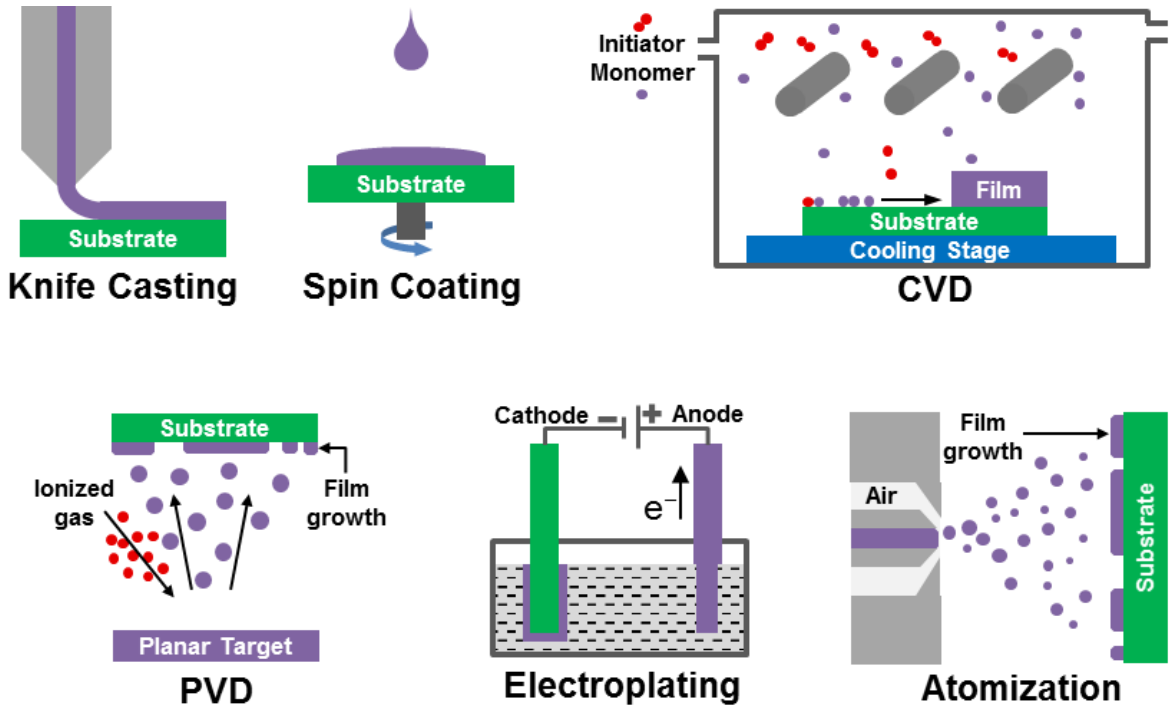

Figure 7.4: Variety of methods for forming films of different material.

Electrospraying (sometimes called electro-hydrodynamic spraying) is a method for atomization of liquids using electrical forces (Fig. 7.5). During an electrospraying process, liquid is pushed out of a nozzle where it is exposed to an extremely powerful electrical potential. The liquid forms a Taylor cone where a jet emerges from the tip of the cone. Cohesive forces cause the jet to form droplets and the droplets are dispersed by Columbic repulsion. The droplets are exceedingly fine, ranging in size from microns down to nanometers in diameter. Flow rate, nozzle geometry, electrical potential, and solvent evaporation during time of flight all impact droplet size [242]. The charged droplets are propelled toward a grounded or oppositely charged collector surface (such as a plate, drum, or belt) where the strike the target and spread to form a film. Unlike electrospinning, electrospraying relies on greater electric repulsion forces than intermolecular forces to break up the jet and create droplets [243]. A common use of electrospray is for ionization of proteins in mass spectrometry. Fenn et al. first demonstrated usage of electrospray ionization

(ESI) for mass spectrometry of large polar biomolecules such as oligonucleotides and proteins [244,245]. This has led to numerous applications in the analytical chemistry field [246–248] and helped establish critical droplet size models.

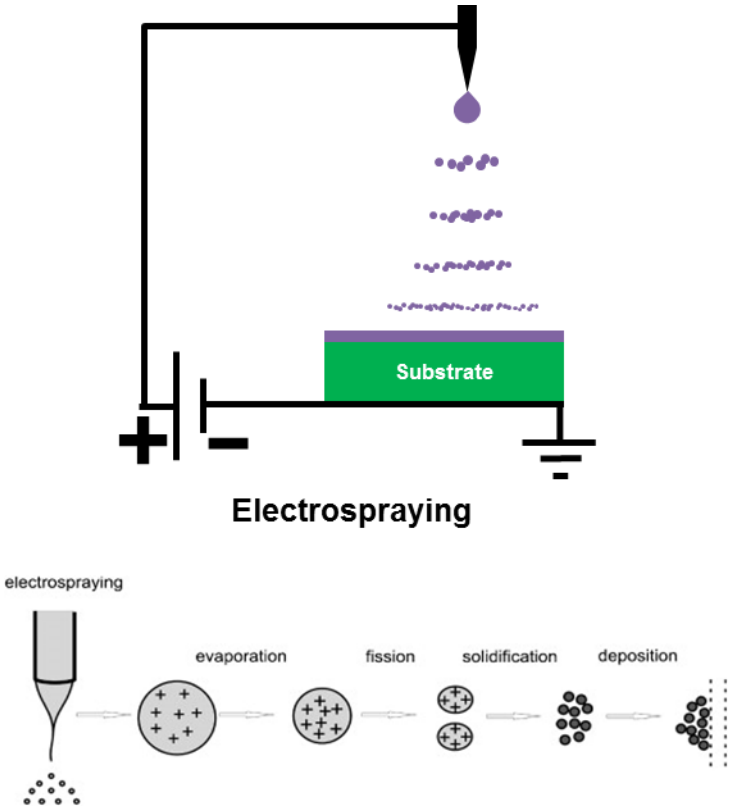

Figure 7.5: Electro-hydrodynamic spray or electrospray method for forming fine droplets (top) and nanomaterials (bottom)

For making films, electrospraying has numerous advantages over conventional mechanical atomizers and spray nozzles. The small droplet sizes and narrow size distributions coupled with better droplet motion control make electrospraying a highly effective film formation approach. These advantages make electrospraying an ideal process to form ultra-thin and uniform films. In particular, the uniformity of the droplet size made electrospraying an idea candidate for producing nanomaterials [242,249–251]. Criticisms for electrospray have centered around their low throughput due to an inability to deliver large amounts of material to a surface. While challenges like this are easily addressed at scale by simply adding needles or nozzles to the process, this is

unnecessary for applications like making TFC membranes since they require only small amounts of material be deposited. This has been the case in other works where ultra-thin functional films produced by electrospray were used in solar cells, lithium ion batteries, MEMS, and nanomaterial production [252–257]. There are no membrane applications involving electrospray published at the time of this proposal, but polymer films have been created by electrospraying dilute polymer solutions [253,258–262]. There are no studies on electrospraying monomers for subsequent polymerization on a surface.

While electrospray has been used to make thin films for numerous applications, it has never been used to deliver monomers to a surface to be subsequently polymerized [263]. There is some work done using both electrospray and electrospinning together for making nanocomposite fabrics [243,264,265], as well as the aforementioned uses above for energy and thin film applications, *but the concept of making an aromatic polyamide is entirely new*. And, unlike many of these studies considering electrospray of a simple dissolved polymer in a solvent, this work considers depositing the monomers that allow polymer formation on the substrate. This is the *only way* to create this type of aromatic polyamide using an additive approach since no solvent can dissolve aromatic polyamide and allow it to be recast in its crosslinked form with the same properties.

The following hypotheses can be proposed based on the *electrosprayed polymerization (ESP)* method:

1. *ESP will enable the formation of defect free polyamide based TFC membrane.*
2. *The method will ensure independent control of thickness and roughness.*
3. *Support independent polyamide will be formed with similar desalination results.*
4. *Bulky polyamide films can be formed using the additive feature of ESP.*
5. *ESP method will have a very low chemical footprint.*

7.2. Electrosprayed polymerization: optimization through modeling

To predict and adjust the thickness of a film created by electrospray, we can draw on the many well-established models that predict droplet size and movement. Many of these models were developed as part of the use of electrospray in high precision analytical tools like mass spectrometry [246,247,266,267]. We can use these same models to help us devise solution properties that will enable sub-10 nm control of film thickness and roughness

During the electrospraying process, the solution leaves the needle or dye and forms a Taylor cone at the needle tip from where droplets start to form and move toward the oppositely charged or grounded substrate. Gañán-Calvo developed scaling laws for current, charge density, and the droplet size during electrospray [257]. The effects of electrical conductivity (K_w), liquid flow rate (Q), permittivity (ε_0), density of liquid (ρ_w), viscosity (μ_w), and surface tension (γ_w) of the liquid-gas interface on the size and charge density of the droplets are considered in the modeling. First, Eqs.7.1-7.2 are used to calculate reference droplet size ($D_{p,0}$), and flowrate (Q_0).

$$D_{p,0} = \left(\gamma_w \varepsilon_0^2 \rho_w {K_w}^2\right)^{1/3} \tag{7.1}$$

$$Q_0 = \gamma_w \varepsilon_0 / (\rho_w K_w) \tag{7.2}$$

The dimensionless parameter that controls the acceleration process of the liquid is $\delta_\mu \delta^{1/3} = \left(\frac{{\gamma_w}^3 \varepsilon_0^2}{\mu_a^3 K_w^2 Q}\right)^{1/3}$. For $\delta_\mu \delta^{1/3} \leq 0$, the following equation provides best fit for particle size (D_p).

$$\frac{D_p}{(\varepsilon_r - 1)^{1/3} D_{p,0}} = 1.6 \left[\frac{Q}{(\varepsilon_r - 1)^{\frac{1}{2}} Q_0}\right]^{\frac{1}{3}} - 1.0 \tag{7.3}$$

For $\delta_\mu \delta^{1/3} \gg 1$, the scaling law for D_p is

$$\frac{D_p}{D_{p,0}} = 1.2 \left[\frac{Q}{Q_0}\right]^{\frac{1}{2}} - 0.3 \tag{7.4}$$

Once the droplet size is calculated using Eq. 7.3 or Eq. 7.4, Eqs. 7.5-7.8 can be used to calculate the velocity (v), time of flight (t_f), mass flow rate of the evaporation from the droplet ($\dot{m}$) as it travels through the air [257]:

$$v = \frac{\left(\varepsilon_0 \gamma_w D_p\right)^{1/2} \Phi}{f_d \mu_a H} \tag{7.5}$$

$$t_f = \frac{f_d \mu_a H^2}{\left(\varepsilon_0 \gamma_w D_p \Phi^2\right)^{1/2}} \tag{7.6}$$

$$\dot{m}_0 = -\rho_a D_{wa} D_p ln\left\{1 - \left(\frac{\dot{M_s}}{M_\infty}\right) exp\left[\frac{LM_s}{RT_{bw}}\left(1 - \frac{T_{bw}}{T_L}\right)\right]\right\} \tag{7.7}$$

$$\frac{\dot{m}}{\dot{m}_0} = 1 + 0.276 Re^{0.5} Sc^{1/3} \tag{7.8}$$

After evaporation during traveling through air for a distance of H, the final droplet size $D_{p,final}$ can be calculated using

$$D_{p,final} = 2\left(\frac{3}{4\pi} \frac{4/3\pi\left(D_p/2\right)^3 \rho_w - \dot{m} t_f}{\rho_w}\right)^{1/3} \tag{7.9}$$

The values of v and $D_{p,final}$ from Eq. 7.5 and Eq. 7.9 are used in another set of equations developed by Mundo et al [268] to calculate the splash diameter of the droplet (D_{Splash}) when it hits the substrate surface

$$\frac{3}{2}\frac{We}{Re}\left(\frac{D_{Splash}}{D_{p,final}}\right)^2 + (1 - cos\theta)\left(\frac{D_{Splash}}{D_{p,final}}\right)^2 - \left(\frac{1}{3}We + 4\right) = 0 \tag{7.10}$$

Finally, the thickness of the liquid layer (h) formed on the substrate can be calculated using the following equation which uses the D_{Splash} from Eq. 7.10 and $D_{p,final}$ from Eq. 7.9

$$h = \frac{2}{3}\frac{D_{p,final}^3}{D_{splash}^2} \tag{7.11}$$

After D_{Splash} is evaluated, one can calculate how much area each droplet would be able to cover. As an example, if 10 mL of 2 % MPD aqueous solution is electrosprayed at a rate of 10

mL/hr, then, it can form droplets of D_p in the size of ~ 1.6 μm. When this droplet reaches the grounded surface, the size reduces to a $D_{p,final}$ of ~ 1 μm which would make a D_{Splash} of ~ 1.8 μm with a film thickness of ~ 200 nm. This means that a 10 mL solution could theoretically cover an area of ~ 45 m^2. It is important to note that an assumed circular splash pattern would require splash overlap to prevent defects in the film. However, even if we needed to provide 10 layers to ensure that coverage was complete (a 10 % deposition efficiency), 10 mL of solution could cover over 4m^2 of substrate area. It is also important to note that even though the deposited film thickness is ~ 200 nm, in this hypothetical case the monomer concentration is only 2 %, meaning that the film thickness would be far lower. Lower concentrations of monomer would make even thinner films.

7.3. Materials and methods

7.3.1. Materials

Several ultrafiltration (UF) membranes including PS 20 (Polysulfone based UF membrane with 20 kDa molecular weight cut-off (MWCO)), PAN 50 (Polyacrylonitrile based UF membrane with 75 kDa MWCO), and PAN 450 (Polyacrylonitrile based UF membrane with 250 kDa MWCO) were provided by Sepro membranes (Currently Nanostone Water) and were used without any kind of chemical treatment. A commercial Dow SW30XLE flat-sheet TFC membrane from Dow was used as a bench-mark for different characterization. Commercial grade aluminum foil (Reynolds Wrap) and silicon wafer were also used as received.

m-phenylenediamine (MPD, > 99 %) (Fig. 7.6), tri-hexyl tetradecyl phosphonium bis-(trifluoro methyl sulfonyl) amide (ionic liquid (IL), > 95 %), 1,3,5- benzenetricarbonyl trichloride (TMC, 98 %), and sodium hydroxide (NaOH, > 97 %) were purchased from Sigma-Aldrich. Hexane (HPLC grade, > 99 %), sodium chloride (NaCl, crystalline, certified ACS), and

isopropanol (IPA, > 99.5 %) were purchased from Fisher Scientific (Pittsburgh, PA). Deionized water (DI) was collected from Millipore Integral 10 water system (Millipore, Billerica, MA).

7.3.2. Electrosprayed polymerization method

The electrosprayed polymerization (ESP) system developed is presented in Figs. 7.6A and 7.6B. A high voltage DC power source (Gamma High Voltage Research, Ormond Beach, FL) which is capable of generating up to 30 kV was connected to the two stainless steel needles (26 gauge). The needles were suspended from a L-shaped arm which is attached to a stage as shown in Fig. 7.6B.

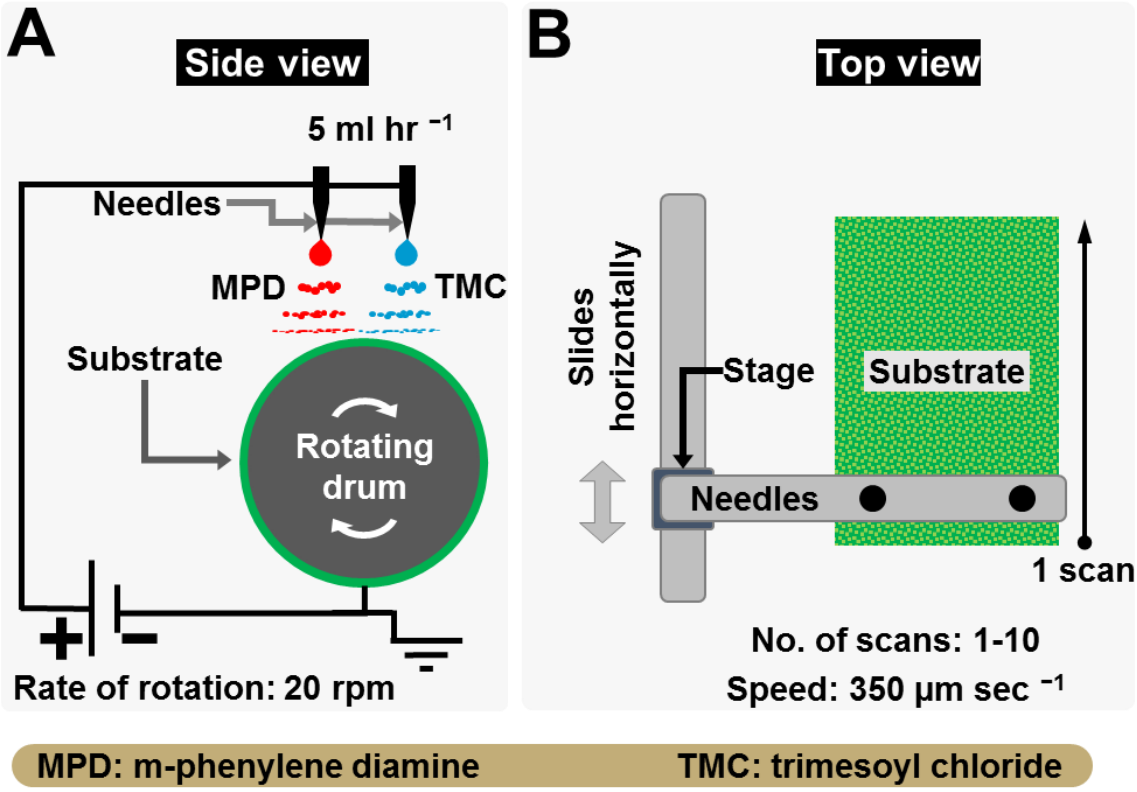

Figure 7.6: Schematic diagram of the ESP system. (A) A side view of a schematic of an electrosprayed polymerization process is shown. The two monomer solutions of MPD and TMC were pumped through the needle tip under an applied potential difference (4-6 kV) across the substrate and needle tips. Three ultrafiltration (UF) membranes were selected as substrate. (B) The top view shows the needles and a stage assembly that can move horizontally. A single sweep across the substrate is denoted as a single scan. The stage speed was kept at 350 µm sec^{-1}.

The distance between the two needles was kept at 6 cm and distance between the needle tips and the rotating drum was kept below 2.5 cm. This was decided based on simulation results using empirical models for electropspraying as discussed in the previous section and from Fig. 7.7. From Fig. 7.7A, we observe that as the tip to drum distance was increased, the final droplet size reduces while the MPD monomer concentration increases significantly. Smaller distance results in minute changes in monomer concentration but it is not practical to use a very small distance between the tip and drum due to arcing. For this reason, a 2.5 cm distance was proven to be ideal for this setup. From Fig. 7.7B, we also observe the effect of changes in substrate properties and its effects on the splash diameter. The splash diameter is the diameter of the droplet once it hits the substrate and spreads. As hydrophobicity could have an impact on the spreading [269], we used the model to understand whether there would be any change or not. According to the model, there is a very small deviation between the two contact angles that we studied.

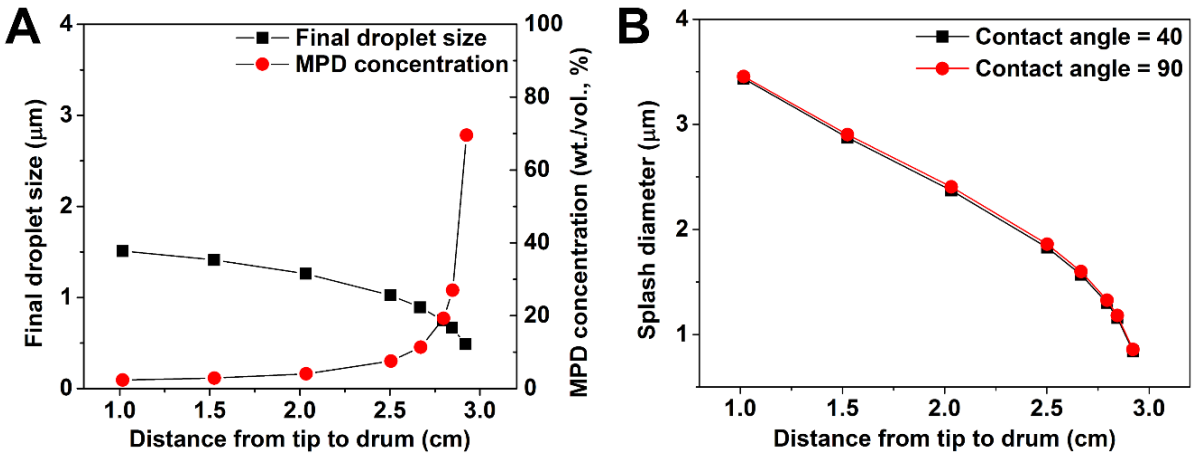

Figure 7.7: The model result showing changes in droplet size, and MPD monomer concentration as it moves through air and deposits on the drum (A), and effect of substrate hydrophilicity on splash diameter (B) with respect to different tip to drum distance. Model conditions- Applied voltage: 10 kV, flowrate: 10 mL hr^{-1}, MPD concentration: 2 % (wt. /vol. of water), viscosity of air (μ_a): 0.000001983 Pa.sec, density of air (ρ_a): 1.225 kg/m^3, viscosity of water (μ_w): 0.001002 Pa.sec, density of water (ρ_w): 1000 kg/m^3, latent heat of vaporization of water (L): 2264760 J kg^{-1}, diffusivity of water in air (D_{wa}): 2.82×10^{-5} $m^2 sec^{-1}$, surface tension of water (γ_w): 0.07197 N/m, conductivity of water (K_w): 0.008 S m^{-1}, boiling point of water (T_{bw}): 100 °C, aqueous

phase temperature (T_L): 25 °C, vacuum permittivity (ε_0): 8.854×10^{-12} $A^2 sec^4/(kg\ m^3)$, relative permittivity (ε_r): 80.1, frictional drag coefficient (f_d): 0.6.

Now going back to Fig. 7.6B, the stage sits on a screw slider that can move horizontally using a stepper motor and can be controlled using a motor controller (Velmex, Bloomfield, NY). For ESP, a horizontal speed of ~350-500 μm sec^{-1} was maintained to ensure uniform and continuous coverage of a liquid film. Next, The UF membrane was attached on to an aluminum foil which was attached to an aluminum cylindrical rotating drum with a diameter of 4 inches using adhesive tape. The aluminum foil covered the 30 cm width of the drum while the width of the UF membranes were kept at 10 cm. The drum was grounded to ensure a polarity and potential difference across the needle tips and drum. Uniform and continuous coverage was ensured by starting the electrospray process on aluminum foil where the individual deposited sprays could be seen very easily. Each deposited sprays were ~1-2 cm in width. This results in a ~95 % overlap at each rotation. Once the deposition was found to be uniform by visual observation, the Velmax controller was programmed to start the movement of the needle stage over a distance of 16 cm. As a result, electrospray was continued beyond the edge of the substrate for at least 3 cm on both sides to ensure uniform film formation on the substrate.

For the monomer solutions being used, several different concentrations of both MPD and TMC were studied as listed in Table 7.1. The MPD and TMC concentrations were chosen such that the MPD/TMC mole ratio remains at 4 and MPD remains as an excess to ensure plenty of MPD monomer remains on the substrate surface when the TMC solution is sprayed subsequently. A crucial development milestone was the introduction of a lipophilic ionic liquid (IL) in to the non-polar hexane solution to improve its electrical conductivity. A 1 μL IL / mL of

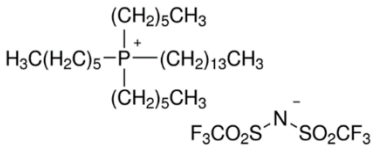

Trihexyl tetradecyl phosphonium bis (trifluoro methyl sulfonyl) amide (IL)

hexane was added based on a previous study on mass spectrometry [270]. This enabled us to effortlessly electrospray the organic phase. In the future, there is scope for replacing this IL with some other solution to improve the conductivity.

Table 7.1: The concentration of MPD and TMC used in ESP.

Test conditions	**MPD concentration in water** (wt./vol. of solvent)	**TMC concentration in hexane** (wt./vol. of solvent)	**Ionic liquid** µL/mL of hexane
1	0.0625	0.0375	1
2	0.0833	0.05	1
3	0.125	0.075	1
4	0.25	0.15	1
5	0.5	0.3	1

Two monomer solutions of MPD and TMC were then fed into two separate needles using a syringe pump at a flowrate of 5 mL hr^{-1} and flexible tubing (McMaster-Carr # 1883T1). Each syringe contains approximately 5 mL of solution. The cylindrical drum is then set to rotate at 20 RPM. The high voltage DC power supply was set at 4-6 kV and was tuned each time to ensure a stable electrospray condition is achieved. A stable electrospraying condition refers to a cone-jet mode where the liquid is elongated into a long, fine jet of sprays which deposits straight onto the substrate surface [242]. The direction at which the sprayed liquids is crucial for a uniform and continuous coverage. Ideally, this was always ensured by the slightly changing the applied voltage (0.1-0.5 kV change). When this occurs, solutions from both MPD and TMC needles spray deposit on to the substrate. As the drum is rotating clockwise (as shown in Fig. 7.6A) and as both of the needles are aligned along the direction of rotation (as shown in Fig. 7.6B), the TMC solution sprays directly on top of the MPD solution sprayed ~ 300 msec earlier. Once a stable spray is formed, the stage holding the two needles was programmed to move horizontally at a velocity of 350 µm sec^{-1}. When the stage moves the complete length of the membrane horizontally, it is considered a single scan. To demonstrate the idea of an additive manufacturing approach with ESP, the number

of scan was varied from 1 to 10 scans or more if needed. Once the ESP was finished for the required no. of scans, the sample was removed and immediately tested to evaluate desalination performance while storing a small dry sample to perform other characterizations. After each ESP, the delivery lines were cleaned with high purity DI water and the needles were replaced to ensure consistency as the tip electrical properties of the needle highly affect the electrospray condition as well.

7.3.3. Membrane characterization

7.3.3.1. Surface hydrophilicity

A sessile drop method was used to find the contact angles of the selective and support layer of the membrane. To do this, a CAM 101 series contact angle goniometer (KSV Company, MD, USA) was used. A droplet volume of 10 ± 1 μL of DI water was used for each test where six different random locations were chosen on the TFC membranes and substrates. The contact angle was measured within a second of the droplet being deposited on the surface. The tests were conducted at room temperature with a relative humidity of 60 %.

7.3.3.2. Scanning electron microscopy and elemental analysis

A scanning electron microscopy (SEM) system was used to image the selective polyamide layer, supporting substrate layer and cross-section morphology of the membrane. A FEI TeneoLoVac SEM (Hillsboro, OR) was used. For imaging surface morphology, membrane samples were dried, attached to the SEM stub, and sputter coated with a thin layer of gold (Au) and platinum (Pt) under vacuum (0.6 torr). A coating time of 30 seconds with 20 mA current was selected which adds approximately 10 nm of coating. After coating, membranes were imaged in the SEM using a 10-15 kV accelerating voltage, a working distance of 5-10 mm, and the ETD detector using SE mode. To perform EDX, only separated polyamide films were used. To do this, a thick 1 µm layer of polyamide as shown on Fig. 7.8 was separated using 1.5 M NaOH aqueous

solution. On Fig. 7.9A, the sequence of the separation of this film is shown. To ensure that the polyamide does not contain any residual NaOH, it was washed with DI water several times. It was then transferred on to a new piece of Al foil and crumpled to form a thick 400 µm layer as shown in Fig. 7.10. The Al foil was attached to a SEM stub and inserted into the microscope without any conductive coating layer. The Al foil was used to ensure that the signal is only coming from the sample as EDX penetrates 1-2 µm into the sample whereas XPS photoelectron penetrates only the top 10 nm of the surface. An accelerating voltage of 15 kV with a probe current of 6.4 nA at a working distance of 14 mm was used.

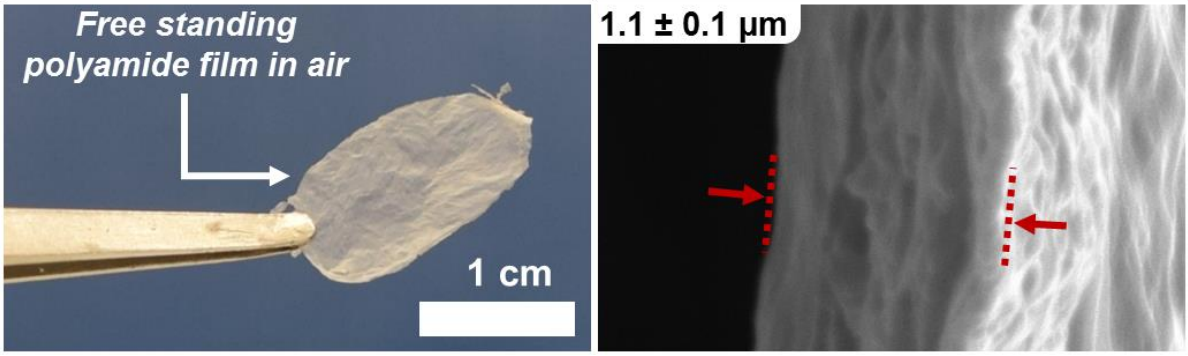

Figure 7.8: A free standing bulky polyamide film (left) and a SEM micrograph showing thickness of the film (right)

7.3.3.3. Roughness measurement

Surface roughness of the polyamide film and the substrate support material were measured using an atomic force microscopy (AFM) instrument (Asylum Research MFP-3D, Santa Barbara, CA) with a silicon AFM tip (Pointprobe, Nanoworld Innovative Technologies Switzerland). A commercial Dow SW30XLE TFC membrane from Dow was used as a bench-mark. The samples were first dried, attached to a glass slides using double sided tape and adhesive glue to ensure there is complete physical contact between slides and the sample. The measurement was taken at 1-3 Hz for a sample area of $3 \times 3\ \mu m^2$ using non-contact mode (AC mode). Three samples were selected

from each membrane and 15 scans were performed for each sample. The results are presented as root mean square roughness (R_r), average roughness (R_a), and surface area difference (SAD) [152].

7.3.3.4. Thickness of polyamide film

The thickness of the polyamide film on a Si wafer was measured using AFM. To avoid cantilever tip damage, a lower scan speed of 0.5 Hz was used and an area of $3 \times 3\ \mu m^2$ was scanned. A schematic of the method to transfer polyamide film is shown in Fig. 7.9A. A sample polyamide film was first formed on to an Al foil using ESP which was etched off using a 1.5 M NaOH aqueous solution. Then it was transferred onto a Si wafer measuring about 2 cm × 2 cm and washed using three different DI water bath. Finally, the polyamide film on Si wafer (referred to as PA-Si) was dried in air at room temperature and stored for AFM characterization. For thickness measurement, a step edge on the sample was located which was then scanned using the AFM cantilever tip in tapping or AC mode as shown in Fig. 7.9B. The cantilever tip responds in Z-direction to the step change from the Si wafer support to the top of the polyamide film (as shown in Fig. 7.9B) and it was then analyzed to find the thickness of the polyamide film. To ensure the polyamide film thickness is consistent with the film thickness on an actual TFC membrane, the polyamide film on Al foil was always taken from the same ESP fabrication experiment where a TFC membrane was formed.

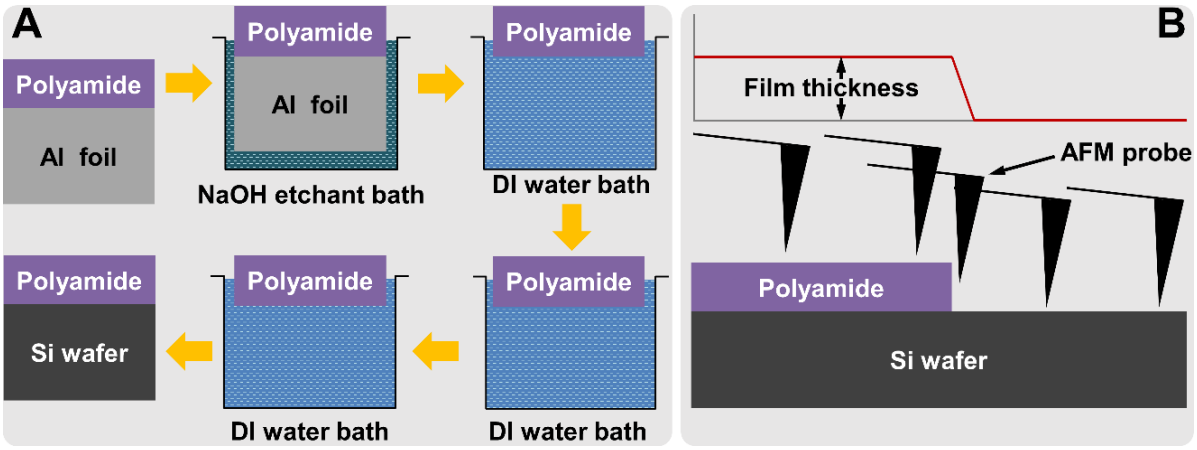

Figure 7.9 (A) A schematic diagram of the etching process to transfer polyamide film on to Si wafer. (B) The AFM scanning method to find the polyamide thickness.

7.3.3.5. Transmission electron microscopy

All the steps were conducted at room temperature in 2 dram glass shell vials with plugs (Fisher Scientific) on a Pelco R2 rotary mixer (Ted Pella, Inc.) at setting 20 to aid the penetration of the chemicals. All the chemicals used to process the samples were EM grade purchased from Electron Microscopy Sciences (EMS). Membrane samples were cut into 1mm x 2 mm pieces and placed into 1% osmium tetroxide for one hour. Shell vials were covered with aluminum foil during this step to prevent osmium photodegradation. Membrane were dehydrated through a series of graded ethanol for 10 minutes each at 30%, 50%, 70%, and 90% and 100% four times. Spurr's resin containing ERL 4221 (3,4-epoxycyclohexane methyl 3',4'-epoxycyclohexyl-carboxylate), DER 736 epoxy resin, NSA (Nonenyl succinic anhydride modified), and DMAE (2-(Dimethylamino)ethanol) was freshly prepared. The membranes were infiltrated in a 1:2 mixture of resin:ethanol for two hours and a 2:1 mixture of resin:ethanol overnight. The following day the membranes were infiltrated in 100% Spurr's resin for 4 hours with one change of resin after 2 hours. Samples were flat embedded in double end molds (Cat # 10590, Ted Pella, Inc.) properly labeled and polymerized in an oven (Lab-Line Instruments, Inc.) under vacuum at 60°C overnight. Semithin sections (~ 1 μm) were cut with a histo 45° Diatome™ diamond knife on a Leica Ultracut UCT microtome and collected on drops of distilled water on Superfrost® Plus microscope slides (Fisher Scientific). Sections were stained with a working solution of 1:1 methylene blue:azure blue II and placed on a 30-8010 AB slide warmer (Buehler Ltd) for 15 seconds at 70°C. Sections were examined at the light microscope level in an Olympus microscope to identify suitable material for electron microscopy. Ultrathin (~ 70-100 nm) sections were cut with an ultra 45°

Diatome™ diamond knife on a Leica Ultracut UCT microtome and collected on 150 mesh copper/palladium grids (Ted Pella, Inc.). Sections were counterstained with 2% aqueous uranyl acetate for eight minutes, rinsed with distilled water, stained with 2.5% Sato's lead citrate for three minutes, and rinsed again with distilled water. Images were obtained using a bright field FEI Tecnai Biotwin G2 Spirit (Hillsboro, OR) transmission electron microscope operated at an accelerating voltage of 80 kV and equipped with an AMT 2k (4 megapixel) XR40 CCD camera.

7.3.3.6. Quartz crystal microbalance

Film density of the polyamide film was found using quartz crystal microbalance (QCM). Following method described in section 7.3.3.4 and Fig. 7.9A, the polyamide was first separated from the Al foil and then transferred onto 14 mm diameter QCM sensors (6 MHz, Platalloy ™ Inficon style sensor, Phillip Technologies). The mass sensitivity factor of the sensor was 0.815 Hz cm ^{2} ng $^{-1}$. The sensors with the polyamide was subsequently washed further with DI water. A sensor without any sample on it was also used in the cleaning and washing process to account for any foreign particle or layer deposition and as a control ($f_{control}$). The sensors were stored QCM sensor holder and were air-dried overnight. Using a QCM (Colnatec Phoenix ™ System with temperature control, Gilbert, AZ) monitoring system, the sensors were placed one at a time in the holder and the oscillation data was recorded ($f_{with\ sample}\ and\ f_{control}$). The oscillation data for all the sensors were also recorded when they were received from the vendor ($f_{blank}\ and\ f_{control\ blank}$). The change in frequency for the two states was calculated using the following equation that provided us with the density of the polyamide.

$$\rho_{polyamide} = \frac{\left(\left(f_{with\ sample} - f_{blank}\right) - \left(f_{control} - f_{control\ blank}\right)\right) \times total\ area\ of\ the\ sensor}{0.815 \times area\ of\ polyamide \times thickness\ of\ the\ polyamide\ from\ AFM}$$

The area of the polyamide was calculated using the image analysis tool ImageJ while the thickness of the polyamide was taken from the AFM thickness measurement data as discussed in section 7.3.3.4.

7.3.4. Membrane desalination tests

Pure water permeance, and solute rejection of the membranes were characterized using a dead-end reverse osmosis bench-scale test setup [44,47] and bench scale cross-flow system. The dead-end test setup includes three dead-end stirred cells where 3 inch diameter membrane coupons were placed. A fine mesh was used beneath each membrane and on the permeate side to increase clearance. Using DI water as feed, the pressure was raised to 10 bar with constant stirring using a magnetic stirring system. The operation was performed at room temperature. Permeate was collected, timed and weighted to get the water flux. Dividing this value with the applied pressure resulted in the pure water permance, A. This was repeated until a stable permeance data was collected. To measure solute rejection, a 2000 ppm feed solution containing NaCl salt was used as the feed without replacing the membranes in the dead-end cell. Permeates were collected for 10 bar which were timed, weighted and the conductivity of permeate was measured using a conductivity probe. This was repeated until a stable rejection was achieved. The solute observed rejection, R, was calculated using the following equation: $\% R = \left(1 - \frac{C_{permeate}}{C_{Feed}}\right) \times 100\%$ Here, $C_{permeate}$ is the concentration of solute in permeate and C_{Feed} is the concentration of solute in the feed solution.

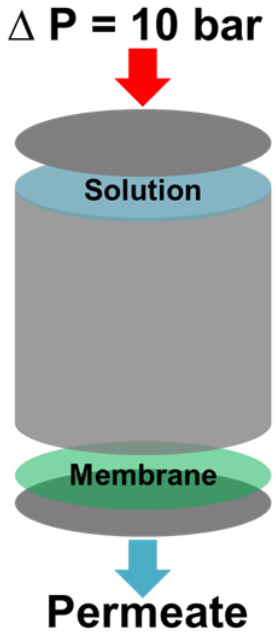

Figure 7.10: Schematic of a dead-end RO stirred cell.

7.4. Results and discussion

7.4.1. Substrate properties

To demonstrate and prove the hypothesis of substrate independence shown in Fig. 7.3, the substrate properties were first evaluated and are presented on Fig. 7.11. While both PAN50 and PAN450 are hydrophilic (contact angle < 90°), the PS20 appears to be mildly hydrophobic (Fig. 7.11A). There is also variation in pure water permeance in the order of PAN450> PS20> PAN50 (Fig. 7.11B). From the SEM images (Fig. 7.11C), it can be seen that, both at macroscopic and microscopic level, the surface properties are different. At the low magnification, PS20 seems to have the smoothest surface while PAN50 has the roughest. At a very high magnification, while the surface pores are more readily visible for PAN450 and PS20, it is very difficult to see for the PAN50. The AFM topography shows the trend seen in SEM image where roughness values decrease in the order of PAN50>PAN450> PS20. Having such diverse characteristics in the

substrate with regard to their hydrophilicity, surface pore size, roughness, and pure water permeance will help establish hypothesis of substrate independence achievable by ESP.

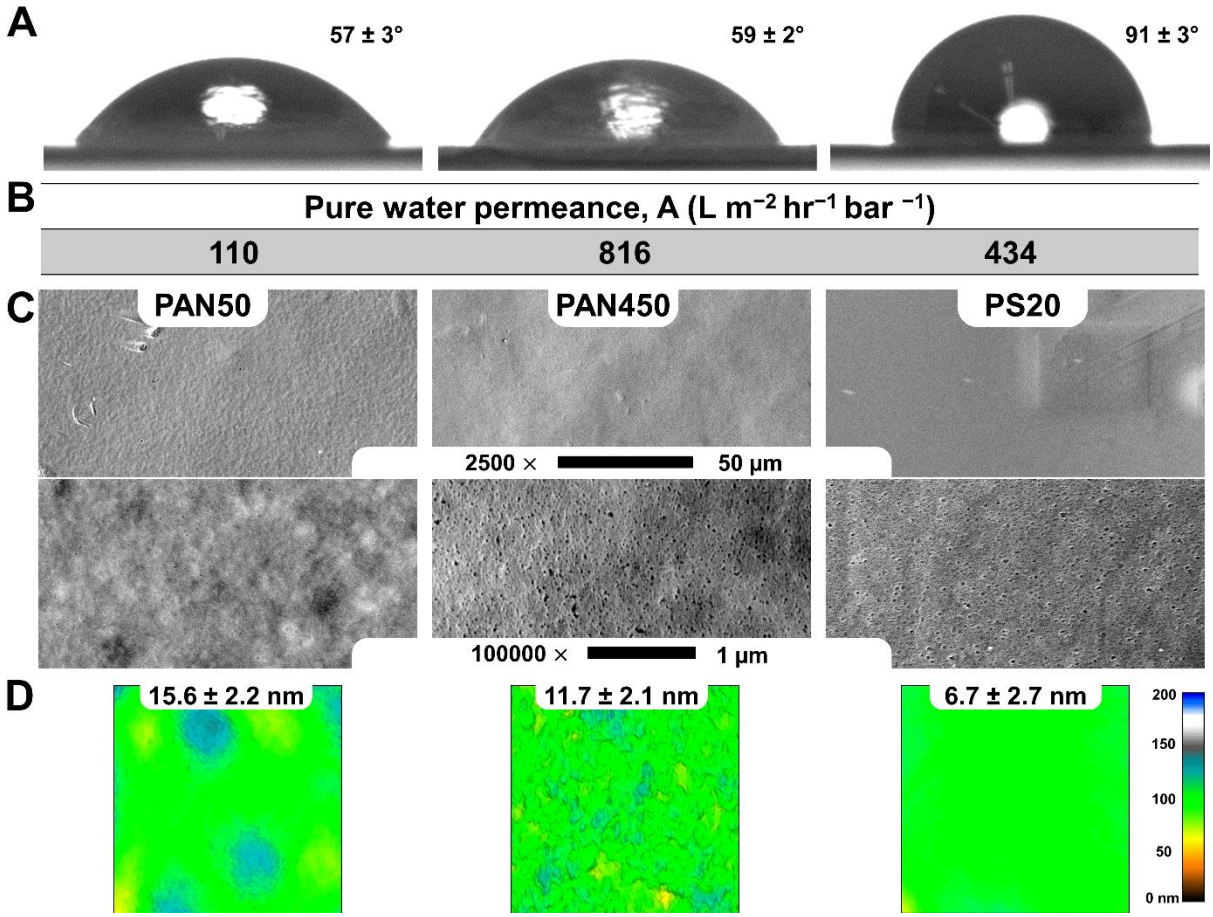

Figure 7.11: Details of the properties of the substrate materials. (A) Contact angle data of the three substrates. (B) Pure water permeance of the three UF membrane. (C) SEM micrographs of the three UF membrane shown at a magnification of 2500 × (top row) and 100000 × (bottom row). (D) AFM topography and roughness of the substrate.

7.4.2. Properties of the TFC membrane

7.4.2.1. Hydrophilicity and cross-linked density

On Table 7.2, the contact angle of all the TFC membranes made at 5 scans are presented. Across all the different substrates, we do not see any clear trend in hydrophilicity for the different type of TFC membrane formed using different MPD : TMC concentration. Typically, polyamide shows a contact angle between 40-70°. The reason we see such high contact angle was probably

due to the use of lypophilic IL which contains organic alkane chains that are hydrophobic. These characteristic would likely change once the IL washes away during operation.

Table 7.2: Contact angle results for all the TFC membranes made at 5 scans.

MPD:TMC	Contact angle		
	PAN50	PAN450	PS20
0.0625:0.0375	88.2 ± 1.1	82.2 ± 4.3	82.2 ± 4.3
0.08333:0.05	81.5 ± 4.5	79.9 ± 1.6	79.9 ± 1.6
0.125:0.075	83.3 ± 2.8	74.5 ± 2.6	74.5 ± 2.6
0.25:0.15	81.2 ± 1.3	75.1 ± 1.4	75.1 ± 1.4
0.5:0.3	85.3 ± 2.6	81.2 ± 1.5	81.2 ± 1.5

We also report for the first time the formation of polyamide film on to aluminum foil in varying thickness and in bulk quantity. While this film can easily be transferred from the aluminum foil (Fig. 7.9A) to any substrate, we also demonstrate the formation of a 1 µm thick polyamide film for the first time which is freely standing in air as shown in Fig. 7.8. This is very useful as it enables us to perform fundamental characterization such as cross-linked density measurement of polyamide films. Typically, this has been done using X-ray photoelectron spectroscopy (XPS) which can only penetrate into the 1-5 nm of the surface of the film [177]. XPS is helpful this way as polyamides are typically formed using CIP and requires a porous substrate and often the thickness of the polyamide is non-uniform and ranges between 100-200 nm. As a result, other method such as EDX would result in erroneous result due to their deeper beam penetration. However, accuracy of XPS falls when the surface is asymmetric with regard to smoothness or elemental composition both of which are typical of polyamide films made through CIP method. Apart from the method developed by Karan et al [214], no other method demonstrated the possibility of forming polyamide films independent of polymeric support and separating them effectively. Even this method is limited to porous substrates and cannot grow film in these bulk quantities. Now, the 1 µm thick polyamide film was transformed into a crumpled film measuring

~ 100 µm that enabled us to perform energy-dispersive X-ray spectroscopy (EDX) on a bulky polyamide (Fig. 7.12). The result indicate a cross-linked density of 88 % which is similar to the one reported in [214] for MPD and TMC chemistry using XPS and verified by EDX. In addition to the carbon (C), oxygen (O), and nitrogen (N) peak found in the spectra, small peaks for fluorine (F), sulfur (S), and phosphorus (P) were also detected which are due to the IL used in the organic phase (Fig. 7.12). Other peaks attributed from the film transfer procedure but were found in a very small quantity (less than 1 wt. %). A typical EDX beam penetration depth ranges between 0.1-2 µm [96] and the bulky polyamide enabled the use of this easy to use method for finding cross-linked density as no signal for aluminum was found where the bulky polyamide was attached.

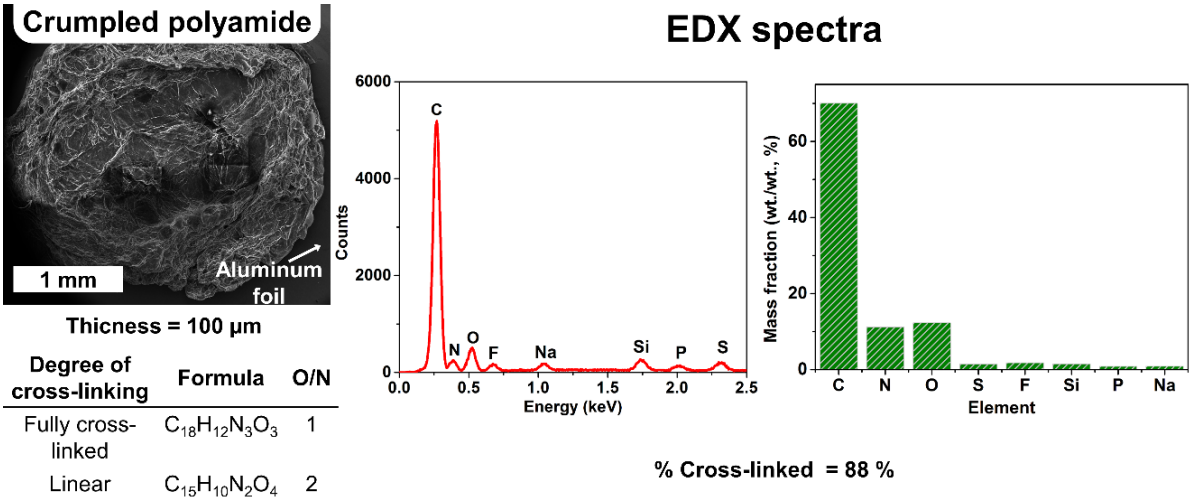

Degree of cross-linking	Formula	O/N
Fully cross-linked	$C_{18}H_{12}N_3O_3$	1
Linear	$C_{15}H_{10}N_2O_4$	2

Figure 7.12: EDX analysis on a crumpled polyamide.

7.4.2.2. Surface morphology

Scanning electron microscopy (SEM) images of the TFC membrane formed using different UF substrates and different monomer concentrations are presented on Figs. 7.13 and 7.14. From Fig. 7.13, we see that at the lowest MPD : TMC concentration ratio of 0.0625 : 0.0375, the polyamide film appears to be very smooth while higher concentrations have noticeably rougher morphologies and this is true for the three different substrates. We can also see some ring like

features on some of the SEM images which is attributed to the fine sprays generated by electrospray. Compared to all the TFC membranes formed using ESP, the commercial Dow SW30XLE shows a different kind of morphology. This is perhaps more apparent when this images were magnified which are shown in Fig. 7.14. At a magnification of 100000 ×, a ridge and valley like morphology of the Dow SW30XLE membrane is revealed which is typical of the polyamide formed using the CIP method. The formation mechanism of this morphology is attributed to the uncontrollable nature of the interfacial polymerization reaction and is highly support depended. A substrate with large and dense surface pores would likely produce more ridges and valleys than a substrate that is hydrophobic and has smaller pores. While this is likely the case with CIP, all the TFC membrane made using ESP at various monomer concentration shows significantly different surface features at this magnification. At the lowest MPD : TMC concentration of 0.0625 : 0.0375, surface pores are covered by the polyamide film if we compared the images between the TFC and substrates. Increasing concentration makes the surface look rougher without any repetitive features. From a qualitative perspective, we do see the substrate independent film formation using ESP based on these SEM images.

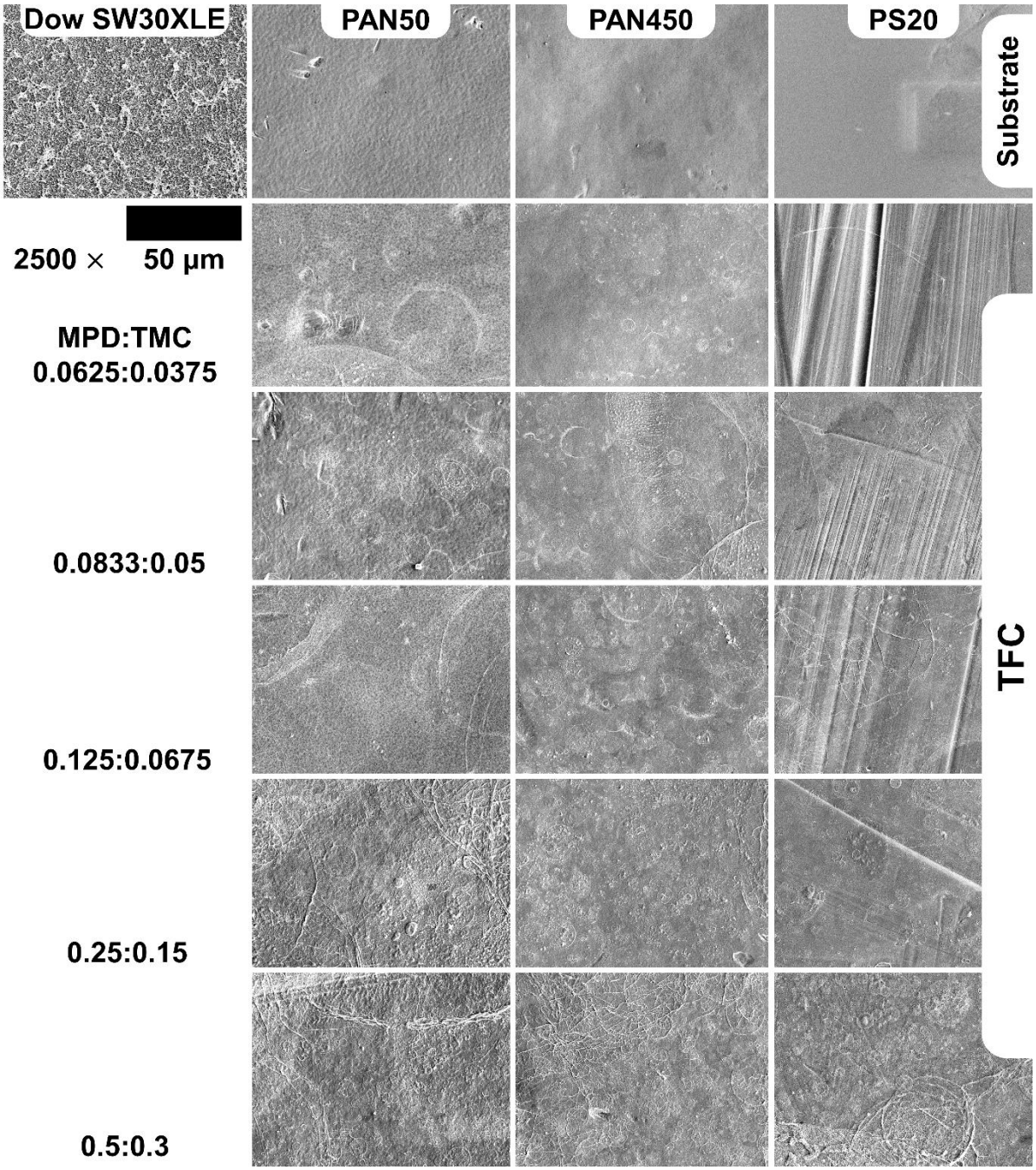

Figure 7.13: SEM image of all the substrates and their TFC membranes at varying MPD : TMC concentration ratio at a magnification of 2500 ×.

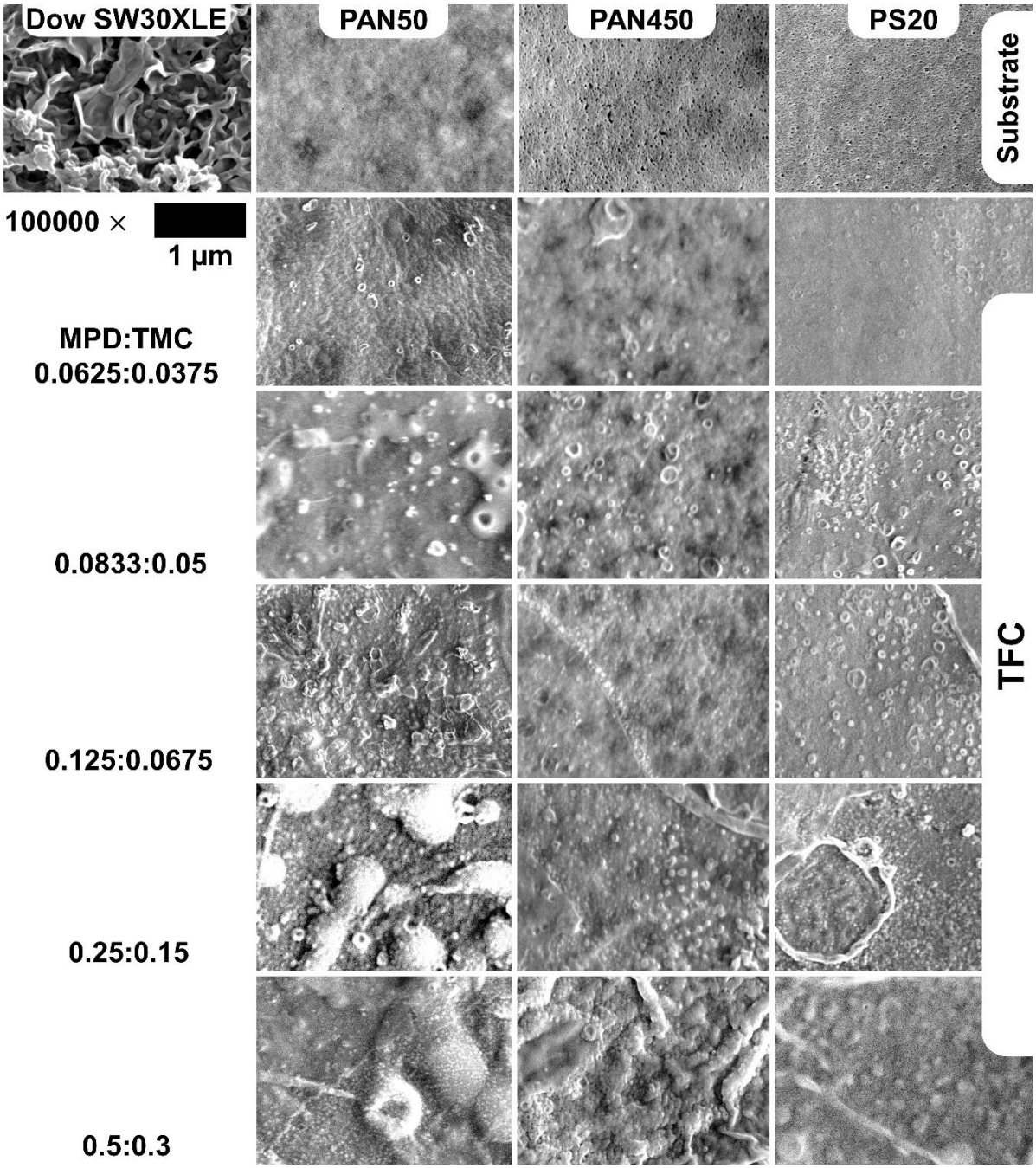

Figure 7.14: SEM image of all the substrates and their TFC membranes at varying MPD : TMC concentration ratio at a magnification of 100000 ×.

7.4.2.3. Control of roughness

One of the hypotheses of this work was to show a control of roughness with the ESP method. While surface morphology revealed smoother surfaces being formed with the ESP

method, quantification would provide a clearer trend. Hence, we performed AFM measurement on these membranes. The AFM topography images are shown on Figs. 7.15 and 7.16. On Fig. 7.15, results are shown for the changes in roughness with regard to the changes in monomer concentration for a fixed number of scans for the three substrate based TFC membranes. Just like the surface morphology, the surface gets rougher as the monomer concentrations were increased. Similar behavior is observed when the no. of scans were increased while keeping the MPD and TMC concentration constant as can be seen from Fig. 16. At higher MPD and TMC concentration, the polymerization occurs more randomly due to an excess of monomers of both type, while the reaction is still fast as we see the ring like features of the droplets once the TMC droplet splashes over the MPD solution covering the surface. At a lower concentration, unavailability of monomers, reduces the film growth dramatically resulting in much smoother films.

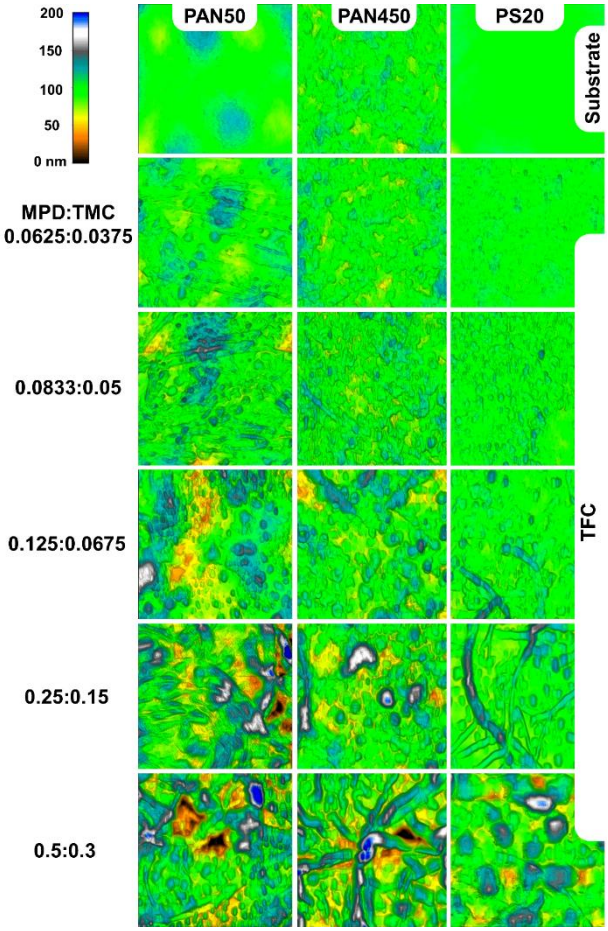

Figure 7.15: AFM surface image of the substrates and their corresponding TFC membranes at various MPD: TMC concentration ratio.

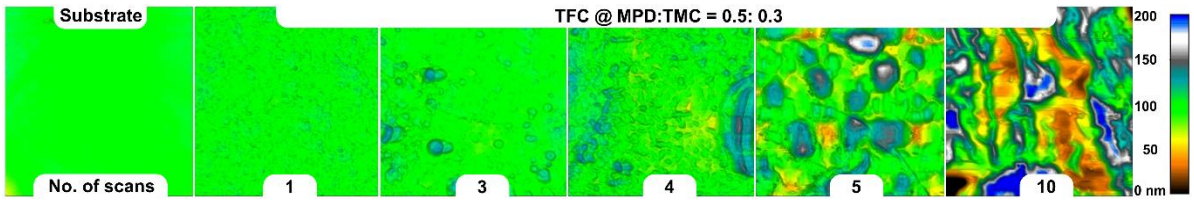

Figure 7.16: AFM surface image of the PS20 substrate and the TFC membrane made by changing no. of scans while keeping the MPD and TMC monomer constant.

A maximum roughness of 40 ± 4 nm for PAN450 TFC at a MPD : TMC loading of 0.5 : 0.3 (Fig. 7.17A) was found which is still significantly lower (~50 %) than the commercial Dow SW30XLE TFC RO membrane. As the monomer concentrations were decreased, smoother films with roughness values of ~1 nm were formed with TFC membranes resembling roughness values

similar to the substrate themselves. Fig. 7.17A also reveals the substrate independent film formation from a quantitative point as we see a similar trend in changes in roughness with monomer concentration across the different substrate.

The surface roughness was also found to reach a maximum of 40.5 ± 4 nm for PS20 TFC membrane for a MPD : TMC loading of 0.5 : 0.3 for 10 scans while decreasing non-linearly with a decrease in number of scans (Fig. 7.17B). Reducing the monomer concentration while still changing the no. of scans shows that the rate at which surface roughness increases with increase in no. of scans, decreases. This shows versatility of the ESP method to tune roughness in a variety of different ways.

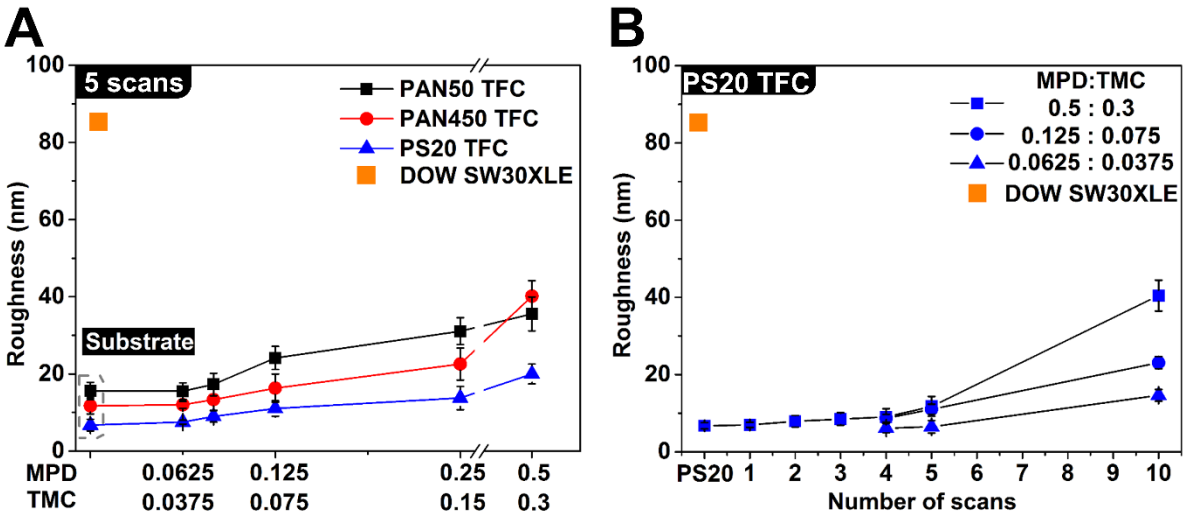

Figure 7.17: (A) Graph showing RMS surface roughness for the three different UF membrane used as substrate for a series of MPD and TMC concentration ratio. The first points in the graph represent the roughness of the substrate only. (B) Changes in surface roughness with number of scans for three different MPD and TMC concentration ratio is presented. The commercial Dow SW30 XLE membrane is shown as an orange square point (A, B) for benchmarking.

The average roughness and surface area difference (SAD) are listed in Tables 7.3 and 7.4. Similar to the RMS roughness, average roughness and SAD follows a very similar trend across the different substrates. The extra surface area added due to higher roughness is often being debated as a reason for increase in permeance in literature [172,271–273]. A common reasoning behind

that is the assumption of the leaf-like polyamide made using the CIP method has a hollow structure which acts as channels for water transport. This will be discussed later where we talk about the transport properties of the membrane.

Table 7.3: Results from AFM roughness measurement for all the TFC membranes made at 5 scans.

Sample		R_{RMS} nm	R_{Avg} nm	SAD %
Substrate	**MPD:TMC**			
PAN50	Substrate only	15.6 ± 2.2	12.5 ± 2.0	0.7 ± 0.1
	0.0625:0.0375	15.5 ± 2.1	12.4 ± 1.9	1.8 ± 0.6
	0.08333:0.05	17.3 ± 2.9	13.8 ± 2.5	6.1 ± 2.0
	0.125:0.075	24.1 ± 5.2	18.8 ± 4.3	6.0 ± 2.7
	0.25:0.15	31.1 ± 6.5	24.1 ± 5.0	15.4 ± 5.4
	0.5:0.3	35.6 ± 4.4	28.3 ± 3.9	12.4 ± 2.8
PAN450	Substrate only	11.7 ± 2.1	9.2 ± 1.6	2.7 ± 0.4
	0.0625:0.0375	12.1 ± 0.9	9.3 ± 0.6	3.4 ± 0.3
	0.08333:0.05	13.4 ± 2.8	10.4 ± 2.1	5.3 ± 0.9
	0.125:0.075	16.3 ± 3.7	12.6 ± 2.8	6.1 ± 2.3
	0.25:0.15	22.6 ± 4.2	17.2 ± 3.2	7.0 ± 1.7
	0.5:0.3	40.2 ± 6.5	31.3 ± 5.2	13.9 ± 2.4
PS20	Substrate only	6.7 ± 2.7	6.4 ± 3.1	1.6 ± 2.6
	0.0625:0.0375	7.5 ± 0.5	6.6 ± 0.3	1.2 ± 0.2
	0.08333:0.05	9.2 ± 1.5	7.3 ± 1.2	1.9 ± 0.8
	0.125:0.075	11.0 ± 4.2	8.2 ± 2.4	2.8 ± 1.0
	0.25:0.15	13.8 ± 6.1	10.5 ± 2.7	3.1 ± 1.7
	0.5:0.3	20.3 ± 2.6	16.0 ± 2.2	2.8 ± 1.5

Table 7.4: Results from AFM roughness measurement for all the TFC membranes made with different no. of scans for PS20 substrate.

Sample		R_{RMS} (nm)	R_{Avg} (nm)	SAD (%)
MPD :TMC	**No. of scans**			
0.0625 : 0.0375	Substrate only	6.7 ± 2.7	6.4 ± 3.1	3.6 ± 2.6
	4	6.8 ± 0.3	6.5 ± 0.9	3.4 ± 0.5
	5	7.1 ± 0.5	7.0 ± 0.3	1.2 ± 0.2
	10	14.6 ± 1.5	11.9 ± 1.2	11.3 ± 1.8

0.125 : 0.075	4	8.7 ± 3.4	6.0 ± 1.9	1.7 ± 0.4
	5	11.0 ± 4.2	7.2 ± 2.4	2.8 ± 1.0
	10	23.1 ± 6.0	23.8 ± 7.6	3.1 ± 1.2
0.5 : 0.3	1	6.9 ± 0.7	6.7 ± 0.4	1.8 ± 0.3
	2	7.9 ± 1.5	7.1 ± 1.0	2.0 ± 0.3
	3	8.5 ± 1.6	7.4 ± 1.1	1.4 ± 0.3
	4	9.0 ± 2.2	8.1 ± 1.4	2.1 ± 0.5
	5	11.8 ± 2.6	9.0 ± 2.2	2.8 ± 1.5
	10	40.5 ± 12.4	40.1 ± 9.9	7.5 ± 3.0

7.4.2.4. Control of thickness

AFM was also used to find thickness of the polyamide film made on aluminum foil. As the polyamide can easily be formed on aluminum foil and transferred onto a silicon wafer, the step scanning method using AFM (Fig. 7.9B) provides a faster way to find the thickness. The AFM topography of these separated films on silicon wafer is shown on Fig. 7.18 where the three line scans are shown as representative AFM step scan with the surface profiles shown beneath every AFM image. It can be seen that the uniform edge is not easy find and some of edges are inhomogeneous. During sample preparation, it was seen that the polyamide film would shrink slightly once it was transferred on to the Si wafer. This could easily result in the inhomogeneity seen on these images. The wrinkling effect was actually used by Karan et al to measure the polyamide mechanical properties [214] but it is beyond the scope of this study. For calculating the thickness from these image, the inflection point at which the AFM amplitude changes dramatically was taken into consideration. These results are presented on Fig. 7.19 where changes of polyamide thickness is plotted with respect to changes in monomer concentration and no. of scans.

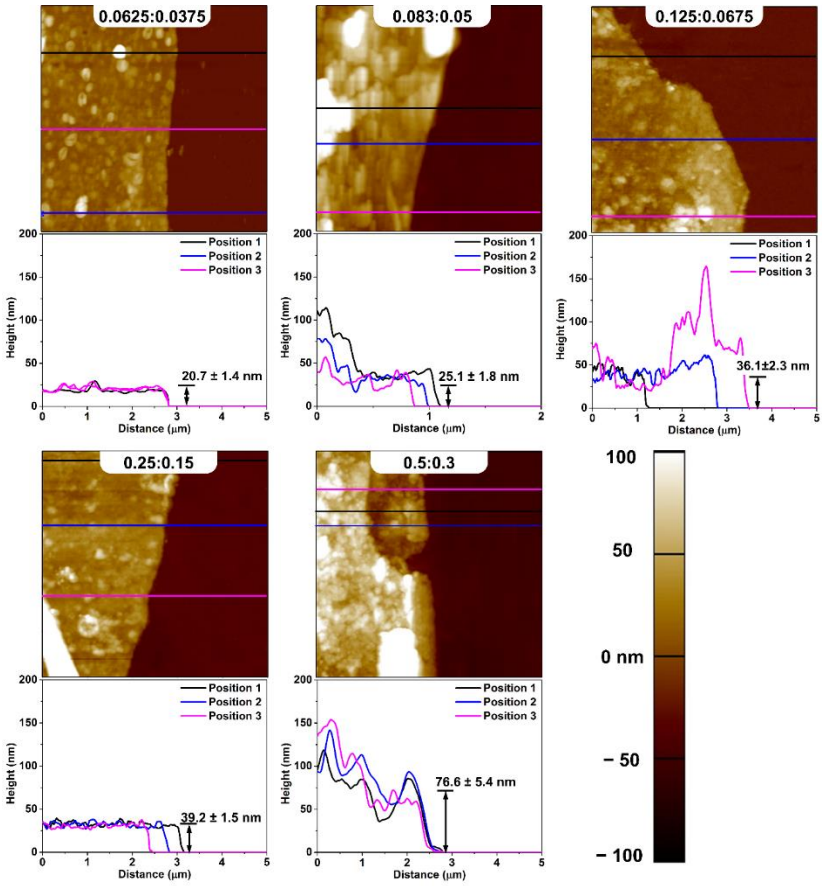

Figure 7.18:
AFM height image was taken by scanning over a scratched polyamide film on silicon wafer for 5 scans of ESP on Al foil for a varying MPD : TMC concentration ratio.

From Fig. 7.19A, two observations can be made. First, as the monomer concentration was increased we see the polyamide thickness increasing. Second, the layer thickness per scan also increases simultaneously. We were able to achieve a 4 nm/scan in layer growth at the lowest monomer concentration studied in this work. We believe we can achieve a higher resolution in thickness growth to the same level as reported by Gu et al in their molecular layer-by-layer method [228]. On the far end, at the highest concentration the layer resolution decreases to 15 nm/ scan. From Fig. 7.19B, we see as the no. of scans were increased, the thickness of the polyamide film was increased very linearly. This is shown for a MPD : TMC of 0.125: 0.075. The linearity in thickness growth also confirms the listed layer resolution of 7 nm/scan for this concentration. From

these results, we were able to see that the ESP method is also capable of tuning the polyamide thickness.

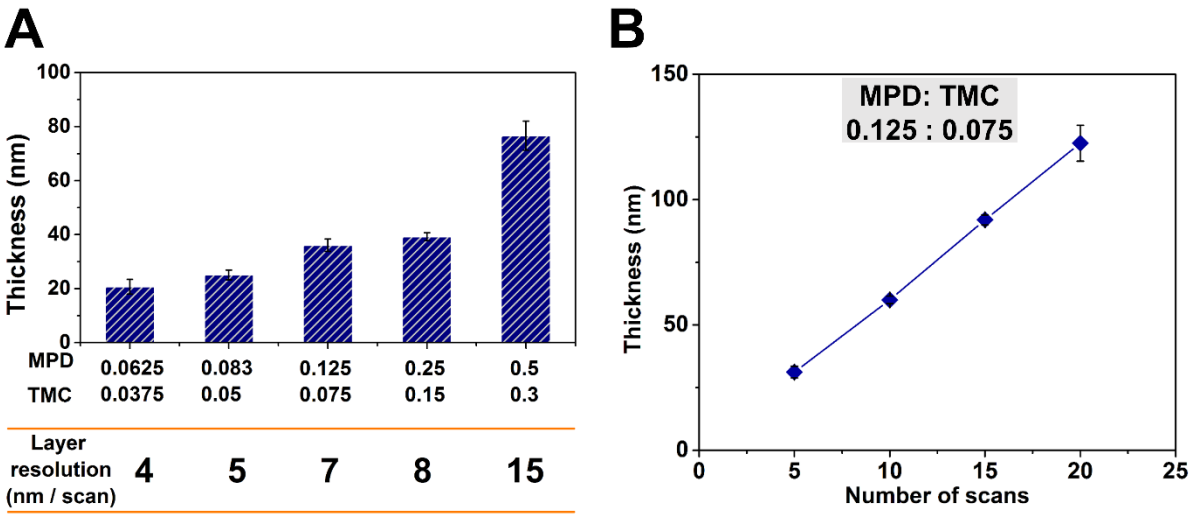

Figure 7.19: (A) Changes in polyamide thickness and ESP layer resolution with different MPD and TMC loading. (B) Changes in polyamide thickness with number of scans at MPD : TMC concentration ratio of 0.125 : 0.075.

7.4.2.5. Substrate independent film formation

On Figs. 7.20 and 7.21, we measured polyamide thickness using TEM. For 5 scans, the polyamide thickness was measured to be 78 ± 5 nm for the PAN50 TFC membrane (Fig. 7.20A) and 75 ± 7 nm for the PS20 TFC membrane (Fig. 7.20B). Although, the substrates are of different properties with regard to their hydrophilicity, the polyamide formed on them is very similar in thickness. Further, when we measured the thickness for PAN450 TFC membrane we were able find zones where the polyamide layers are very close. This measured out to be ~77 nm (Fig. 7.20C). Void features are also visible in some of the TEM micrographs due to air getting trapped in between layers (bright zones in the TEM images in Figs. 7.20C and 7.20D) and which increased the apparent thickness of the polyamide in different areas of the cross-section. Exploring the region in this membrane and also the others, revealed 5 layers of polyamide film because of the 5 no. of scans and each of them measured to be 15 ± 3 nm (Fig. 7.20D). All of these, matches the layer

resolution depicted for 0.5: 0.3 concentration ratio shown in Fig. 7.19A which was formed on an aluminum foil. This is exactly what has been postulated in Fig. 7.3 for substrate independence. Formation of a polyamide film of similar thickness and essentially roughness regardless of the substrate material proves that ESP can be used to form the same polyamide on different substrates.

Furthermore, from Fig. 7.21, we can see a linear growth of polyamide film on the PS20 substrate with changes in no. of scans with a mono layer measuring 15 ± 3 nm. This also directly supports the linearity in film growth as suggested by Fig. 7.19B. Although, the concentrations used to show linearity were different between Figs. 7.19B and 7.21, both show linearity in film growth on two completely different kind of substrate which further bolsters our claim.

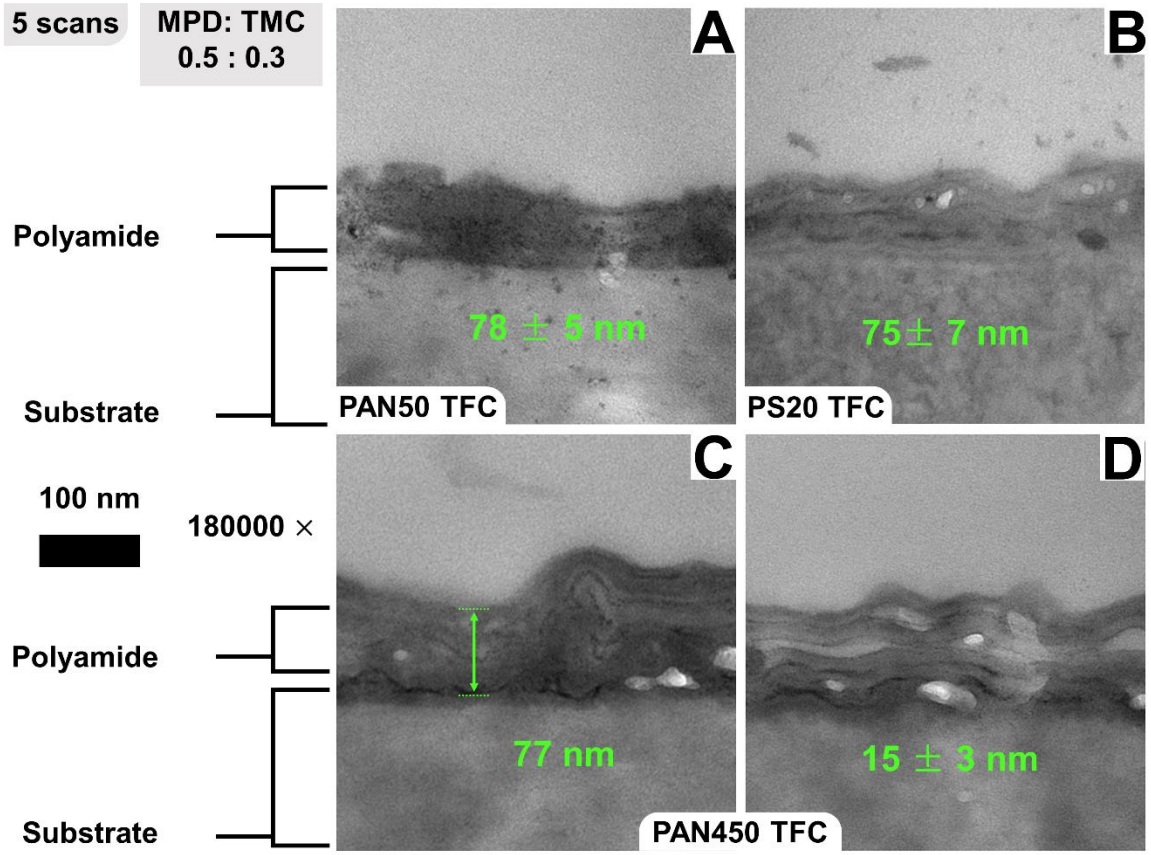

Figure 7.20: Cross-section TEM of PAN50 (A), PS20 (B), and PAN450 (C and D) TFC membrane made with ESP with 5 scans and at a MPD : TMC concentration ratio of 0.5 : 0.3.

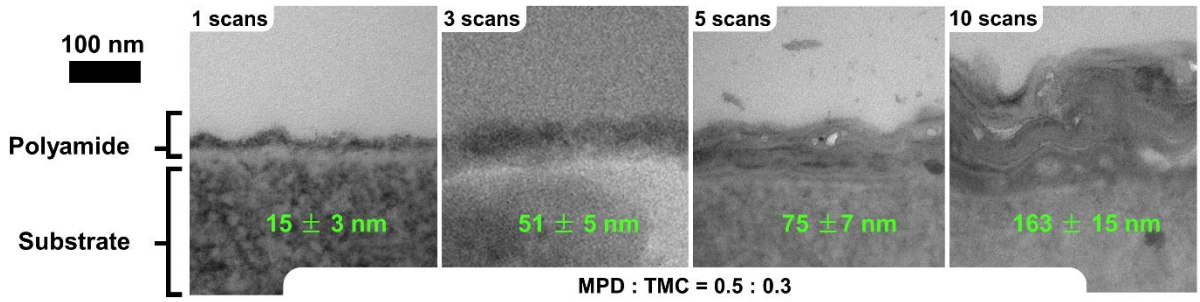

Figure 7.21: A series of TEM cross-sectional image of the polyamide film at 180000 × magnification with different number of scans at a fixed MPD : TMC concentration ratio of 0.5 : 0.3.

7.4.2.6. Polyamide density

We also demonstrate the use of the polyamide formation on aluminum foil to measure the polyamide density. For polyamide made using CIP method, this is typically done by carefully separating the polyamide film from the substrate polymer by dissolving it away using organic solvents such as N,N-dimethylformamide (DMF) [274]. It has been claimed that DMF or other such solvents do not affect the polyamide in any way or form. Although, it would be very difficult to clean the polymer of off the polyamide film completely. Regardless, the ESP method employed in this work to make polyamide film, enables easy separation of films from substrate. Hence, we were able to perform QCM study to find the film density as shown in Fig. 7.22. Analyzing the data from this graph resulted in a polyamide film density of 0.575 g cm^{-3} contrary to 1.24 g cm^{-3} as reported for the polyamide film made using CIP process [274]. This is 50 % less than the reported value and the reason for this we believe are the void spaces between layers which is mentioned in the previous section.

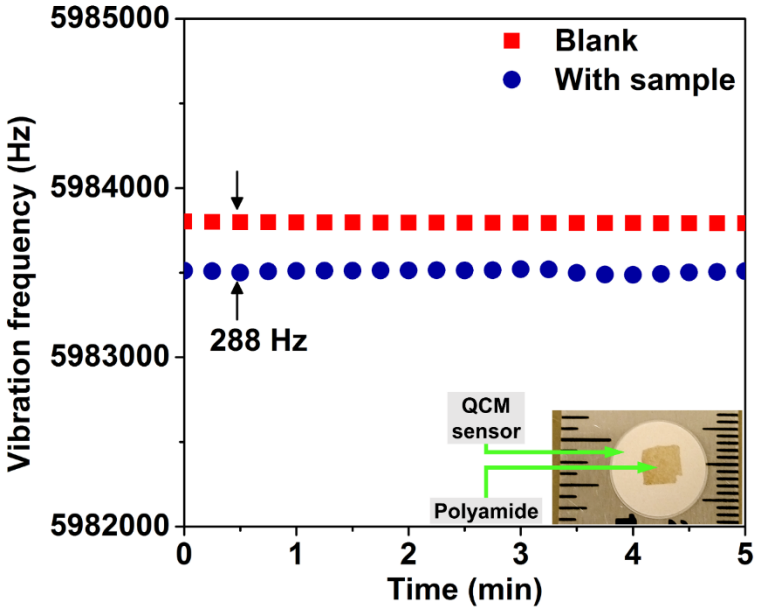

Figure 7.22: QCM characterization of the polyamide film made using ESP with MPD : TMC concentration ratio of 0.0625 : 0.0375 at 5 scans on an Al foil.

7.4.2.7. Membrane separation characteristics

Desalination performance with regard to pure water permeance i.e. A and NaCl salt rejection i.e. R are presented on Figs. 7.23 and 7.24 for the three different substrates. We first take a look at the A values presented on Fig. 7.23A for the PAN50, PAN450, and PS20 substrate based TFC membranes using 5 scans. The horizontal axis represents the concentration of MPD and TMC that is being used to make the TFC membrane. We see that as the monomer concentrations were increased, the permeance for the three membranes decreases. The opposite trend is visible in the rejection data as shown on Fig. 7.23B where it increases dramatically. We anticipated that as all the polyamides were made in a similar way and their thickness did not vary between substrates, the A values would remain similar. Interestingly, the permeance performance of the TFC membranes follow a similar trend found for the substrates as reported in Fig. 7.11B. The dependence of pure water permeance of the TFC membranes on the pure water permeance of the substrates is clear as early work back in the 1970s also reported that RO membrane heavily relies

on parameters such as thickness and roughness of the polyamide, and substrate properties such as porosity, hydrophilicity, and pore size [40]. Ensuring that we formed same polyamide on different substrate having very similar thickness, and roughness and showing that the TFC membranes have similar trend in permeance in comparison to the substrate-only permeance proves this concept. Further, we also see no correlation between the surface roughness and pure water permeance. To the contrary of previous studies, we actually see a reverse relationship between roughness and permeance if Figs. 23A and 17A are compared. There is a correlation between thickness and permeance if we compare Figs. 21A to 23A and we see as thicker polyamides are being formed, the permeance reduces.

Having said these, when we compared the rejection data between the three substrates, we were really surprised to see membranes performing very similarly for any MPD and TMC concentration as though they were made on the same substrate. This is clearly a demonstration of substrate independence.

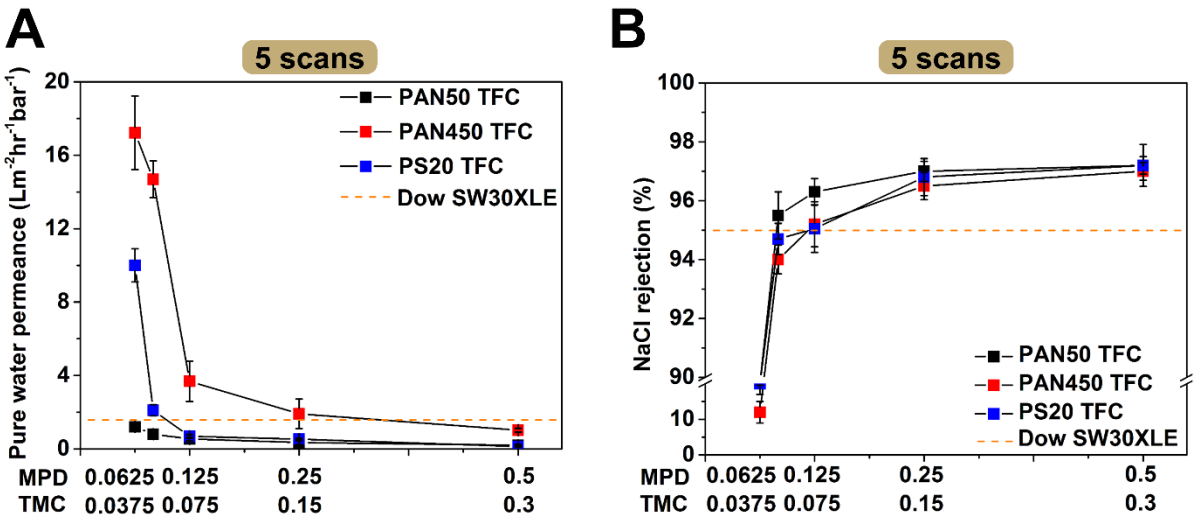

Figure 7.23: Comparison of pure water permeance and NaCl salt rejection between different substrate based TFC membranes made with 5 scans at varying MPD and TMC loading is presented. Operating condition: 10 bar applied pressure with DI water and 2000 ppm NaCl solution as feed stirred with magnetic stirrer system. The commercial Dow SW30XLE TFC RO membrane is shown as an orange dotted line for benchmarking.

We also evaluated the effect of no. of scans on membrane performance. These results are presented on Fig. 7.24 for the three different substrate supported TFC membranes. Between, all of the TFC membranes, the pure water permeance (Figs. 7.24A, B, and C) and rejection (Figs. 7.24D, E, and F) data follows a similar trend when monomer concentrations were changed as discussed in the previous section. When the no. of scans were changed from 4 to 10, we also see dramatic changes in permeance and rejection. Permeance decreases as thicker polyamides are formed with increase in no. of scans (as shown in Fig. 21B). On the other hand, rejection improves as the no. of defects on the surface decreases. We see the best desalination result when we use the lowest concentration of MPD and TMC and highest number of scans. When we compared the desalination data to the performance of the commercial Dow SW30XLE TFC RO membrane, we see some of these membrane outperform the commercial membrane on both front. Although, the typical operating scenario of a Dow SW30XLE membrane does not conform to what we have used here but we feel confident that the membranes made using ESP have competitive desalination performance.

On Table 7.5, the effect of surface area increase due to roughness on changes in pure water permeances for the TFC membranes are shown for 5 scans. We see that at higher monomer concentration, the decrease in A values is higher than at low concentration. When compared to the Dow SW30XLE membrane, we see significant reduction in permeance. The normalized permeances of the ESP based TFC membranes demonstrates much better result compared to the Dow SW30XLE. A number of TFC membranes achieves better results than the Dow SW30XLE in both A_normalized and R.

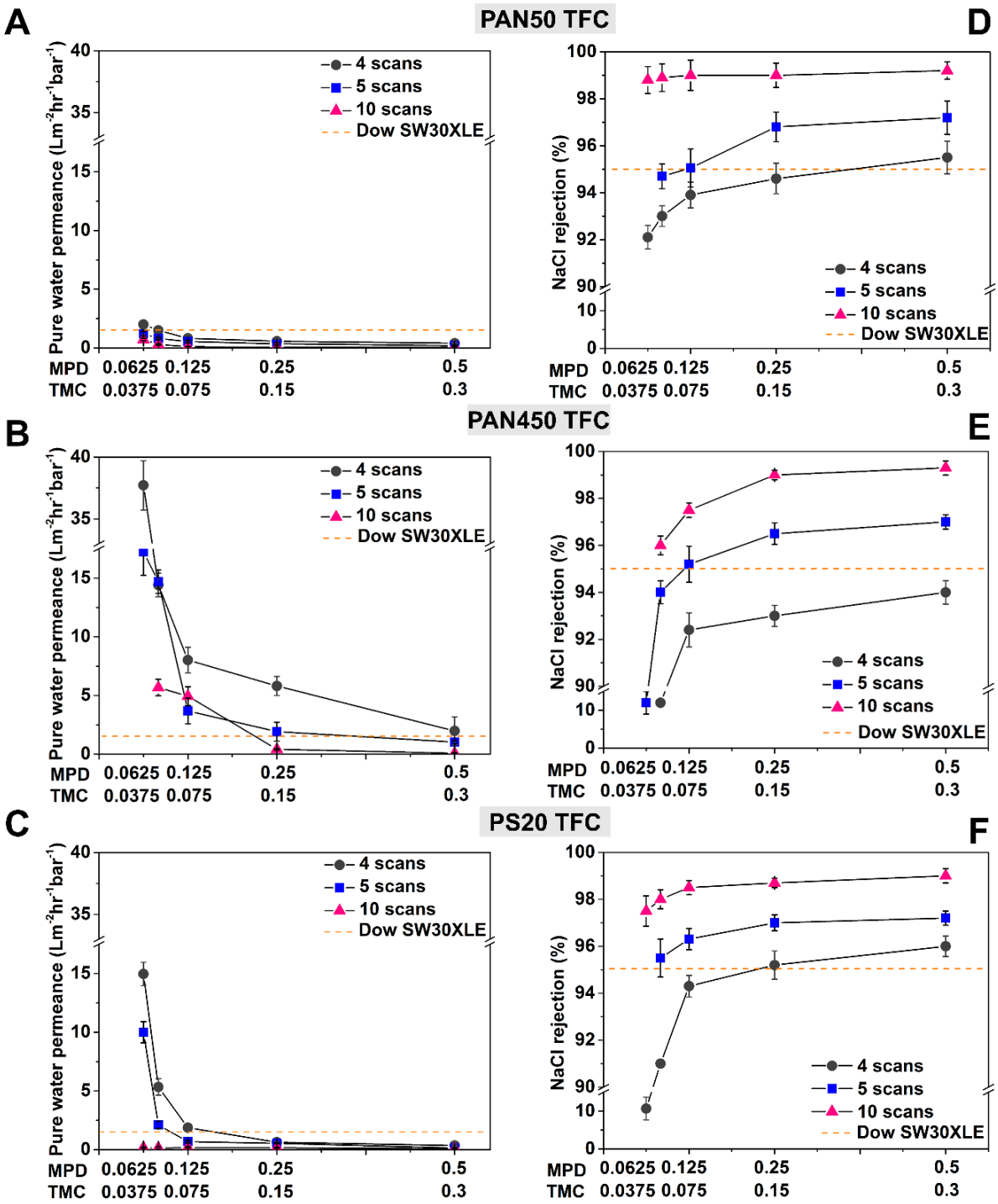

Figure 7.24: Desalination results for the TFC membranes made with ESP. Pure water permeance (A, B, and C) and NaCl salt rejection (D, E, and F) for the PAN50, PAN450, and PS20 TFC membranes at different scans and MPD : TMC concentration ratio. Operating condition: 10 bar applied pressure with DI water and 2000 ppm NaCl solution as feed stirred with magnetic stirrer

system. The commercial Dow SW30XLE TFC RO membrane is shown as an orange dotted line for benchmarking.

Table 7.5: Increased polyamide area normalized pure water permeances of TFC membranes at 5 scans.

Sample		A $LMHbar^{-1}$	A_normalized $LMHbar^{-1}$	A decreased %
Substrate	**MPD:TMC**			
PAN50	0.0625:0.0375	1.20	1.18	1.77
	0.08333:0.05	0.80	0.75	5.75
	0.125:0.075	0.54	0.51	5.66
	0.25:0.15	0.35	0.30	13.35
	0.5:0.3	0.20	0.18	11.03
PAN450	0.0625:0.0375	17.23	16.66	3.29
	0.08333:0.05	14.69	13.95	5.03
	0.125:0.075	3.68	3.47	5.75
	0.25:0.15	1.91	1.79	6.54
	0.5:0.3	1.02	0.90	12.20
PS20	0.0625:0.0375	10.11	9.88	1.19
	0.08333:0.05	2.10	2.06	1.86
	0.125:0.075	0.68	0.66	2.72
	0.25:0.15	0.53	0.52	3.01
	0.5:0.3	0.13	0.13	2.72
DOW SW30XLE	-	1.44	1.12	22.22

7.4.3. Scale up of ESP

While not demonstrated as part of this thesis, we anticipate ESP to be a highly scalable technique. In manufacturing industry, mechanical spray based technique for coating are used extensively [275]. Such industrial setup could essentially be used to match a commercial TFC fabrication line with a 30 m min^{-1} line speed. To do that, the developed lab scale system need to be modified and optimized significantly to achieve such level of speed in a continuous production line. A schematic of such a system is shown on Fig. 7.25. Ideally, depending on how many layers of polyamide needs to be printed on the substrate, the schematic shown below can be repeated. The spacing between the banks of needles would be selected in such a way to ensure that the previously sprayed surface remains at a specified dried state. An inert gas such as nitrogen flow would be introduced to control the rate of drying. The grounded electrode could be installed just beneath the substrate while aligning with the needle banks as can be seen from Fig. 7.25B. The substrate would be unsupported i.e. there will be no belt conveyor to carry the substrate. The final formed polyamide on the substrate will have a section at the two sides where the polyamide will be thinner. This is shown with a light violet color on Fig. 7.25A. These sections could be trimmed or used as the part to seal and glue the membrane leaf during module fabrication. There would also be provision for capturing the expensive solvent such as hexane using a cold trap. As hexane has a boiling point of 68 °C, a chiller operating at a very low temperature of 10 °C, will ensure efficient capture of the solvent which can then be recycled. Post treatment of the TFC membranes could also be installed as it is done in the conventional IP based TFC membrane fabrication. This could be protective layers for module fabrication, anti-scalant etc.

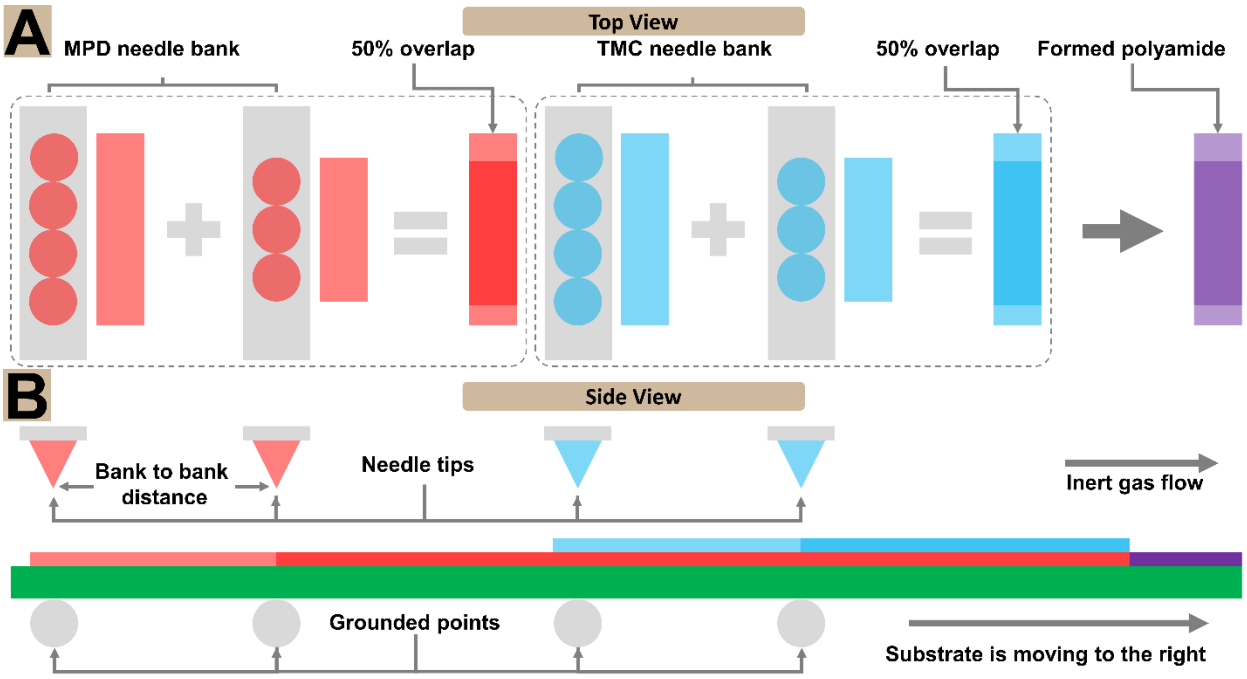

Figure 7.25: A schematic diagram of a continuous process of ESP based polyamide formation on polymeric substrates. (A) Top view of the repetitive block. (B) Side view shows the layers of solution depositing on substrate surface.

7.4.4. Chemical footprint of ESP and CIP

While it is difficult to find actual numbers for volumes of solution industry uses in conventional membrane fabrication and how they manage waste, we can still try to estimate the amount of solution required to make a 1 m^2 of TFC membrane based on laboratory scale setup. In a laboratory setup, support membrane would be introduced into the solution bath by simply immersing them using a secondary substrate to hold them in place such as glass plate. We assume that 2000 mL of solution would be enough to completely cover a 1 m^2 surface with 2 mm of solution layer at the top to ensure complete coverage if the 1 m^2 sheet was laid completely flat on the ground. Typically, these solutions would also get contaminated quickly and not be reusable. Based on the experimental procedure we developed, the ESP method would require less than 50 mL of solution to provide 5 scans to make the same 1 m^2 TFC membrane. Furthermore, the ESP

method essentially is a zero liquid waste generation process thus eliminating the need for systems to handle liquid waste management, solution recovery, and recycle.

Chapter 8

Concluding remarks

8.1. Introduction

Navigating through this dissertation, one might think of it as a disjointed thesis. Taking a broader look will reveal the generic purpose of this work is to optimize currently established osmotic processes, models, and membranes and contribute these novel approaches to the academic literature.

The hybrid dead-end/cross-flow method enabled the study of recovery of impaired water sources using coupon-scale membranes in forward osmosis. We demonstrated that high recovery of raw waters with high fouling propensity can easily be done using small membrane coupons rather than using expensive modules. In addition to saving membranes, this approach significantly reduces process runtime while keeping critical process equipment safe from corrosion. Faster testing enables higher throughput evaluations of membranes, feed solutions, and draw solution options. By using small quantities of feed solution also reduces overall cost of operation as certain feed solution could be expensive. This method can be used to study the concentration of pharmaceutical products such as proteins and drugs or food products such as juices and dairy. The developed mass transfer model enables ease in prediction of recovery of feeds.

We further extended the mass transfer model to better predict real osmotic processes. As FO finds more opportunities in different separations processes, there is a strong likelihood that unique feeds and regenerated draw solutions will be of different temperatures. Models developed

so far only dealt with studies where both feed and draw solutions remains at the same temperature. In addition, using Van't Hoff equation for osmotic pressure calculation would result in erroneous result for non-ideal solutions. The previous generation of models also do not account for variabilities in solution properties at different boundaries and interfaces across the membrane. The developed model tries to address these issues by incorporating both heat and mass transfer effects while coupling them to solution properties as they are temperature and concentration dependent. Further, a Pitzer correlation was used which accounts for the non-ideality that arises from the high salt content for challenging feed and concentrated draw solution. This allowed accurate prediction of real osmotic system where the temperature was varied across the membrane and the model results were compared. We found feed temperature has more of an impact than the draw solution as the direction of heat and mass transfer is in the same direction for elevated feed temperature. Identifying that feed temperature plays a more crucial role in overall osmotic performance than draw temperature does, will enable better system design, process integration in terms of heating and cooling, and economics. The dead-end/cross-flow system was also utilized to experimentally determine the overall heat transfer coefficient for these processes which was also verified by the developed model. For large scale optimization, variability in solution properties due to a change in concentration, temperature, and flow conditions need to be accounted for. Failure to include these variations could lead to erroneous process design and poor performance of the system.

To study this impact of varying operating conditions across the membrane on a large scale system, an element-scale hybrid pilot system coupling forward and reverse osmosis was fabricated. The goal of the FORO system include develop methodology for testing, study performance with changes in operating conditions, compare different kind of module design and how they are impacted differently for the same changes in operating conditions, and finally use raw impaired

waters to study the recovery process. From initial studies, it was observed that flowrate had an immediate impact on FO water flux in a plate and frame membrane module while no significant variation was observed with a spiral wound membrane module. For RO, higher concentration of RO feed results in poor rejection even at high pressure while high pressure such as 700 psi results in the highest rejection of salts. For FORO operation, changing RO pressure abruptly changes the FO water flux immediately as small 15 gallons tanks were used for holding the feed, draw and RO feed solution. Larger tanks would increase this response time significantly. Essentially, we would see a point where the RO pressure would control both the FO and RO system with regard to their water flux through the membrane.

Membrane development is also important for advancement in FO and RO based desalination technology. For FO, very limited number of membranes are out there for use in research. Commercially, Porifera is the only company that sells TFC based FO membrane which has become a standard for academics, national laboratories, and new FO startups who are trying to expand and discover newer application of FO. A detailed characterization of this membrane deemed necessary to understand its higher overall osmotic performance in FO. As we used this membrane module as a plate and frame module in the FORO system, we also characterized this membrane using coupon-size membranes in a bench scale system. The Porifera TFC membrane demonstrated superior performance compared to the HTI TFC membranes which is not available anymore.

While conventional TFC membrane such as Porifera TFC shows very good osmotic performance, it still cannot compete with the unconventional supports such as nanofiber supported TFC membrane for FO application. However, most of these novel membranes are mechanically fragile as these are made in the lab using electrospinning systems. We anticipated that using

commercial grade nanofiber mat as support would improve mechanical strength without sacrificing osmotic performance. Using a commercial nanofiber based support from DuPont, we fabricated a TFC membrane for FO. The membrane exhibited best in class mechanical strength with superior osmotic performance than many lab-made nanofiber based TFC membrane. In addition, optimization of the nanofiber mat structure could potentially enable further performance improvements of these novel nanofiber supported TFC membranes. Furthermore, the availability, the consistency and the uniformity over long lengths (e.g. rolls) of these commercially produced nanofiber products is key to the potential scale up and commercialization of this technology.

The exposure to the conventional interfacial polymerization process to make the nanofiber supported TFC led to the development of a new method for film formation. The ESP method is a first of a kind spray based approach for making highly tunable polyamide films. The method has zero chemical waste footprint with the added benefit of easy retrofitting capability and easy scale-up. It also does not contaminate the monomer solutions. The method also requires far less chemicals than any other process for making this polyamide based TFC membranes. The ESP method developed here, demonstrates capability in controlling thickness at sub-4 nm resolution and roughness at a sub-2 nm resolution while achieving substrate independence in film formation and in desalination by carefully manipulating monomer concentration and no. of scans. Furthermore, formation of bulky aromatic polyamide film has been demonstrated for the first time. Benefit of using this bulky polyamide was demonstrated by finding the cross-linked density using EDX. Forming the polyamide on aluminum foil enabled fast and easy characterization of film thickness using AFM. Polyamide density was also evaluated using QCM. Competitive desalination performance compared to the Dow SW30XLE shows capability of this method as a novel alternative to conventional approaches.

8.2. Expected novel contributions

From all the different topics covered here, several key contributions could be noted.

- The method developed in chapter 2, would reduce experimental runtime significantly. Not only that, the dead-end/cross-flow system would also enable fast study while mimicking module scale performance.
- The coupled heat and mass transfer model will enable more realistic prediction of forward osmosis processes. The benefit of using spatially variable solution properties, Pitzer correlation for accounting non-ideality would be immense as FO dives into more commercial application.
- Pilot system developed will help understand key performance parameters and their impact on process dynamics. The FORO system will also enable understanding the underlying relationship between a coupon-size and element-size membrane characterization through experimental evidence and model based prediction.
- The commercial nanofiber platform will enable taking the next step toward manufacturing TFC membranes for FO using this novel support.
- The electrosprayed polymerization is a unique approach for making tunable polyamide films. We demonstrated that a control over thickness and reduction in roughness could easily be achieved with ESP. It also gives freedom in tuning these by changing no. of scans and monomer concentration. The substrate independent film formation for polyamide films have never been demonstrated before. This allowed us not only to make the same polyamide films having similar thickness, roughness, surface morphology, and salt rejection on a variety of polymeric substrates but also on completely non-permeable and non-porous substrates such as

aluminum foil. Such degree of flexibility will certainly be helpful in using unconventional support material for RO and FO based TFC membrane formulation.

- Thick films of polyamide formed using ESP will enable detailed study of structure-property relationship. These properties include cross-linked density, polyamide density, water uptake, salt uptake, mechanical strength etc. This is a significant improvement for making this polyamide as a thick film which can freely stand in air.

- ESP can also be utilized for making novel thin film nanocomposite membranes by embedding nanoparticles inside the polyamide films thus immobilizing them. Forming antifouling and antiscaling characteristics are important for next generation membrane fabrication. We believe ESP will be a very useful tool in this regard. Other application of ESP could include making pervaporation membranes by making the polyamide as highly thick films (over 10-20 μm).

Appendices

Appendix A: Details on the heat transfer model

A.1. Heat transfer model: Forward osmosis mode (40-20)

The one dimensional heat flux equation is used [119] to calculate the conductive HT through different layers and the generalized equation used is shown below:

$$Q = -\lambda A_m \int \frac{dT}{dx} \quad \text{(A0)}$$

For the feed side B.L., Eq. A0 is integrated using appropriate boundary conditions from Table 3.1 to yield:

$$Q_{\delta tf}^{cond} = \frac{\lambda_{water.\ Fm}}{\delta_{t.f}} A_m (T_{Fb} - T_{Fm}) \quad \text{(A1)}$$

The thermal boundary layer ($\delta_{t.f}$) can be related to the hydrodynamic boundary layer (δ_f) in laminar flow for Prandtl number other than unity using [276]:

$$\frac{\delta_f}{\delta_{t.f}} = Pr_{Fm}^{1/3}; \frac{\delta_f}{\delta_{m.f}} = Sc_{Fm}^{1/3}$$

$$\Rightarrow \frac{\delta_{t.f}}{\delta_{m.f}} = \frac{Sc_{Fm}^{1/3}}{Pr_{Fm}^{1/3}} = \left(\frac{Sc_{Fm}}{Pr_{Fm}}\right)^{1/3} \quad \text{(A2)}$$

Additionally, mass transfer boundary layer can be related to mass transfer coefficient using the following relationship [276]:

$$k_{mt.f} = \frac{D_{Fm}}{\delta_{m.f}} \quad \text{(A3)}$$

Finally, the equation for calculating thermal boundary layer thickness is derived by inserting Eq. A3 in Eq. A2 giving:

$$\delta_{t.f} = \frac{D_{Fm}}{k_{mt.f}} \left(\frac{Sc_{Fm}}{Pr_{Fm}}\right)^{1/3} \quad \text{(A4)}$$

Using Eq. A4, $Q_{\delta t.f}^{cond}$ is calculated using Eq. A1. In a similar manner $Q_{\delta t.d}^{cond}$ for the draw side boundary layer is found using the following two equations.

$$Q_{\delta t.d}^{cond} = \frac{\lambda_{water.\ Dm}}{\delta_{t.d}} A_m (T_{Dm} - T_{Db}) \quad \text{(A5)}$$

$$\delta_{t.d} = \frac{D_{Dm}}{k_{mt.d}} \left(\frac{Sc_{Dm}}{Pr_{Dm}}\right)^{1/3} \quad \text{(A6)}$$

Due to the flow of liquid over the membrane, convective heat transfer also occurs in the two boundary layers. Nusselt correlation for laminar flow is used to find the two convective heat transfer coefficient for the feed and draw side boundary layers.

$$h_{Fm} = \frac{\lambda_{water.\ Fm}}{d_h} 1.86 \left(Re_{Fm} Pr_{Fm} \frac{d_h}{L}\right)^{1/3} \left(\frac{\mu_{Fb}}{\mu_{Fm}}\right)^{0.14} \quad \text{(A7)}$$

$$h_{Dm} = \frac{\lambda_{water.\ Dm}}{d_h} 1.86 \left(Re_{Dm} Pr_{Dm} \frac{d_h}{L}\right)^{1/3} \left(\frac{\mu_{Db}}{\mu_{Dm}}\right)^{0.14} \quad \text{(A8)}$$

The heat transfer due to convection is calculated using Eq. A7 and A8 from the following relations.

$$Q_{\delta t.f}^{conv} = h_{Fm} A_m (T_{Fb} - T_{Fm}) \quad \text{(A9)}$$

$$Q_{\delta t.d}^{conv} = h_{Dm} A_m (T_{Dm} - T_{Db}) \quad \text{(A10)}$$

The convective heat flux due to mass transport occurs throughout the whole system. This convective heat is the product of amount of water being transported, membrane area, heat capacity and temperature difference across the region of interest. The following two equations are developed for convective heat transfer due to mass transfer.

$$Q_{\delta t.f}^{conv} = J_{w.FO} \rho_{Fm} c_{p.Fm} A_m (T_{Fb} - T_{Fm}) \quad \text{(A11)}$$

$$Q_{\delta t.d}^{conv} = J_{w.FO} \rho_{Dm} c_{p.Dm} A_m (T_{Dm} - T_{Db}) \quad \text{(A12)}$$

When combined, Eq. A1, A9 and A11, we get the total amount of heat that is transferred through the boundary layers.

$$Q_{\delta t.f}^{total} = (h_{Fm} + J_{w.FO}\,\rho_{Fm} c_{p.Fm} + \frac{\lambda_{water.\,Fm}}{\delta_{t.f}})(T_{Fb} - T_{Fm})A_m = B_{\delta t.f}(T_{Fb} - T_{Fm})A_m$$

(A13)

$$Q_{\delta t.d}^{total} = (h_{Dm} + J_{w.FO}\,\rho_{Dm} c_{p.Dm} + \frac{\lambda_{water.\,Dm}}{\delta_{t.d}})(T_{Dm} - T_{Db})A_m = B_{\delta t.d}(T_{Dm} - T_{Db})A_m$$

(A14)

To calculate the total heat transfer through the support layer, both conductive and convective heat transfer needs to be considered. Similar to Eq. A1, the conductive heat transfer equation is developed as follows:

$$Q_{ts}^{cond} = \frac{\lambda_{membrane}}{t_s} A_m (T_i - T_{Dm}) \quad \text{(A15)}$$

Where, $\lambda_{membrane} = \lambda_{water.\,i}\,\varepsilon_s + \lambda_{polymer}(1 - \varepsilon_s)$

The convective heat transfer due to the mass transport is similar to Eq. A11 and A12 and is shown below:

$$Q_{ts}^{conv} = J_{w.FO}\,\rho_i c_{p.i} A_m (T_i - T_{Dm}) \quad \text{(A16)}$$

$$Q_{ts}^{total} = (J_{w.FO}\,\rho_i c_{p.i} + \frac{\lambda_{membrane}}{t_s})(T_i - T_{Dm})A_m = B_{ts}(T_i - T_{Dm})A_m \quad \text{(A17)}$$

By comparing the 2nd and 3rd equalities in Eq. 3.11 we get,

$$T_{Fm} - T_i = \frac{B_{ts}}{B_{ta}} T_i - \frac{B_{ts}}{B_{ta}} T_{Dm}$$

$$\Rightarrow\ T_i(1 + \frac{B_{ts}}{B_{ta}}) = T_{Fm} + \frac{B_{ts}}{B_{ta}} T_{Dm}$$

$$\Rightarrow\ T_i = \frac{B_{ta}}{B_{ta} + B_{ts}} T_{Fm} + \frac{B_{ts}}{B_{ta} + B_{ts}} T_{Dm} \quad \text{(A18)}$$

Finally, the equation for T_{Dm} is developed by equating the last equalities in Eq. 3.11 as follows:

$$T_i - T_{Dm} = \frac{B_{\delta t.d}}{B_{ts}} T_{Dm} - \frac{B_{\delta t.d}}{B_{ts}} T_{Db}$$

$$\Rightarrow\ T_{Dm}(1 + \frac{B_{\delta t.d}}{B_{ts}}) = T_i + \frac{B_{\delta t.d}}{B_{ts}} T_{Db}$$

$$\Rightarrow \quad T_{Dm} = \frac{B_{ts}}{B_{ts}+B_{\delta t.d}} T_i + \frac{B_{\delta t.d}}{B_{ts}+B_{\delta t.d}} T_{Db}$$

$$T_{Dm} = \frac{B_{ts}}{B_{ts}+B_{\delta t.d}} T_i + \frac{B_{\delta t.d}}{B_{ts}+B_{\delta t.d}} T_{Db} \tag{A19}$$

A.2. Heat transfer model: Pressure retarded osmosis mode (40-20)

Similar to FO mode 40-20 case, the PRO mode 40-20 model is developed. The boundary layer conditions are similar for both FO and PRO and Eqs. A1-A14 can be used to find the total heat transferred in the two boundary layers. Integrating Eq. A0 for the support layer, the conductive heat transfer due to solid phase and liquid phase can be written as:

$$Q_{ts}^{cond} = \frac{\lambda_{membrane}}{t_s} A_m (T_{Fm} - T_i) \tag{A20}$$

Where, $\lambda_{membrane} = \lambda_{water.\ i}\ \varepsilon_s + \lambda_{polymer}(1 - \varepsilon_s)$

The convective heat transport across the support layer and the total heat transport for this region is then can be found.

$$Q_{ts}^{conv} = J_{w.PRO}\ \rho_i c_{p.i} A_m (T_{Fm} - T_i) \tag{A21}$$

$$Q_{ts}^{total} = (J_{w.PRO}\ \rho_i c_{p.i} + \frac{\lambda\, membrane}{t_s})(T_{Fm} - T_i) A_m = B_{ts}(T_{Fm} - T_i) A_m \tag{A22}$$

For the selective layer, the conductive heat transport is derived by integrating Eq. A0 with appropriate boundary conditions from Table 3.1.

$$Q_{ta}^{cond} = \frac{\lambda\, polymer}{t_a} A_m (T_i - T_{Dm}) \tag{A23}$$

The convective heat transfer due to mass transport is similar to Eq. A21:

$$Q_{ta}^{conv} = J_{w.PRO}\ \rho_i c_{p.i} A_m (T_i - T_{Dm}) \tag{A24}$$

The total heat transfer in the membrane selective layer is found by combining Eq. A23 and A24 to give:

$$Q_{ta}^{total} = (J_{w.PRO}\,\rho_i c_{p.i} + \frac{\lambda_{polymer}}{t_a})(T_i - T_{Dm})A_m = B_{ta}(T_i - T_{Dm})A_m \quad \text{(A25)}$$

Equating Eq. A13, A14, A22 and A25, we get:

$$B_{\delta t.f}(T_{Fb} - T_{Fm})A_m \;\; = B_{ts}(T_{Fm} - T_i)A_m = B_{ta}(T_i - T_{Dm})A_m = B_{\delta t.d}(T_{Dm} - T_{Db})A_m \text{(A26)}$$

Equating the first two equalities in Eq. A26,

$$T_{Fb} - T_{Fm} \;\; = \frac{B_{ts}}{B_{\delta t.f}}T_{Fm} - \frac{B_{ts}}{B_{\delta t.f}}T_i$$

$$\Rightarrow \;\; T_{Fm}(1 \; + \frac{B_{ts}}{B_{\delta t.f}}) = T_{Fb} + \frac{B_{ts}}{B_{\delta t.f}}T_i$$

$$\Rightarrow \;\; T_{Fm} = \frac{B_{\delta t.f}}{(B_{\delta t.f} + B_{ts})}T_{Fb} + \frac{B_{ts}}{(B_{\delta t.f} + B_{ts})}T_i \quad \text{(A27)}$$

By comparing the 2nd and 3rd equalities in Eq. A26,

$$T_{Fm} - T_i \;\; = \frac{B_{ta}}{B_{ts}}T_i - \frac{B_{ta}}{B_{ts}}T_{Dm}$$

$$\Rightarrow \;\; T_i(1 \; + \frac{B_{ta}}{B_{ts}}) = T_{Fm} + \frac{B_{ta}}{B_{ts}}T_{Dm}$$

$$\Rightarrow \;\; T_i = \frac{B_{ts}}{B_{ta} + B_{ts}}T_{Fm} + \frac{B_{ta}}{B_{ta} + B_{ts}}T_{Dm} \quad \text{(A28)}$$

Finally, the equation for T_{Dm} is developed by equating the last equalities in Eq. A26 as follows:

$$T_i - T_{Dm} \;\; = \frac{B_{\delta t.d}}{B_{ta}}T_{Dm} - \frac{B_{\delta t.d}}{B_{ta}}T_{Db}$$

$$\Rightarrow \;\; T_{Dm}(1 \; + \frac{B_{\delta t.d}}{B_{ta}}) = T_i + \frac{B_{\delta t.d}}{B_{ta}}T_{Db}$$

$$\Rightarrow \;\; T_{Dm} = \frac{B_{ta}}{B_{ta} + B_{\delta t.d}}T_i + \frac{B_{\delta t.d}}{B_{ta} + B_{\delta t.d}}T_{Db} \quad \text{(A29)}$$

A.3. Heat transfer model: Forward osmosis mode (20-40)

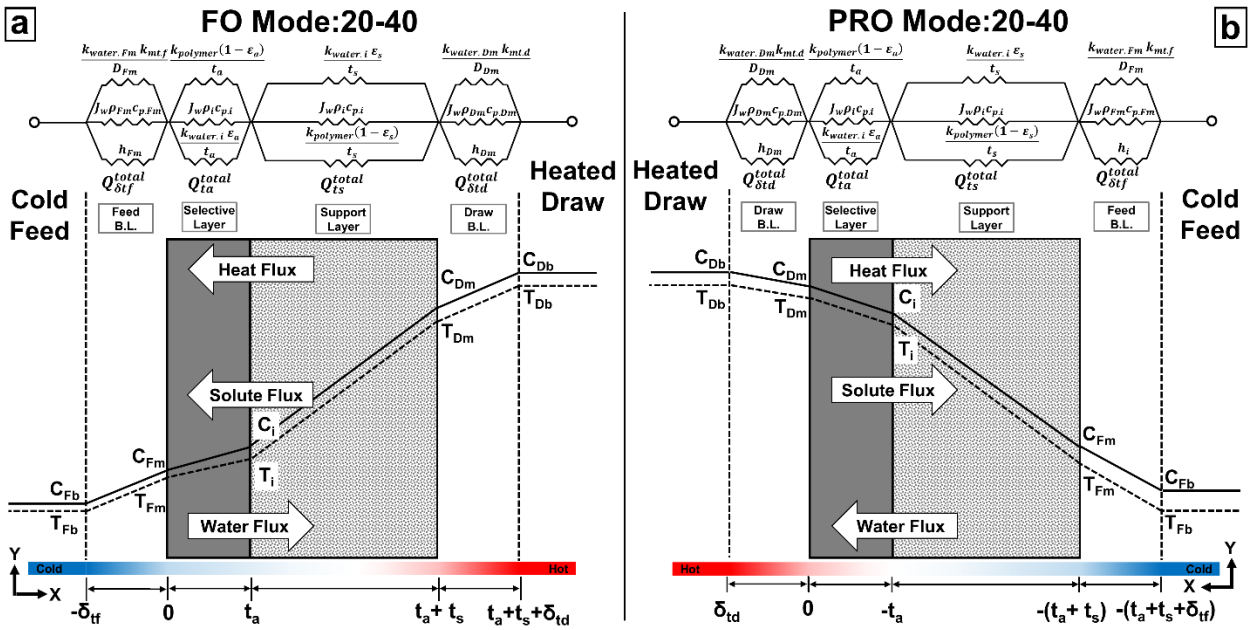

Figure A1: Schematics of heat and mass transfer profiles in forward osmosis mode (FO mode) and pressure retarded osmosis mode (PRO mode) process for 20-40 condition.

Integrating Eq. A0 using boundary conditions from Table 3.1 for FO mode for the feed side and draw side boundary layers we have:

$$Q_{\delta t.f}^{cond} = \frac{\lambda_{water.\,Fm}}{\delta_{t.f}} A_m (T_{Fm} - T_{Fb}) \qquad \text{(A30)}$$

The thermal boundary layer ($\delta_{t.f}$) is calculated using Eq. A4. $Q_{\delta t.d}^{cond}$ for the draw side boundary layer is found using the following equation and $\delta_{t.d}$ is calculated using Eq. A6.

$$Q_{\delta t.d}^{cond} = \frac{\lambda_{water.\,Dm}}{\delta_{t.d}} A_m (T_{Db} - T_{Dm}) \qquad \text{(A31)}$$

Convective heat transfer coefficient found from Eq. A7 and A8. The heat transfer due to convection is calculated using Eq. A32 and A33 as shown below.

$$Q_{\delta t.f}^{conv} = h_{Fm} A_m (T_{Fm} - T_{Fb}) \qquad \text{(A32)}$$

$$Q_{\delta t.d}^{conv} = h_{Dm} A_m (T_{Db} - T_{Dm}) \qquad \text{(A33)}$$

For 20-40 case, the convective heat transport occurs in opposite direction to the mass transport. Similar to Eq. A11, the following two equations are developed for convective heat transfer due to mass transfer.

$$Q_{\delta t.f}^{conv} = -J_{w.FO}\ \rho_{Fm} c_{p.Fm} A_m (T_{Fm} - T_{Fb}) \quad \text{(A34)}$$

$$Q_{\delta t.d}^{conv} = -J_{w.FO}\ \rho_{Dm} c_{p.Dm} A_m (T_{Db} - T_{Dm}) \quad \text{(A35)}$$

Combining Eq. A30-A35, we get the total amount of heat that is transferred through the two boundary layers.

$$Q_{\delta t.f}^{total} = (h_{Fm} - J_{w.FO}\ \rho_{Fm} c_{p.Fm} + \frac{\lambda_{water.\ Fm}}{\delta_{t.f}})(T_{Fm} - T_{Fb}) A_m = B_{\delta t.f}(T_{Fm} - T_{Fb}) A_m \quad \text{(A36)}$$

$$Q_{\delta t.d}^{total} = (h_{Dm} - J_{w.FO}\ \rho_{Dm} c_{p.Dm} + \frac{\lambda_{water.\ Dm}}{\delta_{t.d}})(T_{Db} - T_{Dm}) A_m = B_{\delta t.d}(T_{Db} - T_{Dm}) A_m \quad \text{(A37)}$$

To calculate the support layer heat transfer, a similar equation to Eq. A15 is used.

$$Q_{ts}^{cond} = \frac{\lambda_{membrane}}{t_s} A_m (T_{Dm} - T_i) \quad \text{(A38)}$$

Where, $\lambda_{membrane} = \lambda_{water.i}\ \varepsilon_s + \lambda_{polymer}(1 - \varepsilon_s)$

The convective heat transfer due to the mass transport is similar to Eq. A35 and is shown below:

$$Q_{ts}^{conv} = -J_{w.FO}\ \rho_i c_{p.i} A_m (T_{Dm} - T_i) \quad \text{(A39)}$$

$$Q_{ts}^{total} = (-J_{w.FO}\ \rho_i c_{p.i} + \frac{\lambda_{membrane}}{t_s})(T_{Dm} - T_i) A_m = B_{ts}(T_{Dm} - T_i) A_m \quad \text{(A40)}$$

The selective layer heat transfer is calculated in a similar approach starting with integration of Eq. A0 to yield:

$$Q_{ta}^{cond} = \frac{\lambda_{polymer}}{t_a} A_m (T_i - T_{Fm}) \quad \text{(A41)}$$

The convective heat transfer due to mass transport is similar to Eq. A35:

$$Q_{ta}^{conv} = -J_{w.FO}\ \rho_i c_{p.i} A_m (T_i - T_{Fm}) \quad \text{(A42)}$$

Combining Eqs. A41 and A42, we get the total heat transport through the selective layer.

$$Q_{ta}^{total} = (-J_{w.FO}\,\rho_i c_{p.i} + \frac{\lambda_{polymer}}{t_a})(T_i - T_{Fm})A_m = B_{ta}(T_i - T_{Fm})A_m \quad \text{(A43)}$$

Using Eq. 3.10 and inserting the short form of Eqs. A36, A37, A40 and A43 we have,

$$B_{\delta t.f}(T_{Fm} - T_{Fb})A_m \;\; = B_{ta}(T_i - T_{Fm})A_m = B_{ts}(T_{Dm} - T_i)A_m = B_{\delta t.d}(T_{Db} - T_{Dm})A_m \quad \text{(A44)}$$

By comparing the first two terms in Eq. A44 we get,

$$(T_{Fm} - T_{Fb}) \;\; = \frac{B_{ta}}{B_{\delta t.f}}T_i - \frac{B_{ta}}{B_{\delta t.f}}T_{Fm}$$

$$\Rightarrow \;\; T_{Fm}(1 + \frac{B_{ta}}{B_{\delta t.f}}) = T_{Fb} + \frac{B_{ta}}{B_{\delta t.f}}T_i$$

$$\Rightarrow \;\; T_{Fm} = \frac{B_{\delta t.f}}{(B_{\delta t.f} + B_{ta})}T_{Fb} + \frac{B_{ta}}{(B_{\delta t.f} + B_{ta})}T_i \quad \text{(A45)}$$

By comparing the 2nd and 3rd equalities in Eq. A44 we get,

$$(T_i - T_{Fm}) \;\; = \frac{B_{ts}}{B_{ta}}T_{Dm} - \frac{B_{ts}}{B_{ta}}T_i$$

$$\Rightarrow \;\; T_i(1 + \frac{B_{ts}}{B_{ta}}) = T_{Fm} + \frac{B_{ts}}{B_{ta}}T_{Dm}$$

$$\Rightarrow \;\; T_i = \frac{B_{ta}}{B_{ta}+B_{ts}}T_{Fm} + \frac{B_{ts}}{B_{ta}+B_{ts}}T_{Dm} \quad \text{(A46)}$$

Finally, the equation for T_{Dm} is developed by equating the last equalities in Eq. A44 as follows:

$$(T_{Dm} - T_i) \;\; = \frac{B_{\delta t.d}}{B_{ts}}T_{Db} - \frac{B_{\delta t.d}}{B_{ts}}T_{Dm}$$

$$\Rightarrow \;\; T_{Dm}(1 + \frac{B_{\delta t.d}}{B_{ts}}) = T_i + \frac{B_{\delta t.d}}{B_{ts}}T_{Db}$$

$$\Rightarrow \;\; T_{Dm} = \frac{B_{ts}}{B_{ts}+B_{\delta t.d}}T_i + \frac{B_{\delta td}}{B_{ts}+B_{\delta t.d}}T_{Db} \quad \text{(A47)}$$

A.4. Heat transfer model: Pressure retarded osmosis mode (20-40)

Eq. A36 and A37 are still applicable for the two boundary layers in PRO mode. To calculate the support layer heat transfer due to conduction in the solid and liquid phase, Eq. A0 is integrated using boundary conditions from Table 3.1 to get:

$$Q_{ts}^{cond} = \frac{\lambda_{membrane}}{t_s} A_m (T_i - T_{Fm}) \quad \text{(A48)}$$

Where, $\lambda_{membrane} = \lambda_{water.\ i}\, \varepsilon_s + \lambda_{polymer}(1 - \varepsilon_s)$

The convective heat transfer due to the mass transport is found from the following equation:

$$Q_{ts}^{conv} = -J_{w.PRO}\, \rho_i c_{p.i} A_m (T_i - T_{Fm}) \quad \text{(A49)}$$

The total heat transport in the support is the sum of conductive and convective heat from Eq. A48 and A49

$$Q_{ts}^{total} = (-J_{w.PRO}\, \rho_i c_{p.i} + \frac{\lambda_{membrane}}{t_s})(T_i - T_{Fm})\, A_m = B_{ts}(T_i - T_{Fm})\, A_m \quad \text{(A50)}$$

The selective layer heat transfer is calculated in a similar approach starting with integration of Eq. A0 to yield:

$$Q_{ta}^{cond} = \frac{\lambda_{polymer}}{t_a} A_m (T_{Dm} - T_i) \quad \text{(A51)}$$

The convective heat transfer due to mass transport is similar to Eq. A49:

$$Q_{ta}^{conv} = -J_{w.PRO}\, \rho_i c_{p.i} A_m (T_{Dm} - T_i) \quad \text{(A52)}$$

Combining Eq. A51 and A52, we get the total heat transport through the selective layer.

$$Q_{ta}^{total} = (-J_{w.PRO}\, \rho_i c_{p.i} + \frac{\lambda_{polymer}}{t_a})(T_{Dm} - T_i) A_m = B_{ta}(T_{Dm} - T_i) A_m \quad \text{(A53)}$$

Using Eq. 3.10 and inserting the short form of Eq. A36, A37, A50 and A53 we have,

$$B_{\delta t.f}(T_{Fm} - T_{Fb}) A_m \quad = B_{ts}(T_i - T_{Fm}) A_m = B_{ta}(T_{Dm} - T_i) A_m = B_{\delta t.d}(T_{Db} - T_{Dm}) A_m \quad \text{(A54)}$$

By comparing the first two terms in Eq. A54 we get,

$$(T_{Fm} - T_{Fb}) \quad = \frac{B_{ts}}{B_{\delta t.f}} T_i - \frac{B_{ts}}{B_{\delta t.f}} T_{Fm}$$

$$\Rightarrow \quad T_{Fm}(1 + \frac{B_{ts}}{B_{\delta t.f}}) = T_{Fb} + \frac{B_{ts}}{B_{\delta t.f}} T_i$$

$$\Rightarrow \quad T_{Fm} = \frac{B_{\delta t.f}}{(B_{\delta t.f} + B_{ts})} T_{Fb} + \frac{B_{ts}}{(B_{\delta t.f} + B_{ts})} T_i \quad \text{(A55)}$$

By comparing the 2nd and 3rd equalities in Eq. A54 we get,

$$(T_i - T_{Fm}) = \frac{B_{ta}}{B_{ts}} T_{Dm} - \frac{B_{ta}}{B_{ts}} T_i$$

$$\Rightarrow \; T_i\left(1 + \frac{B_{ts}}{B_{ta}}\right) = T_{Fm} + \frac{B_{ts}}{B_{ta}} T_{Dm}$$

$$\Rightarrow \; T_i = \frac{B_{ta}}{B_{ta}+B_{ts}} T_{Fm} + \frac{B_{ts}}{B_{ta}+B_{ts}} T_{Dm} \qquad \text{(A56)}$$

Finally, the equation for T_{Dm} is developed by equating the last equalities in Eq. A54 as follows:

$$(T_{Dm} - T_i) = \frac{B_{\delta t.d}}{B_{ta}} T_{Db} - \frac{B_{\delta t.d}}{B_{ta}} T_{Dm}$$

$$\Rightarrow \; T_{Dm}\left(1 + \frac{B_{\delta t.d}}{B_{ta}}\right) = T_i + \frac{B_{\delta t.d}}{B_{ta}} T_{Db}$$

$$\Rightarrow \; T_{Dm} = \frac{B_{ta}}{B_{ta}+B_{\delta t.d}} T_i + \frac{B_{\delta t.d}}{B_{ta}+B_{\delta t.d}} T_{Db} \qquad \text{(A57)}$$

Appendix B: Details on the mass transfer model

B.1 Forward osmosis mode

Integration of Eq. 3.16 using the boundary conditions from Table 3.1 provide the concentrations at the feed side boundary layer and membrane interfaces by accounting the different concentration polarization that are known to be present in FO process [64,68,85].

$$\int_{-\delta_{t.f}}^{0} dx = \frac{1}{D_{Fm}} \int_{C_{Fb}}^{C_{Fm}} \frac{dC}{J_{w.FO}C + B(C_i - C_{Fm})}$$

$$\Rightarrow \left[0 - \left(-\delta_{t.f}\right)\right] = \frac{1}{\frac{J_{w.FO}}{D_{Fm}}} \ln \left[\frac{C_{Fm}\frac{J_{w.FO}}{D_{Fm}} + \frac{B}{D_{Fm}}(C_i - C_{Fm})}{C_{Fb}\frac{J_{w.FO}}{D_{Fm}} + \frac{B}{D_{Fm}}(C_i - C_{Fm})}\right]$$

$$\Rightarrow \frac{C_{Fm}\frac{J_{w.FO}}{D_{Fm}} + \frac{B}{D_{Fm}}(C_i - C_{Fm})}{C_{Fb}\frac{J_{w.FO}}{D_{Fm}} + \frac{B}{D_{Fm}}(C_i - C_{Fm})} = exp^{\frac{J_{w.FO}\delta_{t.f}}{D_{Fm}}}$$

$$\Rightarrow C_{Fm}\frac{J_{w.FO}}{D_{Fm}} + \frac{B}{D_{Fm}}(C_i - C_{Fm}) = \left\{C_{Fb}\frac{J_{w.FO}}{D_{Fm}} + \frac{B}{D_{Fm}}(C_i - C_{Fm})\right\} exp\left(\frac{J_{w.FO}}{k_{mt.f}}\right)$$

$$\Rightarrow C_{Fm}\frac{J_{w.FO}}{D_{Fm}} = C_{Fb}\frac{J_{w.FO}}{D_{Fm}} exp\left(\frac{J_{w.FO}}{k_{mt.f}}\right) + \frac{B}{D_{Fm}}(C_i - C_{Fm}) exp\left(\frac{J_{w.FO}}{k_{mt.f}}\right) - \frac{B}{D_{Fm}}(C_i - C_{Fm})$$

$$\Rightarrow C_{Fm} = C_{Fb}P_{\delta m.f} - \frac{B}{J_w}(C_i - C_{Fm})\left(1 - P_{\delta m.f}\right) \quad \text{(B1)}$$

From Eq. 3.15, we have,

$$-D_s\frac{dC}{dx} + J_{w.FO}C = -B(C_i - C_{Fm})$$

$$\Rightarrow \frac{dC}{dx} = \left\{\frac{J_{w.FO}C + B(C_i - C_{Fm})}{D_s}\right\}$$

$$\Rightarrow dx = D_s\left\{\frac{dC}{J_{w.FO}C + B(C_i - C_{Fm})}\right\} \quad \text{(B2)}$$

Integrating Eq. B2 through the support layer thickness and using appropriate boundary condition from table 3.1 we get:

$$\int_{t_a}^{t_a+t_s} dx = \int_{C_i}^{C_{Dm}} D_s \left\{ \frac{dC}{J_{w.FO}C + B(C_i - C_{Fm})} \right\}$$

$$\Rightarrow \; [t_a + t_s - t_a] = \frac{1}{\frac{J_{w.FO}}{D_s}} \ln \left[\frac{C_{Dm}\frac{J_{w.FO}}{D_i} + \frac{B}{D_i}(C_i - C_{Fm})}{C_i\frac{J_{w.FO}}{D_i} + \frac{B}{D_i}(C_i - C_{Fm})} \right]$$

$$\Rightarrow \; \frac{C_{Dm}\frac{J_{w.FO}}{D_i} + \frac{B}{D_i}(C_i - C_{Fm})}{C_i\frac{J_{w.FO}}{D_i} + \frac{B}{D_i}(C_i - C_{Fm})} = exp\left(\frac{J_{w.FO}t_s}{D_s}\right) \qquad \text{(B3)}$$

Support layer effective diffusivity, D_s, can be related to bulk diffusivity, D_i, by accounting for porosity and tortuosity of the support, i.e. $D_s = \frac{D_i \varepsilon_s}{\tau}$ [98]. Additionally, support layer structural parameter is defined by $S = \frac{t_s \tau}{\varepsilon_s}$ [21] where t_s is the support layer thickness. Combining D_s and S yields $\frac{D_s}{t_s} = \frac{D_i}{S}$. Eq. B3 can be rewritten as:

$$\Rightarrow \; C_i \frac{J_{w.FO}}{D_i} exp\left(\frac{J_{w.FO}S}{D_i}\right) + \frac{B}{D_i}(C_i - C_{Fm}) exp\left(\frac{J_{w.FO}S}{D_i}\right) = C_{Dm}\frac{J_{w.FO}}{D_i} + \frac{B}{D_i}(C_i - C_{Fm})$$

$$\Rightarrow \; C_i P_{ts.FO} + \frac{B}{J_{w.FO}}(C_i - C_{Fm}) P_{ts.FO} = C_{Dm} + \frac{B}{J_{w.FO}}(C_i - C_{Fm})$$

$$\Rightarrow \; C_i = \frac{C_{Fm}(1 - P_{ts.FO}) - C_{Dm}\frac{J_{w.FO}}{B}}{1 - P_{ts.FO}\left(\frac{J_{w.FO}}{B} + 1\right)} \qquad \text{(B4)}$$

From Eq. 3.17, we have,

$$-D_{Dm}\frac{dC}{dx} + J_{w.FO}C = -B(C_i - C_{Fm})$$

$$\Rightarrow \; \frac{dC}{dx} = \left\{ \frac{J_{w.FO}C + B(C_i - C_{Fm})}{D_{Dm}} \right\}$$

$$\Rightarrow \; dx = D_{Dm} \left\{ \frac{dC}{J_{w.FO}C + B(C_i - C_{Fm})} \right\} \qquad \text{(B5)}$$

Integrating Eq. B5 through the support layer thickness and using appropriate boundary condition from Table 3.1 we get:

$$\int_{t_a+t_s}^{t_a+t_s+\delta_{t.d}} dx = \int_{C_{Dm}}^{C_{Db}} D_{Dm}\left\{\frac{dC}{J_{w.FO}C + B(C_i - C_{Fm})}\right\}$$

$$\Rightarrow \ [t_a + t_s + \delta_{t.d} - t_a - t_s] = \frac{1}{\frac{J_{w.FO}}{D_{Dm}}} \ln\left[\frac{C_{Db}\frac{J_{w.FO}}{D_{Dm}} + \frac{B}{D_{Dm}}(C_i - C_{Fm})}{C_{Dm}\frac{J_{w.FO}}{D_{Dm}} + \frac{B}{D_{Dm}}(C_i - C_{Fm})}\right]$$

$$\Rightarrow \ \frac{C_{Db}\frac{J_{w.FO}}{D_{Dm}} + \frac{B}{D_{Dm}}(C_i - C_{Fm})}{C_{Dm}\frac{J_{w.FO}}{D_{Dm}} + \frac{B}{D_{Dm}}(C_i - C_{Fm})} = exp\left(\frac{J_{w.FO}\delta_{t.d}}{D_{Dm}}\right) = exp\left(\frac{J_{w.FO}}{k_{mt.d}}\right) = \frac{1}{exp\left(-\frac{J_{w.FO}}{k_{mt.d}}\right)}$$

$$\Rightarrow \ C_{Dm}\frac{J_{w.FO}}{D_{Dm}} + \frac{B}{D_{Dm}}(C_i - C_{Fm}) = \left(C_{Db}\frac{J_{w.FO}}{D_{Dm}} + \frac{B}{D_{Dm}}(C_i - C_{Fm})\right) exp\left(-\frac{J_{w.FO}}{k_{mt.d}}\right)$$

$$\Rightarrow \ C_{Dm} = \left(C_{Db} + \frac{B}{J_{w.FO}}(C_i - C_{Fm})\right) P_{\delta m.d} - \frac{B}{J_{w.FO}}(C_i - C_{Fm})$$

$$\Rightarrow \ C_{Dm} = C_{Db}P_{\delta m.d} + (P_{\delta m.d} - 1)\frac{B}{J_{w.FO}}(C_i - C_{Fm}) \qquad \text{(B6)}$$

Where $P_{ts.FO} = exp\left(\frac{J_{w.FO}S}{D_i}\right)$; $S = \frac{t_s\tau}{\varepsilon}$; $P_{\delta m.f} = exp\left(\frac{J_{w.FO}}{k_{mt.f}}\right)$; $P_{\delta m.d} = exp\left(-\frac{J_{w.FO}}{k_{mt.d}}\right)$

The osmotic coefficient can be evaluated using Eq. B7:

$$\varphi_m - 1 = |z_+z_-|f^{\varphi} + m\left(\frac{2\vartheta_+\vartheta_-}{\vartheta}\right)B_{MX}^{\varphi} + m^2\left(\frac{2(\vartheta_+\vartheta_-)^{3/2}}{\vartheta}\right)C_{MX}^{\varphi} \qquad \text{(B7)}$$

Where,

$$B_{MX}^{\varphi} = \beta_{MX}^{(0)} + \beta_{MX}^{(1)}\exp(-\alpha I^{1/2}) \qquad \text{(B8)}$$

$$\beta_{MX}^{(0)} = 0.0765 - 777.03\left(\frac{1}{T} - \frac{1}{298.15}\right) - 4.4706 \times ln\left(\frac{T}{298.15}\right) + 0.008946(T - 298.15) -$$

$$3.3158 \times 10^{-6}(T^2 - 298.15^2) \qquad \text{(B9)}$$

$$\beta_{MX}^{(1)} = 0.2664 + 6.1608 \times 10^{-5}(T - 298.15) + 1.0715 \times 10^{-6}(T^2 - 298.15^2) \qquad \text{(B10)}$$

$$C_{MX}^{\varphi} = 0.00127 + 33.317\left(\frac{1}{T} - \frac{1}{298.15}\right) + 0.09421 \times ln\left(\frac{T}{298.15}\right) - 4.656 \times 10^{-5}(T - 298.15)$$

(B11)

$$f^{\varphi} = \frac{A_{\varphi}I^{1/2}}{1 + bI^{1/2}} \qquad \text{(B12)}$$

$$I = \frac{1}{2}\sum_i m_i z_i^2 \quad \text{(B13)}$$

$$\vartheta = \vartheta_M + \vartheta_X \quad \text{(B14)}$$

$$A_\varphi = \frac{1}{3}\left(\frac{e^2}{\epsilon_0 \epsilon_r RT}\right)^{3/2} \frac{N_A^2}{8\pi} (2\rho_{Fm})^{1/2} \quad \text{(B15)}$$

Using appropriate values (values for NaCl are provided in the excel spreadsheet) in Eqs. B7-15 for any solutes, osmotic pressure can be calculated using the following equation:

$$\pi = \vartheta RT\varphi^m \frac{M_w m}{v_{water}} \quad \text{(B16)}$$

B.2 Pressure Retarded Osmosis Mode

The solute flux can be related to the water flux and solute concentration similar to FO mode as shown below:

$$-J_{s.PRO} = -D_s \frac{dC}{dx} + J_{w.PRO} C = -B(C_{Dm} - C_i) \quad \text{(B17)}$$

Similarly, two solute mass balances in the feed and draw side boundary layer yields

$$-J_{s.PRO} = -D_{Fm} \frac{dC}{dx} + J_{w.PRO} C = -B(C_{Dm} - C_i) \quad \text{(B18)}$$

$$-J_{s.PRO} = -D_{Dm} \frac{dC}{dx} + J_{w.PRO} C = -B(C_{Dm} - C_i) \quad \text{(B19)}$$

Integration of equation B18 using the boundary conditions from table 3.1 yields:

$$\int_{-(t_a+t_s)}^{-(t_a+t_s+\delta_{t.f})} dx = \int_{C_{Fm}}^{C_{Fb}} \frac{dC}{\frac{J_{w.PRO}}{D_{Fm}} C + \frac{B}{D_{Fm}}(C_{Dm} - C_i)}$$

$$\Rightarrow \left[-\left(t_a + t_s + \delta_{t.f}\right) + (t_a + t_s)\right] = \frac{1}{\frac{J_{w.PRO}}{D_{Fm}}} \ln\left[\frac{C_{Fb}\frac{J_{w.PRO}}{D_{Fm}} + \frac{B}{D_{Fm}}(C_{Dm} - C_i)}{C_{Fm}\frac{J_{w.PRO}}{D_{Fm}} + \frac{B}{D_{Fm}}(C_{Dm} - C_i)}\right]$$

$$\Rightarrow \frac{C_{Fb}\frac{J_{w.PRO}}{D_{Fm}} + \frac{B}{D_{Fm}}(C_{Dm} - C_i)}{C_{Fm}\frac{J_{w.PRO}}{D_{Fm}} + \frac{B}{D_{Fm}}(C_{Dm} - C_i)} = exp^{-\frac{J_{w.PRO}\delta_{t.f}}{D_{Fm}}} = \frac{1}{exp\left(\frac{J_{w.PRO}}{k_{mt.f}}\right)}$$

$$\Rightarrow C_{Fm}\frac{J_{w.PRO}}{D_{Fm}} + \frac{B}{D_{Fm}}(C_{Dm} - C_i) = \left\{C_{Fb}\frac{J_{w.PRO}}{D_{Fm}} + \frac{B}{D_{Fm}}(C_{Dm} - C_i)\right\} exp\left(\frac{J_{w.PRO}}{k_{mt.f}}\right)$$

$$\Rightarrow \; C_{Fm}\frac{J_{w.PRO}}{D_{Fm}} = C_{Fb}\frac{J_{w.PRO}}{D_{Fm}}exp\left(\frac{J_{w.PRO}}{k_{mt.f}}\right) + \frac{B}{D_{Fm}}(C_{Dm} - C_i)exp\left(\frac{J_{w.PRO}}{k_{mt.f}}\right) - \frac{B}{D_{Fm}}(C_{Dm} - C_i)$$

$$\Rightarrow \; C_{Fm} = C_{Fb}exp\left(\frac{J_{w.PRO}}{k_{mt.f}}\right) + \frac{B}{J_{w.PRO}}(C_{Dm} - C_i)exp\left(\frac{J_{w.PRO}}{k_{mt.f}}\right) - \frac{B}{J_{w.PRO}}(C_{Dm} - C_i)$$

$$\Rightarrow \; C_{Fm} = C_{Fb}P_{\delta t.f} + \frac{B}{J_{w.PRO}}(C_{Dm} - C_i)\{P_{\delta t.f} - 1\} \qquad \text{(B20)}$$

From Eq. B17, we have,

$$-D_s\frac{dC}{dx} + J_{w.PRO}C = -B(C_{Dm} - C_i)$$

$$\Rightarrow \; \frac{dC}{dx} = \left\{\frac{J_{w.PRO}C + B(C_{Dm} - C_i)}{D_s}\right\}$$

$$\Rightarrow \; dx = D_s\left\{\frac{dC}{J_{w.PRO}C + B(C_{Dm} - C_i)}\right\} \qquad \text{(B21)}$$

Integrating Eq. B21 through the support layer thickness and using appropriate boundary condition from Table 3.1 we get:

$$\int_{-t_a}^{-(t_a+t_s)} dx = \int_{C_i}^{C_{Fm}} \left\{\frac{dC}{\frac{J_{w.PRO}}{D_s}C + \frac{B}{D_s}(C_{Dm} - C_i)}\right\}$$

$$\Rightarrow \; [-(t_a + t_s) + t_a] = \frac{1}{\frac{J_{w.PRO}}{D_s}}\ln\left[\frac{C_{Fm}\frac{J_{w.PRO}}{D_s} + \frac{B}{D_s}(C_{Dm} - C_i)}{C_i\frac{J_{w.PRO}}{D_s} + \frac{B}{D_s}(C_{Dm} - C_i)}\right]$$

$$\Rightarrow \; \frac{C_{Fm}\frac{J_{w.PRO}}{D_s} + \frac{B}{D_s}(C_{Dm} - C_i)}{C_i\frac{J_{w.PRO}}{D_s} + \frac{B}{D_s}(C_{Dm} - C_i)} = exp\left(-\frac{J_{w.PRO}t_s}{D_s}\right) \qquad \text{(using the relationship } \frac{D_s}{t_s} = \frac{D_i}{S}\text{)}$$

$$\Rightarrow \; C_i exp\left(-\frac{J_{w.PRO}t_s}{D_s}\right) + \frac{B}{J_{w.PRO}}(C_{Dm} - C_i)exp\left(-\frac{J_{w.PRO}t_s}{D_s}\right) = \left(C_{Fm} + \frac{B}{J_{w.PRO}}(C_{Dm} - C_i)\right)$$

$$\Rightarrow \; C_i P_{ts.PRO} + \frac{B}{J_{w.PRO}}(C_{Dm} - C_i)P_{ts.PRO} = C_{Fm} + \frac{B}{J_{w.PRO}}(C_{Dm} - C_i)$$

$$\Rightarrow \; C_i P_{ts.PRO} + \frac{B}{J_{w.PRO}}C_{Dm}P_{ts.PRO} - \frac{B}{J_{w.PRO}}C_i P_{ts.PRO} = C_{Fm} + \frac{B}{J_{w.PRO}}C_{Dm} - C_i\frac{B}{J_{w.PRO}}$$

$$\Rightarrow \quad C_i = \frac{\frac{B}{J_{w.PRO}} C_{Dm}(1-P_{ts.PRO}) + C_{Fm}}{\frac{B}{J_{w.PRO}} + P_{ts.PRO}\left(1-\frac{B}{J_{w.PRO}}\right)} \tag{B22}$$

From Eq. B19, we have,

$$-D_{Dm}\frac{dC}{dx} + J_{w.PRO}C = -B(C_{Dm} - C_i)$$

$$\Rightarrow \quad \frac{dC}{dx} = \left\{\frac{J_{w.PRO}C + B(C_{Dm}-C_i)}{D_{Dm}}\right\}$$

$$\Rightarrow \quad dx = D_{Dm}\left\{\frac{dC}{J_{w.PRO}C + B(C_{Dm}-C_i)}\right\} \tag{B23}$$

Integrating Eq. B23 through the support layer thickness and using appropriate boundary condition from Table 3.1 we get:

$$\int_0^{\delta_{t.d}} dx = \int_{C_{Dm}}^{C_{Db}} \left\{\frac{dC}{\frac{J_{w.PRO}}{D_{Dm}}C + B(C_{Dm} - C_i)}\right\}$$

$$\Rightarrow \quad [\delta_{t.d} - 0] = \frac{1}{\frac{J_{w.PRO}}{D_{Dm}}} \ln\left[\frac{C_{Db}\frac{J_{w.PRO}}{D_{Dm}} + \frac{B}{D_{Dm}}(C_{Dm}-C_i)}{C_{Dm}\frac{J_{w.PRO}}{D_{Dm}} + \frac{B}{D_{Dm}}(C_{Dm}-C_i)}\right]$$

$$\Rightarrow \quad \frac{C_{Db}\frac{J_{w.PRO}}{D_{Dm}} + \frac{B}{D_{Dm}}(C_{Dm}-C_i)}{C_{Dm}\frac{J_{w.PRO}}{D_{Dm}} + \frac{B}{D_{Dm}}(C_{Dm}-C_i)} = exp\left(\frac{J_{w.PRO}\delta_{t.d}}{D_{Dm}}\right) = exp\left(\frac{J_{w.PRO}}{k_{mt.d}}\right) = \frac{1}{exp\left(-\frac{J_{w.PRO}}{k_{mt.d}}\right)}$$

$$\Rightarrow \quad C_{Dm}\frac{J_{w.PRO}}{D_{Dm}} + \frac{B}{D_{Dm}}(C_{Dm} - C_i) = \left(C_{Db}\frac{J_{w.PRO}}{D_{Dm}} + \frac{B}{D_{Dm}}(C_{Dm} - C_i)\right) exp\left(-\frac{J_{w.PRO}}{k_{mt.d}}\right)$$

$$\Rightarrow \quad C_{Dm}\frac{J_{w.PRO}}{D_{Dm}} = C_{Db}\frac{J_{w.PRO}}{D_{Dm}} exp\left(-\frac{J_{w.PRO}}{k_{mt.d}}\right) + \frac{B}{D_{Dm}}(C_{Dm} - C_i) exp\left(-\frac{J_{w.PRO}}{k_{mt.d}}\right) - \frac{B}{D_{Dm}}(C_{Dm} - C_i)$$

$$\Rightarrow \quad C_{Dm} = C_{Db} exp\left(-\frac{J_{w.PRO}}{k_{mt.d}}\right) + \frac{B}{J_{w.PRO}}(C_{Dm} - C_i) exp\left(-\frac{J_{w.PRO}}{k_{mt.d}}\right) - \frac{B}{J_{w.PRO}}(C_{Dm} - C_i)$$

$$\Rightarrow \quad C_{Dm} = C_{Db}P_{\delta t.d} + \frac{B}{J_w}(C_{Dm} - C_i)(P_{\delta t.d} - 1) \tag{B24}$$

Eq. B20, B22 and B24 presents the three equations for the modeling of C_{Fm}, C_i and C_{Dm} in PRO mode.

Appendix C: Modeling membrane intrinsic properties

Membrane intrinsic properties include pure water permeance (denoted as A) and solute permeability coefficient (denoted as B). These intrinsic properties have dependence on temperature. To model this, empirical relationships were developed for the particular membrane used. Using a bench scale RO system, both A, and B were evaluated at temperatures of 20 °C, 30 °C, and 40 °C. These tests were done in triplicates. Once the values of A and B were found, using a linear regression we developed relationships between the intrinsic properties and temperature for FO and PRO mode, and for the two models as shown below:

$$A_{HTMT} = 0.013 * T_i - 3.309 \quad \text{(C1)}$$

$$B_{HTMT} = 0.005 * T_i - 1.225 \quad \text{(C2)}$$

$$A_{MT} = 0.013 * (T_{Fb} + T_{Db})/2 - 3.309 \quad \text{(C3)}$$

$$B_{MT} = 0.005 * (T_{Fb} + T_{Db})/2 - 1.225 \quad \text{(C4)}$$

Appendix D: Modeling solution properties [63]

NaCl diffusivity was first taken from Lobo et al [101] for different temperatures and at different concentration. The tabulated data were fitted to a fifth order polynomial as shown in Eq. D1 with a 98.5% confidence. The unit for diffusivity used is $m^2 s^{-1}$ and the equation is as follows:

$$D = (0.000182327 \times C^5 - 0.0017212 \times C^4 - 0.0014178 \times C^3 + 0.0497 \times C^2 - 0.0987016 \times C + 1.0263) * 0.0000000093223 \times e^{(-\frac{2630000000}{T^{3.7}})} \quad \text{(D1)}$$

Martin et al [121] tabulated data for thermal conductivity of sodium chloride solution at different temperatures. This dataset was fitted to a linear equation with a 100% confidence. The fitted equation for thermal conductivity has units of $W m^{-1} K^{-1}$ and is given below.

$$\lambda_{water} = 0.0013377 \times T + 0.2165 \quad \text{(D2)}$$

Both viscosity and density for the NaCl solution at different concentration and temperature was collected from Comesana et.al. [102]. The viscosity and density data was fitted to two exponential variable for the bulk concentration and temperature with 99.7% confidence. The unit of viscosity used was Pa.s and the unit of density was $Kg m^{-3}$.

$$\mu = 0.4599 \times e^{(0.10495 \times C)} \times e^{(-0.021 \times T)} \quad \text{(D3)}$$

$$\rho = (-1.55 \times C^2 + 45.5 \times C + 1123.3) \times e^{(-0.0004 \times T)} \quad \text{(D4)}$$

Similarly, heat capacity data for pure water was taken from Brown et.al. [122]. It was, then, fitted to a fourth order polynomial of the bulk temperature with a 99.73% confidence. The unit for the heat capacity data was $J Kg^{-1} K^{-1}$. The following equation represent the heat capacity for pure water.

$$c_P = 0.000002 \times T^4 - 0.0028 \times T^3 + 1.449 \times T^2 - 336.87 \times T + 33520 \qquad \text{(D5)}$$

For Model HTMT, these properties are evaluated at their nearest boundary concentration and temperature values. For Model MT, these properties are evaluated at the average bulk temperatures of feed and draw.

Appendix E: Model algorithm

The coupled model uses information from the heat transfer and mass transfer equations to predict the flux at different temperature of the feed and draw solution. The thickness of the active and support layer was taken from cross-sectional images of a scanning electron microscope image of the HTI CTA membrane. The thermal conductivity of the polymer was taken from literature [123] and the porosity was measured to be as 59% according to [124].

Crucial to the modeling of mass transfer is the determination of the S parameter. To determine the structural parameter for FO and PRO mode, Eqs. 3.18-3.27 were utilized at a system temperature of 20 °C without any temperature gradient. At first, the experimental water flux found for FO mode was used and the S parameter was varied until all the constraints were satisfied as shown in Fig. 3.4. The model iterates as long as the difference between the predicted and the experimental value becomes zero while changing the structural parameter S. This was repeated to find the PRO mode structural parameter using water flux at 20 °C without temperature gradient in PRO mode. When the structural parameter was found for 20-20 case, the two models were then utilized to find water and solute flux at different conditions following the flowchart shown in Fig. 3.4.

Appendix F: Sample Microsoft VB code (FO mode HTMT)

```
Sub Find_All()
Dim TempHigh As Double
Dim TempLow As Double
Dim WaterFlux As Double
Dim SoluteFlux As Double
TempHigh = InputBox("Highest temperature for simulation")
TempLow = InputBox("Lowest temperature for simulation")
WaterFlux = InputBox("Water Flux at the lowest temperature")
' Set initial values for temperature and flux to calculate structural parameter
Range("c16").Value = TempLow                                    'Feed Temperature
Range("c17").Value = TempLow                                    'Draw Temperature
' Find structural parameter
SolverAdd CellRef:="$k3$", Relation:=2, FormulaText:="0"         'No change required here
SolverAdd CellRef:="$k5$", Relation:=2, FormulaText:="0"
SolverAdd CellRef:="$k7$", Relation:=2, FormulaText:="0"
SolverAdd CellRef:="$m3$", Relation:=2, FormulaText:="0"
SolverAdd CellRef:="$m5$", Relation:=2, FormulaText:="0"
SolverAdd CellRef:="$m7$", Relation:=2, FormulaText:="0"
```

```
SolverAdd CellRef:="$k9$", Relation:=2, FormulaText:="0"
SolverOptions AssumeNonNeg:=0
SolverOk SetCell:="$K$9", MaxMinVal:=3, ValueOf:=0, ByChange:="$F$5:$F$10,$c$2", _
Engine:=1, EngineDesc:="GRG Nonlinear"
SolverSolve True

'20-20

Range("F11").Select                                    'Copy Water Flux data for storage
Selection.Copy
Range("G16").Select
Selection.PasteSpecial Paste:=xlPasteValues, Operation:=xlNone, SkipBlanks _
        :=False, Transpose:=False
Range("F12").Select                                    'Copy Solute Flux data for storage
Application.CutCopyMode = False
Selection.Copy
Range("H16").Select
Selection.PasteSpecial Paste:=xlPasteValues, Operation:=xlNone, SkipBlanks _
        :=False, Transpose:=False

' This section will run the macro for heated feed condition
Range("C16").Value = TempHigh                          'Feed Temperature
Range("C17").Value = TempLow                           'Draw Temperature
```

```
SolverAdd CellRef:="$k3$", Relation:=2, FormulaText:="0"                'No change required here
SolverAdd CellRef:="$k5$", Relation:=2, FormulaText:="0"
SolverAdd CellRef:="$k7$", Relation:=2, FormulaText:="0"
SolverAdd CellRef:="$m3$", Relation:=2, FormulaText:="0"
SolverAdd CellRef:="$m5$", Relation:=2, FormulaText:="0"
SolverAdd CellRef:="$m7$", Relation:=2, FormulaText:="0"
SolverAdd CellRef:="$k9$", Relation:=2, FormulaText:="0"
SolverOptions AssumeNonNeg:=0
SolverOk SetCell:="$K$9", MaxMinVal:=3, ValueOf:=0, ByChange:="$F$5:$F$11", _
Engine:=1, EngineDesc:="GRG Nonlinear"
SolverSolve True
Range("F11").Select                                    'Copy Water Flux data for storage
Selection.Copy
Range("G18").Select
Selection.PasteSpecial Paste:=xlPasteValues, Operation:=xlNone, SkipBlanks _
        :=False, Transpose:=False
Range("F12").Select                                     'Copy Solute Flux data for storage
Application.CutCopyMode = False
Selection.Copy
Range("H18").Select
Selection.PasteSpecial Paste:=xlPasteValues, Operation:=xlNone, SkipBlanks _
        :=False, Transpose:=False
```

' This section will run the macro for isothermal hot condition

```
Range("C16").Value = TempHigh                                    'Feed Temperature"
Range("C17").Value = TempHigh                                    'Draw Temperature"
SolverAdd CellRef:="$k3$", Relation:=2, FormulaText:="0"          'No change required here
SolverAdd CellRef:="$k5$", Relation:=2, FormulaText:="0"
SolverAdd CellRef:="$k7$", Relation:=2, FormulaText:="0"
SolverAdd CellRef:="$m3$", Relation:=2, FormulaText:="0"
SolverAdd CellRef:="$m5$", Relation:=2, FormulaText:="0"
SolverAdd CellRef:="$m7$", Relation:=2, FormulaText:="0"
SolverAdd CellRef:="$k9$", Relation:=2, FormulaText:="0"
SolverOptions AssumeNonNeg:=0
SolverOk SetCell:="$K$9", MaxMinVal:=3, ValueOf:=0, ByChange:="$F$5:$F$11", _
Engine:=1, EngineDesc:="GRG Nonlinear"
SolverSolve True
Range("F11").Select                                    'Copy Water Flux data for storage
Selection.Copy
Range("G19").Select
Selection.PasteSpecial Paste:=xlPasteValues, Operation:=xlNone, SkipBlanks _
        :=False, Transpose:=False
Range("F12").Select                                     'Copy Solute Flux data for storage
Application.CutCopyMode = False
Selection.Copy
Range("H19").Select
```

```
Selection.PasteSpecial Paste:=xlPasteValues, Operation:=xlNone, SkipBlanks _
        :=False, Transpose:=False


   ' This section will run the macro for heated draw condition
Range("C16").Value = TempLow                                    'Feed Temperature
Range("C17").Value = TempHigh                                   'Draw Temperature
' This sets the model to account for reverse direction of water flux.
Range("Y15").Select
ActiveCell.FormulaR1C1 = _
        "=(kp/ta*(1-ea)-Jwlnew/1000/3600*pDi*CpDi-kwDi*ea/ta)*Ac"
If Range("y15").Value <= 0 Then ActiveCell.FormulaR1C1 = "=((kp/ta*(1-ea)-
Jwlnew/1000/3600*pDi*CpDi-kwDi*ea/ta)*Ac)"
Range("Z15").Select
ActiveCell.FormulaR1C1 = _
        "=(kp/ts*(1-es)-Jwlnew/1000/3600*pDi*CpDi-kwDi*es/ts)*Ac"
If Range("y15").Value <= 0 Then ActiveCell.FormulaR1C1 = "=((kp/ts*(1-es)-
Jwlnew/1000/3600*pDi*CpDi-kwDi*es/ts)*Ac)"
Range("Y11").Select
ActiveCell.FormulaR1C1 = "=(hF-Jwlnew/1000/3600*pFm*CpFm-kwFm/dtf)*Ac"
If Range("y15").Value <= 0 Then ActiveCell.FormulaR1C1 = "=((hF-
Jwlnew/1000/3600*pFm*CpFm-kwFm/dtf)*Ac)"
Range("Y13").Select
ActiveCell.FormulaR1C1 = "=(hD-Jwlnew/1000/3600*pDm*CpDm-kwDm/dtd)*Ac"
```

```
If Range("y15").Value <= 0 Then ActiveCell.FormulaR1C1 = "=((hD-
Jwlnew/1000/3600*pDm*CpDm-kwDm/dtd)*Ac)"

'Solver
SolverAdd CellRef:="$k3$", Relation:=2, FormulaText:="0"          'No change required here
SolverAdd CellRef:="$k5$", Relation:=2, FormulaText:="0"
SolverAdd CellRef:="$k7$", Relation:=2, FormulaText:="0"
SolverAdd CellRef:="$m3$", Relation:=2, FormulaText:="0"
SolverAdd CellRef:="$m5$", Relation:=2, FormulaText:="0"
SolverAdd CellRef:="$m7$", Relation:=2, FormulaText:="0"
SolverAdd CellRef:="$k9$", Relation:=2, FormulaText:="0"
SolverOptions AssumeNonNeg:=0
SolverOk SetCell:="$K$9", MaxMinVal:=3, ValueOf:=0, ByChange:="$F$5:$F$11", _
Engine:=1, EngineDesc:="GRG Nonlinear"
SolverSolve True
Range("F11").Select                          'Copy Water Flux data for storage
Selection.Copy
Range("G17").Select
Selection.PasteSpecial Paste:=xlPasteValues, Operation:=xlNone, SkipBlanks _
    :=False, Transpose:=False
Range("F12").Select                          'Copy Solute Flux data for storage
Application.CutCopyMode = False
Selection.Copy
```

```
Range("H17").Select
Selection.PasteSpecial Paste:=xlPasteValues, Operation:=xlNone, SkipBlanks _
        :=False, Transpose:=False
'Reset System to Isothermal low
Range("c16").Value = TempLow
Range("C17").Value = TempLow
' This resets the model to original format.
Range("Y15").Select
ActiveCell.FormulaR1C1 = _
        "=(kp/ta*(1-ea)+Jwlnew/1000/3600*pDi*CpDi+kwDi*ea/ta)*Ac"
Range("Z15").Select
ActiveCell.FormulaR1C1 = _
        "=(kp/ts*(1-es)+Jwlnew/1000/3600*pDi*CpDi+kwDi*es/ts)*Ac"
Range("Y11").Select
ActiveCell.FormulaR1C1 = "=(hF+Jwlnew/1000/3600*pFm*CpFm+kwFm/dtf)*Ac"
Range("Y13").Select
ActiveCell.FormulaR1C1 = "=(hD+Jwlnew/1000/3600*pDm*CpDm+kwDm/dtd)*Ac"
SolverAdd CellRef:="$k3$", Relation:=2, FormulaText:="0"
SolverAdd CellRef:="$k5$", Relation:=2, FormulaText:="0"
SolverAdd CellRef:="$k7$", Relation:=2, FormulaText:="0"
SolverAdd CellRef:="$m3$", Relation:=2, FormulaText:="0"
SolverAdd CellRef:="$m5$", Relation:=2, FormulaText:="0"
SolverAdd CellRef:="$m7$", Relation:=2, FormulaText:="0"
```

```
SolverAdd CellRef:="$k9$", Relation:=2, FormulaText:="0"

SolverOptions AssumeNonNeg:=0

SolverOk SetCell:="$K$9", MaxMinVal:=3, ValueOf:=0, ByChange:="$F$5:$F$11", _

Engine:=1, EngineDesc:="GRG Nonlinear"

SolverSolve True

End Sub
```

Appendix G: Model sensitivity analysis

Sensitivity analysis was performed for six different input parameters and on two different model equations. The parameters include dense selective layer thickness (t_a), porous support layer thickness (t_s), hydraulic diameter (d_h), selective layer porosity (ε_a), support layer porosity (ε_s), thermal conductivity of the polymer ($\lambda_{polymer}$), structural parameter (S), and fluid velocity in the channel (v). These parameters were varied ± 30 % from the base case which was used in the model for comparison with observed data. Exception to these were the case for t_a and ε_a. While t_a was varied on an order of magnitude scale, ε_a was varied on a 0.05 increment. Each of these parameters was changed in the model at a time while the remaining parameters were at the value of the base case. In each case, the structural parameter was adjusted to predict the 20-20 case experimental data except when the sensitivity of S was evaluated. The result of this analysis is presented in Figs. G1- G4. Five of these parameters that include t_a, d_h, ε_a, λ_p, and v does not affect the model performance significantly. Except for t_a and ε_a, all parameter values were varied in the range of ± 30 % from the base case (defined as the values used in Model HTMT in Figs. 3.7 and 3.8). From Figs. G1- G4, it is clear that the model prediction does not vary significantly for any of these parameters except for S, ε_s, and t_s. The water and solute flux for FO and PRO mode changes linearly with structural parameter. As both ε_s and t_s are incorporated into S, and as S is a fitted parameter and it largely depends on J_w, A, and B, the linear relationship suggests that there is no influence of temperature on this parameter in predicting water and solute flux under a temperature

gradient. This is consistent with early studies on structure parameter and its usefulness in predicting membrane performance at different system conditions [21].

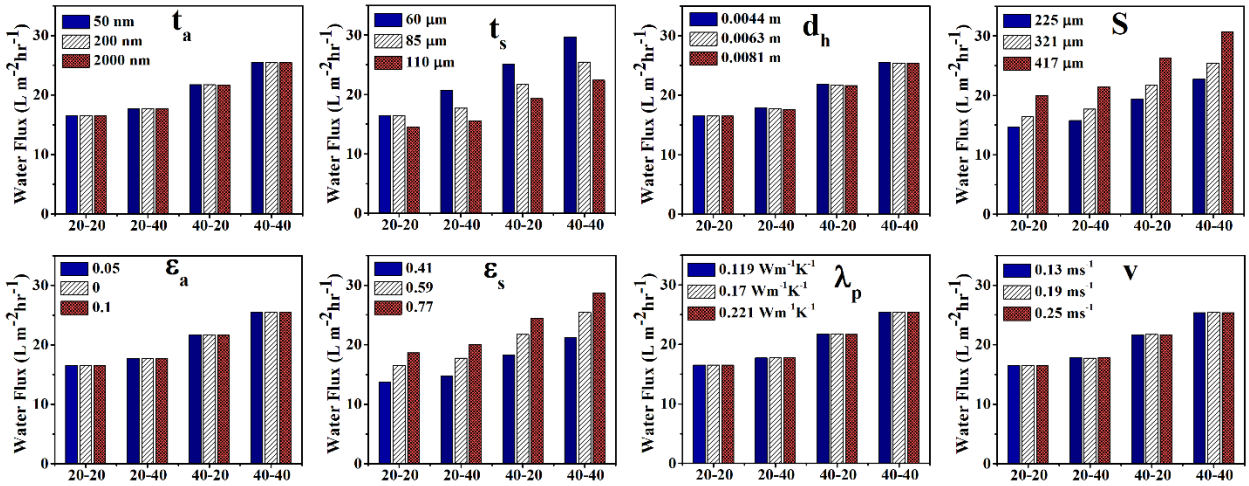

Figure G1: Sensitivity analysis of Model HTMT in predicting FO mode water flux. Each parameter was varied ± 30% from base case shown in neutral color (white) except for t_a (varied on an order of magnitude scale) and ε_a (varied on a 0.05 increment).

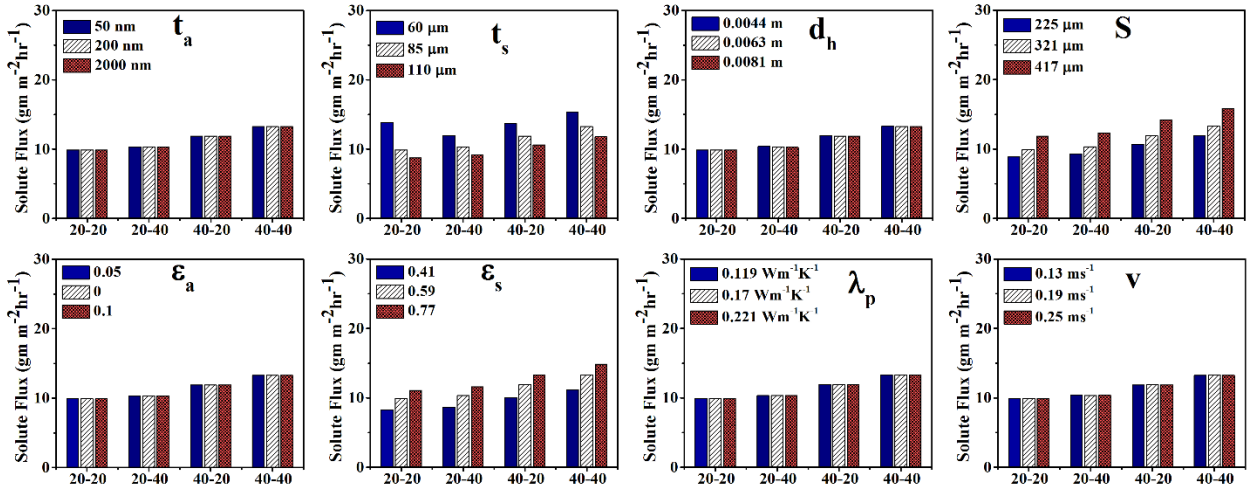

Figure G2: Sensitivity analysis of Model HTMT in predicting FO mode solute flux. Each parameter was varied ± 30% from base value shown in neutral color (white) except for t_a (varied on an order of magnitude scale) and ε_a (varied on a 0.05 increment).

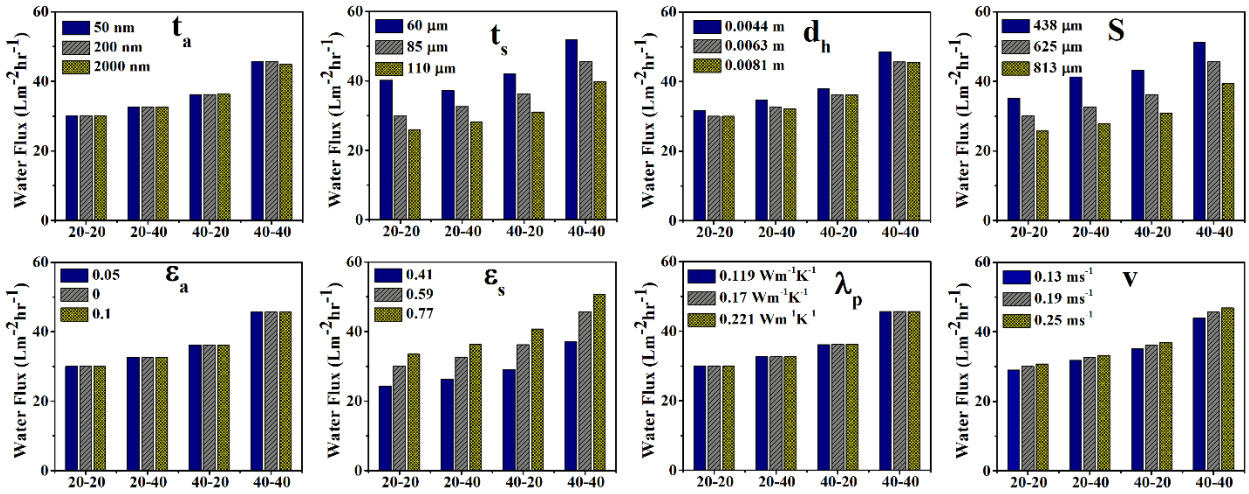

Figure G3: Sensitivity analysis of Model HTMT in predicting PRO mode water flux. Each parameter was varied ± 30% from base value shown in gray color except for t_a (varied on an order of magnitude scale) and ε_a (varied on a 0.05 increment).

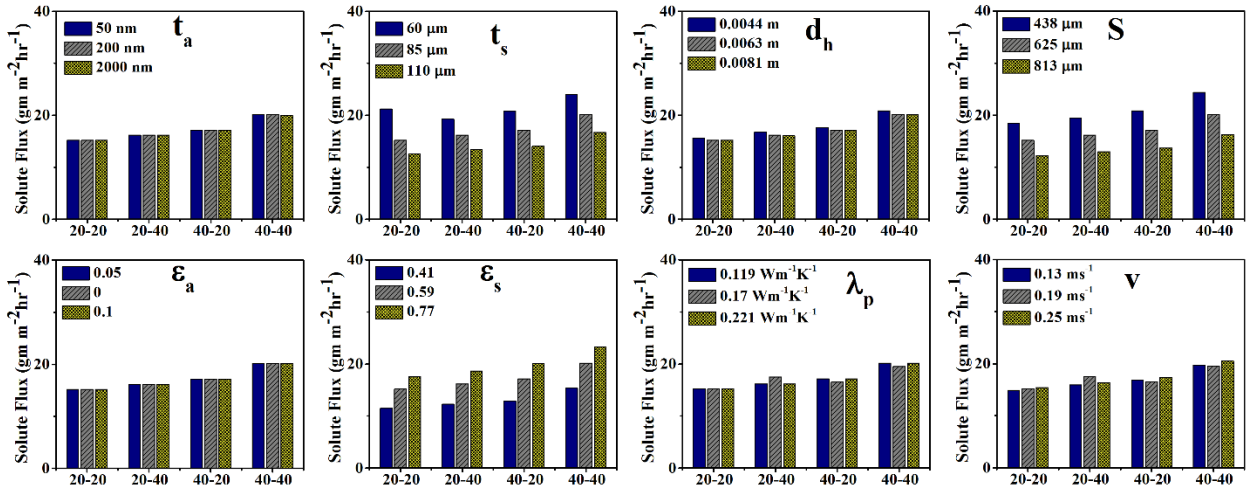

Figure G4: Sensitivity analysis of Model HTMT in predicting PRO mode solute flux. Each parameter was varied ± 30 % from base value shown in gray color except for t_a (varied on an order of magnitude scale) and ε_a (varied on a 0.05 increment).

Appendix H: Dead-end model development

From Eq. 2.1, we have,

$$-D_s\frac{dC}{dy}+J_wC=-B(C_i-C_{Fm})$$

$$\Rightarrow \ \frac{dC}{dy}=\left\{\frac{J_wC+B(C_i-C_{Fm})}{D_s}\right\}$$

$$\Rightarrow \ dy=D_s\left\{\frac{dC}{J_wC+B(C_i-C_{Fm})}\right\} \qquad \text{(H1)}$$

Integrating Eq. H1 through the support layer thickness and using appropriate boundary condition from Table H1 we get:

$$\int_{t_a}^{t_a+t_s}dy=\int_{C_i}^{C_{Dm}}D_s\left\{\frac{dC}{J_wC+B(C_i-C_{Fm})}\right\}$$

$$\Rightarrow \ [t_a+t_s-t_a]=\frac{1}{\frac{J_w}{D_s}}\ln\left[\frac{C_{Dm}\frac{J_w}{D_i}+\frac{B}{D_i}(C_i-C_{Fm})}{C_i\frac{J_w}{D_i}+\frac{B}{D_i}(C_i-C_{Fm})}\right]$$

$$\Rightarrow \ \frac{C_{Dm}\frac{J_w}{D_i}+\frac{B}{D_i}(C_i-C_{Fm})}{C_i\frac{J_w}{D_i}+\frac{B}{D_i}(C_i-C_{Fm})}=exp\left(\frac{J_wt_s}{D_s}\right)$$

$$\Rightarrow \ C_{Dm}\frac{J_w}{D_i}+\frac{B}{D_i}(C_i-C_{Fm})=\left\{C_i\frac{J_w}{D_i}+\frac{B}{D_i}(C_i-C_{Fm})\right\}exp\left(\frac{J_wS}{D_i}\right)$$

$$\Rightarrow \ C_{Dm}\frac{J_w}{D_i}+\frac{B}{D_i}C_i-\frac{B}{D_i}C_{Fm}=C_i\frac{J_w}{D_i}exp\left(\frac{J_wS}{D_i}\right)+\frac{B}{D_i}C_iexp\left(\frac{J_wS}{D_i}\right)-\frac{B}{D_i}C_{Fm}exp\left(\frac{J_wS}{D_i}\right)$$

$$\Rightarrow \ \frac{B}{D_i}C_i\left(1-\frac{J_w}{B}exp\left(\frac{J_wS}{D_i}\right)-exp\left(\frac{J_wS}{D_i}\right)\right)=\frac{B}{D_i}C_{Fm}-C_{Dm}\frac{J_w}{D_i}-\frac{B}{D_i}C_{Fm}exp\left(\frac{J_wS}{D_i}\right)$$

$$\Rightarrow \ C_i=\frac{\frac{B}{D_i}C_{Fm}-C_{Dm}\frac{J_w}{D_i}-\frac{B}{D_i}C_{Fm}exp\left(\frac{J_wS}{D_i}\right)}{\frac{B}{D_i}\left(1-\frac{J_w}{B}exp\left(\frac{J_wS}{D_i}\right)-exp\left(\frac{J_wS}{D_i}\right)\right)}$$

$$\Rightarrow \quad C_i = \frac{\frac{B}{D_i}\left(C_{Fm} - \frac{J_w}{B}C_{Dm} - C_{Fm}exp\left(\frac{J_w S}{D_i}\right)\right)}{\frac{B}{D_i}\left(1 - \frac{J_w}{B}exp\left(\frac{J_w S}{D_i}\right) - exp\left(\frac{J_w S}{D_i}\right)\right)}$$

$$\Rightarrow \quad C_i = \frac{C_{Fm}\left(1 - exp\left(\frac{J_w S}{D_i}\right)\right) - \frac{J_w}{B}C_{Dm}}{1 - exp\left(\frac{J_w S}{D_i}\right)\left(\frac{J_w}{B} + 1\right)} \qquad \text{(H2)}$$

From Eq. 2.3, we have,

$$-D_{Db}\frac{dC}{dy} + J_w C = -B(C_i - C_{Fm})$$

$$\Rightarrow \quad \frac{dC}{dy} = \left\{\frac{J_w C + B(C_i - C_{Fm})}{D_{Db}}\right\}$$

$$\Rightarrow \quad dy = D_{Db}\left\{\frac{dC}{J_w C + B(C_i - C_{Fm})}\right\} \qquad \text{(H3)}$$

Integrating Eq. H3 through the support layer thickness and using appropriate boundary condition from Table H1 we get:

$$\int_{t_a + t_s}^{t_a + t_s + \delta_{td}} dy = \int_{C_{Dm}}^{C_{Db}} D_{Db}\left\{\frac{dC}{J_w C + B(C_i - C_{Fm})}\right\}$$

$$\Rightarrow \quad [t_a + t_s + \delta_{td} - t_a - t_s] = \frac{1}{\frac{J_w}{D_{Db}}}\ln\left[\frac{C_{Db}\frac{J_w}{D_i} + \frac{B}{D_i}(C_i - C_{Fm})}{C_{Dm}\frac{J_w}{D_i} + \frac{B}{D_i}(C_i - C_{Fm})}\right]$$

$$\Rightarrow \quad \frac{C_{Db}\frac{J_w}{D_i} + \frac{B}{D_i}(C_i - C_{Fm})}{C_{Dm}\frac{J_w}{D_i} + \frac{B}{D_i}(C_i - C_{Fm})} = exp\left(\frac{J_w \delta_{td}}{D_{Db}}\right) = exp\left(\frac{J_w}{k_{mtd}}\right) = \frac{1}{exp\left(-\frac{J_w}{k_{mtd}}\right)}$$

$$\Rightarrow \quad C_{Dm}\frac{J_w}{D_i} + \frac{B}{D_i}(C_i - C_{Fm}) = C_{Db}\frac{J_w}{D_i} + \frac{B}{D_i}(C_i - C_{Fm})exp\left(-\frac{J_w}{k_{mtd}}\right)$$

$$\Rightarrow \quad C_{Dm}\frac{J_w}{D_i} = C_{Db}\frac{J_w}{D_i} + \frac{B}{D_i}(C_i - C_{Fm})exp\left(-\frac{J_w}{k_{mtd}}\right) - \frac{B}{D_i}(C_i - C_{Fm})$$

$$\Rightarrow \quad C_{Dm} = C_{Db} + \frac{B}{J_w}(C_i - C_{Fm})exp\left(-\frac{J_w}{k_{mtd}}\right) - (C_i - C_{Fm})$$

$$\Rightarrow \quad C_{Dm} = C_{Db} + (C_i - C_{Fm})\left(\frac{B}{J_w}exp\left(-\frac{J_w}{k_{mtd}}\right) - 1\right) \qquad \text{(H4)}$$

To calculate osmotic pressure, unlike many current mass transfer models that rely on the Van't Hoff equation [99], we used Pitzer correlations for finding osmotic coefficients [99,100]. The correlations are as follows:

$$\varphi_m - 1 = |z_+ z_-| f^{\varphi} + m\left(\frac{2\vartheta_+\vartheta_-}{\vartheta}\right) B_{MX}^{\varphi} + m^2\left(\frac{2(\vartheta_+\vartheta_-)^{3/2}}{\vartheta}\right) C_{MX}^{\varphi} \quad \text{(H5)}$$

Where,

$$B_{MX}^{\varphi} = \beta_{MX}^{(0)} + \beta_{MX}^{(1)}\exp(-\alpha I^{1/2}), \qquad \beta_{MX}^{(0)} = 0.0765 - 777.03\left(\frac{1}{T} - \frac{1}{298.15}\right) - 4.4706 \times ln\left(\frac{T}{298.15}\right) + 0.008946(T - 298.15) - 3.3158 \times 10^{-6}(T^2 - 298.15^2), \qquad \beta_{MX}^{(1)} = 0.2664 + 6.1608 \times 10^{-5}(T - 298.15) + 1.0715 \times 10^{-6}(T^2 - 298.15^2), C_{MX}^{\varphi} = 0.00127 + 33.317\left(\frac{1}{T} - \frac{1}{298.15}\right) + 0.09421 \times ln\left(\frac{T}{298.15}\right) - 4.656 \times 10^{-5}(T - 298.15), \quad A_{\varphi} = \frac{1}{3}\left(\frac{e^2}{\epsilon_0 \epsilon_r RT}\right)^{3/2} \frac{N_A^2}{8\pi}(2d_s)^{1/2},$$

$$f^{\varphi} = \frac{A_{\varphi} I^{1/2}}{1 + bI^{1/2}}, I = \frac{1}{2}\sum_i m_i z_i^2, \vartheta = \vartheta_M + \vartheta_X,$$

$$\pi = \vartheta RT\varphi^m \frac{M_w m}{v_{water}} \quad \text{(H6)}$$

Using Eq. H2, H4 and 2.4, the interface concentration can be calculated which are then used in Eq. H6 to calculate osmotic pressure. Finally, water flux and reverse salt flux can be evaluated using the following two equations and the concentration values from Eq. H2, H4 and 2.4 [19,29,98].

$$J_w = A(\pi_i - \pi_{Fm}) \quad \text{(H7)}$$

$$J_s = B(C_i - C_{Fm}) \quad \text{(H8)}$$

Table H1
Concentration boundary conditions for the mass transfer model for FO mode of operation. Positions are marked in Fig. 2.2.

Position in y-direction	Concentration, C (mol/L)
$-\delta_{tf}$	C_{Fb}

0	C_{Fm}
t_a	C_i
t_a+t_s	C_{Dm}
$t_a+t_s+\delta_{td}$	C_{Db}

To reflect changes in volume in the feed and draw solution on concentration, solution properties and effective driving force, we further extended this analysis. Assuming a starting feed and draw volume of $V_{Feed\_n=0}$ and $V_{Draw\_n=0}$ respectively, the following information for n number of time steps was calculated.

Table H2
Calculation of feed and draw concentration for n steps

Variable description		Equation
Volume of feed that remains in the dead-end cell at time step n	V_{Feed_n}	--
Volume of draw that remains in the cross-flow side at time step n	V_{Draw_n}	--
Volume of water that passes through the membrane to the draw side at time step n,	V_{w_n}	$J_{w_n} \times A_c \times time$
Mass of salt that passes through the membrane to the feed side at time step n,	M_{Salt_n}	$J_{s_n} \times A_c \times time$
New bulk feed concentration at time step n+1,	$C_{Fb_{n+1}}$	$\frac{\left(V_{Feed_n} C_{Fb_n} + \frac{M_{Salt_n}}{58.44}\right)}{\left(V_{Feed_n}\rho_{F_n} + M_{Salt_n} - V_{w_n}\rho_{F_n}\right)/\rho_{F_n}}$
New bulk draw concentration at time step n+1,	$C_{Db_{n+1}}$	$\frac{\left(V_{Draw_n} C_{Db_n} - \frac{M_{Salt_n}}{58.44}\right)}{\left(V_{Draw_n}\rho_{D_n} - M_{Salt_n} + V_{w_n}\rho_{D_n}\right)/\rho_{D_n}}$

The calculated bulk feed and draw concentration is used as the new C_{Fb} and C_{Db} for n+1 step to find water flux and solute flux. At each iteration within each time step, the model results in new C_{Fm}, C_i and C_{Dm} which are used to recalculate solution properties and the concentrations are re-evaluated until no change in values is observed. To calculate the Reynolds number in the feed side two approach were taken. At first, assuming a cross-flow velocity and hydraulic diameter

similar to the cross-flow side, the Reynolds number was calculated. In the second instance, Reynolds number for the impeller was calculated using the following equation [104]:

$$Re = \frac{D_{Impeller}^2 N_{Impeller} \rho_{Fm}}{\mu_{Fm}} \quad \text{(H9)}$$

Solution Properties

Diffusivity of sodium chloride solution at different temperature and concentration was taken from Lobo [101]. The data was fitted against a fifth order polynomial for the change in concentration and an exponential for the change in temperature with 98.5 % confidence. The bulk concentration and temperature was taken as the fitted variables. The final equation for diffusivity in m^2s^{-1} is as follows.

$$D_b = (0.000182327 \times {C_b}^5 - 0.0017212 \times {C_b}^4 - 0.0014178 \times {C_b}^3 + 0.0497 \times {C_b}^2 - 0.0987016 \times C_b + 1.0263) * 0.0000000093223 \times e^{(-\frac{2630000000}{{T_b}^{3.7}})} \quad \text{(H10)}$$

Thermal conductivity of sodium chloride solution at different temperature was taken as the thermal conductivity of water at different temperature from Martin [121]. A linear equation was fitted to the data with the bulk temperature as the variable with 100% confidence. The fitted equation for thermal conductivity has units of $Wm^{-1}K^{-1}$ and is given below.

$$kw_b = 0.0013377 \times T_b + 0.2165 \quad \text{(H11)}$$

Viscosity and density data was collected from Comesana et.al. [102]. The viscosity and density data was fitted to two exponential variable for the bulk concentration and temperature with 99.71% confidence. The unit of viscosity used was Pa.s and the unit of density was Kgm^{-3}.

$$\mu_b = 0.4599 \times e^{(0.10495 \times C_b)} \times e^{(-0.021 \times T_b)} \quad \text{(H12)}$$

$$\rho_b = (-1.55 \times {C_b}^2 + 45.5 \times C_b + 1123.3) \times e^{(-0.0004 \times T_b)} \quad \text{(H13)}$$

Heat capacity data for pure water was taken from Brown et.al. [122]. The data was fitted to a fourth order polynomial of the bulk temperature with a 99.73% confidence. The unit for the heat capacity data was $JKg^{-1}K^{-1}$. The following equation represent the heat capacity for pure water.

$$Cp_b = 0.000002 \times {T_b}^4 - 0.0028 \times {T_b}^3 + 1.449 \times {T_b}^2 - 336.87 \times T_b + 33520 \quad \text{(H14)}$$

Flow Chart

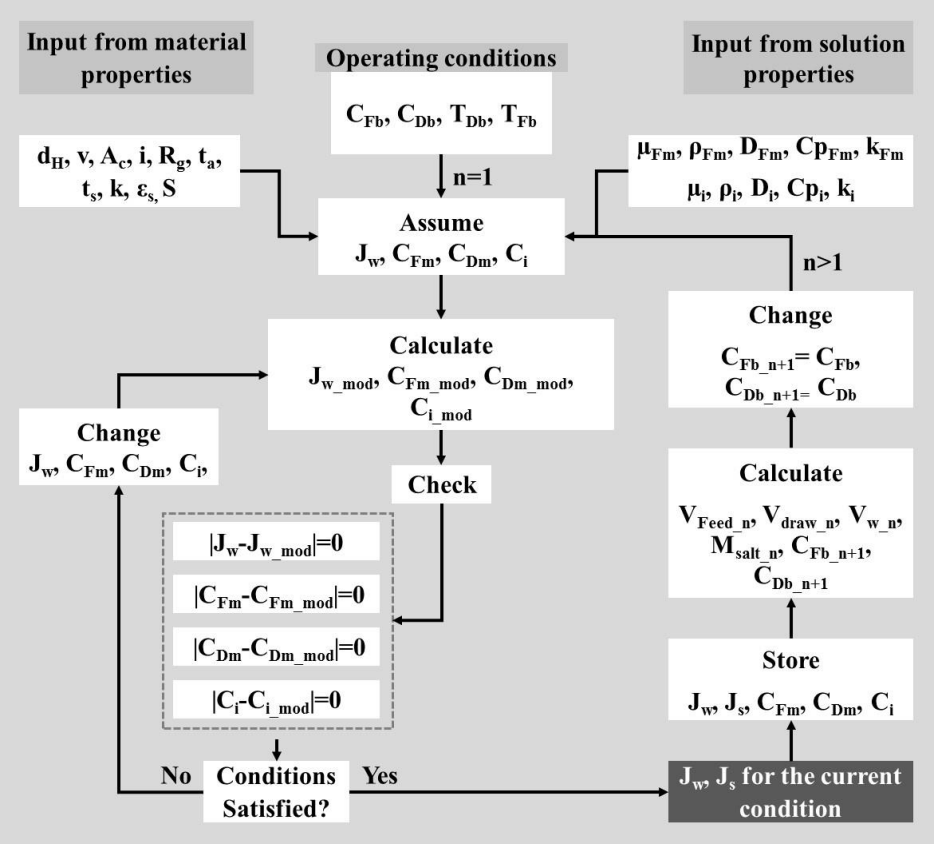

Fig. H1: Flow chart for the calculation of water and solute fluxes, feed and draw concentrations.

Nomenclature

J_W	Water flux (L m^{-2} hr^{-1})
J_s	Salt Flux (gm m^{-2} hr^{-1})
ρ	Density of solution (kg m^{-3})
C_{Fb}	Bulk feed concentration (mol L^{-1})
C_{Fm}	Feed side near membrane concentration (mol L^{-1})
C_i	Interfacial concentration between the active and support layer (mol L^{-1})
C_{Dm}	Draw side near membrane concentration (mol L^{-1})
C_{Db}	Bulk draw concentration (mol L^{-1})

A_m	Membrane area (m^2)
D_{Fb}	Feed side diffusivity of salt ($m^2\ s^{-1}$)
D_{Db}	Draw side diffusivity of salt ($m^2\ s^{-1}$)
Ds	Solute diffusion coefficient inside the support layer ($m^2 s^{-1}$)
k_{mtf}	Feed side mass transfer coefficient ($m\ s^{-1}$)
k_{mtd}	Draw side mass transfer coefficient ($m\ s^{-1}$)
t_s	thickness of support layer of the membrane (m)
B	Salt permeability ($mm\ hr^{-1}$)
S	Structural parameter (Dimensionless)
τ	Membrane support layer tortuosity (Dimensionless)
A	Pure water permeance ($L\ m^{-2}\ hr^{-1}\ bar^{-1}$)
i	Van't hoff coefficient (dimensionless)
R	Ideal gas constant ($L\ atm\ mol^{-1}K^{-1}$)
δ_{tf}	Feed side mass transfer boundary layer thickness (m)
δ_{td}	Draw side mass transfer boundary layer thickness (m)
φ_m	Pitzer osmotic coefficient
z_+	Number of charge on cation
z_-	Number of charge on anion
f^{φ}	Function of ionic strength (also temperature and solvent properties) expressing the effect of the long-range electrostatic forces
m	Molality (mol/Kg)
υ_+	Stoichiometric coefficient of cations
υ_-	Stoichiometric coefficient of anions
B_{MX}^{φ}	Pairwise ion-interaction parameter of Pitzer's equation for the Gibbs energy
α	Universal parameter
$\beta_{MX}^{(0)}$	1st virial coefficient
$\beta_{MX}^{(1)}$	2nd virial coefficient
A_{φ}	Debye-Hùckel constant for the osmotic coefficient
e	Electronic charge of an electron
ε_0	Vacuum permittivity
ε_r	Relative permittivity
d_s	Dielectric constant of the solvent at temperature T
N_A	Avogadro's number
I	Ionic strength of the liquid
b	Empirical parameter
C_{MX}^{φ}	Triplet ion-interaction parameter of Pitzer's equation for the Gibbs energy
π	Osmotic pressure
T	Temperature
M_w	Molecular weight of water (Kg/mol)
υ_{water}	Molar volume of pure water (m^3/mol)
π_i	Osmotic pressure at the selective and support layer interface
π_{Fm}	Osmotic pressure at the feed side B.L. and selective layer interface
$D_{impeller}$	Diameter of impeller (m)
impeller	Speed of impeller (sec^{-1})

Appendix I: standard operating procedure of FORO

FO Operation

Start-up

- Drain and clean system if necessary.
- Check status of filters on pumps; replace if necessary.
- Ensure all drain valves are closed.
- Ensure all pressure valves are fully open.
- Close bypass lines and open valves in line.
- Connect respective tubing to membrane as labeled.
- Connect yellow tubing to chiller; turn on chiller.
- Twist tops of tanks to remove; fill feed tank (left) and draw tank (right) with respective solutions.
- Double check that valves are aligned correctly: drain valves are closed, bypass lines are closed, in-line valves are open.
- Turn on system by switching both power boxes to "On."
- Turn on system by rotating large black knob (located between feed and draw tanks) 90 degrees to the right.
- Connect vertical lines (in front of tanks) to the tops of tanks.
- Press "Run" on each pump control (Feed and Draw, labeled "FP" and "DP", respectively).
- Use black knobs to adjust pumping of each solution simultaneously. Use pressure gauges on membrane to monitor the pressure, making sure that there is not a significant difference across the membrane (to prevent damage).
- Adjust pressure needles and chiller settings as desired.
- Follow "Collecting Data" procedure to collect data.
- Use Productivity Suite software to measure flux, amp usage, etc.
- Use Logger Lite software to measure conductivity, ORP, pH, etc.
- Power Down
- Fully open pressure needles
- Rotate pump control knobs completely counter-clockwise (screen should say "0").
- Press "Stop" on both panels.
- Rotate black knob 90 degrees counter-clockwise to shut off.
- Switch power boxes to "Off."
- Draining
- Ensure drain outlets are connected to a drain.
- Open all drain valves and allow tanks to drain fully.

RO Operation

- Drain and clean system if necessary.
- Ensure all drain valves are closed.
- Close bypass lines and open valves in line.
- Make sure pressure knob is all the way open before turning up the pump
- Twist tops of tank to remove; fill feed tank with desired solution.
- Turn on system by switching both power boxes to "On."
- Turn on system by rotating large black knob (located between feed and draw tanks) 90 degrees to the right.
- To turn on box, press green "run" button
- Flashing red light indicates that box is on
- Turn on system by rotating large black knob (located between feed and draw tanks) 90 degrees to the right. See red zeroes appear on monitors.
- Double check that valves are aligned correctly: drain valves are closed, bypass lines are closed, in-line valves are open.
- Press "Run" on monitor.
- Adjust the box setting by using black dial to start RO pump. Notice numbers on screen increasing.
- Use pressure valve to increase applied pressure by rotating clockwise to obtain the desired flowrates. Use pressure gauge to monitor pressure; do not exceed 800 psi.
- Follow "Collecting Data" procedure to collect data.
- Use Productivity Suite software to measure flux, amp usage, etc.
- Use Logger Lite software to measure conductivity, ORP, pH, etc.
- During operation, make sure permeate tanks do not overfill with water
- Use FO pump to transfer permeate to feed tank of FO (ensure tank is completely empty and clean).
- Ensure valve underneath permeate tanks is open/line is connected to FO line before pump.
- Ensure valve underneath feed tank is closed (otherwise solution will not flow from permeate tanks)
- Follow FO procedure for starting pump.
- To power-down
- Fully open pressure valve
- Rotate black dial on monitor completely counter-clockwise, notice zeroes appear.
- Press red "Stop" button.
- Switch power boxes to "Off."
- Draining
- Ensure drain outlets are connected to a drain.
- Open all drain valves and allow tanks to drain fully.

Collecting Data

- Ensure all connections to computer are secure: dials (labeled with which sensors they are for), computer is on, all USB ports are plugged in)

- Open Productivity Suite software on laptop.
- Select “Read project from CPU,” select the reading from the following box, press “Connect.”
- On left-hand-side, click on “Data View” under “Data Analysis.”
- Right-click on desired tags under the “Tag name” column and select “Graph tags” to see changes over time.
- Returning to the desktop, open Logger Lite software.
- Run the experiment by selecting the green play button in the top right of the screen.

FORO operation

- Follow start-up procedure from FO instruction.
- Connect FO draw outlet to Feed tank of RO.
- If operating in closed-loop with DI water as feed: Fill draw tank with draw solution; fill RO permeate tank with feed solution. If operating in batch with a different feed: Fill FO feed tank with feed solution; ensure valve located underneath RO permeate tank is closed.

References

[1] World Economic Forum, The Global Risks Report 2017 12th Edition, 2017. doi:10.1017/CBO9781107415324.004.

[2] Water.org, Water, (n.d.). http://water.org/ (accessed January 1, 2015).

[3] UNEP, Vital Water Graphics - An Overview of the State of the World's Fresh and Marine Waters, 2nd ed., Nairobi, Kenya, 2008.

[4] G.Z. Ramon, E.M.V. Hoek, Transport through composite membranes, part 2: Impacts of roughness on permeability and fouling, J. Memb. Sci. 425–426 (2013) 141–148.

[5] B. Van der Bruggen, C. Vandecasteele, Distillation vs. membrane filtration: Overview of process evolutions in seawater desalination, Desalination. 143 (2002) 207–218. doi:10.1016/S0011-9164(02)00259-X.

[6] S. Loeb, S. Sourirajan, Sea Water Demineralization by Means of an Osmotic Membrane, in: Saline Water Conversion—II, American Chemical Society, Washington, D. C., 1963: pp. 117–132.

[7] E.R. Reahl, Half A Century of Desalination With Electrodialysis, GE Water Process Technol. (2004).

[8] M. Al-Shammiri, M. Safar, Multi-effect distillation plants: state of the art.pdf, Desalination. 126 (1999) 45–59.

[9] K.W. Lawson, D.R. Lloyd, Membrane distillation, J. Memb. Sci. 124 (1997) 1–25. http://linkinghub.elsevier.com/retrieve/pii/S0376738896002360.

[10] T.Y. Cath, A.E. Childress, M. Elimelech, Forward osmosis: Principles, applications, and recent developments, J. Memb. Sci. 281 (2006) 70–87.

[11] J.R. McCutcheon, R.L. McGinnis, M. Elimelech, A novel ammonia—carbon dioxide forward (direct) osmosis desalination process, Desalination. 174 (2005) 1–11.

[12] R.K. McGovern, J.H. Lienhard V, On the potential of forward osmosis to energetically outperform reverse osmosis desalination, J. Memb. Sci. 469 (2014) 245–250.

[13] D.L. Shaffer, J.R. Werber, H. Jaramillo, S. Lin, M. Elimelech, Forward osmosis: Where are we now?, Desalination. 356 (2015) 271–284. doi:10.1016/j.desal.2014.10.031.

[14] T. Cath, a Childress, M. Elimelech, Forward osmosis: Principles, applications, and recent developments, J. Memb. Sci. 281 (2006) 70–87. doi:10.1016/j.memsci.2006.05.048.

[15] Q. Ge, J. Su, G.L. Amy, T.S. Chung, Exploration of polyelectrolytes as draw solutes in forward osmosis processes, Water Res. 46 (2012) 1318–1326.

[16] D. Li, X. Zhang, J. Yao, G.P. Simon, H. Wang, Stimuli-responsive polymer hydrogels as a new class of draw agent for forward osmosis desalination., Chem. Commun. 47 (2011) 1710–1712.

[17] M.M. Ling, K.Y. Wang, T.S. Chung, Highly Water-Soluble Magnetic Nanoparticles as Novel Draw Solutes in Forward Osmosis for Water Reuse, Ind. Eng. Chem. Res. 49 (2010) 5869–5876.

[18] M.L. Stone, C. Rae, F.F. Stewart, A.D. Wilson, Switchable polarity solvents as draw solutes for forward osmosis, Desalination. 312 (2013) 124–129.
[19] J.R. McCutcheon, R.L. McGinnis, M. Elimelech, Desalination by ammonia–carbon dioxide forward osmosis: Influence of draw and feed solution concentrations on process performance, J. Memb. Sci. 278 (2006) 114–123.
[20] W.C.L. Lay, J. Zhang, C. Tang, R. Wang, Y. Liu, A.G. Fane, Factors affecting flux performance of forward osmosis systems, J. Memb. Sci. 394–395 (2012) 151–168. doi:10.1016/j.memsci.2011.12.035.
[21] J.R. McCutcheon, M. Elimelech, Modeling water flux in forward osmosis: Implications for improved membrane design, AIChE J. 53 (2007) 1736–1744. doi:10.1002/aic.
[22] D. Xiao, W. Li, S. Chou, R. Wang, C.Y. Tang, A modeling investigation on optimizing the design of forward osmosis hollow fiber modules, J. Memb. Sci. 392–393 (2012) 76–87. doi:10.1016/j.memsci.2011.12.006.
[23] S. Zhao, L. Zou, Effects of working temperature on separation performance, membrane scaling and cleaning in forward osmosis desalination, Desalination. 278 (2011) 157–164.
[24] M. Xie, W.E. Price, L.D. Nghiem, M. Elimelech, Effects of feed and draw solution temperature and transmembrane temperature difference on the rejection of trace organic contaminants by forward osmosis, J. Memb. Sci. 438 (2013) 57–64.
[25] R.L. McGinnis, N.T. Hancock, M.S. Nowosielski-Slepowron, G.D. McGurgan, Pilot demonstration of the NH3/CO2 forward osmosis desalination process on high salinity brines, Desalination. 312 (2013) 67–74.
[26] B. Mi, M. Elimelech, Gypsum scaling and cleaning in forward osmosis: measurements and mechanisms., Environ. Sci. Technol. 44 (2010) 2022–8. doi:10.1021/es903623r.
[27] J. Ren, J.R. McCutcheon, A new commercial thin film composite membrane for forward osmosis, Desalination. 343 (2014) 187–193.
[28] J.E. Cadotte, Reverse Osmosis Membrane, 4,259,183, 1981.
[29] R.W. Baker, Membrane Technology and Applications, 2nd ed., John Wiley & Sons Ltd, The Atrium, Southern Gate, Chichester, West Sussex PO19 8SQ, England, 2004. doi:10.1016/S0376-7388(00)83139-7.
[30] K.P. Lee, T.C. Arnot, D. Mattia, A review of reverse osmosis membrane materials for desalination-Development to date and future potential, J. Memb. Sci. 370 (2011) 1–22. doi:10.1016/j.memsci.2010.12.036.
[31] A.Y. Hoekstra, A.K. Chapagain, Globalization of Water: Sharing the Planet's Freshwater Resources, Wiley-Blackwell, n.d.
[32] J.W. Wrasidlo, Semipermeable Membranes and the Method for the Prepara- tion Thereof, 4,005,012, 1977.
[33] P.L. Riley, C.E. Milstead, A.L. Lloyd, M.W. Seroy, M. Tagami, Spiral-wound thin-film composite membrane systems for brackish and seawater desalination by reverse osmosis, Desalination. 23 (1977) 331–355. doi:10.1016/S0011-9164(00)82535-7.
[34] C.E. Hickman, I. Jamjoom, A.B. Riedinger, R.E. Seaton, Jeddah seawater reverse osmosis installation, Desalination. 30 (1979) 259–281. doi:10.1016/S0011-9164(00)88453-2.
[35] W.G. Light, J.L. Perlman, A.B. Riedinger, D.F. Needham, Desalination of non-chlorinated surface seawater using TFCR membrane elements, Desalination. 70 (1988) 47–64. doi:10.1016/0011-9164(88)85043-4.
[36] J.E. Cadotte, Interfacially Synthesized Reverse Osmosis Membrane, 4,277,344, 1981.
[37] Y. Kamiyama, N. Yoshioka, K. Matsui, K. Nakagome, New thin-film composite reverse

osmosis membranes and spiral wound modules, Desalination. 51 (1984) 79–92. doi:10.1016/0011-9164(84)85054-7.
[38] P. Eriksson, Water and salt transport through two types of polyamide composite membranes, J. Memb. Sci. 36 (1988) 297–313. doi:10.1016/0376-7388(88)80024-3.
[39] J.E. Cadotte, R.J. Petersen, R.E. Larson, E.E. Erickson, A new thin-film composite seawater reverse osmosis membrane, Desalination. 32 (1980) 25–31.
[40] R.L. Riley, R.L. Fox, C.R. Lyons, C.E. Milstead, M.W. Seroy, M. Tagami, SPIRAL-WOUND POLY(ETHER/AMIDE) THIN-FILM COMPOSITE MEMBRANE SYSTEMS, Desalination. 19 (1976) 113–126.
[41] S.H. Kim, S.Y. Kwak, B.H. Sohn, T.H. Park, Design of TiO2 nanoparticle self-assembled aromatic polyamide thin-film-composite (TFC) membrane as an approach to solve biofouling problem, J. Memb. Sci. 211 (2003) 157–165. doi:10.1016/S0376-7388(02)00418-0.
[42] B.-H. Jeong, E.M.V. Hoek, Y. Yan, A. Subramani, X. Huang, G. Hurwitz, A.K. Ghosh, A. Jawor, Interfacial polymerization of thin film nanocomposites: A new concept for reverse osmosis membranes, J. Memb. Sci. 294 (2007) 1–7.
[43] M.L. Lind, A.K. Ghosh, A. Jawor, X. Huang, W. Hou, Y. Yang, E.M. V Hoek, Influence of zeolite crystal size on zeolite-polyamide thin film nanocomposite membranes, Langmuir. 25 (2009) 10139–10145. doi:10.1021/la900938x.
[44] J.T. Arena, B. McCloskey, B.D. Freeman, J.R. McCutcheon, Surface modification of thin film composite membrane support layers with polydopamine: Enabling use of reverse osmosis membranes in pressure retarded osmosis, J. Memb. Sci. 375 (2011) 55–62.
[45] R. Zimmermann, Condensation Polymers: By Interfacial and Solution Methods. Von P. W. Morgan. John Wiley & Sons, New York London-Sydney 1965. 1. Aufl., XVIII, 561 S., zahlr. Abb., mehrere Tab., geb. £ 9.10.–, Angew. Chemie. 78 (1966) 787–787. doi:10.1002/ange.19660781632.
[46] N.Y. Yip, A. Tiraferri, W.A. Phillip, J.D. Schiffman, M. Elimelech, High performance thin-film composite forward osmosis membrane, Environ. Sci. Technol. 44 (2010) 3812–3818.
[47] N.-N. Bui, J.R. Mccutcheon, Hydrophilic Nanofibers as New Supports for Thin Film Composite Membranes for Engineered Osmosis, Environ. Sci. Technol. 47 (2013) 1761–1769.
[48] R. Wang, L. Shi, C.Y. Tang, S. Chou, C. Qiu, A.G. Fane, Characterization of novel forward osmosis hollow fiber membranes, J. Memb. Sci. 355 (2010) 158–167. doi:10.1016/j.memsci.2010.03.017.
[49] N. Cecilia E, G. Ashok Kumar, Oil & Natural Gas Technology Membrane Technology for Produced Water in Lea County, 2011.
[50] B.D. Coday, P. Xu, E.G. Beaudry, J. Herron, K. Lampi, N.T. Hancock, T.Y. Cath, The sweet spot of forward osmosis: Treatment of produced water, drilling wastewater, and other complex and difficult liquid streams, Desalination. 333 (2014) 23–35.
[51] M. Garcia, Barrufet Maria, Desalination of Produced Water Using Reverse Osmosis, (2002) 1–9.
[52] D.L. Shaffer, L.H. Arias Chavez, M. Ben-Sasson, S. Romero-Vargas Castrillón, N.Y. Yip, M. Elimelech, Desalination and reuse of high-salinity shale gas produced water: drivers, technologies, and future directions., Environ. Sci. Technol. 47 (2013) 9569–83. doi:10.1021/es401966e.

[53] B.D. Coday, T.Y. Cath, Forward osmosis: Novel desalination of produced water and fracturing flowback, J. Am. Water Works Assoc. 106 (2014) 37–38. doi:10.5942/jawwa.2014.106.0016.
[54] J. Minier-Matar, A. Hussain, A. Janson, R. Wang, A.G. Fane, S. Adham, Application of forward osmosis for reducing volume of produced/Process water from oil and gas operations, Desalination. 376 (2015) 1–8. doi:10.1016/j.desal.2015.08.008.
[55] B. Khorshidi, A. Bhinder, T. Thundat, D. Pernitsky, M. Sadrzadeh, Developing high throughput thin film composite polyamide membranes for forward osmosis treatment of SAGD produced water, J. Memb. Sci. 511 (2016) 29–39. doi:10.1016/j.memsci.2016.03.052.
[56] R.M. Abousnina, L.D. Nghiem, Removal of dissolved organics from produced water by forward osmosis, Desalin. Water Treat. 52 (2014) 570–579. doi:10.1080/19443994.2013.827292.
[57] M. Çakmakce, N. Kayaalp, I. Koyuncu, Desalination of produced water from oil production fields by membrane processes, Desalination. 222 (2008) 176–186. doi:10.1016/j.desal.2007.01.147.
[58] K.L. Hickenbottom, N.T. Hancock, N.R. Hutchings, E.W. Appleton, E.G. Beaudry, P. Xu, T.Y. Cath, Forward osmosis treatment of drilling mud and fracturing wastewater from oil and gas operations, Desalination. 312 (2012) 60–66. doi:10.1016/j.desal.2012.05.037.
[59] D. Roy, M. Rahni, P. Pierre, V. Yargeau, Forward osmosis for the concentration and reuse of process saline wastewater, Chem. Eng. J. 287 (2016) 277–284.
[60] S. Lee, Y.C. Kim, Calcium carbonate scaling by reverse draw solute diffusion in a forward osmosis membrane for shale gas wastewater treatment, J. Memb. Sci. 522 (2017) 257–266.
[61] J.R. Werber, C.O. Osuji, M. Elimelech, Materials for next-generation desalination and water purification membranes, Nat. Rev. Mater. (2016) 16018. doi:10.1038/natrevmats.2016.18.
[62] R. Valladares Linares, Z. Li, S. Sarp, S.S. Bucs, G. Amy, J.S. Vrouwenvelder, Forward osmosis niches in seawater desalination and wastewater reuse, Water Res. 66 (2014) 122–139. doi:10.1016/j.watres.2014.08.021.
[63] M.R. Chowdhury, J. Ren, K. Reimund, J.R. McCutcheon, A hybrid dead-end forward osmosis system for evaluation of osmotic flux performance in recovering produced water, Desalination. (2016). doi:10.1016/j.desal.2016.08.021.
[64] N.-N. Bui, J.T. Arena, J.R. McCutcheon, Proper accounting of mass transfer resistances in forward osmosis: Improving the accuracy of model predictions of structural parameter, J. Memb. Sci. 492 (2015) 289–302.
[65] C.H. Tan, H.Y. Ng, Modified models to predict flux behavior in forward osmosis in consideration of external and internal concentration polarizations, J. Memb. Sci. 324 (2008) 209–219. doi:10.1016/j.memsci.2008.07.020.
[66] C. Suh, S. Lee, Modeling reverse draw solute flux in forward osmosis with external concentration polarization in both sides of the draw and feed solution, J. Memb. Sci. 427 (2013) 365–374. doi:10.1016/j.memsci.2012.08.033.
[67] J.R. McCutcheon, M. Elimelech, Influence of concentrative and dilutive internal concentration polarization on flux behavior in forward osmosis, J. Memb. Sci. 284 (2006) 237–247.
[68] A. Tiraferri, N.Y. Yip, A.P. Straub, S. Romero-Vargas Castrillon, M. Elimelech, A

method for the simultaneous determination of transport and structural parameters of forward osmosis membranes, J. Memb. Sci. 444 (2013) 523–538.
[69] M. Park, J.J. Lee, S. Lee, J.H. Kim, Determination of a constant membrane structure parameter in forward osmosis processes, J. Memb. Sci. 375 (2011) 241–248.
[70] S.-J. You, X.-H. Wang, M. Zhong, Y.-J. Zhong, C. Yu, N.-Q. Ren, Temperature as a factor affecting transmembrane water flux in forward osmosis: Steady-state modeling and experimental validation, Chem. Eng. J. 198–199 (2012) 52–60.
[71] P.A. Charlez, Rock Mechanics: Petroleum Applications, Volume 2, Editions TECHNIP, 1997. http://books.google.com/books?id=NigwG_BYRsYC&pgis=1 (accessed August 26, 2014).
[72] E. Ridlington, K. Norman, R. Richardson, Fracking by the Numbers: The damage to our water, land and climate from a decade of dirty drilling, 2016. http://www.environmentamerica.org/sites/environment/files/reports/EA_FrackingNumbers_scrn.pdf.
[73] D.M. Kargbo, R.G. Wilhelm, D.J. Campbell, Natural gas plays in the Marcellus Shale: challenges and potential opportunities., Environ. Sci. Technol. 44 (2010) 5679–84. doi:10.1021/es903811p.
[74] V. Velmurugan, K. Srithar, Prospects and scopes of solar pond: A detailed review, Renew. Sustain. Energy Rev. 12 (2008) 2253–2263. doi:10.1016/j.rser.2007.03.011.
[75] A. Fakhru'l-Razi, A. Pendashteh, L.C. Abdullah, D.R.A. Biak, S.S. Madaeni, Z.Z. Abidin, Review of technologies for oil and gas produced water treatment., J. Hazard. Mater. 170 (2009) 530–51. doi:10.1016/j.jhazmat.2009.05.044.
[76] S. Mondal, S.R. Wickramasinghe, Produced water treatment by nanofiltration and reverse osmosis membranes, J. Memb. Sci. 322 (2008) 162–170. doi:10.1016/j.memsci.2008.05.039.
[77] D. Singh, P. Prakash, K.K. Sirkar, Deoiled Produced Water Treatment Using Direct-Contact Membrane Distillation, Ind. Eng. Chem. Res. 52 (2013) 13439–13448. doi:dx.doi.org/10.1021/ie4015809.
[78] B. Mi, M. Elimelech, Chemical and physical aspects of organic fouling of forward osmosis membranes, J. Memb. Sci. 320 (2008) 292–302. doi:10.1016/j.memsci.2008.04.036.
[79] E. Cornelissen, D. Harmsen, K. Dekorte, C. Ruiken, J. Qin, H. Oo, L. Wessels, Membrane fouling and process performance of forward osmosis membranes on activated sludge, J. Memb. Sci. 319 (2008) 158–168. doi:10.1016/j.memsci.2008.03.048.
[80] T.Y. Cath, N.T. Hancock, C.D. Lundin, C. Hoppe-Jones, J.E. Drewes, A multi-barrier osmotic dilution process for simultaneous desalination and purification of impaired water, J. Memb. Sci. 362 (2010) 417–426. doi:10.1016/j.memsci.2010.06.056.
[81] R.W. Holloway, A.E. Childress, K.E. Dennett, T.Y. Cath, Forward osmosis for concentration of anaerobic digester centrate, Water Res. 41 (2007) 4005–4014. doi:10.1016/j.watres.2007.05.054.
[82] D. Anastasio, J.R. McCutcheon, Using forward osmosis to teach mass transfer fundamentals to undergraduate chemical engineering students, Desalination. 312 (2013) 10–18.
[83] Z. Wang, J. Zheng, J. Tang, X. Wang, Z. Wu, A pilot-scale forward osmosis membrane system for concentrating low-strength municipal wastewater: performance and implications, Sci. Rep. 6 (2016) 21653. doi:10.1038/srep21653.

[84] M.M. Pendergast, M.S. Nowosielski-Slepowron, J. Tracy, Going big with forward osmosis, Desalin. Water Treat. 3994 (2016) 1–10. doi:10.1080/19443994.2016.1168581.
[85] G.T. Gray, J.R. McCutcheon, M. Elimelech, Internal concentration polarization in forward osmosis: role of membrane orientation, Desalination. 197 (2006) 1–8.
[86] S.S. Manickam, J. Gelb, J.R. McCutcheon, Pore structure characterization of asymmetric membranes: Non-destructive characterization of porosity and tortuosity, J. Memb. Sci. 454 (2014) 549–554. doi:10.1016/j.memsci.2013.11.044.
[87] N.O. Becht, D.J. Malik, E.S. Tarleton, Evaluation and comparison of protein ultrafiltration test results: Dead-end stirred cell compared with a cross-flow system, Sep. Purif. Technol. 62 (2008) 228–239. doi:10.1016/j.seppur.2008.01.030.
[88] O. Smithies, A dynamic osmometer for accurate measurements on small quantities of material: osmotic pressures of isoelectric beta-lactoglobulin solutions., Biochem. J. 55 (1953) 57–67.
[89] EPA, Methods for Chemical Analysis of Water and Wastes, 1983.
[90] APHA-AWWA, Standard methods for the examination of water and waste water, 18–20 th E ed., n.d.
[91] ASTM, Water, Am. Soc. Test. Mater. 11.01-02 (2007).
[92] API, Analysis of Oil-Field Waters, Am. Pet. Inst. 2nd (1981) API RP 45.
[93] W.F. Langelier, Chemical Equilibria in Water Treatment, J. Am. Water Work. Assoc. 38 (1946) 169–178.
[94] D19 Committee, Practice for Calculation and Adjustment of the Stiff and Davis Stability Index for Reverse Osmosis, ASTM International, 2010.
[95] Dow Water Solutions, FILMTEC ™ Membranes Water Chemistry and Pretreatment : Biological Fouling Prevention, 2012.
[96] J.J. Friel, X-ray and image analysis in electron microscopy, Princeton Gamma-Tech, 1995. http://www.amazon.com/X-ray-image-analysis-electron-microscopy/dp/0964145502.
[97] R.H. Perry, D.W. Green, Perry's Chemical Engineers' Handbook, 8th ed., McGraw-Hill, 2008. doi:10.1036/0071422943.
[98] W.A. Phillip, J.S. Yong, M. Elimelech, Reverse Draw Solute Permeation in Forward Osmosis: Modeling and Experiments., Environ. Sci. Technol. 44 (2010) 5170–5176.
[99] J.M. Prausnitz, R.N. Lichtenthaler, E.G. de Azevedo, Molecular Thermodynamics of Fluid-Phase Equilibria, Pearson Education, 1998.
[100] L.F. Silvester, K.S. Pitzer, Thermodynamics of Electrolytes. 8. High-Temperature Properties, Including Enthalpy and Heat Capacity, with Application to Sodium Chloride, J. Phys. Chem. 81 (1977) 1822–1828.
[101] V.M.M. Lobo, Mutual diffusion coefficients in aqueous electrolyte solutions, Pure Appl. Chem. 65 (1993) 2613–2640.
[102] J.F. Comesana, J.J. Otero, E. Camesella, A. Correa, Densities and Viscosities of Ternary Systems of Water + Fructose + Sodium Chloride from 20 to 40 °C, J. Chem. Eng. Data. 46 (2001) 1153–1155.
[103] G.D. Mehta, S. Loeb, Internal polarization in the porous substructure of a semipermeable membrane under pressure retarded osmosis, J. Memb. Sci. 4 (1978) 261–265. doi:10.1016/S0376-7388(00)83301-3.
[104] L.F. Albright, Albright's chemical engineering handbook, 2008.
[105] D. Agitators, Mixing 101: Optimal Tank Design, (2015).

http://www.dynamixinc.com/optimal-tank-design (accessed January 1, 2016).
[106] P. Eriksson, M. Kyburz, W. Pergande, NF membrane characteristics and evaluation for sea water processing applications, Desalination. 184 (2005) 281–294.
[107] R.W. Schofield, A.G. Fane, C.J.D. Fell, HEAT AND MASS TRANSFER IN MEMBRANE DISTILLATION, J. Memb. Sci. 33 (1987) 299–313.
[108] E. Drioli, A. Ali, F. Macedonio, Membrane distillation: Recent developments and perspectives, Desalination. 356 (2015) 56–84.
[109] A. Alkhudhiri, N. Darwish, N. Hilal, Membrane distillation: A comprehensive review, Desalination. 287 (2012) 2–18.
[110] K.W. Lawson, D.R. Lloyd, Review: Membrane distillation, J. Memb. Sci. 124 (1997) 1–25.
[111] L. Song, J.Y. Hu, S.L. Ong, W.J. Ng, M. Elimelech, M. Wilf, Emergence of thermodynamic restriction and its implications for full-scale reverse osmosis processes, Desalination. 155 (2003) 213–228.
[112] H.Y. Ng, W. Tang, W.S. Wong, Performance of Forward (Direct) Osmosis Process: Membrane Structure and Transport Phenomenon, Environ. Sci. Technol. 40 (2006) 2408–2413.
[113] T.Y. Cath, M. Elimelech, J.R. McCutcheon, R.L. McGinnis, A. Achilli, D. Anastasio, A.R. Brady, A.E. Childress, I. V. Farr, N.T. Hancock, J. Lampi, L.D. Nghiem, M. Xie, N.Y. Yip, Standard Methodology for Evaluating Membrane Performance in Osmotically Driven Membrane Processes, Desalination. 312 (2012) 31–38.
[114] S. Phuntsho, S. Vigneswaran, J. Kandasamy, S. Hong, S. Lee, H.K. Shon, Influence of temperature and temperature difference in the performance of forward osmosis desalination process, J. Memb. Sci. 415–416 (2012) 734–744.
[115] S. Adham, A. Hussain, J.M. Matar, R. Dores, A. Janson, Application of Membrane Distillation for desalting brines from thermal desalination plants, Desalination. 314 (2013) 101–108.
[116] R. Mcginnis, G. McGurgan, United States Patent 8,181,794 B2, FORWARD OSMOSIS MEMBRANES, 8,181,794 B2, 2012.
[117] H. Klm, W.J. Frederick Jr., Evaluation of Pitzer Ion Interaction Parameters of Aqueous Electrolytes at 25°C. 1 . Single Salt Parameters, J. Chem. Eng. Data. 33 (1988) 177–184. doi:10.1021/je00052a035.
[118] J. Li, Z. Xu, H. Yang, Microporous polyethersulfone membranes prepared under the combined precipitation conditions with non-solvent additives, Polym. Adv. Technol. 19 (2008) 251–257.
[119] W.M.. Kays, M.E.. Crawford, B. Weigand, Convective Heat and Mass Transfer, 4th ed., Mc Graw Hill, 2005.
[120] K.L. Lee, R.W. Baker, H.K. Lonsdale, Membranes for power generation by pressure-retarded osmosis, J. Memb. Sci. 8 (1981) 141–171.
[121] L.H. Martin, The thermal conductivity of water, Proc. Phys. Soc. (1933).
[122] A.I.Brown and S.M.Macro, Introduction to Heat Transfer, 3rd ed., McGraw-Hill, New York, 1958.
[123] Thermal Conductivity of some common materials and gases, (n.d.). http://www.engineeringtoolbox.com/thermal-conductivity-d_429.html (accessed January 1, 2015).
[124] A.G. Fane, C. QIU, C. TANG, R. Wang, J. Wei, A forward osmosis membrane and

method of forming a forward osmosis membrane, WO2012102680 A1, 2012.
[125] D.D. Anastasio, J.T. Arena, E.A. Cole, J.R. Mccutcheon, Impact of temperature on power density in closed-loop pressure retarded osmosis for grid storage, J. Memb. Sci. 479 (2015) 240–245.
[126] P.G. Nicoll, Forward osmosis as a pre-treatment to reverse osmosis, Int. Desalin. Assoc. World Congr. Desalin. Water Reuse 2013. (2013) 1–21. http://www.modernwater.com/assets/downloads/Papers/Forward Osmosis as a Pre-treatment to Reverse Osmosis.pdf.
[127] K.L. Tu, A.R. Chivas, L.D. Nghiem, Effects of chemical preservation on flux and solute rejection by reverse osmosis membranes, J. Memb. Sci. 472 (2014) 202–209. doi:10.1016/j.memsci.2014.08.052.
[128] F. Zaviska, Y. Chun, M. Heran, L. Zou, Using FO as pre-treatment of RO for high scaling potential brackish water: Energy and performance optimisation, J. Memb. Sci. 492 (2015) 430–438. doi:10.1016/j.memsci.2015.06.004.
[129] Y.J. Choi, J.S. Choi, H.J. Oh, S. Lee, D.R. Yang, J.H. Kim, Toward a combined system of forward osmosis and reverse osmosis for seawater desalination, Desalination. 247 (2009) 239–246. doi:10.1016/j.desal.2008.12.028.
[130] D.L. Shaffer, N.Y. Yip, J. Gilron, M. Elimelech, Seawater desalination for agriculture by integrated forward and reverse osmosis: Improved product water quality for potentially less energy, J. Memb. Sci. 415–416 (2012) 1–8. doi:10.1016/j.memsci.2012.05.016.
[131] T.N. Bitaw, K. Park, D.R. Yang, Optimization on a new hybrid Forward osmosis-Electrodialysis-Reverse osmosis seawater desalination process, Desalination. 398 (2016) 265–281. doi:10.1016/j.desal.2016.07.032.
[132] Y. Choi, H. Cho, Y. Shin, Y. Jang, S. Lee, Economic evaluation of a hybrid desalination system combining forward and reverse osmosis, Membranes (Basel). 6 (2015). doi:10.3390/membranes6010003.
[133] O.A. Bamaga, A. Yokochi, B. Zabara, A.S. Babaqi, Hybrid FO/RO desalination system: Preliminary assessment of osmotic energy recovery and designs of new FO membrane module configurations, Desalination. 268 (2011) 163–169. doi:10.1016/j.desal.2010.10.013.
[134] Y. Chun, F. Zaviska, S.J. Kim, D. Mulcahy, E. Yang, I.S. Kim, L. Zou, Fouling characteristics and their implications on cleaning of a FO-RO pilot process for treating brackish surface water, Desalination. 394 (20167) 91–100.
[135] L. Chekli, S. Phuntsho, J.E. Kim, J. Kim, J.Y. Choi, J.S. Choi, S. Kim, J.H. Kim, S. Hong, J. Sohn, H.K. Shon, A comprehensive review of hybrid forward osmosis systems: Performance, applications and future prospects, J. Memb. Sci. 497 (2016) 430–449. doi:10.1016/j.memsci.2015.09.041.
[136] B.G. Choi, M. Zhan, K. Shin, S. Lee, S. Hong, Pilot-scale evaluation of FO-RO osmotic dilution process for treating wastewater from coal-fired power plant integrated with seawater desalination, J. Memb. Sci. (2017). doi:10.1016/j.memsci.2017.06.036.
[137] R.V. Linares, Z. Li, V. Yangali-quintanilla, N. Ghaffour, G. Amy, T. Leiknes, J.S. Vrouwenvelder, Life cycle cost of a hybrid forward osmosis e low pressure reverse osmosis system for seawater desalination and wastewater recovery, Water Res. 88 (2016) 225–234. doi:10.1016/j.watres.2015.10.017.
[138] N.M. Mazlan, D. Peshev, A.G. Livingston, Energy consumption for desalination - A comparison of forward osmosis with reverse osmosis, and the potential for perfect

membranes, Desalination. 377 (2016) 138–151. doi:10.1016/j.desal.2015.08.011.
[139] N. Akther, A. Sodiq, A. Giwa, S. Daer, H.A. Arafat, S.W. Hasan, Recent advancements in forward osmosis desalination: A review, Chem. Eng. J. 281 (2015) 502–522. doi:10.1016/j.cej.2015.05.080.
[140] M. Qasim, N.A. Darwish, S. Sarp, N. Hilal, Water desalination by forward (direct) osmosis phenomenon: A comprehensive review, Desalination. 374 (2015) 47–69. doi:10.1016/j.desal.2015.07.016.
[141] S. Zhao, L. Zou, C.Y. Tang, D. Mulcahy, Recent developments in forward osmosis: Opportunities and challenges, J. Memb. Sci. 396 (2012) 1–21. doi:10.1016/j.memsci.2011.12.023.
[142] T.-S. Chung, S. Zhang, K.Y. Wang, J. Su, M.M. Ling, Forward osmosis processes: Yesterday, today and tomorrow, Desalination. 287 (2012) 78–81. doi:10.1016/j.desal.2010.12.019.
[143] Porifera, PFO Technology, (n.d.). http://porifera.com/pfo-advantages/ (accessed January 1, 2016).
[144] Aquaporin, (n.d.). http://aquaporin.dk/ (accessed January 1, 2016).
[145] FTSH2O, (n.d.). http://www.ftsh2o.com/ (accessed January 1, 2016).
[146] R. Revanur, I. Roh, J.E. Klare, A. Noy, O. Bakajin, United States Patent, US 8,920,654, B2, 2014.
[147] G. Blandin, H. Vervoort, P. Le-Clech, A.R.D. Verliefde, Fouling and cleaning of high permeability forward osmosis membranes, J. Water Process Eng. 9 (2016) 161–169. doi:10.1016/j.jwpe.2015.12.007.
[148] Y.-E. Lee, A. Jang, Effect of forward osmosis (membrane) support layer fouling by organic matter in synthetic seawater solution, Desalin. Water Treat. 57 (2016) 24595–24605.
[149] C.J. Orme, A.D. Wilson, 1-Cyclohexylpiperidine as a thermolytic draw solute for osmotically driven membrane processes, Desalination. 371 (2015) 126–133. doi:10.1016/j.desal.2015.05.024.
[150] G. Blandin, H. Vervoort, A. D'Haese, K. Schoutteten, J. Vanden Bussche, L. Vanhaecke, D.T. Myat, P. Le-Clech, A.R.D. Verliefde, Impact of hydraulic pressure on membrane deformation and trace organic contaminants rejection in pressure assisted osmosis (PAO), Process Saf. Environ. Prot. 102 (2016) 316–327.
[151] P. Nasr, H. Sewilam, Investigating fertilizer drawn forward osmosis process for groundwater desalination for irrigation in Egypt, Desalin. Water Treat. 57 (2016) 26932–26942.
[152] I. Koyuncu, J. Brant, A. Lüttge, M.R. Wiesner, A comparison of vertical scanning interferometry (VSI) and atomic force microscopy (AFM) for characterizing membrane surface topography, J. Memb. Sci. 278 (2006) 410–417.
[153] V. Gekas, B. Hallstrom, Mass transfer in the membrane concentraion polarization layer under turbulent cross flow I. Critical literature review and adaptation of existing sherwood correlations to membrane operations, J. Memb. Sci. 30 (1987) 153–170.
[154] J. Mulder, Basic Principles of Membrane Technology, 2nd ed., Springer Netherlands, 1996.
[155] J.T. Arena, M. Chwatko, H.A. Robillard, J.R. McCutcheon, pH Sensitivity of Ion Exchange through a Thin Film Composite Membrane in Forward Osmosis, Environ. Sci. Technol. Lett. 2 (2015) 177–182.

[156] S. Loeb, L. Titelman, E. Korngold, J. Freiman, Effect of porous support fabric on osmosis through a Loeb-Sourirajan type asymmetric membrane, J. Memb. Sci. 129 (1997) 243–249.
[157] J.R. McCutcheon, M. Elimelech, Influence of membrane support layer hydrophobicity on water flux in osmotically driven membrane processes, J. Memb. Sci. 318 (2008) 458–466.
[158] N.-N. Bui, M.L. Lind, E.M.V. Hoek, J.R. McCutcheon, Electrospun nanofiber supported thin film composite membranes for engineered osmosis, J. Memb. Sci. 385–386 (2011) 10–19.
[159] L. Huang, N.-N. Bui, M.T. Meyering, T.J. Hamlin, J.R. Mccutcheon, Novel hydrophilic nylon 6,6 microfiltration membrane supported thin film composite membranes for engineered osmosis, J. Memb. Sci. 437 (2013) 141–149.
[160] X. Song, Z. Liu, D.D. Sun, Nano Gives the Answer: Breaking the Bottleneck of Internal Concentration Polarization with a Nanofiber Composite Forward Osmosis Membrane for a High Water Production Rate, Adv. Mater. 23 (2011) 3256–3260.
[161] A. Tiraferri, Y. Kang, E.P. Giannelis, M. Elimelech, Highly Hydrophilic Thin-Film Composite Forward Osmosis Membranes Functionalized with Surface-Tailored Nanoparticles, ACS Appl. Mater. Interfaces. 4 (2012) 5044–5053.
[162] D.L. Shaffer, H. Jaramillo, S. Romero-Vargas Castrillon, X. Lu, M. Elimelech, Post-fabrication modification of forward osmosis membranes with a poly(ethylene glycol) block copolymer for improved organic fouling resistance, J. Memb. Sci. 490 (2015) 209–219.
[163] M. Tian, C. Qiu, Y. Liao, S. Chou, R. Wang, Preparation of polyamide thin film composite forward osmosis membranes using electrospun polyvinylidene fluoride (PVDF) nanofibers as substrates, Sep. Purif. Technol. 118 (2013) 727–736.
[164] J.M.C. Puguan, H.-S. Kim, K.-J. Lee, H. Kim, Low internal concentration polarization in forward osmosis membranes with hydrophilic crosslinked PVA nanofibers as porous support layer, Desalination. 336 (2014) 24–31.
[165] L. Huang, J.T. Arena, J.R. McCutcheon, Surface modified PVDF nanofiber supported thin film composite membranes for forward osmosis, J. Memb. Sci. 499 (2016) 352–360. doi:10.1016/j.memsci.2015.10.030.
[166] S. Pan, Y. Dong, Y.-M. Zheng, L. Zhong, Z. Yuan, Self-sustained hydrophilic nanofiber thin film composite forward osmosis membranes: Preparation, characterization and application for simulated antibiotic wastewater treatment, J. Memb. Sci. 523 (2017) 205–215.
[167] N. Bui, J.R. Mccutcheon, Nanoparticle-embedded nanofibers in highly permselective thin-film nanocomposite membranes for forward osmosis, J. Memb. Sci. 518 (2016) 338–346.
[168] M. Tian, Y.N. Wang, R. Wang, A.G. Fane, Synthesis and characterization of thin film nanocomposite forward osmosis membranes supported by silica nanoparticle incorporated nanofibrous substrate, Desalination. 401 (2017) 142–150.
[169] K.Y. Wang, T.-S. Chung, J.-J. Qin, Polybenzimidazole (PBI) nanofiltration hollow fiber membranes applied in forward osmosis process, J. Memb. Sci. 300 (2007) 6–12.
[170] J. Su, Q. Yang, J.F. Teo, T.-S. Chung, Cellulose acetate nanofiltration hollow fiber membranes for forward osmosis processes, J. Memb. Sci. 355 (2010) 36–44. doi:10.1016/j.memsci.2010.03.003.
[171] F. Edwie, T.-S. Chung, Development of hollow fiber membranes for water and salt recovery from highly concentrated brine via direct contact membrane distillation and

crystallization, J. Memb. Sci. 421–422 (2012) 111–123.
[172] S.Y. Kwak, S.G. Jung, Y.S. Yoon, D.W. Ihm, Details of surface features in aromatic polyamide reverse osmosis membranes characterized by scanning electron and atomic force microscopy, J. Polym. Sci. Part B Polym. Phys. 37 (1999) 1429–1440.
[173] D. Rana, T. Matsuura, Surface Modifications for Antifouling Membranes, Chem. Rev. 110 (2010) 2448–2471.
[174] Y. Gu, Y.N. Wang, J. Wei, C.Y. Tang, Organic fouling of thin-film composite polyamide and cellulose triacetate forward osmosis membranes by oppositely charged macromolecules, Water Res. 47 (2013) 1867–1874. doi:10.1016/j.watres.2013.01.008.
[175] X. Wang, V.W.C. Chang, C.Y. Tang, Osmotic membrane bioreactor (OMBR) technology for wastewater treatment and reclamation: Advances, challenges, and prospects for the future, J. Memb. Sci. 504 (2016) 113–132. doi:10.1016/j.memsci.2016.01.010.
[176] J. Wei, C. Qiu, C.Y. Tang, R. Wang, A.G. Fane, Synthesis and characterization of flat-sheet thin film composite forward osmosis membranes, J. Memb. Sci. 372 (2011) 292–302.
[177] C.Y. Tang, Y.N. Kwon, J.O. Leckie, Probing the nano- and micro-scales of reverse osmosis membranes-A comprehensive characterization of physiochemical properties of uncoated and coated membranes by XPS, TEM, ATR-FTIR, and streaming potential measurements, J. Memb. Sci. 287 (2007) 146–156.
[178] R.J. Petersen, Composite reverse osmosis and nanofiltration membranes, J. Memb. Sci. 83 (1993) 81–150.
[179] T.N. Corso, G.A. Schultz, S.J. Prosser, X. Huang, United States Patent: Separation media, multiple electrospray nozzle system and method, US 6596988 B2, 2003.
[180] L.A. Hoover, J.D. Schiffman, M. Elimelech, Nanofibers in thin-film composite membrane support layers: Enabling expanded application of forward and pressure retarded osmosis, Desalination. 308 (2013) 73–81.
[181] N.-N. Bui, J.R. McCutcheon, Nanofiber Supported Thin-Film Composite Membrane for Pressure-Retarded Osmosis, Environ. Sci. Technol. 48 (2014) 4129–4136.
[182] G. Han, B. Zhao, F. Fu, T.S. Chung, M. Weber, C. Staudt, C. Maletzko, High performance thin-film composite membranes with mesh-reinforced hydrophilic sulfonated polyphenylenesulfone (sPPSU) substrates for osmotically driven processes, J. Memb. Sci. 502 (2016) 84–93. doi:10.1016/j.memsci.2015.12.023.
[183] N. Widjojo, T.S. Chung, M. Weber, C. Maletzko, V. Warzelhan, The role of sulphonated polymer and macrovoid-free structure in the support layer for thin-film composite (TFC) forward osmosis (FO) membranes, J. Memb. Sci. 383 (2011) 214–223. doi:10.1016/j.memsci.2011.08.041.
[184] M. Yasukawa, S. Mishima, M. Shibuya, D. Saeki, T. Takahashi, T. Miyoshi, H. Matsuyama, Preparation of a forward osmosis membrane using a highly porous polyketone microfiltration membrane as a novel support, J. Memb. Sci. 487 (2015) 51–59. doi:10.1016/j.memsci.2015.03.043.
[185] R.J. Petersen, J.E. Cadotte, Thin Film Composite Reverse Osmosis Membranes, in: Handb. Ind. Membr. Technol., Noyes Publications, Park Ridge, NJ, 1990: pp. 307–348.
[186] A. Tiraferri, N.Y. Yip, W.A. Phillip, J.D. Schiffman, M. Elimelech, Relating performance of thin-film composite forward osmosis membranes to support layer formation and structure, J. Memb. Sci. 367 (2011) 340–352.
[187] L. Huang, S.S. Manickam, J.R. McCutcheon, Increasing strength of electrospun nanofiber

membranes for water filtration using solvent vapor, J. Memb. Sci. 436 (2013) 213–220.
[188] L. Huang, J.R. McCutcheon, Impact of support layer pore size on performance of thin film composite membranes for forward osmosis, J. Memb. Sci. 483 (2015) 25–33.
[189] L. Huang, N.-N. Bui, S.S. Manickam, J.R. McCutcheon, Controlling Electrospun Nanofiber Morphology and Mechanical Properties Using Humidity, J. Polym. Sci. Part B Polym. Phys. 49 (2011) 1734–1744.
[190] L. Huang, J.T. Arena, S.S. Manickam, X. Jiang, B.G. Willis, J.R. Mccutcheon, Improved mechanical properties and hydrophilicity of electrospun nanofiber membranes for filtration applications by dopamine modification, J. Memb. Sci. 460 (2014) 241–249.
[191] L. Song, M. Elimelech, Theory of Concentration Polarization in Crossflow Filtration, J. Chem. Soc. Faraday Trans. 91 (1995) 3389–3398.
[192] S. Zhang, K.Y. Wang, T.S. Chung, H. Chen, Y.C. Jean, G. Amy, Well-constructed cellulose acetate membranes for forward osmosis: Minimized internal concentration polarization with an ultra-thin selective layer, J. Memb. Sci. 360 (2010) 522–535.
[193] S. Petrik, M. Maly, Production Nozzle-Less Electrospinning Nanofiber Technology, Elmarco s.r.o. V Horkach 76/18, CZ-46007 Liberec, Czech Republic, n.d.
[194] Inovenso, Inovenso, Off. Page. (2016). http://inovenso.com/ (accessed January 1, 2016).
[195] J. Xu, C. Liu, P. Hsu, K. Liu, R. Zhang, Y. Liu, Roll-to-Roll Transfer of Electrospun Nanofiber Film for High-Efficiency Transparent Air Filter, Nano Lett. 16 (2016) 1270–1275.
[196] J. Yao, C. Bastiaansen, T. Peijs, High Strength and High Modulus Electrospun Nanofibers, Fibers. 2 (2014) 158–186. doi:10.3390/fib2020158.
[197] C. Carrizales, S. Pelfrey, R. Rincon, T.M. Eubanks, A. Kuang, M.J. McClure, G.L. Bowlin, J. Macossay, Thermal and mechanical properties of electrospun PMMA, PVC, Nylon 6, and Nylon 6,6, Polym. Adv. Technol. 19 (2008) 124–130.
[198] E. Zussman, M. Burman, A.L. Yarin, R. Khalfin, Y. Cohen, Tensile Deformation of Electrospun Nylon-6,6 Nanofibers, J. Polym. Sci. Part B Polym. Phys. 44 (2006) 1482–1489.
[199] F. Hang, D. Lu, R.J. Bailey, I. Jimenez-Palomar, U. Stachewicz, B. Cortes-Ballesteros, M. Davies, M. Zech, C. Bödefeld, A.H. Barber, In situ tensile testing of nanofibers by combining atomic force microscopy and scanning electron microscopy, Nanotechnology. 22 (2011) 365708.
[200] J. Yao, C. Bastiaansen, T. Peijs, High Strength and High Modulus Electrospun Nanofibers, Fibers. 2 (2014) 158–187.
[201] J.G. Cook, Handbook of Textile Fibres: Man-Made Fibres, Woodhead Publishing Limited, Cambridge, UK, 1984.
[202] A. Ajji, P. Coates, M. Dumoulin, I. Ward, Solid Phase Processing of Polymers, Carl Hanser Verlag, Munich, Germany, 2000.
[203] Hills Inc, Meltblown, Off. Page. (2015). http://hillsinc.net/ (accessed January 11, 2015).
[204] Xanofi, Shear Thinning, Off. Page. (2015). http://xanofi.com/ (accessed January 11, 2015).
[205] Fiberio Tech, Melt Spinning, Off. Page. (2015). http://fiberiotech.com/ (accessed January 11, 2015).
[206] Donaldson, Air Filtration, Off. Page. (2015). http://www.donaldson.com/en/ (accessed January 11, 2015).
[207] Dupont, Dupont, Prod. Page. (2016). http://www.dupont.com/ (accessed January 1, 2016).

[208] Y. Yuan, T.R. Lee, Contact Angle and Wetting Properties, in: G. Bracco, B. Holst (Eds.), Surf. Sci. Tech., Springer Berlin Heidelberg, Berlin, Heidelberg, 2013: pp. 3–34.
[209] L. Huang, J.T. Arena, J.R. McCutcheon, Surface modified PVDF nanofiber supported thin film composite membranes for forward osmosis, J. Memb. Sci. 499 (2016) 352–360.
[210] S.D. Arthur, STRUCTURE-PROPERTY COMPOSITE REVERSE RELATIONSHIP IN A THIN FILM OSMOSIS MEMBRANE, J. Memb. Sci. 46 (1989) 243–260.
[211] V. Freger, Swelling and Morphology of the Skin Layer of Polyamide Composite Membranes: An Atomic Force Microscopy Study, Environ. Sci. Technol. 38 (2004) 3168–3175.
[212] R.N. Wenzel, Surface Roughness and Contact Angle., J. Phys. Colloid Chem. 53 (1949) 1466–1467. doi:10.1021/j150474a015.
[213] M. Miwa, A. Nakajima, A. Fujishima, K. Hashimoto, T. Watanabe, Effects of the Surface Roughness on Sliding Angles of Water Droplets on Superhydrophobic Surfaces, Langmuir. 16 (2000) 5754–5760.
[214] S. Karan, Z. Jiang, A.G. Livingston, Sub-10 nm polyamide nanofilms with ultrafast solvent transport for molecular separation, Science. 348 (2015) 1347–1351.
[215] M. Tian, R. Wang, K. Goh, Y. Liao, A.G. Fane, Synthesis and characterization of high-performance novel thin film nanocomposite PRO membranes with tiered nano fiber support reinforced by functionalized carbon nanotubes, J. Memb. Sci. 486 (2015) 151–160.
[216] L.S. Schadler, S.C. Giannaris, P.M. Ajayan, Load transfer in carbon nanotube epoxy composites, Appl. Phys. Lett. 73 (1998) 3842–3844. doi:10.1063/1.122911.
[217] J.W. Gillespie Jr., J.B. DeVault, D.D. Edie, V. Gabara, T.J. Haulik, J.L. Kardos, L.S. Schadler, High-Performance Structural Fibers for Advanced Polymer Matrix Composites Committee, 2005. doi:10.177266/11268.
[218] H. Hou, J.J. Ge, J. Zeng, Q. Li, D.H. Reneker, A. Greiner, S.Z.D. Cheng, Electrospun Polyacrylonitrile Nanofibcrs Containing a High Concentration of Well-Aligned Multiwall Carbon Nanotubes, Chem. Mater. 17 (2005) 967–973.
[219] S.K. Smoukov, T. Tian, N. Vitchuli, S. Gangwal, P. Geisen, M. Wright, E. Shim, M. Marquez, J. Fowler, O.D. Velev, Scalable Liquid Shear-Driven Fabrication of Polymer Nanofibers, Adv. Mater. (2015) n/a-n/a. doi:10.1002/adma.201404616.
[220] S. Pan, Y. Dong, L. Zhong, Z. Yuan, Self-sustained hydrophilic nanofiber thin film composite forward osmosis membranes: Preparation, characterization and application fro simulated antibiotic wastewater treatment, J. Memb. Sci. 523 (2017) 205–215.
[221] E.L. Tian, H. Zhou, Y.W. Ren, X.Z. Wang, S.W. Xiong, Novel design of hydrophobic / hydrophilic interpenetrating network composite nanofibers for the support layer of forward osmosis membrane, Desalination. 347 (2014) 207–214.
[222] S. Loeb, S. Sourirajan, Saline Water Conversion—II, Adv. Chem. ACS. 38 (1963) 117–132. doi:10.1021/ba-1963-0038.
[223] S. Loeb, The Loeb-Sourirajan Membrane: How It Came About, ACS Symp. Ser. 153–154 (1981) 1–9. doi:10.1021/bk-1981-0153.ch001.
[224] H. Strathmann, P. Scheible, R.W. Baker, A rationale for the preparation of Loeb-Sourirajan-type cellulose acetate membranes, J. Appl. Polym. Sci. 15 (1971) 811–828. doi:10.1002/app.1971.070150404.
[225] W.J. Lau, A.F. Ismail, N. Misdan, M.A. Kassim, A recent progress in thin film composite membrane: A review, Desalination. 287 (2012) 190–199.

[226] N.K. Saha, S. V. Joshi, Performance evaluation of thin film composite polyamide nanofiltration membrane with variation in monomer type, J. Memb. Sci. 342 (2009) 60–69. doi:10.1016/j.memsci.2009.06.025.
[227] A.K. Ghosh, B.H. Jeong, X. Huang, E.M. V Hoek, Impacts of reaction and curing conditions on polyamide composite reverse osmosis membrane properties, J. Memb. Sci. 311 (2008) 34–45. doi:10.1016/j.memsci.2007.11.038.
[228] J.E. Gu, S. Lee, C.M. Stafford, J.S. Lee, W. Choi, B.Y. Kim, K.Y. Baek, E.P. Chan, J.Y. Chung, J. Bang, J.H. Lee, Molecular layer-by-layer assembled thin-film composite membranes for water desalination, Adv. Mater. 25 (2013) 4778–4782. doi:10.1002/adma.201302030.
[229] A.K. Ghosh, E.M.V. Hoek, Impacts of support membrane structure and chemistry on polyamide–polysulfone interfacial composite membranes, J. Memb. Sci. 336 (2009) 140–148.
[230] E.M.V. Hoek, S. Hong, M. Elimelech, Influence of membrane surface properties on initial rate of colloidal fouling of reverse osmosis and nanofiltration membranes, J. Memb. Sci. 188 (2001) 115–128. doi:10.1016/S0376-7388(01)00376-3.
[231] P.M. Johnson, J. Yoon, J.Y. Kelly, J. a. Howarter, C.M. Stafford, Molecular layer-by-layer deposition of highly crosslinked polyamide films, J. Polym. Sci. Part B Polym. Phys. 50 (2012) 168–173. doi:10.1002/polb.23002.
[232] A. Asatekin, S. Kang, M. Elimelech, A.M. Mayes, Anti-fouling ultrafiltration membranes containing polyacrylonitrile-graft-poly(ethylene oxide) comb copolymer additives, J. Memb. Sci. 298 (2007) 136–146. doi:10.1016/j.memsci.2007.04.011.
[233] A.C. Sagle, E.M. Van Wagner, H. Ju, B.D. McCloskey, B.D. Freeman, M.M. Sharma, PEG-coated reverse osmosis membranes: Desalination properties and fouling resistance, J. Memb. Sci. 340 (2009) 92–108. doi:10.1016/j.memsci.2009.05.013.
[234] S. Kasemset, A. Lee, D.J. Miller, B.D. Freeman, M.M. Sharma, Effect of polydopamine deposition conditions on fouling resistance, physical properties, and permeation properties of reverse osmosis membranes in oil/water separation, J. Memb. Sci. 425–426 (2013) 208–216. doi:10.1016/j.memsci.2012.08.049.
[235] G.Z. Ramon, M.C.Y. Wong, E.M.V. Hoek, Transport through composite membrane, part 1: Is there an optimal support membrane?, J. Memb. Sci. 415–416 (2012) 298–305. http://linkinghub.elsevier.com/retrieve/pii/S0376738812003778 (accessed July 15, 2014).
[236] T. Tsuru, S. Sasaki, T. Kamada, T. Shintani, T. Ohara, H. Nagasawa, K. Nishida, M. Kanezashi, T. Yoshioka, Multilayered polyamide membranes by spray-assisted 2-step interfacial polymerization for increased performance of trimesoyl chloride (TMC)/m-phenylenediamine (MPD)-derived polyamide membranes, J. Memb. Sci. 446 (2013) 504–512. doi:10.1016/j.memsci.2013.07.031.
[237] E.P. Chan, A.P. Young, J.H. Lee, C.M. Stafford, Swelling of ultrathin molecular layer-by-layer polyamide water desalination membranes, J. Polym. Sci. Part B Polym. Phys. 51 (2013) 1647–1655. doi:10.1002/polb.23380.
[238] S. Badalov, Y. Oren, C.J. Arnusch, Ink-jet printing assisted fabrication of patterned thin film composite membranes, J. Memb. Sci. 493 (2015) 508–514. doi:10.1016/j.memsci.2015.06.051.
[239] W. Choi, S. Jeon, S. Jin, H. Park, Y. Park, S. Nam, P. Soo, J. Suk, J. Choi, S. Hong, E.P. Chan, H. Lee, Thin film composite reverse osmosis membranes prepared via layered interfacial polymerization, J. Memb. Sci. 527 (2017) 121–128.

doi:10.1016/j.memsci.2016.12.066.
[240] S. Park, W. Choi, S. Nam, S. Hong, J. Suk, H. Lee, Fabrication of polyamide thin film composite reverse osmosis membranes via support-free interfacial polymerization, J. Memb. Sci. 526 (2017) 52–59.
[241] N. Chen, D.H. Kim, P. Kovacik, H. Sojoudi, M. Wang, K.K. Gleason, Polymer Thin Films and Surface Modification by Chemical Vapor Deposition: Recent Progress, Annu. Rev. Chem. Biomol. Eng. 7 (2016) 373–393. doi:10.1146/annurev-chembioeng-080615-033524.
[242] A. Jaworek, A.T. Sobczyk, Electrospraying route to nanotechnology: An overview, J. Electrostat. 66 (2008) 197–219. doi:10.1016/j.elstat.2007.10.001.
[243] A. Jaworek, A. Krupa, M. Lackowski, A.T. Sobczyk, T. Czech, S. Ramakrishna, S. Sundarrajan, D. Pliszka, Nanocomposite fabric formation by electrospinning and electrospraying technologies, J. Electrostat. 67 (2009) 435–438. doi:10.1016/j.elstat.2008.12.019.
[244] J. Fenn, M. Mann, C. Meng, S. Wong, C. Whitehouse, Electrospray ionization for mass spectrometry of large biomolecules, Science (80-.). 246 (1989) 64–71.
[245] J. Fenn, Electrospray ionization mass spectrometry: How it all began, J. Biomol. Tech. JBT. 13 (2002) 101–118. doi:PMC2279858.
[246] M. Wilm, Principles of electrospray ionization., Mol. Cell. Proteomics. 10 (2011) M111.009407. doi:10.1074/mcp.M111.009407.
[247] S.J. Gaskell, SPECIAL FEATURE : Electrospray : Principles and Practice, J. Mass Spectrom. 32 (1997) 677–688. doi:10.1002/(SICI)1096-9888(199707)32:7<677::AID-JMS536>3.0.CO;2-G.
[248] J.B. Fenn, Electrospray wings for molecular elephants (Nobel lecture), in: Angew. Chemie - Int. Ed., 2003: pp. 3871–3894. doi:10.1002/anie.200300605.
[249] a. Jaworek, Micro- and nanoparticle production by electrospraying, Powder Technol. 176 (2007) 18–35. doi:10.1016/j.powtec.2007.01.035.
[250] X. Hou, K.L. Choy, Deposition mechanism and structural characterization of TiO2 films produced using ESAVD method, Surf. Coatings Technol. 180–181 (2004) 15–19. doi:10.1016/j.surfcoat.2003.10.023.
[251] N.M. Muhammad, S. Sundharam, H.W. Dang, A. Lee, B.H. Ryu, K.H. Choi, CIS layer deposition through electrospray process for solar cell fabrication, Curr. Appl. Phys. 11 (2011) 68–75. doi:10.1016/j.cap.2010.11.059.
[252] J.-U. Park, M. Hardy, S.J. Kang, K. Barton, K. Adair, D. kishore Mukhopadhyay, C.Y. Lee, M.S. Strano, A.G. Alleyne, J.G. Georgiadis, P.M. Ferreira, J.A. Rogers, High-resolution electrohydrodynamic jet printing, Nat. Mater. 6 (2007) 782–789. doi:10.1038/nmat1974.
[253] R. Saf, M. Goriup, T. Steindl, T.E. Hamedinger, D. Sandholzer, G. Hayn, Thin organic films by atmospheric-pressure ion deposition., Nat. Mater. 3 (2004) 323–329. doi:10.1038/nmat1117.
[254] R. Chandrasekhar, K.L. Choy, Electrostatic spray assisted vapour deposition of fluorine doped tin oxide, J. Cryst. Growth. 1 (2001) 215–221.
[255] A.A. van Zomeren, E.M. Kelder, J.C.M. Marijnissen, J. Schoonman, The production of thin films of LiMn2O4 by electrospraying, J.Aerosol Sci. 25 (1994) 1229–1235.
[256] B. Su, K.L. Choy, Structure and growth characteristics of BaZrO3 films produced using an electrostatic assisted aerosol–gel deposition method, J. Mater. Chem. 9 (1999) 1629–

1633.
[257] A.M. Gañán-Calvo, J. Dávila, A. Barrero, Current and droplet size in the electrospraying of liquids. Scaling laws, J. Aerosol Sci. 28 (1997) 249–275. doi:10.1016/S0021-8502(96)00433-8.
[258] J. Sakata, M. Mochizuki, Preparation of organic thin films by an electrospray technique I. Crystal forms and their orientation in poly(vinylidene flouride) films, Thin Solid Films. 195 (1991) 175–184. doi:10.1016/0040-6090(91)90269-4.
[259] N. Dam, M.M. Beerbom, J.C. Braunagel, R. Schlaf, Photoelectron spectroscopic investigation of in-vacuum-prepared luminescent polymer thin films directly from solution, J. Appl. Phys. 97 (2005) 24909. doi:10.1063/1.1833582.
[260] I.B. Rietveld, K. Kobayashi, H. Yamada, K. Matsushige, Morphology control of poly(vinylidene fluoride) thin film made with electrospray, J. Colloid Interface Sci. 298 (2006) 639–651. doi:http://dx.doi.org/10.1016/j.jcis.2005.12.028.
[261] I.B. Rietveld, K. Kobayashi, H. Yamada, K. Matsushige, Electrospray deposition producing ultra-thin polymer films with a regular surface structure, Soft Matter. 5 (2009) 593. doi:10.1039/b812702f.
[262] B. Hoyer, G. Sørensen, N. Jensen, D.B. Nielsen, B. Larsen, Electrostatic spraying: a novel technique for preparation of polymer coatings on electrodes., Anal. Chem. 68 (1996) 3840–3844. doi:10.1021/ac9605509.
[263] A. Jaworek, Electrospray droplet sources for thin film deposition, J. Mater. Sci. 42 (2007) 266–297. doi:10.1007/s10853-006-0842-9.
[264] N. Lavielle, A. Hébraud, G. Schlatter, L. Thöny-Meyer, R.M. Rossi, A.-M. Popa, Simultaneous electrospinning and electrospraying: a straightforward approach for fabricating hierarchically structured composite membranes., ACS Appl. Mater. Interfaces. 5 (2013) 10090–7. doi:10.1021/am402676m.
[265] M. Yanilmaz, Y. Lu, M. Dirican, K. Fu, X. Zhang, Nanoparticle-on-nanofiber hybrid membrane separators for lithium-ion batteries via combining electrospraying and electrospinning techniques, J. Memb. Sci. 456 (2014) 57–65. doi:10.1016/j.memsci.2014.01.022.
[266] O. V. Salata, Tools of Nanotechnology: Electrospray, Curr. Nanosci. 1 (2005) 25–33. doi:10.2174/1573413052953192.
[267] J.B. Fenn, M. Mann, C.K. Meng, S.F. Wong, Electrospray ionization-principles and practice, Mass Spectrom. Rev. 9 (1990) 37–70.
[268] C. Mundo, M. Sommerfeld, C. Tropea, Droplet-Wall collisions: Experimental studies of the deformation and breakup process, Int. J. Multiph. Flow. 21 (1995) 151–173.
[269] V. Bergeron, D. Bonn, J. Martin, L. Vovelle, Controlling droplet deposition with polymer additives, Nature. 405 (2000) 772–5. doi:10.1038/35015525.
[270] M.A. Henderson, J.S. McIndoe, Ionic liquids enable electrospray ionisation mass spectrometry in hexane, Chem. Commun. (2006) 2872–2874. doi:10.1039/b606938j.
[271] M. Hirose, H. Ito, Y. Kamiyama, Effect of skin layer surface structures on the flux behaviour of RO membranes, J. Memb. Sci. 121 (1996) 209–215. doi:10.1016/S0376-7388(96)00181-0.
[272] V. Freger, Nanoscale heterogeneity of polyamide membranes formed by interfacial polymerization, Langmuir. 19 (2003) 4791–4797. doi:10.1021/la020920q.
[273] S.Y. Kwak, S.G. Jung, S.H. Kim, Structure-motion-performance relationship of flux-enhanced reverse osmosis (RO) membranes composed of aromatic polyamide thin films,

Environ. Sci. Technol. 35 (2001) 4334–4340. doi:10.1021/es010630g.
[274] L. Lin, C. Feng, R. Lopez, O. Coronell, Identifying facile and accurate methods to measure the thickness of the active layers of thin-film composite membranes - A comparison of seven characterization techniques, J. Memb. Sci. 498 (2016) 167–179. doi:10.1016/j.memsci.2015.09.059.
[275] Spraying System Co., Automatic and Air Atomizing Spray Nozzles, Spray Syst. Co. (2015) 1. http://www.spray.com/cat76/automatic/offline/download.pdf.
[276] J.R. Welty, C.E. Wicks, R.E. Wilson, G.L. Rorrer, Fundamentals of Momentum, Heat, and Mass Transfer, 2008. doi:10.1016/0017-9310(70)90063-3.